ANALYSIS OF SURFACE AND DOWNHOLE MICROSEISMIC MONITORING COUPLED WITH HYDRAULIC FRACTURE MODELING IN THE WOODFORD SHALE

by

Carl Wilbur Neuhaus

AFFIDAVIT

I declare in lieu of oath that I have composed this thesis and performed the associated research myself using only literature cited in this volume.

Leoben, Austria

Date:_____

Signed:_____

Carl Wilbur Neuhaus

Author

ABSTRACT

The work presented in this thesis focuses on using analyzed surface and downhole microseismic data for a horizontal well in the Woodford Shale in Oklahoma and compares those results with calibrated hydraulic fracture modeling. It shows the importance of microseismic monitoring of hydraulic fracturing treatments and discusses the information that can be gained by thoroughly analyzing the recorded data in conjunction with hydraulic fracture modeling. Technologies to accurately monitor fracture growth as well as to determine hydraulic fracture properties are necessary to improve our understanding of the processes occurring in the reservoir in order to optimize stimulation treatments.

Hydraulic fracture models were created for each of five stages with a three-dimensional modeling software, incorporating available petrophysical data in order to match the recorded treatment pressure and microseismic data. The hydraulic fracture models for this thesis were developed in three steps. First, a basic model for each step was built incorporating available logs, and modifying parameters to achieve a reasonable representation of the reservoir geology. These models were run to simulate fracture growth and generate pumping data. The second step was to match the observed pressure to the simulated pressure for each stage. In the third step this preliminary calibration was further enhanced and verified by matching fracture geometry to microseismic data to produce a model that reflects actual reservoir parameters on all three levels (i.e. rock properties/logs, treatment pressure data, and microseismic recordings).

Further analysis investigated how well surface and downhole microseismic data match, what difference they produced in a match if used exclusively, the errors that are associated with the data set, and if the degree of complexity of the created fractures could be assessed from the available data. It also evaluated the data in terms of reservoir characterization since communication between the hydraulic fracture network and natural fractures and faults can affect the efficiency of a stimulation treatment. The availability of both surface and downhole microseismic recordings for a multi-stage

treatment in one well provided the opportunity to directly compare the two data sets on different levels. In order to evaluate how reliable and accurate the individual technologies are, and to determine advantages and disadvantages, this thesis investigated the congruency between the surface and downhole data, as well as tried to estimate how many events are actually necessary to produce a good and fairly accurate match with a hydraulic fracture model. In the ensuing step, the recorded data was analyzed in terms of fracture complexity, as well as in terms of the relationship between the magnitude of events, time and location of occurrence, and seismic deformation in conjunction with reservoir characterization.

The fracture models produced good matches for both pressure and fracture geometry, with average deviations of -17% for the longitudinal stretch and -10% for the fracture length. Fracture height, on the other hand, could not be very well matched, with average deviations of -59% for the longitudinal models and -55% for the transverse models, which could be attributed to re-fracturing of parts and leak-off into parts of the reservoir that were already stimulated in a previous stage. Surface and downhole microseismic data overlapped in certain regions and picked up on different things in others, giving a more complete picture of microseismic activity and fracture growth if used together. However, they deviated in terms of vertical event location with surface data showing more upward growth and downhole data showing more downward growth.

In general, the downhole microseismic data showed that the stimulation treatment was successful in creating a fairly complex hydraulic fracture network for all stages, with microseismic recordings making flow paths visible governed by both paleo and present day stress. A plot of event magnitude versus event-to-receiver distance identified Stages III and V as the stages with the most events of larger magnitude, implying interaction with pre-existing structures which facilitate large magnitude events. This was supported by analyzing the speed of event generation, as well as the cumulative moment for all stages. Overall, the link between ‘loud’ events and the intersection of faults lead to the assumption that the fracture network generated during Stage V most likely communicated with a fault structure.

TABLE OF CONTENTS

LIST OF FIGURES

LIST OF TABLES

ACKNOWLEDGMENTS

First and foremost, I would like to thank my advisor Univ.-Prof. Dipl.-Ing. Dr. mont. Herbert Hofstätter for his ceaseless support throughout the years. Dr. Jennifer L. Miskimins, thank you for giving me the opportunity to work on this challenging project. I would also like to express my gratitude and appreciation to Dr. Leen Weijer and Dr. Azra Tutuncu for their valuable feedback and support. I am deeply indebted to the FAST Consortium for generously funding my work and for providing the chance to get first-hand industry feedback.

Furthermore, I would like to thank the Petroleum Engineering Department Head at the Colorado School of Mines Dr. Ramona M. Graves for her support and integrity, as well as her wit and humor which made my stay in Golden an unforgettable experience. A special thanks goes to Denise Winn-Bower for her open door and for resolving every imaginable problem that occurred along the way. Thank you so much for your ceaseless help and for constantly going way beyond the scope of your job description to make sure everything is going to be fine. Patrizia Haberl and Irene Jauck, thank you not only for resolving countless small issues but also for always making time for a little chat.

I am indebted to Devon Energy Corporation for providing the data set that made this work possible, as well as to the Stimlab Division of Core Laboratories, Pinnacle a Halliburton Service, and Transform Software and Services for providing software to analyze, evaluate, and visualize the data. Mr. Wally Frank, thank you for helping me to get all the data I needed. Mr. Rod Gertson, I am very grateful for your input and feedback. Thank you for taking the time to answer my questions. Mrs. Amelia Webster, thank you for helping me to learn how to use the Transform software.

Zu guter Letzt möchte ich meinen Eltern DDr. Barbara Neuhaus und Jörg W. Neuhaus, sowie meiner Großmutter Barbara Warbichler, für ihre bedingungslose Liebe und Unterstützung in allen meinen Anstrengungen danken. Carola, danke, dass Du zu Hause alles zusammen hälst. Ohne euren ungebrochenen Glauben an mich könnte ich meine Träume nicht verwirklichen. Diese Arbeit ist euch gewidmet.

CHAPTER 1

INTRODUCTION

This thesis focuses on using analyzed surface and downhole microseismic data for a horizontal well in the Woodford Shale in Oklahoma and compares those results with calibrated hydraulic fracture modeling. Hydraulic fracture models were created for each of five stages with a three-dimensional modeling software, incorporating available petrophysical data in order to match the recorded treatment pressure and microseismic data. Further analysis investigates how well surface and downhole microseismic data match, what difference they produce in a match if used exclusively, the errors that are associated with the data set, and if the degree of complexity of the created fractures can be assessed from the available data. This work also evaluates the relationship between event magnitude, time and location of occurrence, and seismic deformation.

1.1 Objectives

This project shows the importance of microseismic monitoring of hydraulic fracturing treatments and the information that can be gained by thoroughly analyzing the recorded data in conjunction with hydraulic fracture modeling.

The following objectives are accomplished in this thesis:

1. Develop hydraulic fracture models for each stage (five total) that match actual pressure data only for a horizontal well data set in the Woodford shale;
2. Develop hydraulic fracture models for each stage that match microseismic and pressure data;
3. Investigate the congruency between the surface and downhole microseismic data, and how many microseisms are actually needed to produce a match with a model;

4. Analyze the recorded data in terms of fracture complexity;
5. Evaluate the perceived accuracy of the processed data and estimate the error of the microseismic event location; and,
6. Investigate the relationship between the magnitude of events, time and location of occurrence, and seismic deformation in conjunction with reservoir characterization.

1.2 Data Set

The analyzed data set was obtained from a five-stage hydraulic fracturing treatment of a horizontal well in Hughes County, Oklahoma. Microseismic recordings for Stages 2-5 were available for 9-sensor downhole monitoring from an offset well, as well as recordings for Stages 1-5 for surface monitoring. Also available were hydraulic fracturing pump data and a microseismic quality report for the downhole recordings. The quality report includes plots of:

- average noise level vs. time,
- sensor specific noise levels,
- signal-to-noise ratio statistics,
- hodogram consistency,
- time-residual statistics,
- moment magnitude vs. time and vs. distance,
- data and event confidence, and
- location error.

1.3 Geology

The Woodford Shale spreads from Kansas to west Texas and was first produced in southeast Oklahoma in 1939. Although hydrocarbon production in this region originally occurred from deeper horizons, the Woodford Shale now shows the highest drilling activity for that area of Oklahoma (Vulgamore et al., 2007). The most prominent deposition of the Woodford Shale is found in the western Arkoma Basin,

which is a restricted foreland basin, stretching from southeast Oklahoma to northwest Arkansas (Jacobi et al., 2009).

Petrophysically, the Woodford Shale shows very high gamma ray measurements, has water saturations from 30-45% and is lightly under-pressured with pore pressure gradients ranging from 0.35-0.45 psi/ft (Vulgamore et al., 2007). Logs and cores indicate that it is organic-rich and siliceous with 48-74% quartz, 3-10% feldspar, 7-25% illite clay, 0-10% pyrite, 0-5% carbonate, and 7-16% kerogen (Waters et al., 2009).

As of January 2009, over 520 Woodford Shale wells have been completed in the Arkoma Basin since January 2004, most being horizontal and multi-stage hydraulically fractured (Waters et al., 2009). Well depths range from 900 ft (TVD) in northeast Oklahoma up to 13,000 ft (TVD) in west Texas. As of 2007, more than 100 stages of hydraulic fracturing treatments have been monitored and analyzed with surface tiltmeter and microseismic mapping. Hydraulic stimulation seems to create complex fracture networks showing various orientations comparable to treatments in the Barnett Shale, although with a higher degree of communication with pre-existing fractures and faults (Vulgamore et al., 2007).

1.4 Benefits to Industry

Analyzing simultaneously acquired downhole and surface microseismic data in terms of congruency and respective bias of the data set promotes an understanding of which technique leads to an accurate picture of the hydraulic fracturing treatment. Matching simulation models with microseismic data enhances the accuracy of such models for a particular region as well as their predictive qualities. Evaluating the observed complexity of the created fracture network and the interaction with natural fractures is beneficial for characterizing the stimulated reservoir. If done thoroughly, future hydraulic fracturing treatments of the same formation can be optimized increasing production while decreasing costs.

Future research on enhancing the processing and analysis of microseismic data could lead to real-time detection of screen-outs, enabling the engineer to intervene and improve proppant placement (Maxwell et al., 2002). Improvement in real-time

monitoring could also lead to detecting unwanted re-fracturing of previous stages, which decreases the efficiency of a treatment. Mutiplet identification can be used to restrict cross-stage fracturing by recognizing it early and counteract by modifying fluid properties or injection rate (Eisner et al., 2006).

CHAPTER 2

LITERATURE REVIEW

Technologies to accurately monitor fracture growth as well as to determine hydraulic fracture properties are necessary to improve our understanding of the processes occurring in the reservoir in order to optimize stimulation treatments. There are surface and downhole, real-time and post-treatment, direct and indirect, and near wellbore and far field methods. Table 2.1 gives an overview of technologies currently used in the industry.

Table 2.1: Capabilities and Limitations of Fracture Diagnostics (from Cipolla and Wright, 2000)

Technology	*Azimuth*	*Height*	*Length*	*Asymmetry*	*Width*	*Dip*	*Direct/ Indirect*	*Range*
Microseismic	X	X	X	O		O	D	Far Field
Tiltmeter (downhole)	O	X	X	O	O		D	Far Field
Tiltmeter (surface)	X	O	O	O		X	D	Far Field
Radioactive Tracer	O	O			O		D	Near Wellbore
Temperature Log		O					D	Near Wellbore
Fracture Models		O	O		O		I	Far Field
Well Testing			O		O		I	Far Field
Production Analysis			O		O		I	Far Field

X … can determine
O … may determine
D … direct diagnostic
I … indirect diagnostic

2.1 Microseismic Imaging

For over ten years, microseismic monitoring has been a valuable tool in the hydraulic fracturing industry. Ever since its commercialization, it has gained more and more popularity due to improved equipment that can be used repeatedly, improved processing and understanding of limitations, improved methods of analyzing the data, and due to its utilization in unconventional reservoirs (Weijers, 2010). As proven by field studies, hydraulic fractures are far more complicated structures than had previously been assumed. They are usually not as geometrically simple as the industry would like to think they are. It is important to know how and where the fracture is growing with time as well as its final length, azimuth and inclination to optimize hydraulic fracture modeling. Microseismic fracture monitoring can provide this information (Quirein et al., 2006). Furthermore fracturing is driven by economic issues, as there is an exponential relationship between treatment costs and length; and even though production can increase substantially with length, the additional production due to the treatment tends to become less with increasing (half-) length (Zhu et al., 1996).

Due to fracture growth and fluid leak-off very small earthquakes (i.e. microseisms) are created in the reservoir. During the hydraulic fracturing treatment the fracture gains width, height and length under very high pressure, which changes the downhole stress environment as well as the pore pressure (Warpinski et al., 2006). The basic principle can be seen in Fig. 2.1.

> "These earthquakes are shear slippages that generally occur along existing failure planes. Such failure planes could be faults, natural fractures, bedding planes, shale dewatering features, and various other discontinuities in the rock. These microseisms form a 'cloud' around the hydraulic fracture, outlining its shape and azimuth."
>
> (Warpinski et al., 2006)

Factors influencing the generation of microseismic events as well as their magnitude can be separated into formation conditions and conditions caused by the hydraulic fracture itself, which depend on reservoir as well as treatment properties. Crucial for the occurrence of events is also "the existence of favorably oriented

weakness planes such as natural fractures or bedding planes" (Warpinski et al., 2004). A list of these type of potential factors include:

- Formation factors:
  - Stress
  - Pore pressure
  - Mechanical properties
  - Planes of weakness
- Fracture generated factors:
  - Stress
  - Leak-off
  - Temperature

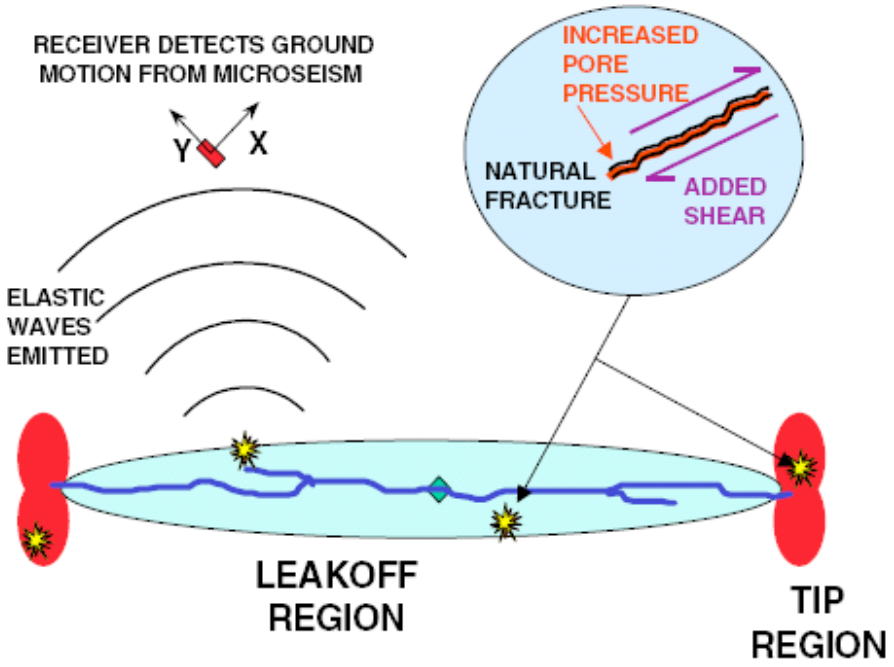

Figure 2.1: Principle of microseismic fracture mapping (from Cipolla and Wright, 2000).

The width of the zone in which microseismic events are generated mainly depends on the leak-off behavior of the formation. The expansion of the fracture and high shear stress generated around the fracture induce stress changes in the reservoir. Fluid leak-off also governs the changes in pore pressure, although the fluids present

determine the amount of change. In oil reservoirs, pressure variations can be transmitted over larger distances, creating a larger zone of microseismic activity. In gas reservoirs on the other hand, the microseismic cloud would generally be narrower and somewhat smaller. In this case, the compressibility of the reservoir fluid is much higher and there is only a limited amount of fracturing fluid available to better conduct the change in pressure (Cipolla et al., 2008).

Microseismic monitoring can also be used in a variety of other applications apart from hydraulic fracturing. In the Valhall and Cold Lake Fields, it successfully identified active shear deformation that caused well and casing failure. In the Ekofisk Field, microseismic imaging was used to map the fault system under a gas accumulation. Outside of the petroleum industry it is employed to determine the stability of excavations and mining operations (Maxwell and Urbancic, 2001).

The accuracy of determining the actual position of the microseismic event in the reservoir is limited and depends on:

- the accuracy of receiver positioning in location as well as orientation;
- knowledge of the geological velocity structure; and
- the carefulness of picking the direct arrivals of the acoustic wave, as well as, appraising the particle motion (Le Calvez et al., 2005).

Restraints can be related to the tool itself and minimized by adjusting and improving the tool (e.g. sensors, electrical noise, vector fidelity, coupling or sampling rates) but may also be dependent on signal processing, correlations or adaptive filtering (Le Calvez et al., 2005).

2.1.1 Active

Active microseismic imaging is based on the same method as active seismic for reservoir monitoring and generates a geological image. A source emits acoustic waves, which are then transmitted through the formation and propagate through the fracture to be recorded by a receiver. Acoustic waves will excite diffractions at the fracture tip, which can be localized by measuring direct compressional and shear diffractions (Groenenboom et al., 2001).

A process called ‘shear wave shadowing’ is observed when shear waves hit a hydraulic fracture perpendicularly. In this case, due to the shear wave particle motion, which is normal to the direction of propagation, the shear wave will not be transmitted through the fracture. The main fracture is surrounded by somewhat weakened rock, which may also cause an offset in shear wave propagation and of the acoustic velocity of the rock (Wills et al., 1992).

Shear waves originating from an offset well are analyzed in terms of amplitude and travel time at the receiver and are able to give an image of the extent of the created fracture. Fracturing experiments using water, without proppants to keep the fracture open, have been conducted to investigate fracture closure. Shear wave arrivals were proven to be restored to initial amplitude and travel time at the time estimated from pressure decline analysis for fracture closure to occur (Wills et al., 1992).

2.1.2 Passive

As mentioned, stress and pressure changes in the reservoir, due to injection, production, or hydraulic stimulation, generate seismic events where these changes cause rock to fail. Passive microseismic monitoring records the compressional (P or primary) and shear (S or secondary) waves emitted by these events as seen in Fig. 2.2. P- and S-waves propagate through the formation at different velocities and therefore arrive at a receiver at different times. A simple array of three receivers with a velocity model for that particular geology can determine the location of the event, also called the hypocenter, by recording these arrival times and triliterating the origin (Eisner et al., 2009).

The longer the emitted waves travel, the longer and more significant the difference between P- and S-wave arrival will be. As each receiver in the array records a different arrival time separation, the traveled distance of the waves can be determined.

> “For a homogeneous velocity model with only a single P-wave velocity and a single S-wave velocity, this is also the direction toward the microseismic event. With azimuth, inclination, and distance, the location of the event is determined. In a more general-layered

medium, the location of a microseism is more complicated, because the ray-paths through the various layers need to be factored into the determination of event location, but the overall influence of azimuth, P-S-separation, and [receiver] move-out is still the same."

(Zimmer et al., 2009)

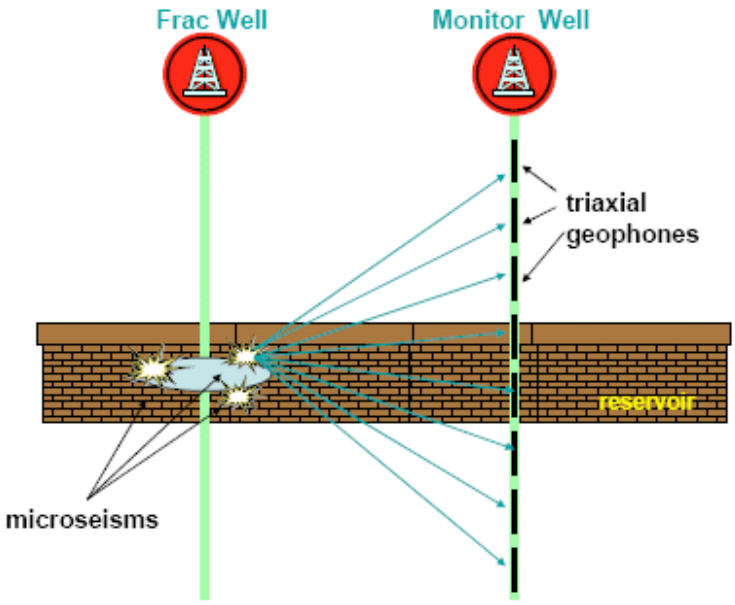

Figure 2.2: Generated microseisms are detected by receivers in monitoring well (from Quirein et al., 2006).

2.1.2.1 Downhole

Microseismic events can be measured downhole by lowering an array of receivers into either a monitoring well, or by monitoring the treatment with receivers directly in the well that is actually being hydraulically fractured. If the array covers a depth from above the zone being fractured to below that zone, the measurements tend to be the most accurate. However this may not always be possible (Mohammad, 2009).

Originating at the point of tensile failure and shear slippage, the P- and S-waves travel through the formation, undergoing attenuation and generating secondary events, such as:

- reflections,
- refractions, and
- mode conversions at interface boundaries.

The effective composite acoustic wave is a superposition of the direct waves with waves coming from these secondary events.

> "Within most formations of interest, the first wavelet in the complex wave field is the direct P-wave energy that has traveled in a quasi straight line from the source mechanism to the observation location. For the direct P-wave to arrive first and along a straight path, the formation must be weakly layered and must not contain large seismic velocity contrasts. If these conditions are met, then one can assume that the first arrival in the wave field has a particle motion that is collinear with the straight line path between the microseismic origin and the observation point."
>
> (Sleefe et al., 1995)

The general relationship between distance and time is given with velocity

$$v = \frac{dx}{dt} \qquad \text{(Eq. 2.1)}$$

or without differentials:

$$v = \frac{x}{t} \qquad \text{(Eq. 2.2)}$$

where,

v … velocity [ft/sec]
x … distance [ft]
t … time [sec]

Recording the acoustic waves arriving at the receiver we can pick arrival times for both P- and S-waves, as seen in Fig. 2.3. The difference between the tagged arrival

time and the actual time of origin is the time it took the acoustic signal to travel. Eq. 2.2 can therefore be modified to:

$$x = v \cdot (t_a - t_0) \qquad \text{(Eq. 2.3)}$$

or for multiple receivers and both waveforms:

$$x_n = v_P \cdot (t_{Pan} - t_0) = v_S \cdot (t_{San} - t_0) \qquad \text{(Eq. 2.4)}$$

where,

x_n	…	distance of event from n-th receiver [ft]
v_P	…	compressional velocity [ft/sec]
t_{Pan}	…	arrival time of P-wave at n-th receiver [sec]
t_a	…	tagged arrival time [sec]
t_0	…	time of event generation [sec]
v_S	…	shear velocity [ft/sec]
t_{San}	…	arrival time of S-wave at the n-th receiver [sec]

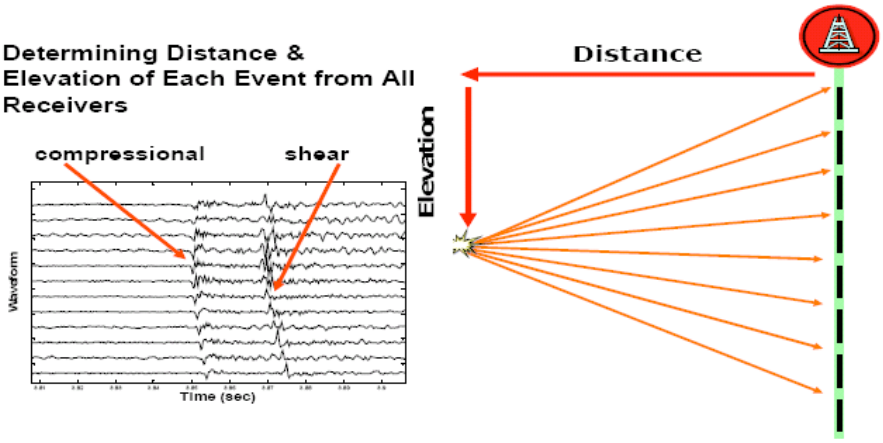

Figure 2.3: Arrival time picks and distance determination (from Quirein et al., 2006).

This can now be rearranged to give the distance of the event from the receiver, which then can be used to calculate the actual time of event generation for event-location versus time purposes.

$$x_n = \frac{v_P v_S}{v_P - v_S} \cdot (t_{San} - t_{Pan}) \qquad \text{(Eq. 2.5)}$$

It is obvious that the accuracy of both the calculated distance between event and receiver and also t_0 depends on the accuracy of the seismic velocities as well as the arrival time picks (Quirein et al., 2006).

Depending on the circumstances and field configuration, more than one well can be used to monitor the treatment and improve the accuracy of the determined event location. In this situation more events should be detected and therefore produce a more precise picture of fracture growth. However, due to the small magnitude of microseismic events and common well spacing, all off-set wells will not necessarily detect the same events (Eisner et al., 2009).

2.1.2.2 Surface

Hydraulic fracture treatments can also be monitored from the surface with an array of geophones, similar to how active reservoir seismic monitoring is done. It can be beneficial in two ways: if the treatment is already being monitored by downhole measurement, it gives additional information, and in case there is no downhole monitoring available, from either an offset well or the treatment well itself, it is an alternative source of information.

There are advantages of surface over downhole imaging as well as disadvantages: surface receivers usually have a higher threshold for detecting events and are only able to record lower frequency signals, but due to the geometry and extent of the array they provide a broader and more uniform coverage. However, downhole receivers are usually closer to the area of treatment, if not in the treatment well itself, and are therefore able to record more signals; although, depending on the monitoring well location, probably with a bias. For surface geophones it may be hard to detect microseisms if they have to travel through a couple of thousand feet of formation, so one technique exclusively will always be a trade-off (Abbot et al., 2007).

An additional benefit of surface imaging is a more stable velocity model. Surface monitoring only requires the P-wave velocity model, which can be determined by:

- sonic logs,

- a checkshot/VSP, or
- a 3D velocity model from earlier regular 3D surface seismics.

However, the vertical uncertainty will not be as well constrained as the horizontal uncertainty (Eisner et al., 2009). Table 2.2 compares downhole, dual downhole, and surface monitoring in terms of errors in the vertical and horizontal component of the event location, and how sensitive the techniques are to the velocity model.

Table 2.2: Monitoring Methods and Associated Errors (from Eisner et al., 2009)

Method	*Error in vertical position*	*Error in horizontal position*	*Sensitivity to the velocity model*
Surface (1:1 depth:offset)	Several 10s (40+) of meters for most common scenarios	No specific bias in any direction, below 10 m for most common scenarios	Vertical position is very sensitive, horizontal position is very robust
Single Downhole	1-10s of meters for most common scenarios	Significantly better in radial direction, azimuthal uncertainty in 10s of meters	All coordinates are affected (poor vertical, and horizontal)
Dual Downhole	Similar as single monitoring array with good velocity model	Significantly dependent on relative position to the plane of symmetry	Very sensitive

2.2 Geology

Even though gas production from shale reservoirs has just recently expanded throughout the U.S., the idea has been around for quite some time (an overview of U.S. shale gas production can be seen in Fig. 2.4). In Fredonia, NY, natural gas was produced from a Devonian shale as early as 1821, and during the late 1880's Appalachian Devonian formations delivered relatively substantial amounts (Matthews et al., 2007). Hydrocarbon production from shale reservoirs today would not economically successful without the employment of two technologies: horizontal drilling and well stimulation. Ever since the first development of the Barnett Shale in the 1980's, the constant improvement of these core technologies has enabled the industry to further explore shale reservoirs with advanced horizontal wells and hydraulic fracturing

treatments, i.e. better reservoir penetration due to longer wells and multiple fracturing stages (Arthur et al., 2009).

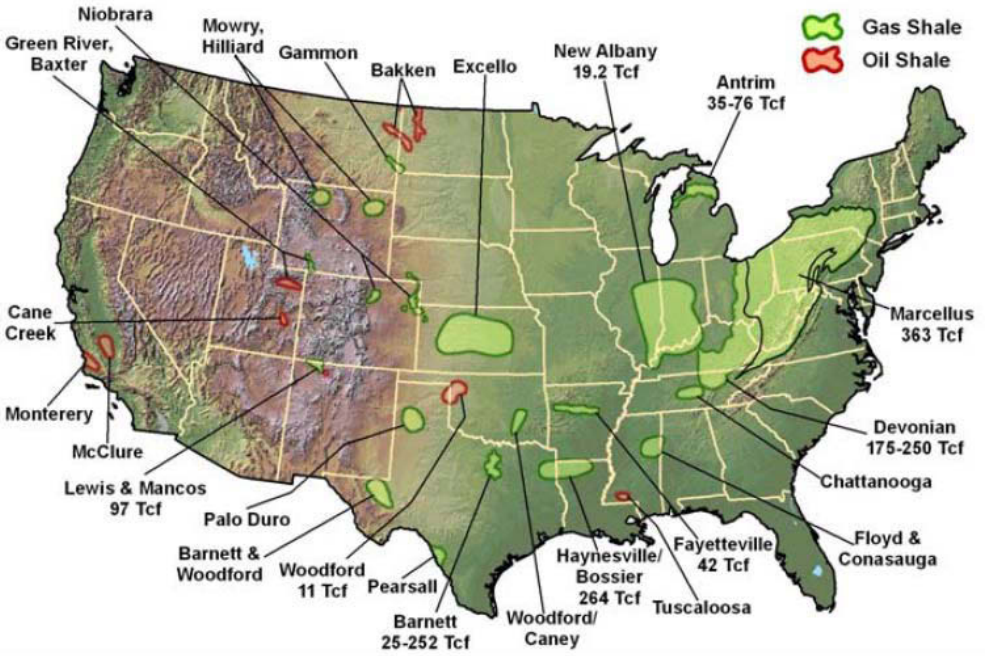

Figure 2.4: Shale basins of the U.S. with estimated gas reserves. North is up (from Arthur et al., 2009).

The most 'famous' of the North-American shale formations, the Barnett Shale, has encouraged companies to explore for similarly successful reservoirs. Being part of the so-called black shale belt, which can be seen in Fig. 2.5, the Woodford Shale is such a formation. It spreads from Kansas to west Texas and was first produced in southeast Oklahoma in 1939. Although hydrocarbon production in this region originally occurred from deeper horizons, the Woodford Shale now shows the highest drilling activity for that area of Oklahoma (Vulgamore et al., 2007).

The most prominent deposition of the Woodford Shale is found in the western Arkoma Basin, a restricted foreland basin, stretching from southeast Oklahoma to northwest Arkansas, as seen in Fig. 2.6 (Jacobi et al., 2009). As the Ouachita thrust front advanced westwards, the Arkoma Basin formed along a fault boundary together with other basins. The Woodford Shale, dating from late Devonian to early Mississippian, is overlain by the Caney Shale with a clear boundary formed by the thick, silty, clay-rich

Mayes Limestone from the Mississippian. Below the Woodford, a carbonate formation, the Hunton, is found. Its surface shows some erosion with deep channels sometimes even eroding all of it. Depending on the degree of erosion, the Woodford can be very thick in these channels, in cases even being in direct contact with the Sylvan Shale or the deeper Viola Limestone from the Ordovician, both deposited before the Hunton. On the other hand the Woodford can also be thin if it rests on un-eroded plateaus of the Hunton, resulting in a total thickness variation of 50 – 250 ft (Jacobi et al., 2009).

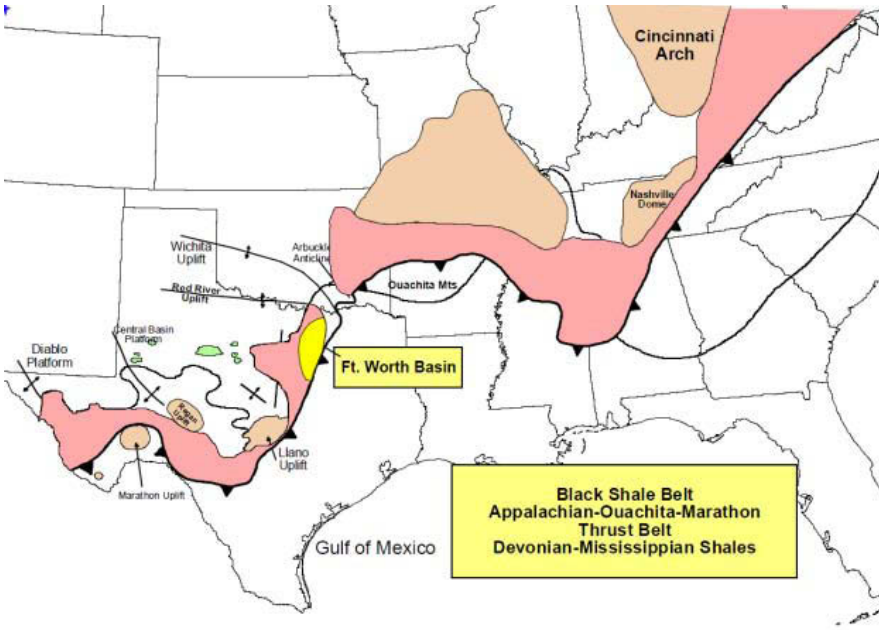

Figure 2.5: The black shale belt. North is up (from Vulgamore et al., 2007).

> "Shale is a sedimentary rock predominantly comprised of consolidated clay sized particles that were deposited as muds in low-energy depositional environments. Low-energy depositional environments include tidal flats and deep water basins where the fine-grained particles fall out of suspension in quiet waters. Deposited with these very fine grained sediments is organic matter in the form of algae, plant, and animal derived organic debris. The naturally tabular clay grains tend to lay flat as the sediments accumulate and subsequently become compacted as additional sediments are deposited. These muds lithify into thin laminar bedding that forms thinly layered shale rock."
>
> (Arthur et al., 2009)

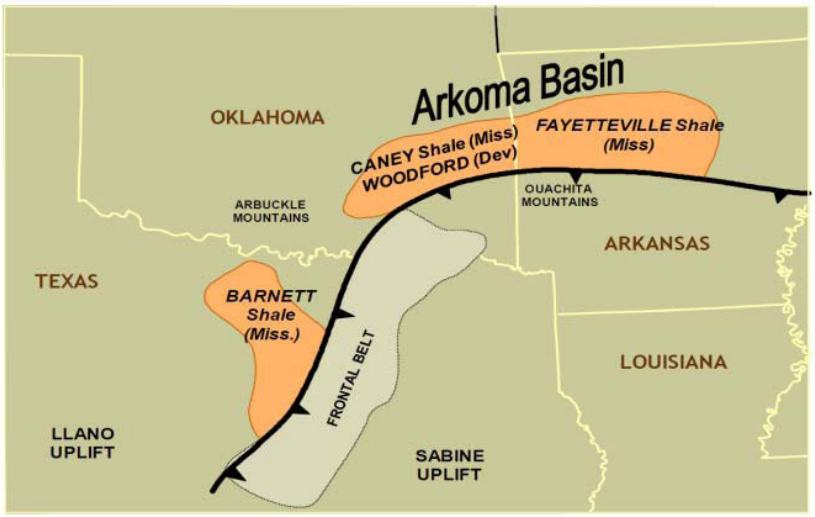

Figure 2.6: Arkoma Basin and Ouachita Thrust Belt. North is up (from Jacobi et al., 2009).

Petrophysically, the Woodford Shale shows very high gamma ray measurements, has water saturations from 30-45% and is lightly under-pressured with gradients ranging from 0.35-0.45 psi/ft (Vulgamore et al., 2007). Logs and cores indicate that it is organic-rich and siliceous with 48-74% quartz, 3-10% feldspar, 7-25% illite clay, 0-10% pyrite, 0-5% carbonate, and 7-16% kerogen. As of January 2009, over 520 Woodford wells have been completed in the Arkoma Basin since January 2004, most being horizontal and multi-stage hydraulically fractured (Waters et al., 2009). Well depths range from 900 ft in northeast Oklahoma up to 13,000 ft in west Texas. As of the end of 2007, more than 100 stages of hydraulic fracturing treatments have been monitored and analyzed with surface tiltmeters and microseismic mapping. Hydraulic stimulation seems to create complex fracture networks showing various orientations comparable to treatments in the Barnett Shale, although with a higher degree of communication with pre-existing fractures and faults (Vulgamore et al., 2007).

Table 2.3 gives an overview of the most important gas shales in the U.S. and compares various parameters.

Table 2.3: Comparison of Data for the Gas Shales in the United States (from Arthur et al., 2009)

Gas Shale Basin	Woodford	Barnett	Marcellus	Fayetteville	Haynesville	Antrim	Lewis
Estimated Basin Area [sq. miles]	11,000	5,000	95,000	9,000	9,000	12,000	10,000
Depth [ft]	6,000-11,000	6,500-8,500	4,000-8,500	1,000-7,000	10,500-13,500	600-2,200	3,000-6,000
Net Thickness [ft]	120-220	100-600	50-200	20-200	200-300	70-120	200-300
Total Organic Carbon [%]	1-14	4.5	3-12	4.0-9.8	0.5-4.0	1-20	0.45-2.5
Total Porosity [%]	3-9	4-5	10	2-8	8-9	9	3.0-5.5
Gas Content [scf/ton]	200-300	300-350	60-100	60-220	100-330	40-100	15-45
Well Spacing [acres]	640	60-160	40-160	80-160	40-560	40-160	80-320
OGIP [tcf]	52	327	1,500	52	717	76	61.4
Reserves [tcf]	11.4	44	262 (500)	41.6	251	20	20
Est. Gas Prod. per Well [mcf/day]	415	338	3,100	530	625-1,800	125-200	100-200

2.3 Matching Process and Model Calibration

Calibrating a hydraulic fracture model with available data has to meet three essential requirements: it should

- match observed net fracture pressure,
- approximately match monitored fracture dimensions, and

- honor known rock properties.

(Liu et al., 2006)

Even though a lot of information about reservoir geology, downhole stresses, permeability, rock moduli and other important parameters is generally available, truly accurate design and analysis of hydraulic fracture treatments and fracture geometry requires more. Fracture diagnostics in combination with simulation models are able to produce results that improve our knowledge of propagation processes, which is especially of importance in regions with complex geological structures and for unconventional reservoirs. Populating a hydraulic fracture model with known petrophysical properties and modifying it consecutively in order to mirror microseismic recordings provides a calibrated model for a specific area to more accurately characterize the reservoir. The information gained from that helps to improve future treatments as well as reservoir management in the long run (Warpinski et al., 2006).

Although microseismic monitoring is a valuable technology to match actual treatment data to a simulation model, and therefore provide a calibrated model for a specific region, it is sensitive to and dependent on the number of recorded microseisms as well as the accuracy of these events. Since there are different errors associated with surface and downhole monitoring, using one technology exclusively to match and calibrate the model can produce skewed results. The match achieved with surface data will have a different bias than the match achieved with downhole data. Assuming that a monitoring well is somewhat close to the treatment well, downhole measurements can give a more accurate match. Surface receivers can have a higher sensitivity to the velocity model which may decrease the accuracy in determining the vertical position of an event. They also often record fewer events because of the higher distance. It is therefore important to understand how many microseismic events are actually necessary to produce a good match with a model from a software package, as well as, if and what the difference between the match with surface data and the match with downhole data is able to tell us about data recording and the reservoir in general.

For both the vertical and the horizontal position of the receivers there is a maximum distance above which receivers cannot detect microseismic events. An abundance of events is generated throughout every treatment, yet only a small amount is actually recorded and accurately detected. The extent to which the amplitude of a

microseismic event decreases with distance depends on the geology, so surface monitoring can give a result of the same accuracy as obtained through downhole monitoring, depending on the relative position of the recording array. The cumulative error increases with distance, regardless whether it is horizontal or vertical distance. However, more geological layers mean a less uniform acoustic velocity, which might cause errors if the velocity model is not accurate (Warpinski 2009a).

Experiments have also shown that microseismic activity depends on treatment parameters such as pressure and injection rate as well. If one of these two parameters changes, the reservoir can respond to it and the observed microseismicity can be altered (Sleefe et al., 1995).

Another factor to keep in mind is the effect of the pore fluid on the generation of microseismic events. Oil reservoirs facilitate pressure coupling better because the reservoir fluid is relatively incompressible. Events are therefore more scattered and give a picture of pressure transmission as well as the actual fracture growth. Determination of fracture dimensions is usually easier for gas reservoirs because changes in pressure travel shorter distances and thus produce a more dense cloud of events. If natural fractures are opened however, they provide additional flowpaths for both the reservoir and the treatment fluid, which can also lead to a wider distribution of the events (Warpinski et al., 2004; Warpinski, 2009a). The difference between a gas reservoir and an oil reservoir can be seen in Figures 2.7 and 2.8, which show simulated microseismic data for a 5,000 ft deep sandstone reservoir.

2.4 Reservoir Characterization

Reservoir dynamics can be monitored by microseismic mapping to some extent. If geophone arrays are permanently installed in monitoring wells, microseisms associated with changes in stress and/or pressure can be recorded and then processed the same way it is done in monitoring of hydraulic fracturing treatments (Maxwell and Urbancic, 2005).

Analyzing the microseismic data may have the "potential to identify fault structures acting as flow channels or flow barriers, image flow anisotropy in fracture

dominated reservoirs, monitor fluid pressure front movement during water flood, assist in targeting production and injection wells, identify areas of reservoir compaction and potential wellbore instability, provide high resolution time-lapse images of seismic velocity and anisotropy, and provide information for the conditioning of reservoir simulators" (Jupe et al., 2000).

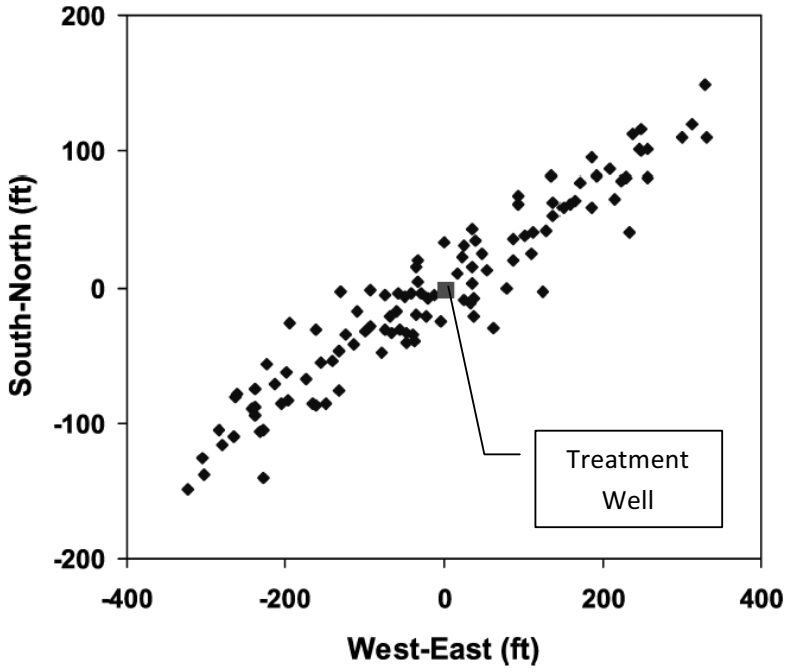

Figure 2.7: Simulated microseismic map for a gas reservoir (from Warpinski et al, 2004).

In Clinton County, KY, microseismic imaging has been used to identify fracture zones which were determined to dip at a very small angle. Horizontal wells were therefore found to not increase productivity, which might have saved money in future field development (Jupe et al., 2000). Microseismic monitoring in the Talco Field in Texas was successful in mapping channel structures that basically construed the overall structure of the reservoir (Maxwell and Urbancic, 2005). The location of the microseisms can indicate a hydraulic path if they are prominent enough for a trend to be observed. This association between microseismic connectivity and hydraulic connectivity can also be used to improve the grid structure of simulators (Jupe et al., 1998). The technology has also been successfully implemented in the North Sea. In the Valhall Field, areas of rock deformation were identified, indicating regions prone to well failure, and in the

Ekosfisk Field a fault system under the gas reservoir was mapped (Maxwell and Urbancic, 2005).

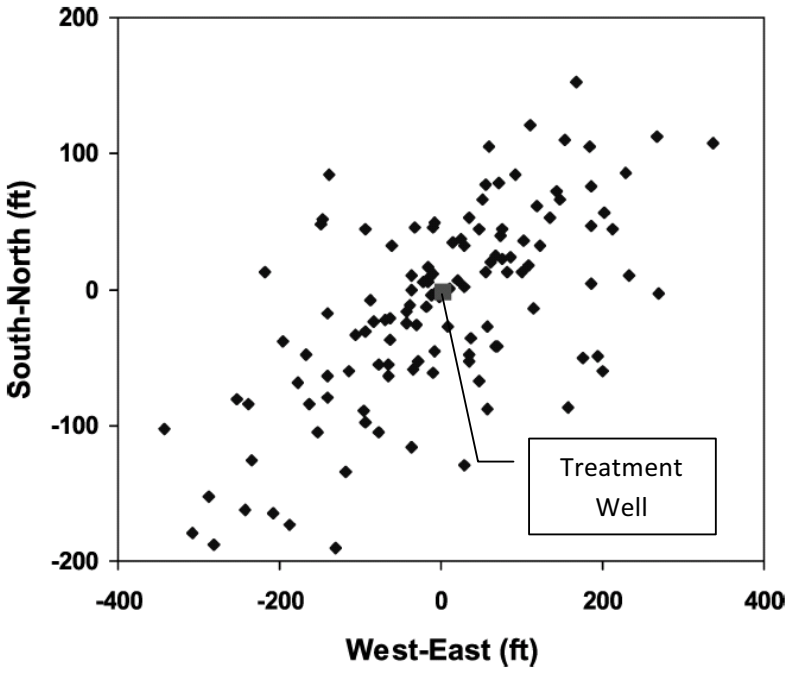

Figure 2.8: Simulated microseismic map for an oil reservoir (from Warpinski et al, 2004).

In reservoirs with naturally occurring pre-existing fractures, hydraulic stimulation is aggravated if these fractures are somewhat flow-dominating. In some areas in the Barnett Shale in Texas hardly any artificial fractures have been created during treatments because the pre-existing network has taken all the stimulation fluid. The created drainage pattern substantially differs from the anticipated ellipsoid but could be assessed by microseismic imaging of the treatment (Maxwell and Urbancic, 2005).

2.5 Fracture Complexity, Natural Fractures and Faults

Complexity in terms of hydraulic fracturing is usually linked to the intercommunication between artificially created hydraulic fractures and naturally present fractures. Monitoring of hydraulic treatments has shown that fracture growth is much more diverse than previously thought. Everything in between the base case of a simple

planar fracture and systems with a high degree of complexity involving phenomena that cannot be explained by rock or stress heterogeneities is observed, as seen in Fig. 2.9 (Cipolla et al., 2008).

Important factors in gas production from shale reservoirs are natural fractures and how much stimulation treatments are able to open them. Knowledge of a present system and its reaction to the injection of fluid can be crucial. Even when they are not just closed and filled with minerals, natural fractures tend to open up fairly easily and before artificial fractures are created, at less than the breakdown pressure of rock that is not naturally fractured. If part of the fracturing fluid is diverted into a network of opened natural flowpaths, it is important to understand the pressure behavior throughout the treatment and to know when to increase the injection rate to optimize proppant placement and fracture propagation (King, 2010).

The more delineation from a planar fracture and the higher the deviation from linear elastic mechanics to describe simple fracture propagation is, in both horizontal and vertical directions, the higher the degree of complexity. It can be assessed by:

- pressure decline analysis,
- evaluation of proppant placement and tortuosity, and
- net pressure history matching (Cipolla et al., 2008).

However, focusing exclusively on pressure behavior and analysis may lead to non-unique solutions. Microseismic and tiltmeter fracture monitoring are able to provide more insight into the true nature of the created hydraulic fracture, making it many times a more reliable tool than investigation that is solely pressure-based (Cipolla et al., 2008).

In case faults are present and in contact with the injected fracturing fluid, they can shift the microseismic picture and lead to misinterpretation and incorrect analysis of the treatment. However, they can be identified by examining the recorded data. Microseismic activity occurring after the job has been executed on the one hand can be explained as “aftermath” shear deformation due to the treatment, but if the events are of an unusually large magnitude on the other hand, they can be attributed to activation of and interaction with present faults, as seen in Fig. 2.10. Also, large magnitude events throughout the treatment can identify involvement of a fault when looking at a plot of event magnitude versus distance from the receiver (Downie et al., 2010).

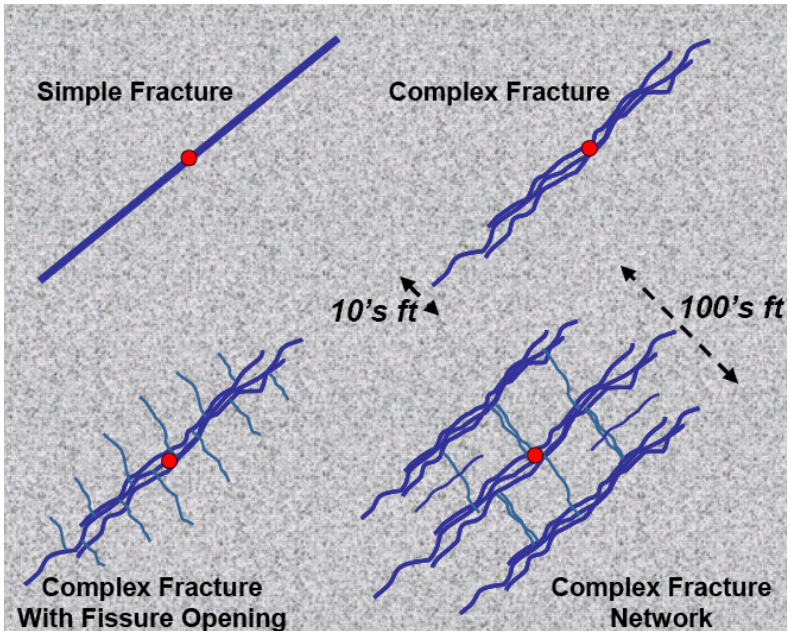

Figure 2.9: Fracture complexity (from Cipolla et al., 2008).

2.6 Magnitude

The strength of an earthquake is defined in terms of seismic moment that the earthquake generates:

$$M_0 = dAG \qquad \text{(Eq. 2.6)}$$

M_0 … seismic moment [g-cm^2/sec^2, i.e. dyne-cm]
d … amount of shear displacement along the fault plane [cm]
A … area of the fault plane [cm^2]
G … shear modulus [g/cm-sec^2]

As the area of slip and the displacement cannot be measured by microseismic monitoring, the seismic moment is calculated with the following equation:

$$M_0 = \frac{4\pi\rho_0 c_0^3 R\Omega_0}{F_c} \qquad \text{(Eq. 2.7)}$$

ρ_0 … density [g/cm^3]
c_0 … wave velocity [cm/sec]
R … source-receiver distance [cm]

Ω_0 … low frequency level of a displacement seismogram [1/sec]
F_c … radiation pattern coefficient [1/sec^2-cm]

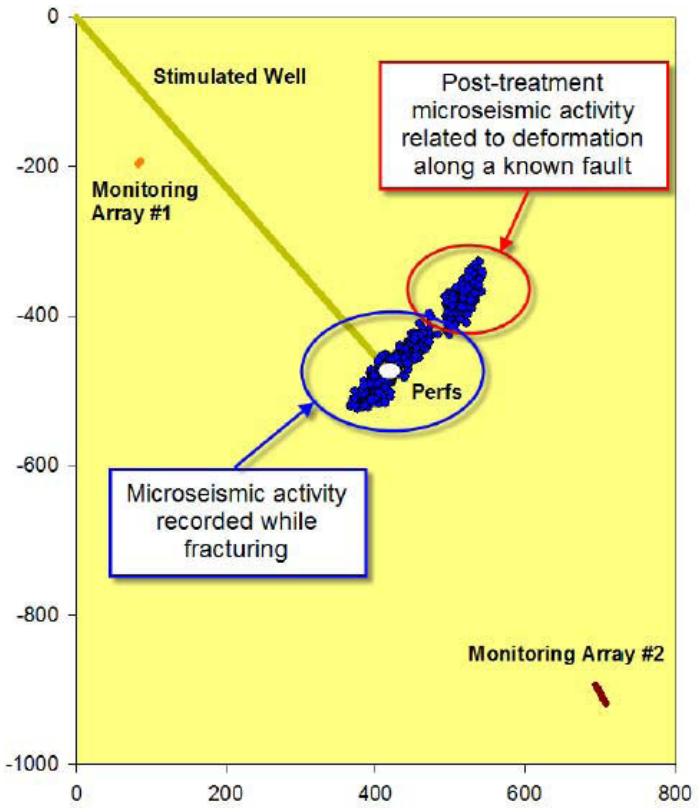

Figure 2.10: Post-treatment fault interaction (from Downie et al., 2010).

From this moment, the moment magnitude can be computed with the following equation, assuming the commonly used seismological units of dyne-cm are used:

$$M = \frac{2}{3}[\log_{10}(M_0) - 16.1] \qquad \text{(Eq. 2.8)}$$

M … moment magnitude [log scale]

The earthquake magnitude is the logarithmic Richter scale, commonly used in seismology to classify earthquakes. Microseismic events created by hydraulic stimulation, with a magnitude of -4 to -2, are usually five to seven orders of magnitude smaller than seismic events that can be perceived on the surface (+3 or higher). If the

seismic moments of all events are summed up throughout the treatment, a plot of the cumulative seismic moment versus time for each stage of the hydraulic fracturing job can be generated, as seen in Fig. 2.11. The cumulative moment is a rather stable parameter that is quite resistant against environmental noise. Being a sum it is naturally mostly dependent on the larger events, therefore being fairly accurate as long as enough microseisms are above the detection threshold (Warpinski, 2009b).

Various changes of the seismic moment can be observed throughout the treatment as pictured in Fig. 2.11. Sometimes an increase can be seen in consecutive stages, depicting the effect of previous stages. In other cases that increase might be followed by an unexpected decrease, i.e. a stage that shows a smaller cumulative moment than the previous one, indicating interaction with faults, natural fractures, or extension of the fracture into a part of the reservoir with deviating properties. If the hydraulic fracture intersects a fault, the cumulative plot is usually shifted upwards due to the generation of very 'loud' microseisms. Some stages may also come to a plateau after some time, implying that even though more volume is injected, not much shearing related to that additional volume is occurring (Warpinski, 2009b).

Although the exact relation between event strength, microseismic signal and actual shear deformation is not fully understood, analyzing the microseismic signals may also be valuable for examining characteristics of shear deformation. Some of the parameters having an effect on the magnitude are:

- injection rates and pressures,
- fluid type,
- proppant concentration,
- temperature of the injected fluids,
- stiffness of the rock,
- tectonic stresses,
- pre-existing fractures or faults, and probably also
- production history (Maxwell et al., 2008).

To better assess the interaction between these parameters and the seismic deformation, it may be more helpful to look at the cumulative seismic energy. Although it

can be calculated with equation, it is rather difficult to obtain for a microseism, unfortunately (Maxwell et al., 2008).

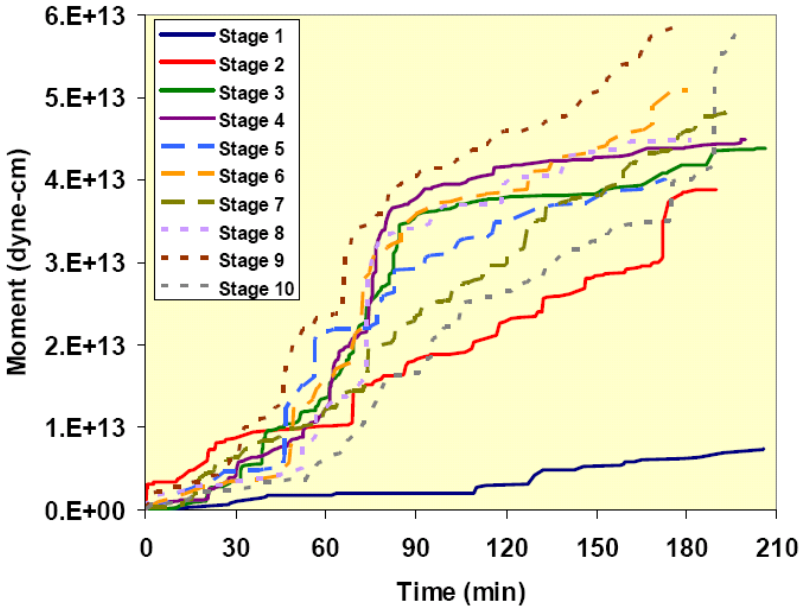

Figure 2.11: Cumulative moment plot for stimulation in the Barnett Shale (from Warpinski, 2009b).

> "Accurate computation of energy requires the recording of a broad frequency bandwidth, which is problematic because high frequency seismic energy is rapidly attenuated by the reservoir, and high frequencies are difficult to accurately record with a mechanically clamped geophone array. Furthermore the seismic energy requires knowledge of the radiation pattern, and is more sensitive than [the seismic] moment to uncertainties in the radiation pattern. Nevertheless seismic energy is a useful parameter to compare with the energy associated with a hydraulic fracture."
>
> (Maxwell et al., 2008)

The energy needed to create a specific tensile fracture can also be estimated by calculating the work performed, by simply multiplying fracture volume with pressure. This of course requires a previous determination of fracture geometry. Another way to assess the amount of deformation is comparing minimum to maximum principal stress. If

the difference between the two is large, the event magnitude is also likely to be larger (Maxwell et al., 2008).

2.7 Error Analysis

A combination of accurate travel time tagging, geological velocity model, event signal strength and other influences composedly create the overall accuracy for one event. This means that every single event occurring during the stimulation and being recorded has a certain accuracy level of its own. A plot showing all events can therefore be misleading because it does not include a tool to display how accurately each location was determined. Furthermore the location uncertainty consists of three parts: error in azimuth, distance from microseismic receiver, and depth. Important quality control criteria are signal-to-noise ratio and arrival time residuals (Zimmer et al., 2009).

> "Based on the event location and the assumed velocity model, the theoretical arrival times of P- and S-waves can be calculated at the different geophone levels. The difference between the theoretical arrival time and the actually picked arrival time is called the residual, which can be positive or negative. The hypocentral location is computed by minimizing these arrival time residuals, so that ideally this arrival time residual should be zero or at least close to zero."
>
> (Zimmer et al., 2009)

Another quality control parameter is a plot of event magnitude versus receiver-to-event distance. The farther away an event occurs from the tool, the larger its moment magnitude has to be in order to be distinguished from environmental noise and accurately detected. The so-called 'viewing limit' of a receiver, which can be determined from the aforementioned plot, is a characteristic of the formation, and determines how accurate microseismic imaging will be in the first place, considering location of events, location of monitoring tools, noise, and specific geology (Zimmer et al., 2009).

CHAPTER 3

HYDRAULIC FRACTURE MODELING

> "Fracture dimensions and conductivity can be estimated from fracture modeling. The 'observed' net-pressure history is matched with the calculated 'model' net pressure by adjusting various model parameters. The observed net pressure is the fracturing pressure minus the minimum rock stress or closure pressure. The observed net pressure is calculated from surface or downhole treatment pressure by correcting for frictional effects and hydrostatic pressure and subtracting the fracture closure pressure. Model net pressure can be changed to match observed net pressures using several 'assumptions'".
>
> (Cipolla et al., 2009)

The hydraulic fracture models for this chapter were obtained in three steps. First a basic model for each stage was built incorporating available logs, and modifying parameters to achieve a reasonable representation of the reservoir geology. These models were run to simulate fracture growth and generate pumping data. The second step was to match the observed pressure to the simulated pressure for each stage. In the third step, this preliminary calibration was further enhanced and verified by matching fracture geometry to microseismic data to produce a model that reflects actual reservoir responses on all three levels (i.e. rock properties/logs, treatment pressure data, and microseismic recordings).

3.1 Well Data

This study analyzes a data set that was obtained from a five-stage hydraulic fracturing treatment of a well in Hughes County, OK. Microseismic recordings for Stages II through V were available for 9-sensor downhole monitoring from an offset well, as well as recordings for Stages I through V from surface monitoring. Further available were

logs from an offset well in the same field, hydraulic fracturing pump curves and a microseismic quality report for the downhole recordings.

The well is located in Hughes County, OK, and was drilled to produce from the Woodford Shale from a horizontal interval of about 2,300 ft. The following list gives an overview of the most important well specifications:

- Measured Depth: 10,692 ft
- Total Vertical Depth: 7,879 ft
- Kick-off Point: 7,090 ft
- End of Build: 7,858 ft (8,490 ft MD)
- Woodford Shale Top: 7,758 ft
- Hole Sizes:
  - 0 - 398 ft: 17 1/2 in.
  - 398 - 4,985 ft: 12 3/4 in.
  - 4,985 - 10,692 ft: 8 3/4 in.
- Casing Program:
  - 0 - 398 ft: 13 3/8 in.
  - 398 - 4,985 ft: 9 5/8 in.
  - 4,985 - 10,692 ft: 5 1/2 in.

The perforation scheme consists of 15 intervals grouped to five fracturing stages with a shot density of 6 spf (60 degree phasing) and a perforation diameter of 0.42 in.

- Stage I:
  - 10,262 - 10,264 ft (MD): 12 shots
  - 10,388 - 10,390 ft (MD): 12 shots
  - 10,513 - 10,516 ft (MD): 18 shots
  - 10,639 - 10,642 ft (MD): 18 shots
- Stage II:
  - 9,764 - 9,768 ft (MD): 24 shots
  - 9,889 - 9,893 ft (MD): 24 shots
  - 10,015 - 10,019 ft (MD): 24 shots
  - 10,141 - 10,145 ft (MD): 24 shots

- Stage III:
    - 9,342 - 9,350 ft (MD): 48 shots
    - 9,590 - 9,598 ft (MD): 48 shots
- Stage IV:
    - 8,951 - 8,966 ft (MD): 90 shots
- Stage V:
    - 8,273 - 8,276 ft (MD): 18 shots
    - 8,399 - 8,401 ft (MD): 12 shots
    - 8,524 - 8,527 ft (MD): 18 shots
    - 8,650 - 8,653 ft (MD): 18 shots

3.2 Fracturing Treatment Data

All fracturing stages were executed with the same underlying design. The fluid was treated water with only friction reducer, various surfactants, and a biocide added. In the beginning of the treatment a small pad of acid was pumped. As seen in Figures 3.1 through 3.5, the slurry rate was increased to about 60 bpm, which was held for about 10 minutes, until the rate was increased to the final treatment rate of about 95 bpm. Approximately 50 minutes into the treatment, proppant was added to the slurry. A sand slug was always followed by a pad of treated water. The first three sand slugs were 100 mesh sand starting with a concentration of 0.25 lbm/gal, increased by 0.25 lbm/gal increments, followed by 13 slugs of 30/70 sand starting with a concentration of 0.1 lbm/gal, increased by 0.1 lbm/gal increments, followed by one final slug of 20/40 sand with a concentration of 1.0 lbm/gal. It should be noted that the modeling software allows the input of 100 mesh sand as fluid loss additive only, even when it was intended as proppant. In the Bakken formation for example, 100 mesh sand was used at low concentrations during early stages of the treatment in order to establish conductivity at the tips of the fractures hundreds of feet out into the reservoir (Lolon et al., 2009).

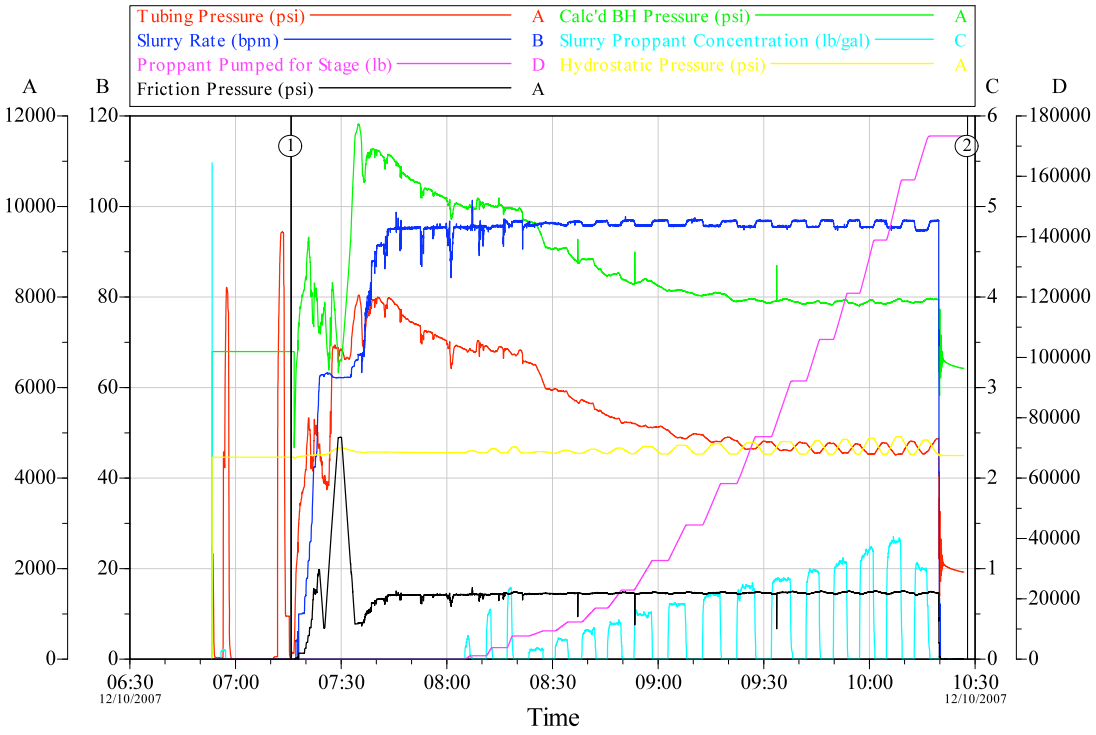

Figure 3.1: Stage I hydraulic fracturing treatment.

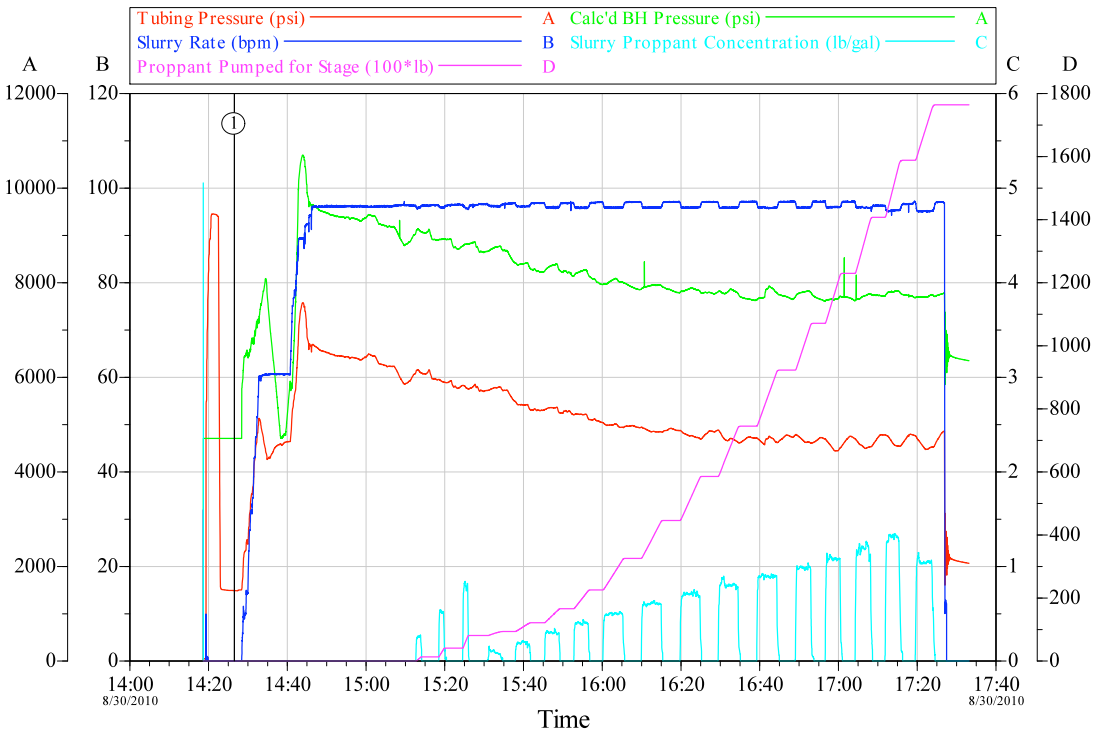

Figure 3.2: Stage II hydraulic fracturing treatment.

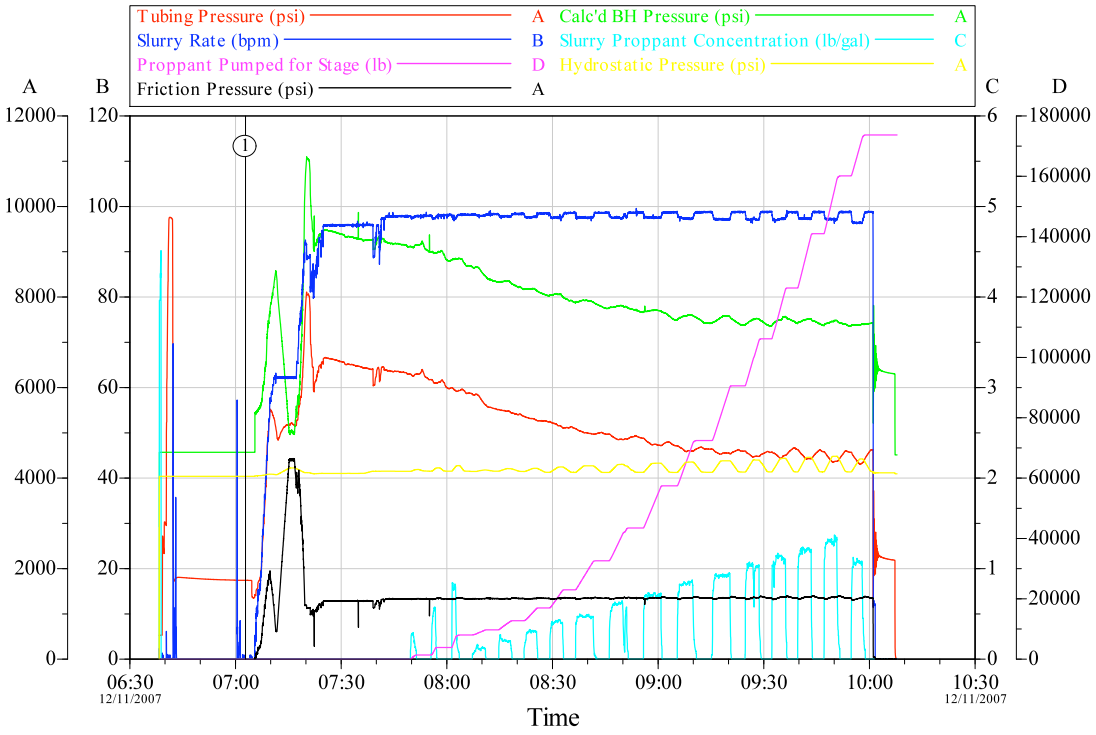

Figure 3.3: Stage III hydraulic fracturing treatment.

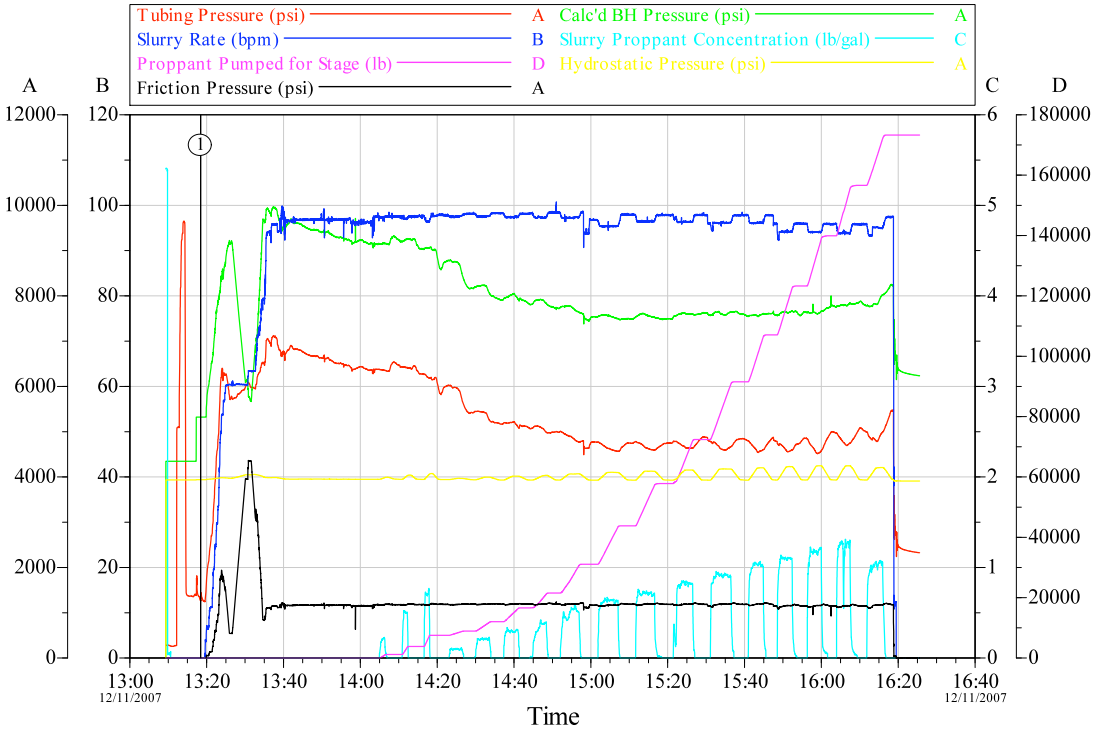

Figure 3.4: Stage IV hydraulic fracturing treatment.

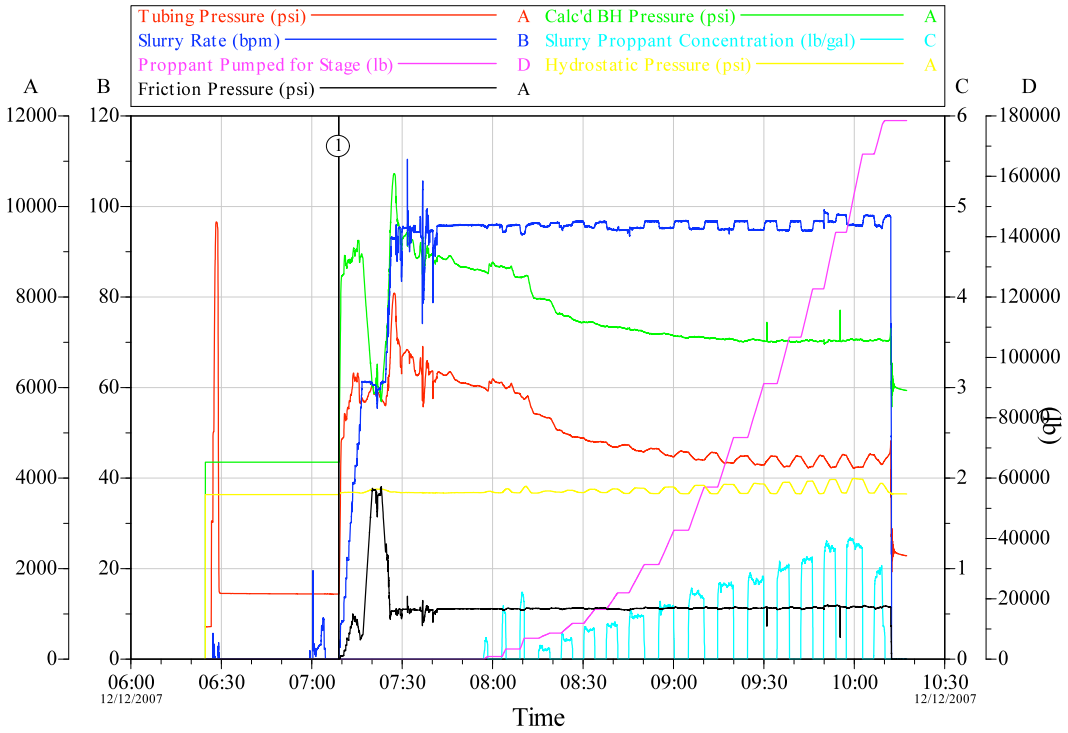

Figure 3.5: Stage V hydraulic fracturing treatment.

3.3 GOHFER™

The Grid Oriented Hydraulic Fracture Extension Replicator (GOHFER™) is a powerful software package simulating hydraulic fractures as well as fluid flow and proppant transport in 3-D. The simulator operates with a simple grid structure to describe the reservoir, with the capability to change rock, pressure, and perforation properties of each individual grid cell. Actual treatment data can be visualized and imported in order to match the simulated data. A built-in log analysis suite populates the grid and allows for manual modifications in order to describe the reservoir and the treatment interval more accurately.

The GOHFER™ workflow is simple and consists of a few easy steps. A new 'Job' file is created into which a simulator module and technical graph module for the actual treatment data is uploaded. The simulator module consists of four input tabs:

- Customer and Reservoir Information
- Log Calculations

- Formation Zone Setup and Grid
- Pumping Schedule

3.3.1 Customer and Reservoir Information

This section is basically an input area for various kinds of reservoir parameters; basic ones such as reservoir fluid viscosity, bottomhole temperature, and various gradients; and advanced parameters. There are pre-defined default values for every parameter that are reasonable general assumptions, but some should be changed to known reservoir properties if such data is available.

The default value for the overburden stress gradient is 1.0 psi/ft accounting for an average porosity of 20%, a grain density of 2.65 g/cm^3 (i.e. quartz sand), and a pore fluid density of 1.0 g/cm^3 (i.e. water) (WinGOHFER^{TM} User Manual). For the subject well, integration of the log-measured bulk density along the depth, divided by the depth, gives an overburden gradient of 1.09 psi/ft which was used as input value for the subject models. Pore water gradient was left at the default value of 0.442 psi/ft.

A parameter called Pressure Dependent Modulus Stiffness Factor (PDMSF) accounts for the change of Young's modulus as fracturing fluid is injected into the reservoir and natural fractures, if present, are opened. When the pressure exceeds the fissure opening pressure, Young's modulus will begin to change in an exponential fashion, controlled by the value of PDMSF (WinGOHFER^{TM} User Manual). For the models used in this study a positive value is used, meaning that Young's modulus increases throughout the stimulation treatment.

As natural fractures open up, the reservoir's leak-off behavior changes. The parameter accounting for this is called Pressure Dependent Leak-off Coefficient (PDL). Again, when the pressure exceeds the fissure opening pressure, leak-off changes exponentially, and increases because matrix leak-off is no longer the only effect occurring. Additional flow-paths of potentially higher conductivity have an effect on proppant transport and may eventually lead to screen-outs in certain locations if leak-off is very high. Also, fracture (half-) lengths will generally be shortened by increased leak-off due to natural fractures (WinGOHFER^{TM} User Manual).

Another effect that can occur throughout the treatment is transverse storage. Together with the main fracture a more or less developed network of fractures, both parallel and transverse, is created. As fluid is pumped into the reservoir and flows through the main fractures, a part of it can be diverted into transverse fractures and is stored there. The magnitude of this parameter depends on the net pressure and is characterized by the Transverse Storage Coefficient (TSC). It can be used to match simulated and microseismic (half-) lengths in case this cannot be achieved by modification of other parameters or explained by other effects (WinGOHFER™ User Manual).

Drilling and perforation induced damage and fractures, together with debris, and cement result in an additional pressure loss that is accounted for by the Tortuosity Pre-Factor. The naturally present tortuous flowpaths of the reservoir, characterized and defined by porosity and permeability, are additionally complicated by the drilling and completion operations which lead to a “disturbed” flow in the near wellbore region.

3.3.2 Log Calculations

In order to create an accurate lithologic model of the reservoir, GOHFER™ has a built-in log analysis suite that available logs can be loaded into. It is able to calculate parameters necessary for the simulation of mechanical hydraulic fracture propagation which are often not accurately obtainable by logs, or simply not included in log suites. GOHFER™ LAS is able to read both LAS and CSV files and lets the user modify source curves as well as output curves. The user is able to choose which curves are used in certain correlations to sequentially calculate a parameter and furthermore can decide which of the generated curves are used to populate the grid of the simulator.

One of the most important input values for the calculation of rock mechanical parameters is the compressional sonic travel time (DTC). In case sonic data has not been collected when running a log, it can be synthetically generated from Gamma Ray, neutron porosity, average porosity, or resistivity curves. Naturally, the four curves will not be the same due to the different input parameters. They especially deviate from each other in areas of higher gas saturation due to the individual behavior of each parameter the curves are based on (GOHFER™ LAS User Manual). As sonic data was not

available for this project, synthetic DTC curves were used to generate further parameters.

3.3.3 Formation Zone Setup and Grid

This part of the software package lets the user build the actual geological model. The grid for the simulator is defined by top and bottom depths, node size, and number of grid columns. Although initializing the grid automatically populates the created grid with values from the assigned log file, every single cell can be modified manually. The user then goes through various tabs to review, alter, or assign the following grid properties: perforation diameter, holes perforated, effective porosity, permeability, Poisson's ratio, Young's modulus, pore pressure gradient, pore pressure offset, pore pressure, horizontal Biot's constant, vertical Biot's constant, process zone stress, total stress, fissure opening pressure, tectonic strain, tectonic stress, percentage of dolomite, percentage of limestone, transmissibility multiplier, and proppant hold-up factor.

3.3.3.1 Poisson's Ratio

> "Poisson's ratio is defined as the ratio of lateral to axial strain under conditions of axial loading. If a load is applied along a given axis a strain results which is proportional to the Young's modulus of the sample. Strains perpendicular to the axis of the applied load also occur. The magnitude of these lateral strains depends on Poisson's ratio of the sample. The numerical value of Poisson's ratio lies between 0.0 and 0.5"
>
> (WinGOHFER™ User Manual)

Material like cork representing the lower extreme of the range with a Poisson's ratio of nearly 0.0 will not strain laterally when a load is applied. Rubber on the other hand, with a Poisson's ratio of 0.5, will show just as much lateral expansion as axial compaction under loading.

If both shear and compressional travel times are available, Poisson's ratio is simply calculated from the ratio of both. If (full) sonic measurements are not available, it can also be derived from Gamma Ray, resistivity, (synthetic) DTC, and from average porosity (GOHFER™ LAS User Manual). For these models the Poisson's ratio turned out to be most reasonable when calculated from the synthetic DTC curve by correlations based on volume fraction weighted lithology, which is backed up by Barree et al., 2009a.

3.3.3.2 Young's Modulus

> "Young's modulus describes the stiffness of the formation. In general a relationship exists between stress and strain. A higher applied load, or stress, usually causes a larger strain. For a perfectly linear, elastic medium the relationship between stress and strain follows a single straight line.[…] [However] actual rock samples are generally not linearly elastic. As the rock begins to deform, the mechanical properties of the sample change. The stress-strain curve for an actual rock sample is a very irregular curve rather than a straight line."
>
> (GOHFER™ LAS User Manual)

The values for Young's modulus are calculated by GOHFER™ in two stages. In a first step it calculates a dynamic modulus, because it is usually derived from sonic measurements. As these were not available for this project, the synthetic DTC curve turned out to produce the most reasonable result, as opposed to Gamma Ray, resistivity, or average porosity. It is calculated with an equation derived from lab experiments on 327 tight-gas and shale-gas core samples, using the compressional travel time as the only variable, as seen in Fig. 3.6 (Barree et al., 2009a). In a second step, it converts the dynamic to a static modulus by taking the bulk density into account, as shown in Eq. 3.1 (Win GOHFER™ User Manual).

$$\log(E_{static}) = \log(\rho_{bulk} E_{dyn}) - 0.55 \qquad \text{(Eq. 3.1)}$$

E_{static} … static Young's modulus [MMpsi]
ρ_{bulk} … bulk density [g/cm3]
E_{dyn} … dynamic Young's modulus [MMpsi]

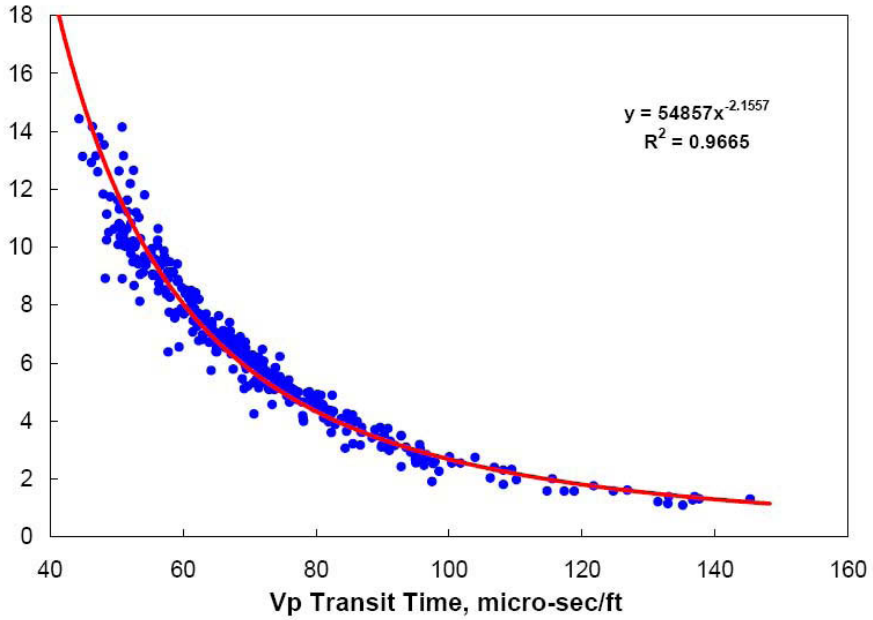

Figure 3.6: Estimation of dynamic Young's modulus from Vp travel time. The vertical axis shows Young's modulus in MMpsi (from Barree et al., 2009a).

Interestingly it is not a disadvantage that sonic data is not available and therefore compressional travel time has to be synthetically generated. Measurements of acoustic velocities, of which travel times are simply the reciprocal, are subjected to a variety of influences that can, and will, produce an error that propagates into the calculation of mechanical rock properties. Often times these errors due to fractures, external stress, temperature, borehole conditions such as breakouts, mud weight, borehole size, tool eccentricity, pore pressure and pore fluid saturation, are not being corrected for. Assuming an error of just +/- 5% in the measurement of the acoustic velocities, leads to an error of +/- 20% in the calculation of Poisson's ratio, and +/- 26% for Young's modulus. Using synthetic DTC values with an inherent error of +/- 5% on the other hand leads to an error of +/- 9% for Poisson's ratio, and only +/- 11% for Young's modulus (Barree et al., 2009a).

3.3.3.3 Biot's Constant

> "[Due to] irregularity of pore and grain shapes, and because grains can be partially cemented, internal fluid pressure is not transmitted

perfectly to the rock matrix. A correction factor, called Biot's poro-elastic constant, is applied to account for imperfect pressure support."

(WinGOHFER™ User Manual)

Fluid pressure can be transmitted vertically and horizontally. Therefore, there is a vertical and a horizontal Biot's constant. The horizontal one was left at the default value of 1.0, assuming that the fracturing fluid directly communicates with the pore fluid, whereas the vertical one is calculated by GOHFER™ using the effective porosity.

3.3.3.4 Process Zone Stress

This parameter can be directly measured in an injection test and depends on factors such as fluid lag, rock tensile strength, and stress effects at the fracture tip. It is defined as the difference between ISIP and the closure pressure, giving a value that can be seen as the net pressure for fracture extension (WinGOHFER™ User Manual). As there was no injection test performed for this study, GOHFER™ automatically calculates the process zone stress with log data from the volume fraction of shale according to the Equation 3.2. Due to the lack of measurements, default values of 500 psi were used for factors a_1 and a_2.

$$PZS = a_1 \cdot V_{SH} + a_2 \qquad \text{(Eq. 3.2)}$$

PZS … process zone stress [psi]
a_1 … shale fraction multiplier [psi]
V_{SH} … shale fraction [-]
a_2 … measured difference between ISIP and closure pressure [psi]

3.3.3.5 Total Stress

Fractures open up perpendicular to the least principal stress, which is assumed to be horizontal in most fracturing situations. If the pressure falls below this value, the propagating fracture closes, hence the name fracture closure pressure. This closure pressure is controlled by the following parameters:

- Poisson's ratio
- Overburden stress
- Vertical and horizontal Biot's constant
- Pore pressure
- Tectonic strain
- Tectonic stress

The following equation from the WinGOHFER™ User Manual shows how the simulator computes total stress:

$$p_c = \frac{\nu}{(1-\nu)}\left[D_{TV}\gamma_{ob} - \alpha_V\left(D_{TV}\gamma_P + P_{off}\right)\right] + \alpha_H\left(D_{TV}\gamma_P + P_{off}\right) + \varepsilon_x E + \sigma_t$$

(Eq. 3.3)

p_c … closure pressure [psi]
ν … Poisson's ratio [-]
D_{TV} … true vertical depth [ft]
γ_{ob} … overburden stress gradient [psi/ft]
α_V … vertical Biot's Constant [-]
γ_P … pore fluid gradient [psi/ft]
P_{off} … pore pressure offset [psi]
α_H … horizontal Biot's Constant [-]
ε_x … tectonic strain [microstrains]
E … Young's modulus [MMpsi]
σ_t … tectonic stress [psi]

Barree et al. (2009a) discusses this equation and states that considering the "complex deposition, diagenetic, and deformational history of most reservoir systems" it gives a rather simplified picture of the actual in-situ stress state of the reservoir. The first part, $\left[D_{TV}\gamma_{ob} - \alpha_V\left(D_{TV}\gamma_P + P_{off}\right)\right]$, reflects the "vertical net effective stress" that is responsible for the compression of the rock matrix, which is converted into a horizontal stress by the Poisson's ratio term. As can be seen, the overburden stress acting on the grains is reduced by the pore pressure term, giving an effective inter-granular stress. There are two corrections applied to the pore pressure: the vertical Biot's constant accounts for effects such as cementation and consolidation (see Section 3.3.3.3 Biot's Constant), and the pore pressure offset represents over-pressurized or depleted zones. The second part, $\alpha_H\left(D_{TV}\gamma_P + P_{off}\right) + \varepsilon_x E + \sigma_t$, represents horizontal components that

contribute to the total stress such as a pore pressure term reflecting only internal fluid pressure, and local tectonic stress and strain, if present. Assuming that the fracturing fluid directly communicates with the pore fluid the horizontal Biot's constant can be set to 1.0.

3.3.3.6 Fissure Opening Pressure

The fissure opening pressure is the additional pressure on top of the total stress (i.e. fracture closure pressure) needed to open up natural fractures and fissures. GOHFER™ uses this value together with the PDMSF and PDL to account for the increase of Young's modulus and additional leak-off into open natural fractures throughout the treatment. The latter effect also ties back into the TSC accounting for the loss of stimulation fluid into transverse fractures (WinGOHFER™ User Manual).

3.3.3.7 Tectonic Strain and Tectonic Stress

Values for tectonic strain that are entered into the grid are multiplied by Young's modulus in order to increase total stress due to tectonic activity. Tectonic stress on the other hand is a direct offset that also increases total stress. Unlike tectonic strain it does not create a different offset for each grid row because it is independent of Young's modulus. Both values cannot really be accurately obtained unless measured (WinGOHFER™ User Manual). In this work tectonic strain was used as a "last resort" to modify the simulated pressure, in case such modification (i.e. shift of the pressure curve) was not achievable through a change in other parameters, or where change in other parameters was not found reasonable.

3.3.4 Pumping Schedule

This last section houses the input area for general wellbore information, design and actual pumping data, as well as for injection tests, if performed. The wellbore information tab requires input of the inner diameter of the tubing, the true vertical depth

at which GOHFER™ will calculate the bottomhole pressure, and the measured depth (i.e. treatment tubing length), from which GOHFER™ computes the volume present in the tubing prior to the treatment.

3.3.4.1 Perforation Coefficient of Discharge

Another important parameter is the Perforation Coefficient of Discharge representing a factor to assess friction pressure loss caused at the perforations. The value entered is a starting value at the beginning of the treatment that will increase as more and more fracturing fluid and proppant is pumped through the perforations. As seen in Eq. 3.3 (WinGOHFER™ User Manual), this leads to a decrease in perforation friction, due to the increase of the perforation diameter as the proppant exerts abrasive action on the steel of the tubing.

$$P_{pf} = \frac{1.975 q^2 \rho_f}{C_D^2 N_p^2 d_p^4} \qquad \text{(Eq. 3.4)}$$

P_{pf} … friction pressure at the perforations [psi]
q … total pump rate [bpm]
ρ_f … slurry density [g/cm^3]
C_D … perforation coefficient of discharge [-]
N_p … number of open perforations [-]
d_p … diameter of perforations [in]

3.3.4.2 Actual Treatment Pumping Data

The pumping schedule tab allows the user to import actual pumping data from a specific treatment, as done in this study, in order to match the simulated and the real pressures. The technical graph program with which the actual pumping data is processed automatically recognizes stages based on a user-defined sensitivity. Stage durations, volumes, and slurry rates are imported leaving the user with only a couple of things to define. Fluid and proppant used can be selected from a large library with most of the commercial hydraulic fracturing fluids and proppants offered today. The user also gets to input two important additional parameters: a friction correction factor and a perforation factor.

3.3.4.3 Friction Correction Factor

> "The Friction Correction Factor allows the overall pipe friction to be adjusted to match observed treating pressures more conveniently. A value greater than 1.0 increases total pipe friction and a value less than 1.0 reduces friction. Pipe friction can vary from the ideal based on small concentrations of contaminants in the fluid, pipe conditions, and other physical and chemical effects. The effects are non-linear as the rate-friction response is typically log-log linear."
>
> (WinGOHFER™ User Manual)

The difference between surface and bottomhole treating pressure is composed of hydrostatic pressure and friction pressure. Friction pressure is made up by friction inside the pipe, pressure loss at the perforations, and near-wellbore effects. The pressure drop along the tubing due to friction for laminar flow is governed by six factors (Barree et al., 2009b):

- Tubing inner diameter,
- Pipe friction crosslink delay factor that depends on the crosslink properties of the fracturing fluid,
- A factor accounting for the increase in friction with solids addition,
- The fluid density,
- The friction correction factor,
- And, assuming a power law behavior for the fluid, the power law parameters n and k'.

Calculations get more complicated for turbulent flow, but it is still directly proportional to the laminar pressure drop, and therefore the listed factors still dominate the friction pressure loss. All chemical additives (gelling agents, friction reducers, surfactants etc.) that make up the final treatment fluid, as well as the added proppant, have an impact on the power law parameters n and k', above all other fluid properties controlling friction effects. Experiments show that for turbulent flow, which is usually the regime applicable to hydraulic fracturing operations, friction pressure is strongly dependent on and basically dictated by the exponent n. As pressure loss decreases with decreasing n, a low n is a desired property for the fracturing fluid, which can be achieved

with friction reducer (Barree et al., 2009 b). The results of a flow experiment with a 57 ft. long tubing section and an ID of 0.43 in are shown in Fig. 3.7. Three different fluids have been used:

- Pure water with a power law exponent of 1.0,
- Water with 0.1% friction reducer (or 1 gallon-per-thousand-gallons), with a substantially decreased n,
- And a linear gel with 35 lbs/Mgal of guar that also has an exponent of less than 1.0.

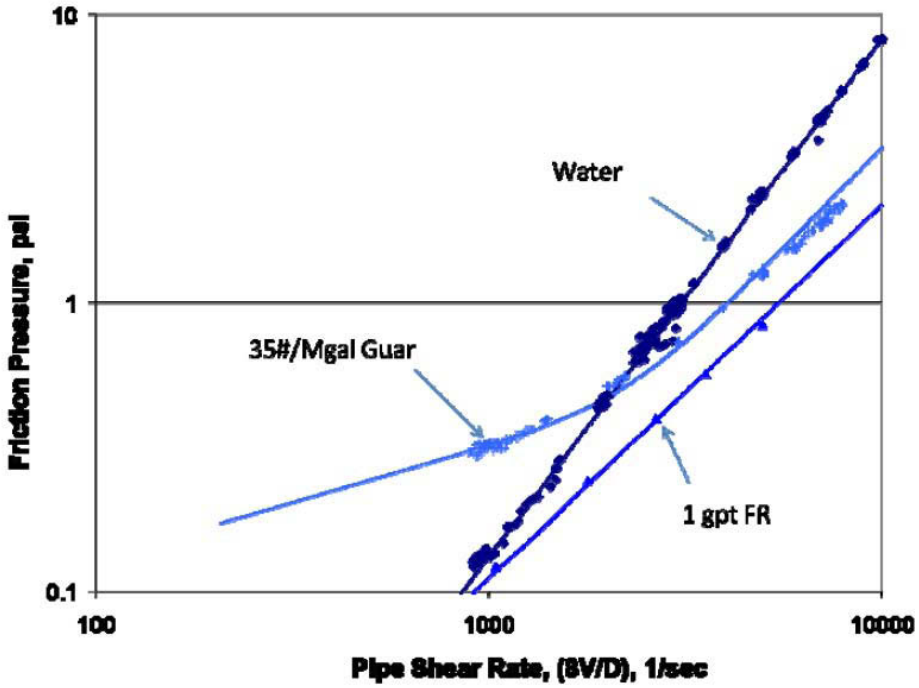

Figure 3.7: Friction pressure loss of different fluids (from Barree et al., 2009b).

For the turbulent regime on the right side of the graph with the higher pipe shear rates, it can be seen that water with the largest power law exponent shows the most friction pressure loss. The guar gel and the water with added friction reducer clearly show a lower pressure drop, and more closely resemble an actual fracturing fluid than pure water. The logarithmic scale emphasizes the significant difference between treated fluid and untreated water. The Friction Correction Factor can therefore be substantially lower than 1.0 in order to mimic this large decrease in friction pressure loss.

3.3.4.4 Perforation Factor

As seen in Eq. 3.4, the number of perforations that are open to flow is another value governing the pressure loss at the perforations. The perforation factor controls what percentage of the perforations entered into the grid are actually open, with values between 1.0 (100% of perforations open) and 0.0 (all perforations plugged) (WinGOHFER™ User Manual). A value of e.g. 0.5 may not necessarily mean that half of the perforations are open and half are plugged. It rather means that 50% of the total area of perforation holes (i.e. the contact area with the reservoir) is open to flow. The change of proppant, pumping rate, and sometimes even the stimulation fluid throughout the treatment all have an effect on how easily the slurry moves through the perforations. Perforations taking fluid may also modify the stress regime around the perforations that are not taking fluid, potentially leading to these perforations opening up. In this work, the factor is utilized to manage these effects by representing an opening up or partial plugging of the perforations.

3.4 Geological Model Configuration

The log data available for this study was obtained from an offset well and not from the treatment well itself. Based on information from the perforation scheme for the treatment well and an analysis of the log data, the top of the Woodford Shale for the treatment well was found to be approximately 18 ft above where the top of the Woodford Shale for the offset well is located. Therefore a depth shift of -18 ft (i.e. upwards) of the log data was performed in GOHFER™'s log analysis suite.

When the grid is being initialized GOHFER™ automatically reads the assigned log file and populates the grid with averaged values for every 10 ft grid cell. However, some of the log derived values are unreasonable and therefore have to be corrected by either modifying the log or the grid.

Since there were no measurements of acoustic velocities available, the compressional travel time curve was artificially generated from the built-in log calculation module. GOHFER™ offers four options to derive the curve based on Gamma Ray, neutron porosity, average porosity, or resistivity. All synthetically derived curves had a

default offset of +50 micsec/ft which was corrected to zero, since there was no obvious reason for this shift. As Poisson's ratio is calculated from the synthetically derived DTC curve, the offset would have produced a clear overestimation of this parameter. Gamma Ray measurements produced DTC values that were unreasonably high, whereas calculations based on neutron porosity and resistivity clearly underestimated the compressional travel time. Therefore the curve using the average porosity was selected to be the basis for all further calculations using DTC values.

Another property that had to be corrected was the effective porosity. The pre-set curve that GOHFER™ reads to populate the grid with effective porosity values is the effective porosity curve generated in the log calculation module, which seemed to be a little too high based on general Woodford Shale information. Thus the average porosity curve was manually selected to populate the grid. In a further step, permeability had to be corrected because it is also determined from the unreasonable effective porosity in the log analysis package. This was done directly in the formation zone setup and grid section, by letting GOHFER™ calculate permeability values for the whole grid with a function based on the effective porosity. The porosity values are read directly from the grid, and not from the log curve. As seen in Eq. 3.5, permeability further depends on two coefficients which have to be adjusted in order to produce a sensible profile.

$$\mu = k_1 \Phi^{k_2} \qquad \text{(Eq. 3.5)}$$

μ … permeability [mD]
k_1 … adjustable coefficient [mD]
k_2 … adjustable coefficient [-]
Φ … effective porosity [-]

The equation is a "power law curve fit for a k-phi crossplot" (WinGOHFER™ User Manual), with coefficient k_1 set to 65, in order to reflect the low permeability shale reservoir, and exponent k_2 set to 3.5.

Due to errors at the end of the log curves, the last three rows of the grid, covering the interval from 8,020 ft to 8,050 ft, had to be manually corrected to whatever value the last correct row above the first incorrect one showed. Also, pore pressure offset was set to zero for the whole grid as there was no indication for any offset.

The following list gives an overview of the most important parameters and properties from the Formation Zone Setup and Grid tab.

- Zone Setup:
  - Top Depth: 7,300 ft
  - Bottom Depth: 8,049 ft
  - Top Woodford Shale: 7,758 ft
  - Bottom Woodford Shale: 7,870 ft
  - Node Size: 10 x 10 ft
  - Number of Grid Columns: 300
- Reservoir Properties at Perforation Depth *(7,860 – 7,870 ft)*
  - Effective porosity: 15.8%
  - Permeability: 0.101909 mD
  - Poisson's ratio: 0.3066
  - Young's modulus: 2,611,400 psi
  - Pore pressure: 3,477 psi
  - Vertical Biot's constant: 0.9339
  - Prozess zone stress: 1,100 psi
  - Total stress: 6,093 psi
  - Fissure Opening Pressure: 650 psi
  - Tectonic strain: depending on stage

Figure 3.8 gives an overview of all averaged properties for each 10 ft grid cell, and Figures 3.9 through 3.18 show the entire profile for various grid properties. The values for Young's modulus and Poisson's ratio for the Woodford Shale (Figs. 3.11 and 3.12) align very well with the values shown in Fig. 3.19 (Poisson's ratio of 0.085 – 0.325, Young's modulus of 2.8 – 4.9 MMpsi). Tectonic strain of 100 microstrains was used as an example to visualize the increase in total stress for the shale interval in Fig. 3.18. Tectonic strain was a necessary modification to match the pressure curves, as it increased the simulated pressure in a way that a modification of other parameters could not achieve, or where adjustment of other parameters was not found to be reasonable. With this additional stress of about 100 microstrains the total stress for the perforation depth gives a gradient of about 0.775 psi/ft, which agrees with the fracture gradient of

0.78 psi/ft that was anticipated by the service company in their proposal for the treatment design. A tectonic strain of 100 microstrains is a reasonable value for the subject models and on the lower end of the range that can be used (Mohammad, 2009). As tectonic strain is being multiplied by the Young's modulus in order to produce an increase in stress, 100 microstrains give about 260 psi of additional stress with a Young's modulus of about 2.6 MMpsi for the perforation depth.

Additional feedback for the geological model set-up was a second log suite from an offset well that shows the same stratigraphy as the treatment well, and is located about three miles south of it (Gertson, 2011). Neutron porosity was calculated between 15% and 18%, which agrees with the effective porosity value of 15.8% for the perforation depth in the geological model. Porosity calculated from the density log track however showed a lower porosity between 6% and 9%. Permeability values from the log suite varied between 10 and 30 nD for the Woodford Shale, whereas the permeability for the model is about one order of magnitude higher, at about 0.1 mD. It should be noted that while shale matrix permeability is usually very low in the nano-Darcy range, the overall permeability taking into account natural fractures can be substantially higher. The values that populate the permeability grid of the geological model represent a combined permeability.

Poisson's ratio varied between 0.15 and 0.25 for the Woodford Shale in the additional log suite, which doesn't necessarily make the Poisson's ratio of 0.3 at the perforation depth in the GOHFER^{TM} model incorrect, since this value is still in the possible range seen in Fig. 3.19. The Young's modulus values that can be read from the log were found to be between 3.5 and 5.5 MMpsi agreeing with Fig. 3.19 and possibly indicate that the Young's modulus populating the grid is slightly too low. The total stress read from the log is about 5,500 psi for the perforation depth, which is about 600 psi lower than what the value found in the model. However, since the overall stress and fracture gradient agree with what the service company anticipated, the stress-related values used in the model were considered fairly accurate.

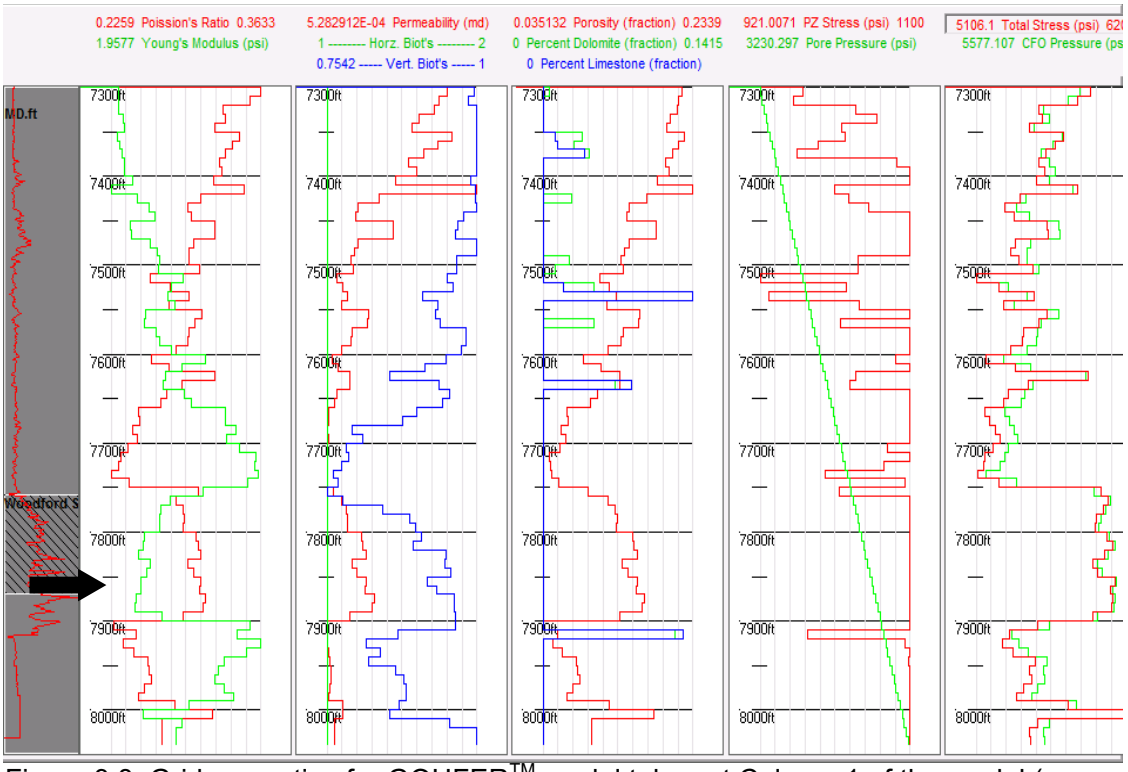

Figure 3.8: Grid properties for GOHFER™ model taken at Column 1 of the model (arrow indicates perforation depth).

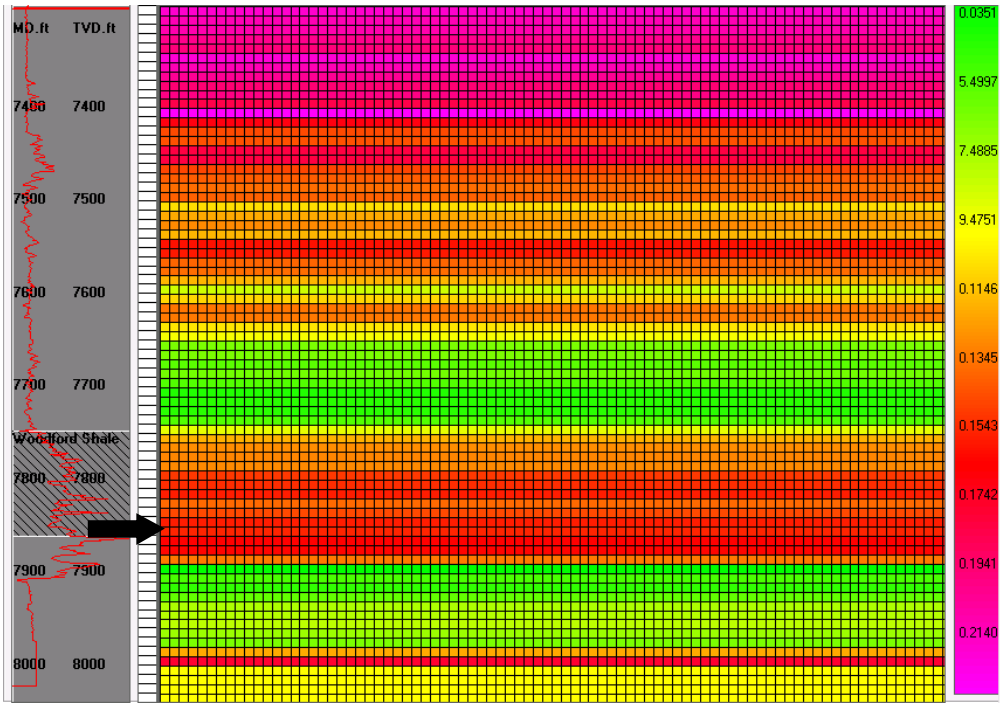

Figure 3.9: Effective porosity in % profile (arrow indicates perforation depth). Depths are on the left. Porosity scale is on the right.

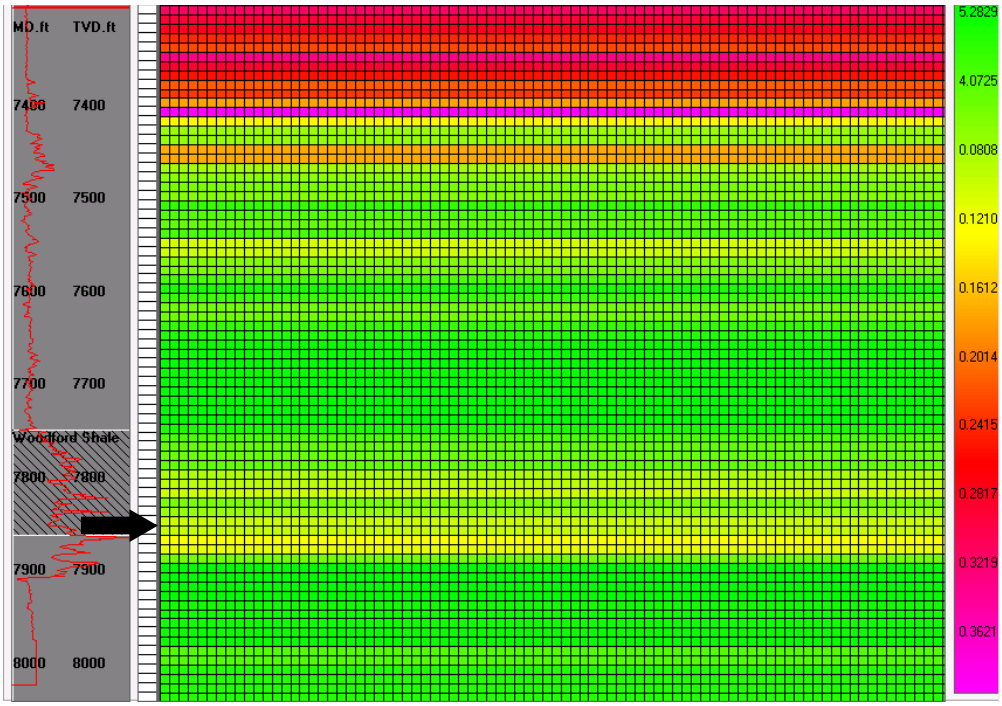

Figure 3.10: Permeability in mD profile (arrow indicates perforation depth). Depths are on the left. Permeability scale is on the right.

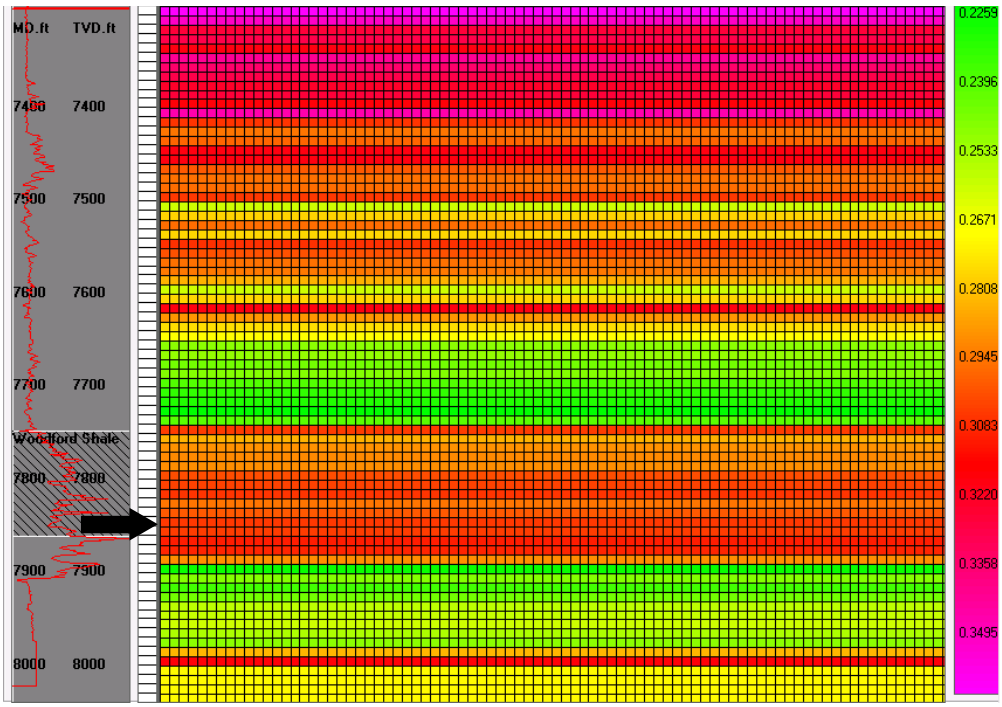

Figure 3.11: Poisson's ratio profile (arrow indicates perforation depth). Depths are on the left. Poisson's ratio scale is on the right.

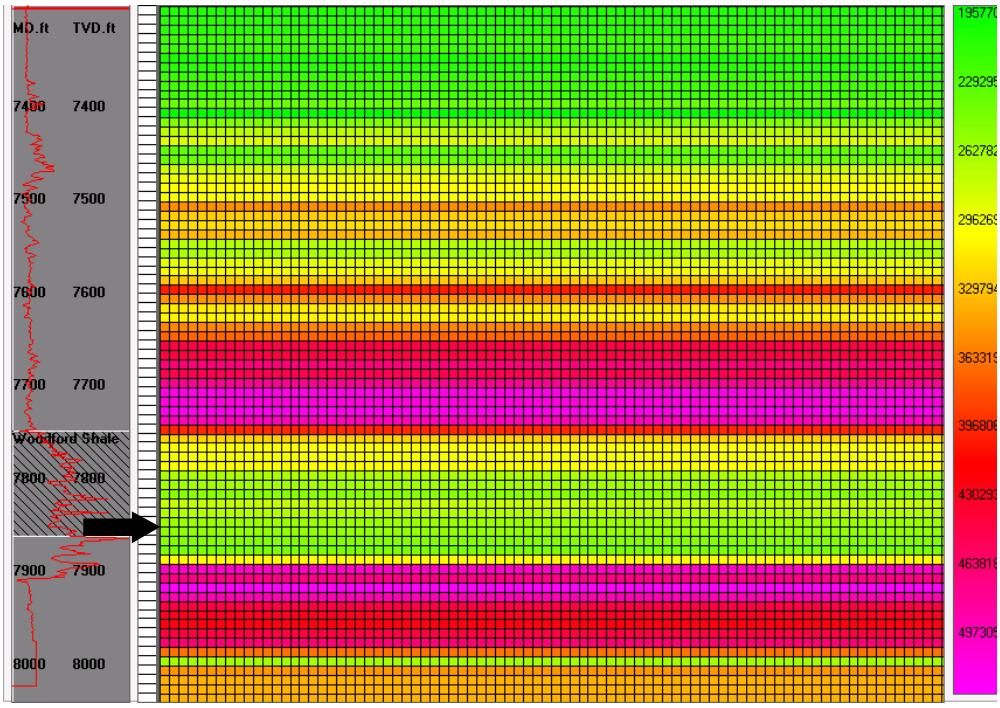

Figure 3.12: Young's modulus in psi profile (arrow indicates perforation depth). Depths are on the left. Young's modulus scale is on the right.

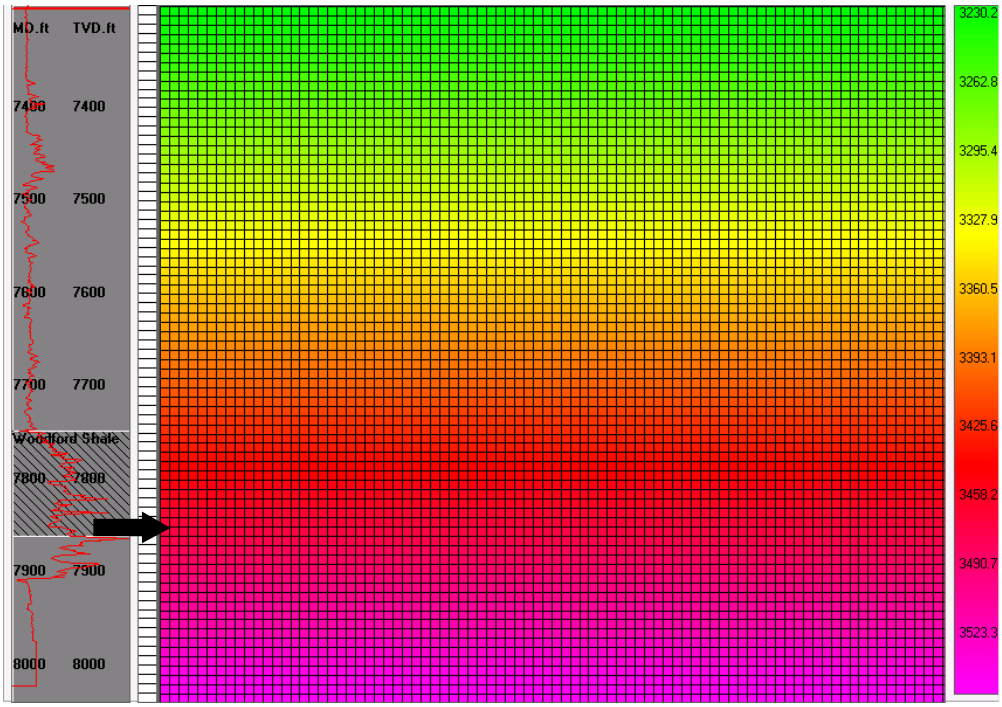

Figure 3.13: Pore pressure in psi profile (arrow indicates perforation depth). Depths are on the left. Pore pressure scale is on the right.

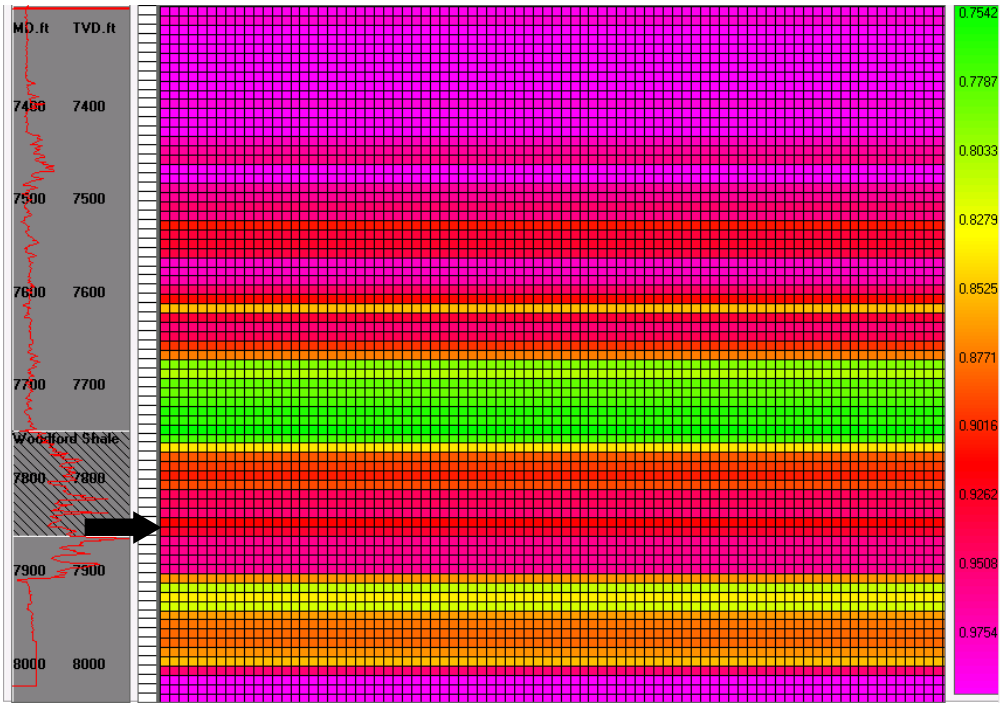

Figure 3.14: Vertical Biot's constant profile (arrow indicates perforation depth). Depths are on the left. Vertical Biot's Constant scale is on the right.

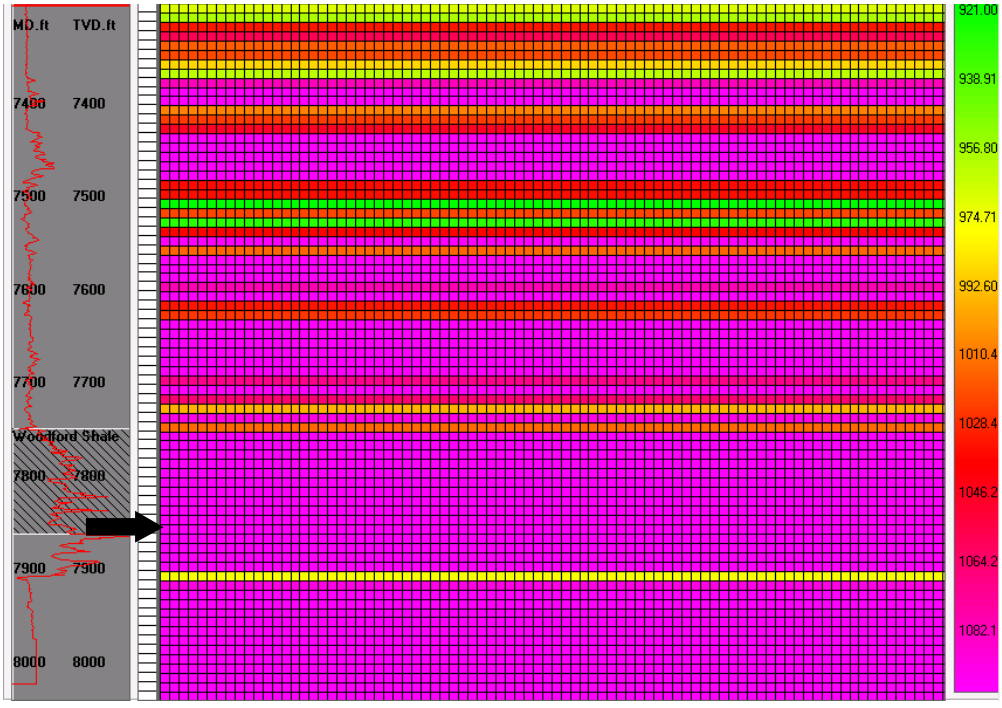

Figure 3.15: Process zone stress in psi profile (arrow indicates perforation depth). Depths are on the left. Process Zone Stress scale is on the right.

Figure 3.16: Total stress in psi profile (arrow indicates perforation depth). Depths are on the left. Total Stress scale is on the right.

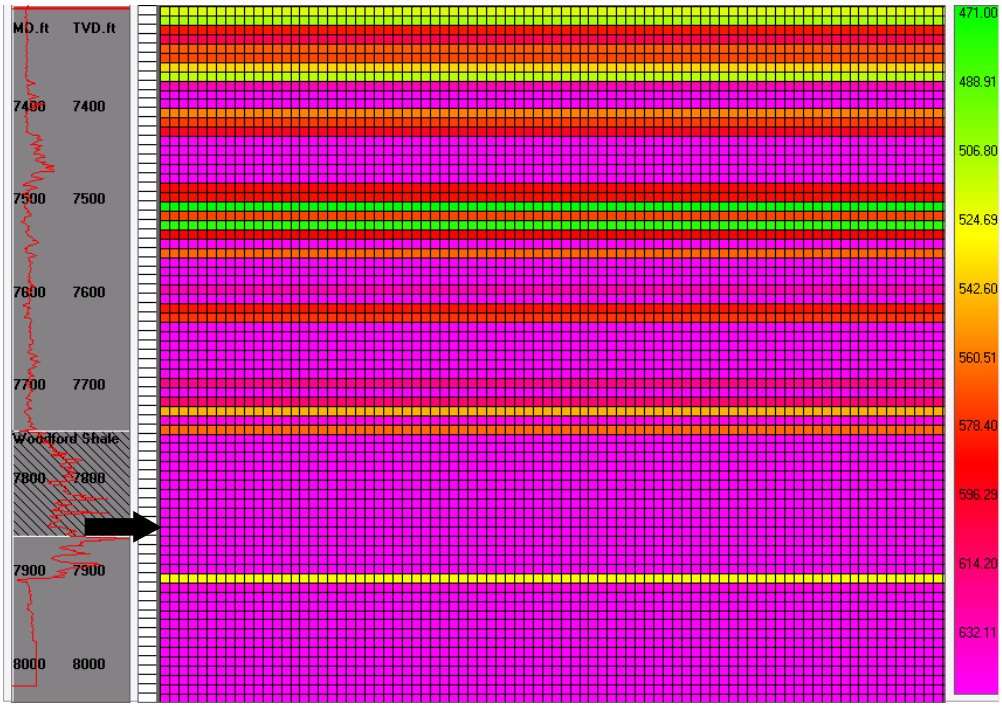

Figure 3.17: Fissure Opening Pressure in psi profile (arrow indicates perforation depth). Depths are on the left. Fissure Opening Pressure scale is on the right.

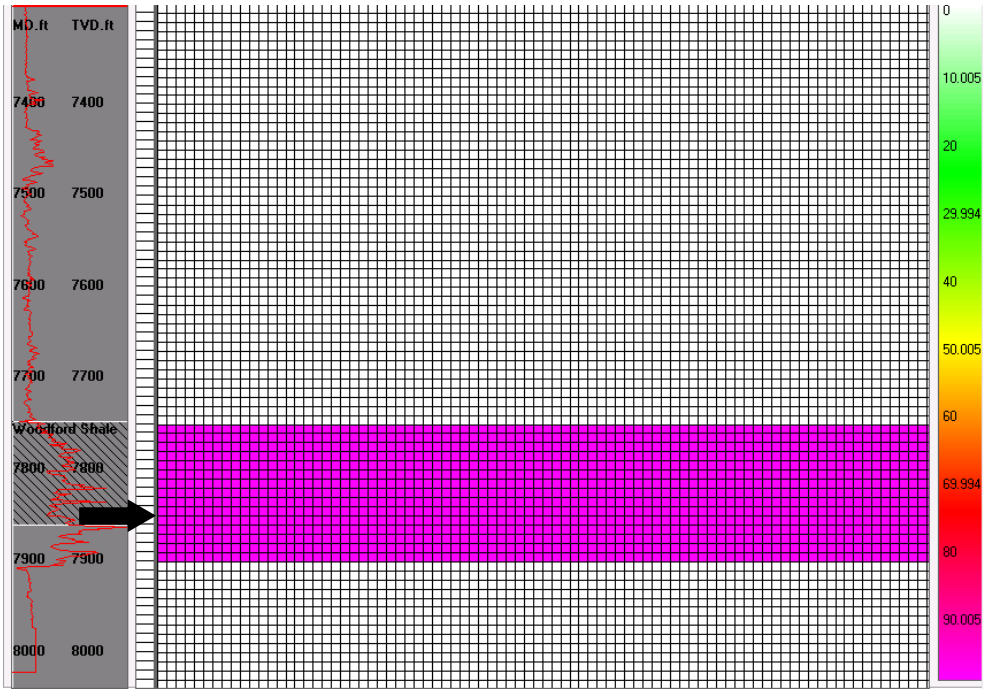

Figure 3.18: Tectonic strain in microstrains profile (arrow indicates perforation depth). Depths are on the left. Tectonic strain scale is on the right.

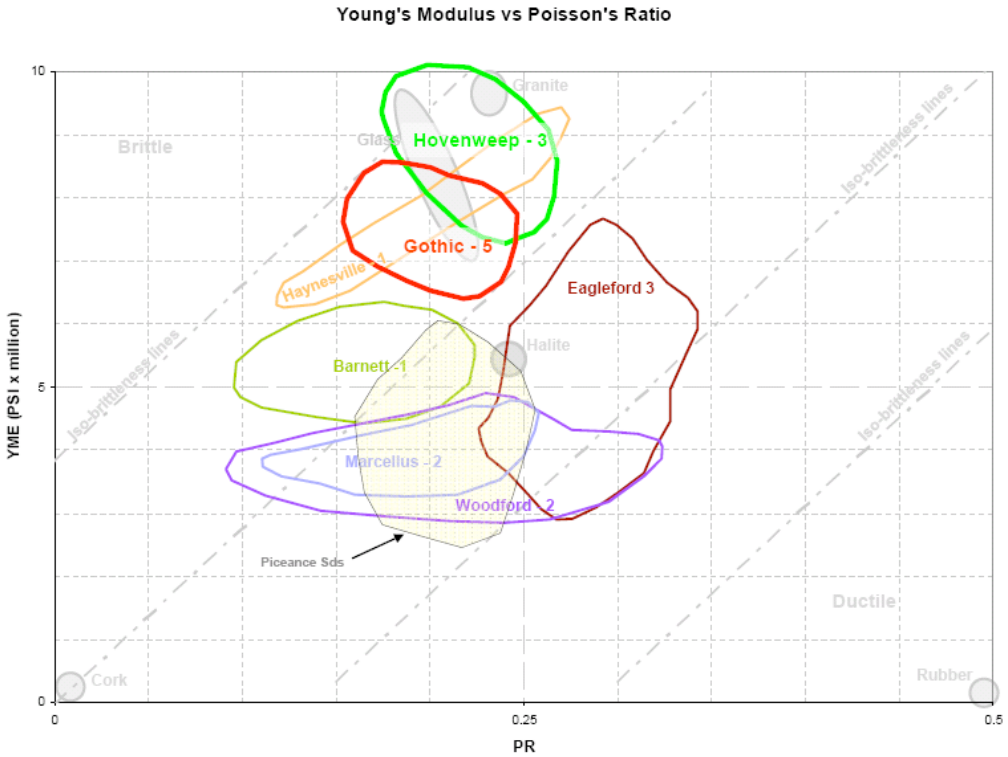

Figure 3.19: Young's modulus vs. Poisson's ratio. Woodford Shale properties can be seen at 0.085 – 0.325 for the Poisson's ratio, and 2.8 – 4.9 MMpsi for the Young's modulus. (Courtesy of P. Moreland, Bill Barrett Corporation, 2010)

3.5 Pressure and Geometry Matching

The process of post-treatment pressure matching and model calibration brings together the two ends of hydraulic fracturing analysis. Although a model, on the one hand, is able to calculate fracture growth and to anticipate properties, the results are often questionable and "suffer from a tenuous and generally unknown relationship with reality" (Weijers et al., 2005).

The danger of fracture modeling lies in non-unique solutions that produce the desired outcome but are detached and not representative of the processes occurring in a particular reservoir (Cipolla et al., 2009). Direct measuring technologies like microseismic fracture mapping, on the other hand, can just record what is occurring in the reservoir but lack the ability of parameter variation to prognosticate a different outcome. Without any further information they also fail to deliver satisfactory explanation of why the fracture growth occurred the way it did. Pressure matching incorporating actual treatment data and measurements makes a model more accurate and 'real', and also makes it capable of illustrating how a particular reservoir will react to a certain stimulation (Weijers et al., 2005). It should always be remembered, though, that any output generated is only as good as the input that goes into creating it. As mentioned in the introduction to this chapter, the GOHFER^{TM} models for each stage are calibrated in two steps: first pressure only, and then pressure and geometry matching.

Although it is best to use all available parameters, a few are needed in any case, and should be of the highest accuracy possible (Weijers et al., 2005):

- Mechanical rock properties:
    - Young's modulus
    - (Closure) stress profile
    - Permeability
- Well completion and perforation data
- Fracture treatment data:
    - Treatment schedule
    - Proppant and fluid characteristics
    - Pressure, slurry rate, proppant concentration

The relationship between all parts contributing to the observed bottomhole (or net) pressure is illustrated by the following equation:

$$p_{BH} = p_c + \left(p_{nwb} + p_{tort} + p_{perf}\right) = p_{surface} + p_{hydrostatic} - p_{friction} \qquad \text{(Eq. 3.5)}$$

p_{BH}	…	bottomhole (or net) pressure [psi]
p_c	…	closure pressure [psi]
p_{nwb}	…	pressure loss due to near wellbore effect [psi]
p_{tort}	…	pressure loss due to tortuosity [psi]
p_{perf}	…	pressure loss at perforations [psi]
$p_{surface}$	…	surface pressure [psi]
$p_{hydrostatic}$	…	hydrostatic pressure [psi]
$p_{friction}$	…	pressure loss due to friction [psi]

- Closure pressure is computed by GOHFER™ according to Eq. 3.3 as explained in Section 3.3.3.5.
- Near wellbore, tortuosity, and perforation effects are being accounted for by the Tortuosity Pre-Factor, the Perforation Coefficient of Discharge, and the Perforation Factor. Additional change in the bottomhole pressure can be achieved by modification of the Pressure Dependent Modulus Stiffness Factor, and Pressure Dependent Leak-Off.
- Hydrostatic pressure is dependent on the treatment fluid and proppant.
- Friction pressure is also dependent on the fluid and proppant used, and can be adjusted by modification of the Friction Correction Factor.
- Treatment tubing diameter is 4.892 in. for all stages, since the jobs are pumped through the same casing.

GOHFER™ simulates fracture geometry in terms of length, height, and width. One of the shortcomings of trying to simulate horizontal wells with GOHFER™ is the fact that length and height are simulated in the plane of the grid. For the models in this work, the plane of the grid is a longitudinal cross-section of the wellbore, as illustrated in Fig. 3.20, which means that the simulated fractures are longitudinal as well, i.e. along the horizontal wellbore. Looking at the microseismic data however, it can be seen that the fractures are actually transverse, meaning more or less perpendicular to the wellbore. Thus the simulated fracture length from GOHFER™ represents the longitudinal stretch of the fracture network, i.e. the area where we see microseismic activity, rather than what is usually referred to as fracture length. Matching is therefore done in two steps. Two

models are built for each stage: one in the longitudinal direction of the well, simulating the longitudinal dimension of the fracture network, and one perpendicular to the well, simulating the actual length of the transverse fractures. Fracture height is not affected since it is the same for the center of the wellbore or perforation cluster regardless of the orientation of the cross-section. The simulated fracture width on the other hand is incorrect for the longitudinal models, because it is the width of a longitudinal fracture, and does not give any information about the actual fracture width of the transverse fractures.

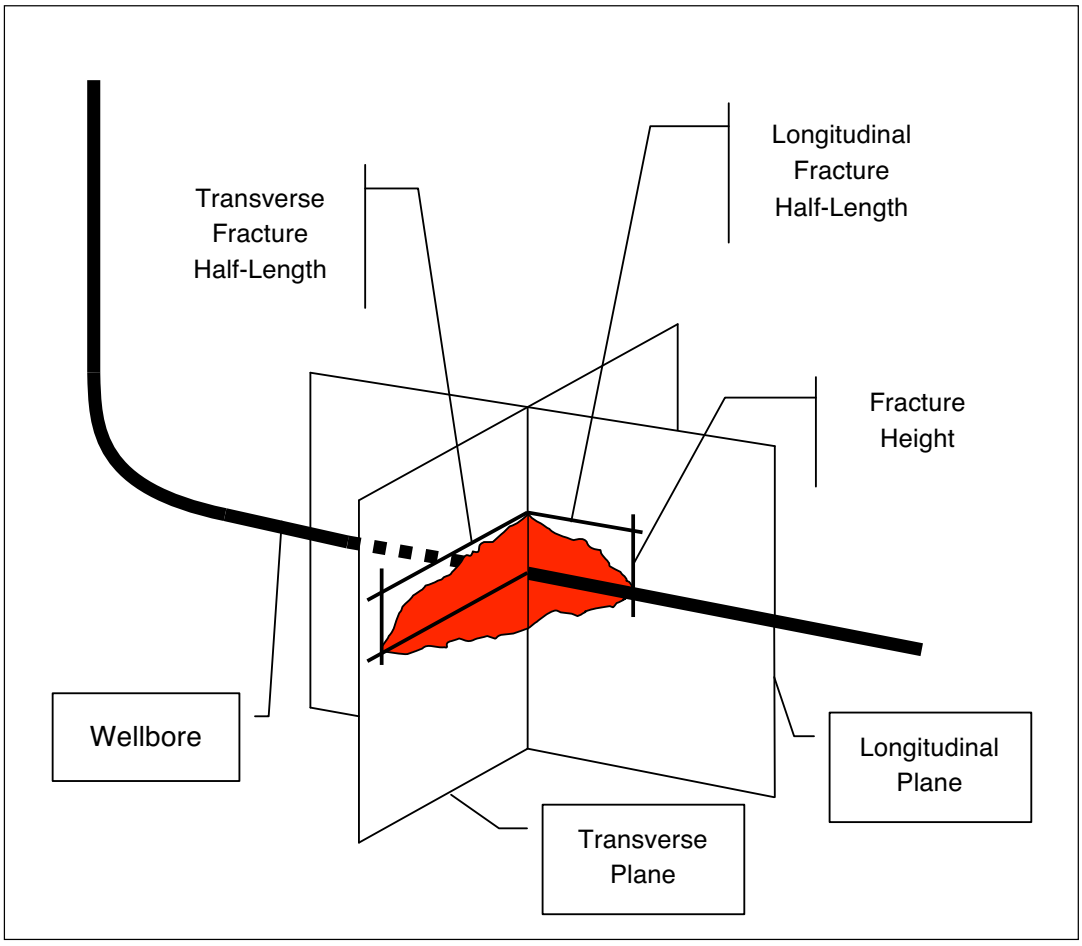

Figure 3.20: Longitudinal vs. transverse fracture planes in conjunction with a horizontal wellbore.

Since the treatment was performed on a well with a horizontal interval of about 2,300 ft, some variation of parameters from stage to stage can be expected. The matches were achieved by modifying the following parameters:

- Pressure Dependent Modulus Stiffness Factor
- Pressure Dependent Leak-off
- Tortuosity pre-factor
- Tectonic strain
- TSC
- Perforation coefficient
- Friction factor
- Perforation factor

In general, it was attempted not to vary the parameters too much and instead find some that work well for all stages within a certain range, in order to provide some consistency. However, they do change throughout the reservoir and along the wellbore, in order to match the simulated and the actual pressure curves, as well as observed fracture geometry from miscroseismic data and simulated fracture geometry. Modification of the last three parameters in the list reflects heterogeneity in terms of perforations and friction, although friction was found to be roughly the same in all stages. Modification of TSC represents the diversion of fracturing fluid into transverse fractures, which ultimately results in shorter (half-) lengths. For matching the pressure only, TSC was set to 0 for all stages, and for both longitudinal and transverse models.

One thing that all stages had in common is that the simulated pressure plummeted during the injection of the first three sand slugs. In order to correct for this, the perforation factor was adjusted in a certain pattern which will be explained for each stage individually. As seen in Figs. 3.1 through 3.5, this produced a zig-zag pattern of the simulated pressure during the injection of the 100-mesh sand. Although the pressure would have leveled out and matched the actual treatment pressure during the last third of the treatment, eventually, the adjustment of the perforation factor was found to produce a more reasonable match.

3.5.1 Longitudinal Models

As discussed above, matching is done with two types of models: a longitudinal and a transverse representation of the wellbore. The longitudinal direction allows for modeling the fracture network along the longitudinal stretch of the wellbore.

3.5.1.1 Stage I

In order to achieve a complete match with both pressure and geometry, the model was first adjusted to match only the observed treatment pressure regardless of the fracture geometry. It was then further modified to match the obtained geometry parameters as well.

3.5.1.1.1 Pressure Match

As mentioned before, PDMSF reflects the increase of Young's modulus throughout the treatment if, like for this model, a positive value is assumed. A value of 0.005 1/psi was found to increase the simulated pressure sufficiently. PDL accounts for the increase of leak-off due to the opening of natural fractures and fissures and was found to give reasonable results for all stages at a value of 0.003 1/psi. Eq. 3.2 shows how tectonic strain increases the total stress in order to match the simulated pressure. It was set to 100 microstrains for all of the Woodford Shale to achieve an upward shift in treatment pressure needed which could not have been achieved in this fashion by modification of other parameters. The Tortuosity Pre-Factor was set to 0.15 psi/bpm^2. The default perforation coefficient of 0.55 was changed to 0.37 to reflect the actual pressure, meaning that at the beginning of the treatment the perforations were partially clogged. Since the hydraulic pressure of the fluid in the tubing cannot be altered the simulated surface pressure has to be adjusted by modifying the friction factor. Pressure loss due to friction could apparently be minimized throughout the treatment, which is represented by a friction factor of 0.03. Treatment tubing length was set to the measured depth until the first perforation, which was 10,262 ft for this stage.

As mentioned, proppant, pumping rate, and even the stimulation fluid have an effect on how easily the slurry moves through the perforations and through the near wellbore area. Although the Tortuosity Pre-Factor accounts for near wellbore tortuosity, the perforation factor reflects both perforation and near wellbore effects and is therefore not uniform throughout the treatment. Representing the ease with which fluid moves through the perforations, it accounts for (partially) plugged perforations as well as resistance to injection exhibited by the formation. Perforations taking fluid may also modify the stress regime around the perforations that are not taking fluid, potentially

leading to these perforations opening up. For this stage it was set to 0.35 for the interval from the beginning of the treatment on Dec. 10th, 2007 at 07:15:47 to 07:37:56.

Fig. 3.1 shows that no proppant was pumped yet, but a small perforation factor accounts for the pressure peak at the beginning due to the injection of fluid into the reservoir, as well as probably partially plugged perforations. For the next interval until 07:40:06 the perforation factor was increased to 0.45 as the resistance to fluid injection decreases. This can be due to the fact that debris is pumped away and partially plugged perforations open up a little, or because the near wellbore area is altered because of the created hydraulic fractures. When fractures are generated the stress regime in the near wellbore area changes which can also lead to the opening of previously plugged perforations.

The perforation factor is a single number to account for all of the above effects, regardless of which of them is more prominent than others and affects the injection behavior more. It should be noted that it is therefore not completely correct to say that a perforation factor of 0.45 means that 45% of the perforations are open. The combination of the occurring effect rather leads to a condition that can be represented by a perforation factor of 0.45, since it is the only factor to assess these effects at this point of the calibration. The perforation factor was further increased to 0.57 until 07:47:09 to make the increase more gradual; as seen in Fig. 3.1, still no proppant was pumped yet. In the next interval until 08:12:56 it was increased to 0.62 during the injection of the first two slugs of 100-mesh sand, at concentrations of 0.25 lbm/gal and 0.50 lbm/gal, respectively. Between the second and the third slug of proppant with a concentration of 0.75 lbm/gal, the factor was set to 0.39 until 08:16:31. As more and more proppant and fluid are pumped into the reservoir, the proppant concentration at the perforations and in the near wellbore area increases, so the perforation factor has to be lowered again in order for the simulated pressure to match actual treatment data. From then on until the end of the treatment at about 10:20:00, it was further decreased to 0.35 to further simulate the behavior explained above. However, the perforation factor doesn't seem to matter as much towards the end of the treatment. This is probably because the reservoir is becoming more and more saturated with proppant and pressure effects tend to become more uniform and homogeneous and apparently can be modeled more accurately by the simulator without user-defined modifications.

3.5.1.1.2 Geometry Match

To accomplish the pressure and geometry match for Stage I, PDMSF was set to 0.0045 1/psi, PDL to 0.00025 1/psi, and tectonic strain for the Woodford Shale to 70 microstrains. The Tortuosity Pre-Factor was set to 0.15 psi/bpm^2. The perforation coefficient was decreased from the default value to 0.37, with a friction factor of 0.03 in order to achieve a match. TSC was adjusted to 0.00025. Treatment tubing length was set to the measured depth until the first perforation, which was 10,262 ft for this stage.

The perforation factor was set to 0.35 for the interval from the beginning of the treatment on Dec. 10th, 2007, at 07:15:47 to 07:37:56. For the next interval until 07:40:06 the perforation factor was increased to 0.45 as the resistance to fluid injection decreases. It was then further increased to 0.57 until 07:47:09 to make the increase more gradual. During the injection of the first two slugs of 100-mesh sand, it was increased to 0.62 until 08:12:56. Between the second and the third slug of proppant with a concentration of 0.75 lbm/gal, the factor was set to 0.38 until 08:16:31 and then further decreased to 0.35 until the end of the treatment at about 10:29:00.

The microseismic data showed that the main fracture has a longitudinal dimension of about 630 ft, and a height of about 630 ft. Microseismic activity was not well contained to the Stage I perforations. The above parameters led to a simulated longitudinal stretch of fracturing activity of 500 ft, and a simulated height of 150 ft. Fig. 3.21 shows the final pressure match.

As seen in Figure 3.22, the final fracture width is about 0.1 in after the pumps have been shut off. Fig. 3.23 shows that the final proppant concentration around the perforations is up to 0.79 lb/ft^2. Although more height growth occurred above the wellbore, it can be seen that most proppant was deposited below the wellbore. The time-lapse visualization showed that upward and downward growth seemed to occur simultaneously. There is not only a transition from low to high proppant concentration between above and below the wellbore, but also between the perforation intervals toward the end of the wellbore (right of figures) and between those further up the horizontal section (left of figures). Fig. 3.24 shows the final proppant concentration overlaid with surface microseismic data for Stage I. After the pumps were shut-off the

proppant concentration does not extend over the full height of the created fracture. Height issues are discussed in detail in Section 8.1.

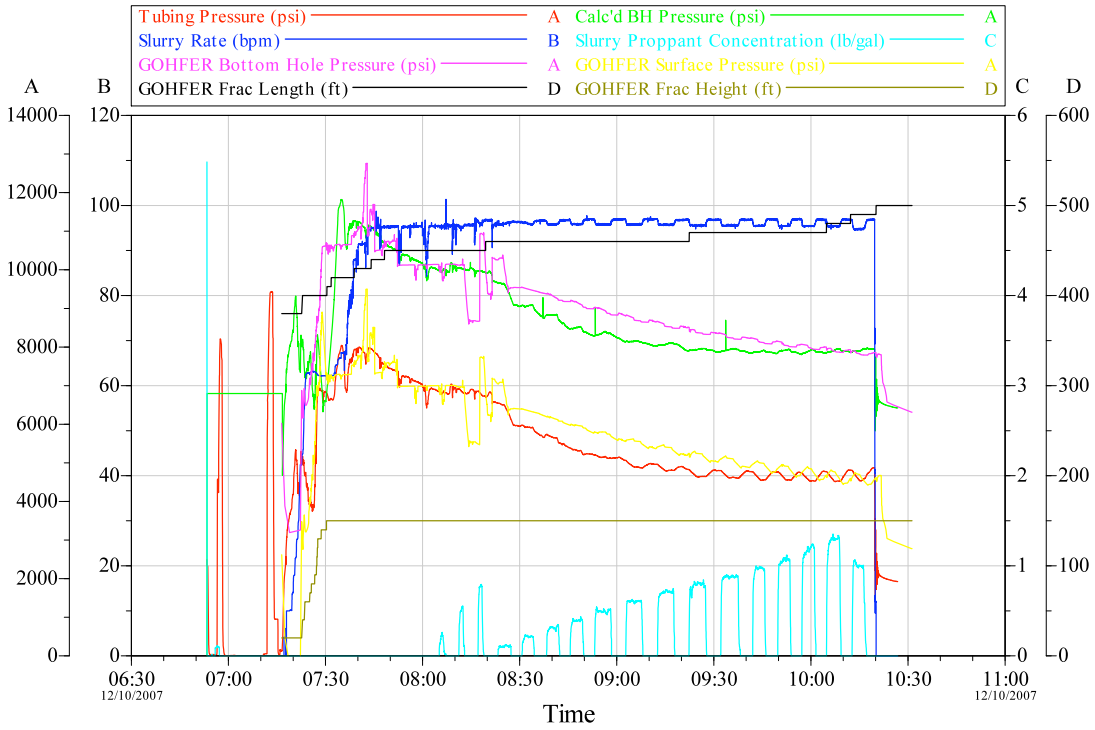

Figure 3.21: Longitudinal pressure match for Stage I. Final fracture geometry from the model is also shown.

3.5.1.2 Stage II

In order to achieve a complete match with both pressure and geometry, the model was first adjusted to match only the observed treatment pressure regardless of the fracture geometry. It was then further modified to match the obtained geometry parameters as well.

3.5.1.2.1 Pressure Match

As in the first stage, PDMSF was set to 0.005 1/psi, PDL to 0.003 1/psi, and tectonic strain for the Woodford Shale to 100 microstrains. The Tortuosity Pre-Factor was set to 0.15 psi/bpm^2. The perforation coefficient was decreased from the default

value to 0.3, with a friction factor of 0.05 in order to achieve a pressure match. Treatment tubing length was set to the measured depth until the first perforation, which was 9,764 ft for this stage.

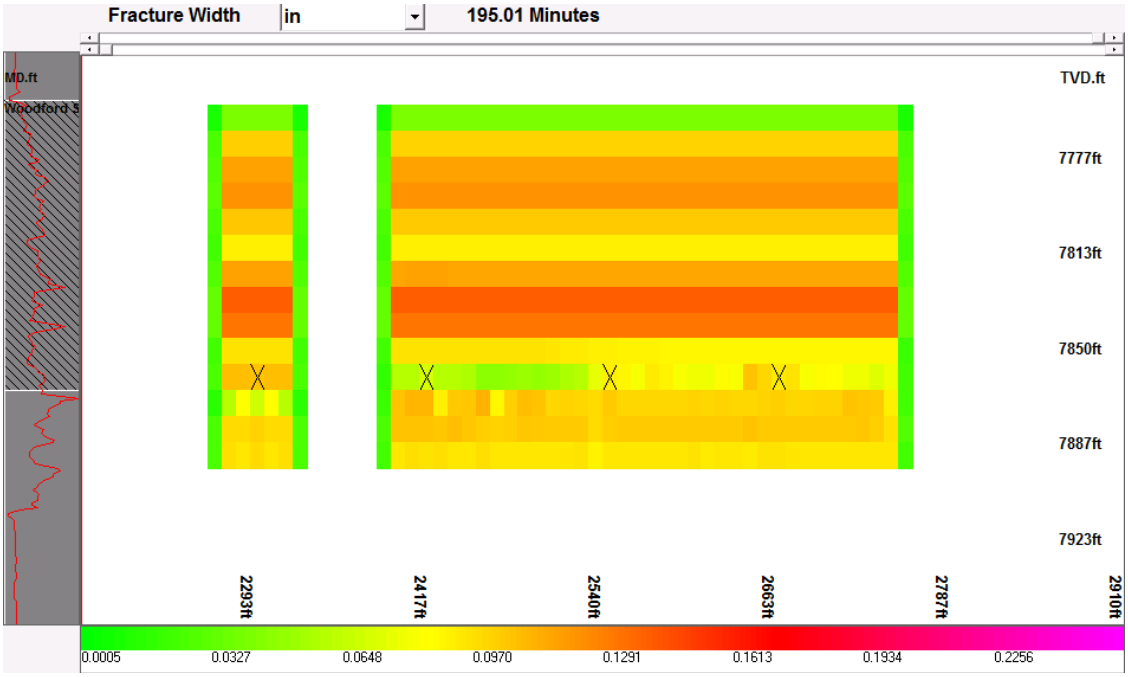

Figure 3.22: Fracture width for longitudinal pressure and geometry match for Stage I (X represents perforations).

For this stage, the perforation factor was set to 0.45 for the first interval from the beginning of the treatment on Dec. 10th, 2007 at about 14:26:30 until 14:50:00; no proppant was pumped and the initially low value is necessary to simulate the pressure peak at the beginning of the treatment as the injection starts, as seen in Fig. 3.2. The factor was then increased to 0.6 for the next interval until 15:18:27, after the first slug of 0.25 lbm/gal 100-mesh is pumped. When the second slug of 0.50 lbm/gal is being pumped, the proppant concentration around the wellbore increases and has an effect on the treatment pressure. In order to simulate this, a gradual decrease of the perforation factor is necessary; otherwise the simulated pressure would decrease too fast. For the next interval until the onset of the third slug being pumped at 0.75 lbm/gal at 15:24:34, it was set to 0.35. It was then further decreased to 0.3 until after the third slug was pumped at 15:27:00. From then on until the end of the treatment at about 17:34:00, it was set to 0.25.

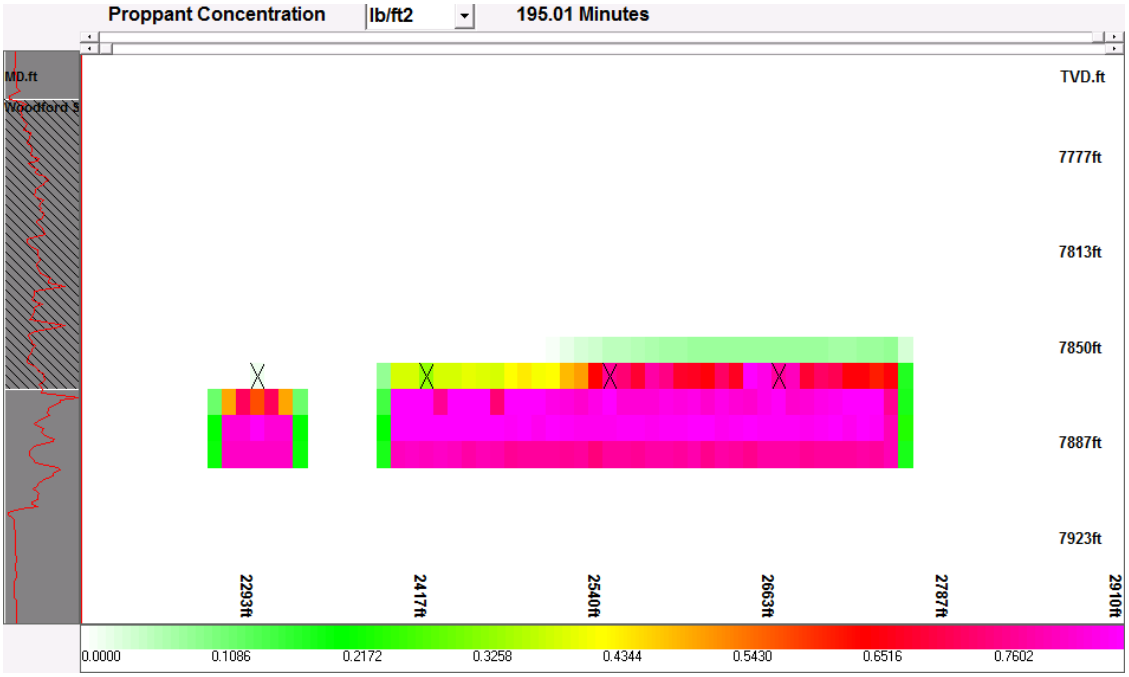

Figure 3.23: Proppant concentration for longitudinal pressure and geometry match for Stage I (X represents perforations).

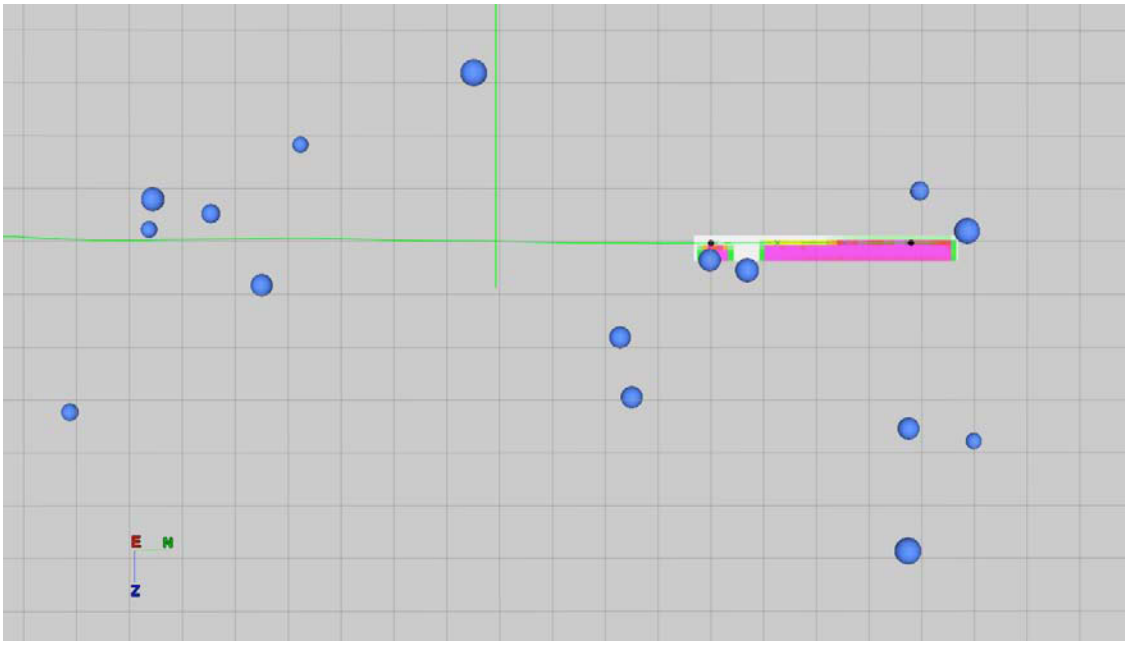

Figure 3.24: Proppant concentration and microseismic data for the longitudinal model of Stage I shown in a south-north plane. Blue spheres show surface recordings. Final proppant concentration does not extend over the total height of the created fracture. The perforation cluster reaches from the black dot on the left end of the proppant concentration to the black dot on the right end. The treatment wellbore can be seen in green from left to right. The grid shown is 100 by 100 ft.

3.5.1.2.2 Geometry Match

For this match scenario, PDMSF was set to 0.005 1/psi, PDL to 0.0003 1/psi, and tectonic strain for the Woodford Shale to 65 microstrains. The Tortuosity Pre-Factor was set to 0.15 psi/bpm^2. The perforation coefficient was decreased from the default value to 0.3, with a friction factor of 0.05 in order to achieve a match. TSC was adjusted to 0.00029. Treatment tubing length was set to the measured depth until the first perforation, which was 9,764 ft for this stage.

The perforation factor was set to 0.45 for the first interval from the beginning of the treatment on Dec. 10th, 2007 at about 14:26:30 until 14:50:00. The factor was then increased to 0.6 for the next interval until 15:18:27, after the first slug of 0.25 lbm/gal 100-mesh is pumped, as seen in Fig. 3.2. For the next interval until the onset of the third slug being pumped at 0.75 lbm/gal at 15:24:34, it was set to 0.35. It was then further decreased to 0.3 until after the third slug was pumped at 15:27:00. From then on until the end of the treatment at about 17:34:00, it was set to 0.25.

The microseismic data showed that the microseismic cloud has a longitudinal dimension of about 830 ft, and a height of about 290 ft. Microseismic activity was well contained to Stage II perforations. Above parameters led to a simulated longitudinal stretch of fracturing activity of about 790 ft, and a simulated height of about 240 ft. Fig. 3.25 shows the final pressure match.

Fracture growth occured first upward and only toward the very end of the treatment does the fracture breaks out downward. After the pumps were shut off, a final width around 0.07 in could be observed, as seen in Fig. 3.26. Most proppant was deposited above the wellbore, but in the end when the fracture suddenly begins to grow downwards, a lot of proppant also transports downward, and not into the fracture half above the wellbore anymore. This results in a final proppant concentration below the wellbore of around 0.40 lb/ft^2, which is substantially higher than above the wellbore, as seen in Fig. 3.27. Fig. 3.28 shows the final proppant concentration overlaid with both surface and downhole microseismic data for Stage II. After the pumps were shut-off the proppant concentration does not extend over the full height of the created fracture. Height issues are discussed in detail in Section 8.1.

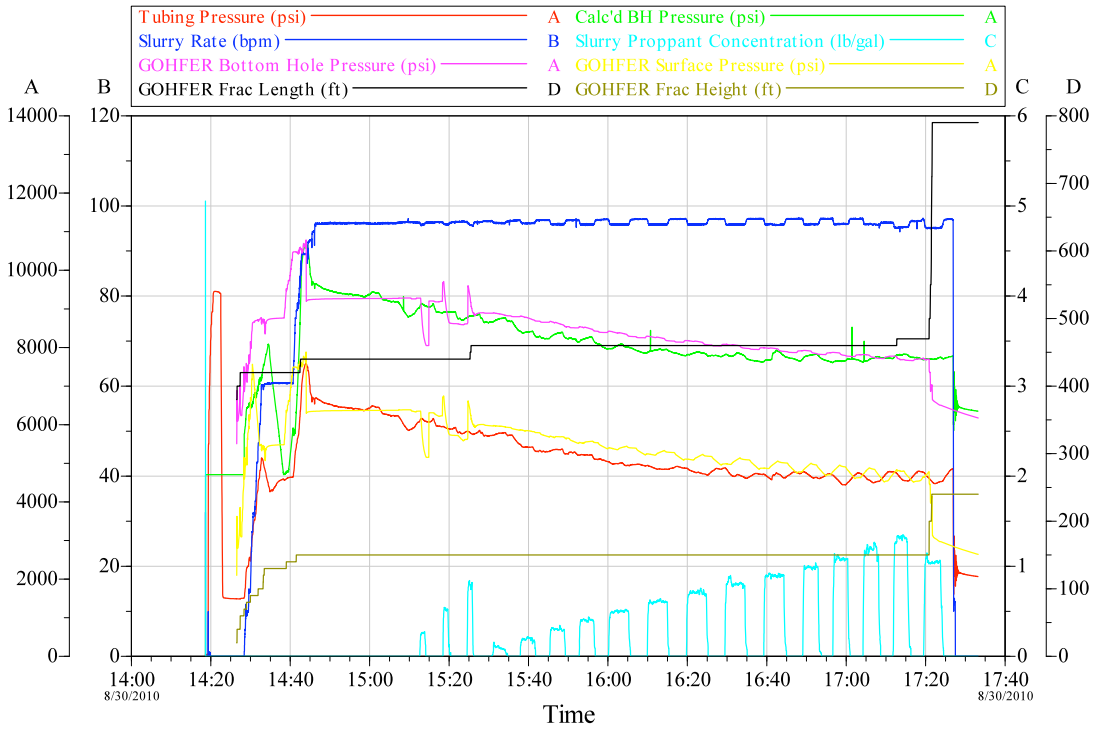

Figure 3.25: Longitudinal pressure match for Stage II. Final fracture geometry from the model is also shown.

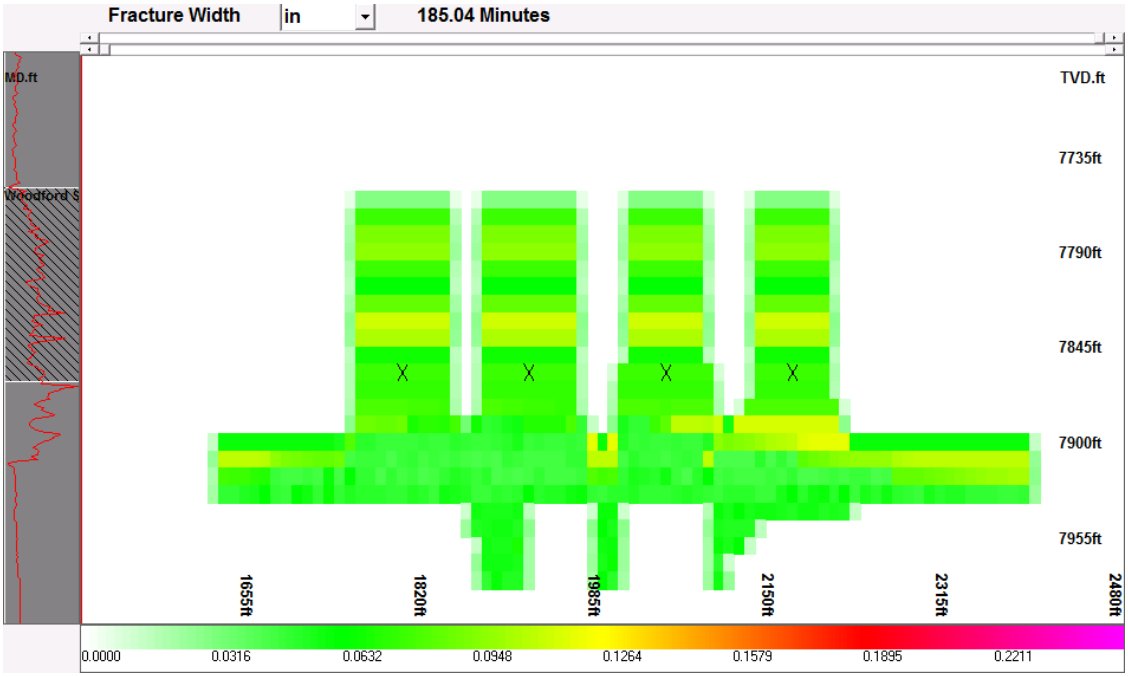

Figure 3.26: Fracture width for longitudinal pressure and geometry match for Stage II (X represents perforations).

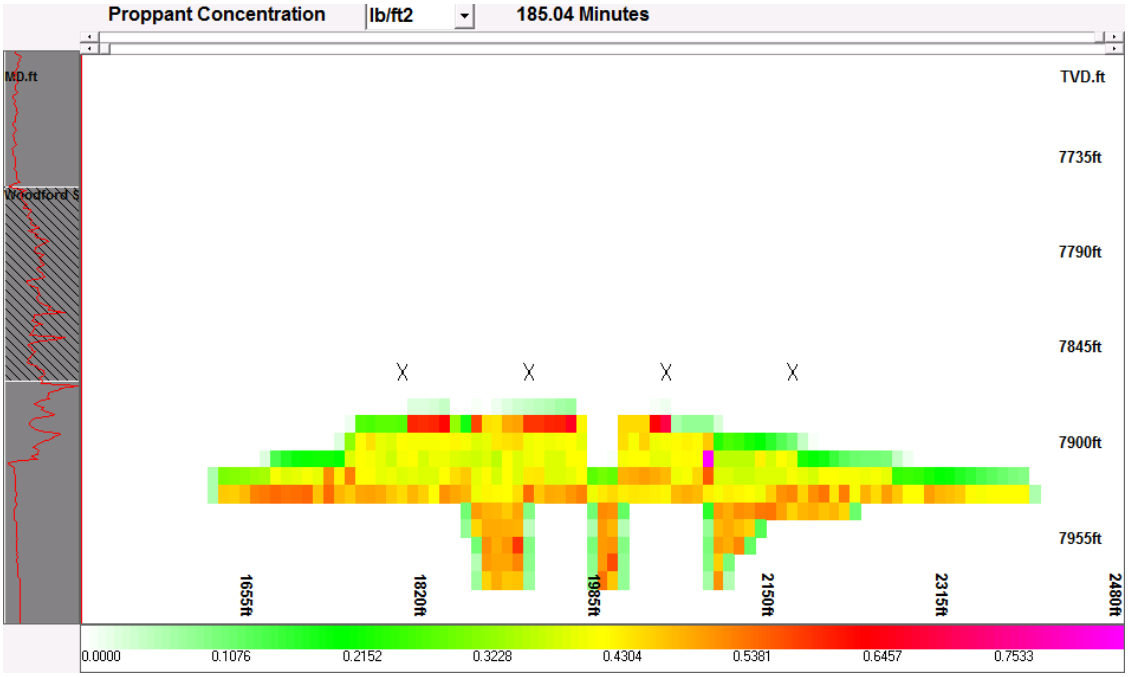

Figure 3.27: Proppant concentration for longitudinal pressure and geometry match for Stage II (X represents perforations).

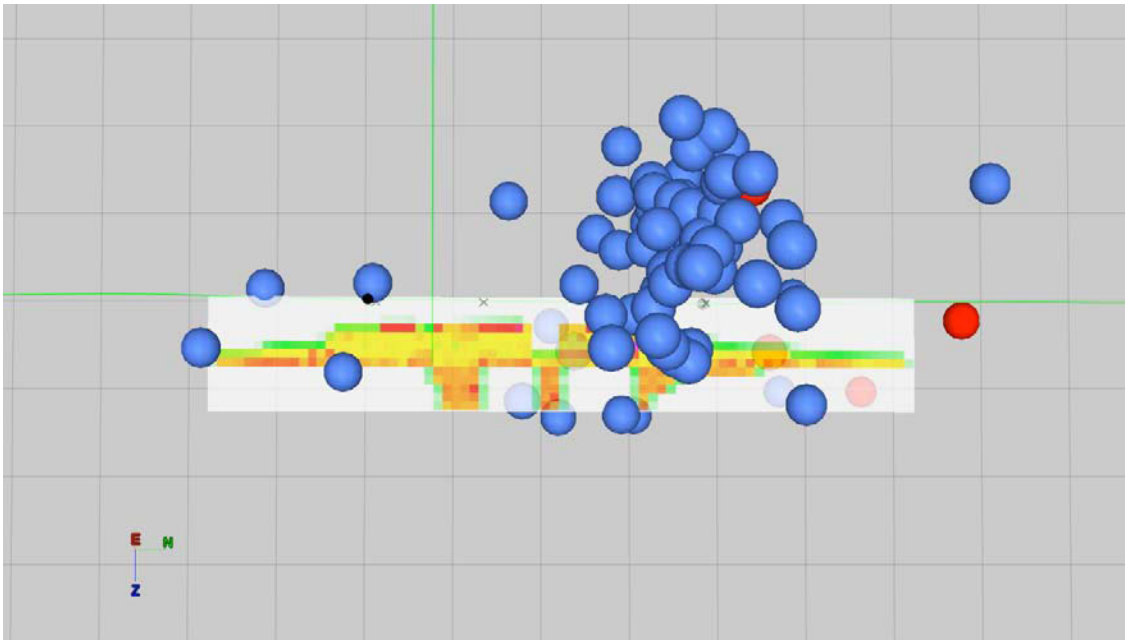

Figure 3.28: Proppant concentration and microseismic data for the longitudinal model of Stage II shown in a south-north plane. Blue spheres show downhole recordings, whereas red spheres show surface recordings. Final proppant concentration does not extend over the total height of the created fracture. The perforation cluster reaches from the black dot on the left end of the proppant concentration to the black dot on the right end. The treatment wellbore can be seen in green from left to right. The grid shown is 100 by 100 ft.

3.5.1.3 Stage III

In order to achieve a complete match with both pressure and geometry, the model was first adjusted to match only the observed treatment pressure regardless of the fracture geometry. It was then further modified to match the obtained geometry parameters as well.

3.5.1.3.1 Pressure Match

As for the previous stages, PDMSF was set to 0.005 1/psi, PDL to 0.003 1/psi, and tectonic strain for the Woodford Shale to 100 microstrains. The Tortuosity Pre-Factor was set to 0.15 psi/bpm^2. The perforation coefficient was decreased from the default value to 0.24, with a friction factor of 0.06 in order to achieve a pressure match. Treatment tubing length was set to the measured depth until the first perforation, which was 9,342 ft for this stage.

The perforation factor for the first interval from the beginning of the job on Dec. 11th, 2007, at about 07:02:50 until 07:20:14 was set to 0.55 to reflect the pressure peak shown in Fig. 3.3 as injection begins. It is slightly higher compared to the initial perforation factor in the previous stages due to a slightly lower perforation coefficient. Increasing the first perforation factor while decreasing the perforation coefficient was found to produce the best match with the observed pressure. Until the pumping of the first slug at 0.25 lbm/gal is completed at 07:51:23 the factor was increased to 0.81 to simulate an improvement in how easily fluid is being injected. The proppant concentration around the wellbore increases and in order to keep the simulated pressure up, at the level of the observed pressure, the perforation factor has to be decreased. For this stage a good match could be achieved without much gradual decrease. Until after the second slug with 0.50 lbm/gal is pumped at 07:57:09 it was set to 0.3, to be further lowered to 0.22 until the end of the treatment at about 10:08:00.

3.5.1.3.2 Geometry Match

In this match, PDMSF was set to 0.002 1/psi, PDL to 0.0015 1/psi, and tectonic strain for the Woodford Shale to 45 microstrains. The Tortuosity Pre-Factor was set to 0.10 psi/bpm^2. The perforation coefficient was decreased from the default value to 0.24, with a friction factor of 0.06 in order to achieve a match. TSC was set to 0.0015. Treatment tubing length was set to the measured depth until the first perforation, which was 9,342 ft for this stage.

For the first interval from the beginning of the job on Dec. 11th, 2007, at about 07:02:50 until 07:20:14, the perforation factor was set to 0.55. Until the pumping of the first slug at 0.25 lbm/gal is completed at 07:51:23, the factor was increased to 0.83. Until after the second slug with 0.50 lbm/gal is pumped at 07:57:09 it was set to 0.32, to be further lowered to 0.20 until the end of the treatment at about 10:08:00.

From the microseismic data is can be seen that the microseismic cloud has a longitudinal dimension of about 1,100 ft, and a height of about 550 ft. The microseismic activity of Stage III mostly overlapped with the region around Stage II perforations. Looking at the Stage III perforations, as discussed in detail in Chapter IV, it is obvious that the fracture height for this part of the reservoir is substantially lower, at only 270 ft. Since the already weakened reservoir around the Stage II perforation cluster and the total height of microseismic activity could not be modeled accurately, this height was used for achieving the match. The longitudinal stretch along the wellbore was simulated for this stage with 1,100 ft with a height of 240 ft. Fig. 3.29 shows the final pressure match.

Time-lapse analysis showed that the fracture grew upwards first, with downward growth occurring after the first half of the treatment. As seen in Fig. 3.30, the final width around the perforations is very small at 0.01 in, as opposed to a higher value of 0.05 in in the part of the fracture below the wellbore. Fig. 3.31 shows that only very little proppant was deposited in the part of the fracture above the wellbore. When the fracture started growing downhole almost all proppant seemed to go into that part of the fracture immediately with final concentrations of up to 0.65 lb/ft^2 in that region. Fig. 3.32 shows the final proppant concentration overlaid with microseismic data for Stage III. Height issues are discussed in detail in Section 8.1.

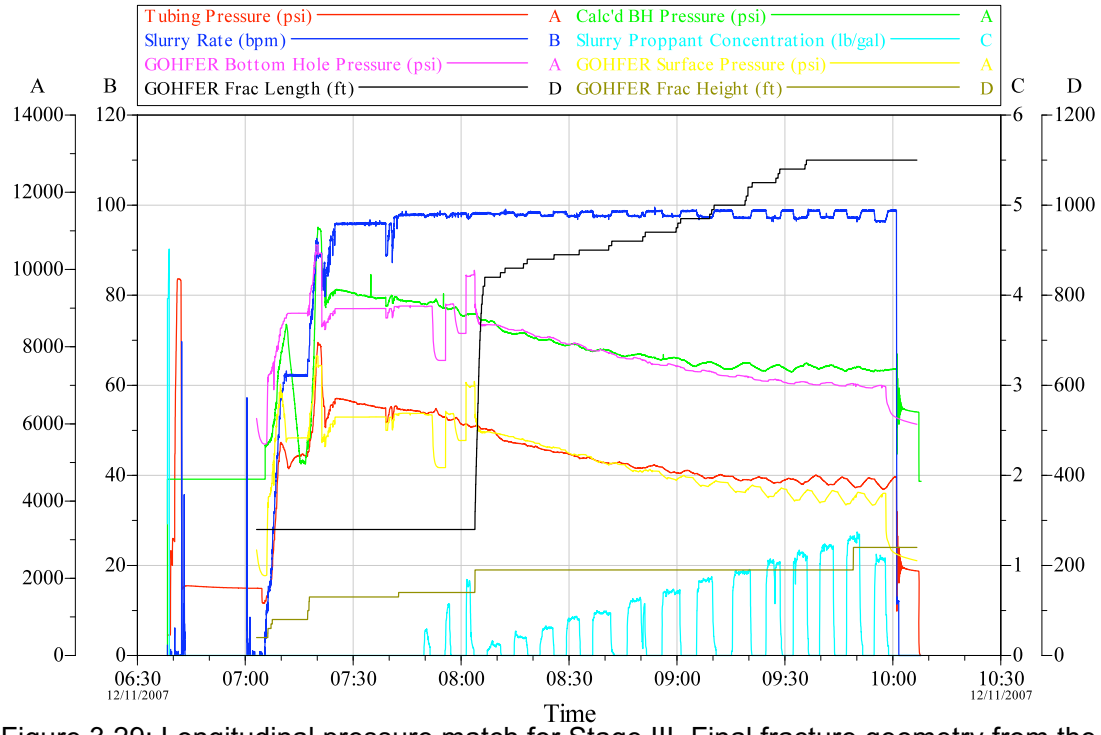

Figure 3.29: Longitudinal pressure match for Stage III. Final fracture geometry from the model is also shown.

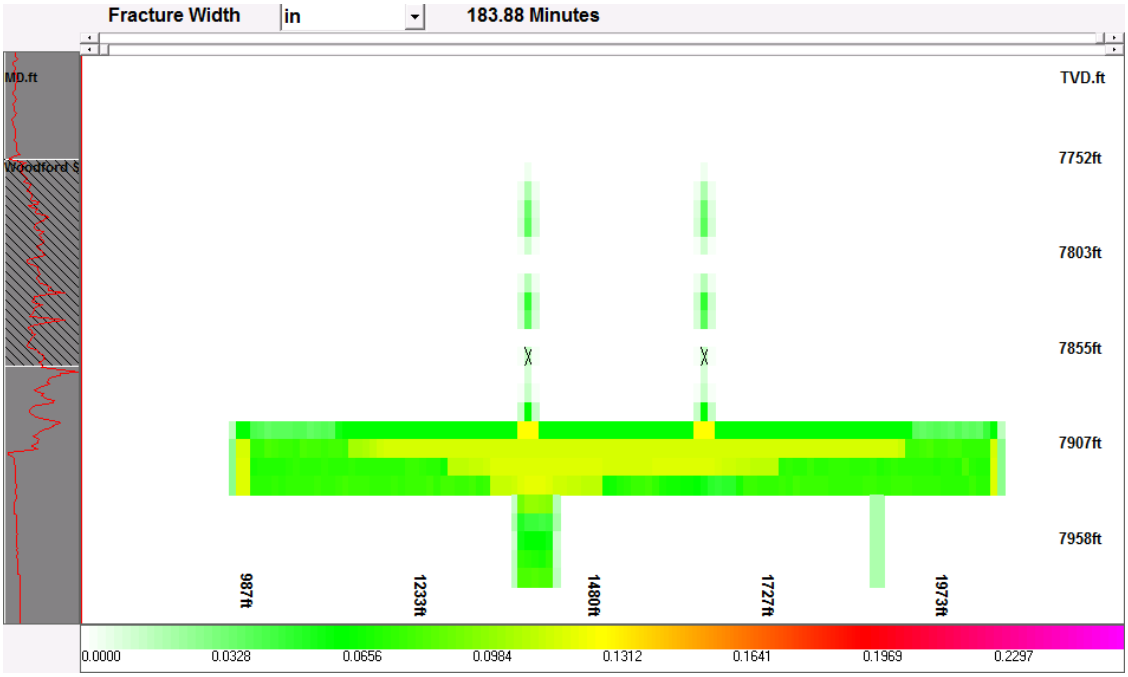

Figure 3.30: Fracture width for longitudinal pressure and geometry match for Stage III (X represents perforations).

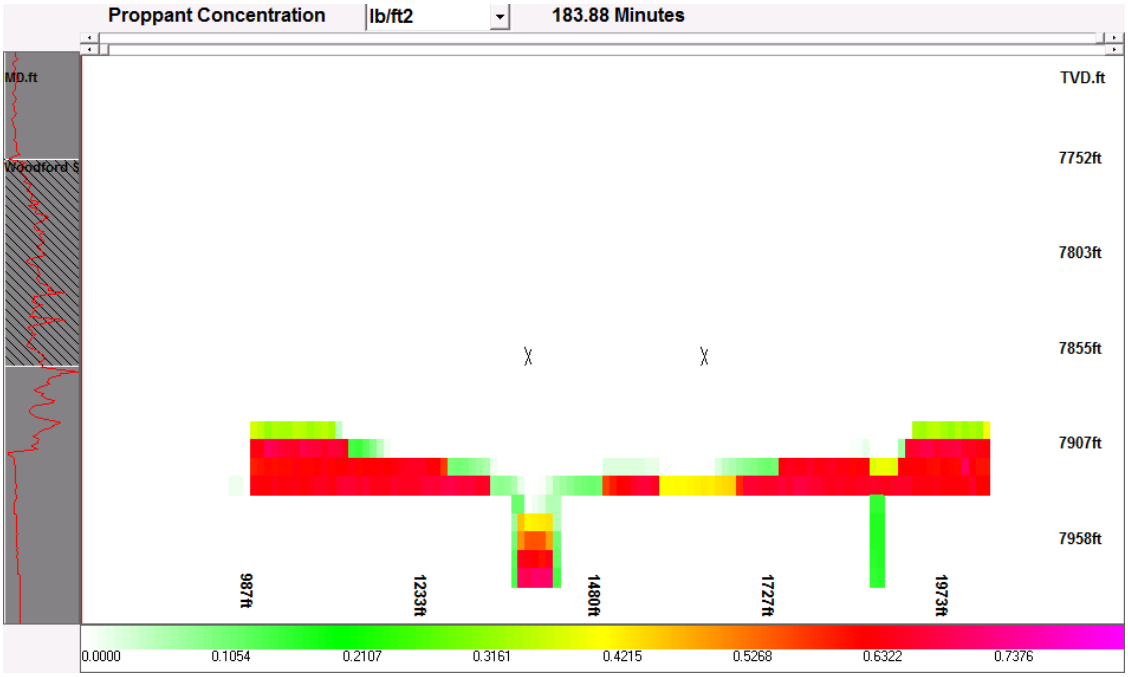

Figure 3.31: Proppant concentration for longitudinal pressure and geometry match for Stage III (X represents perforations).

3.5.1.4 Stage IV

In order to achieve a complete match with both pressure and geometry, the model was first adjusted to match only the observed treatment pressure regardless of the fracture geometry. It was then further modified to match the obtained geometry parameters as well.

3.5.1.4.1 Pressure Match

In this match scenario, PDMSF was set to 0.005 01/psi, PDL to 0.003 1/psi, and tectonic strain for the Woodford Shale to 100 microstrains. The Tortuosity Pre-Factor was set to 0.15 psi/bpm^2. The perforation coefficient was decreased from the default value to 0.25, with a friction factor of 0.07 in order to achieve a pressure match. Treatment tubing length was set to the measured depth until the first perforation, which was 8,951 ft for this stage.

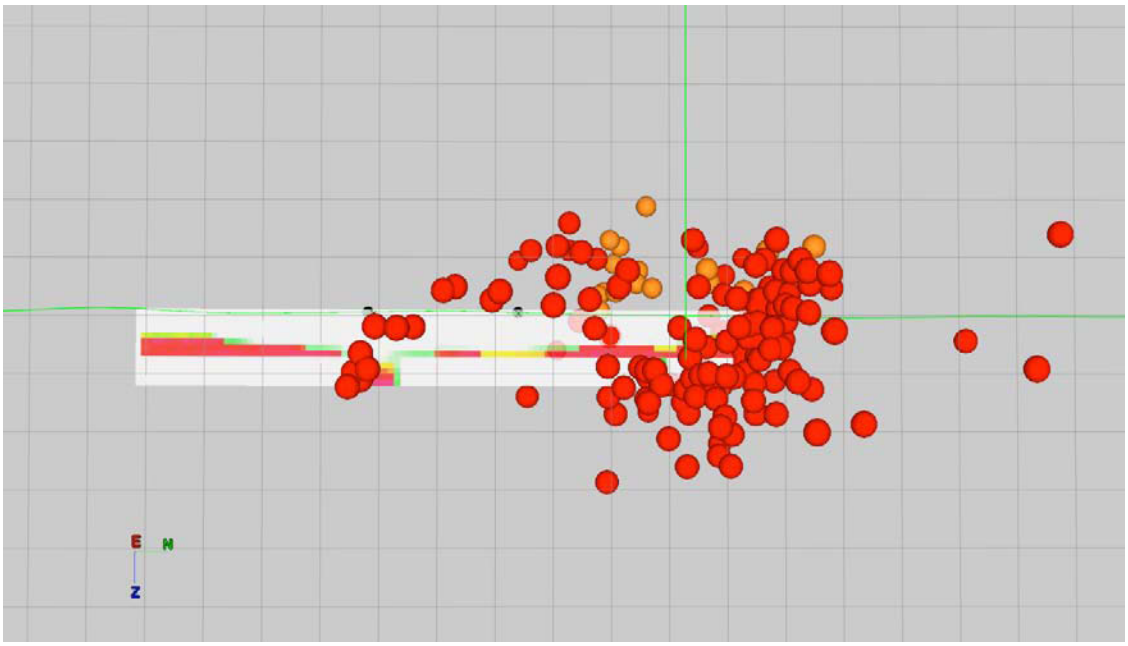

Figure 3.32: Proppant concentration and microseismic data for the longitudinal model of Stage III shown in a south-north plane. Red spheres show downhole recordings, whereas orange spheres show surface recordings. Final proppant concentration does not extend over the total height of the created fracture. The perforation cluster reaches from the black dot on the left end of the proppant concentration to the black dot on the right end. The grid shown is 100 by 100 ft. The treatment wellbore can be seen in green from left to right. Most microseismic activity occurred away from the Stage III perforation cluster in the weakened formation around the Stage II perforation cluster, which the model was not set up to simulate.

In general, the perforation factor for this stage shows the same pattern as for the previous stages. However, especially towards the end of the treatment, it was necessary to perform the decrease in a more gradual fashion. From the beginning of the treatment on Dec. 11th, 2007, at about 13:18:00 until right after the first pressure peak, as seen in Fig. 3.4, it was set to 0.7; no proppant was pumped yet. To reflect the opening up of perforations the factor was increased to 0.82 until after the first slug of 100-mesh sand at 0.25 lbm/gal was pumped at 14:08:18. It was then substantially decreased to 0.35 until the middle of pumping the second slug of 100-mesh sand at 0.5 lbm/gal at 14:12:00 to accurately match the simulated pressure to the observed one. From there on, the factor had to be gradually decreased until the end of the treatment. Until the beginning of the eighth slug of 30/70 proppant at 0.8 lbm/gal at 15:22:20 it was set to 0.25. It was then further decreased to 0.23 until the beginning of the ninth slug of

30/70 proppant at 0.9 lbm/gal at 15:30:26; then to 0.22 until the middle of the tenth slug of 30/70 sand at 1.0 lbm/gal at 15:42:42; further to 0.2 until the eleventh slug of 30/70 at 1.1 lbm/gal was pumped at 15:53:04; and finally to 0.17 until the end of the treatment at about 16:26:00.

3.5.1.4.2 Geometry Match

For the geometry match, PDMSF was set to 0.0025 1/psi, PDL to 0.0018 1/psi, and tectonic strain for the Woodford Shale to 55 microstrains. The Tortuosity Pre-Factor was set to 0.10 psi/bpm^2. TSC was adjusted to 0.0018. The perforation coefficient was decreased from the default value to 0.25, with a friction factor of 0.07 in order to achieve a pressure match. Treatment tubing length was set to the measured depth until the first perforation, which was 8,951 ft for this stage.

From the beginning of the treatment on Dec. 11th, 2007, at about 13:18:00 until right after the first pressure peak, as seen in Fig. 3.4, the perforation factor was set to 0.69. The factor was increased to 0.77 until after the first slug of 100-mesh sand at 0.25 lbm/gal was pumped at 14:08:18. It was then substantially decreased to 0.35 until the middle of pumping the second slug of 100-mesh sand at 0.5 lbm/gal at 14:12:00 to accurately match the simulated pressure to the observed one. From there on, the factor had to be gradually decreased until the end of the treatment. Until the beginning of the eighth slug of 30/70 proppant at 0.8 lbm/gal at 15:22:20 it was set to 0.25. It was then further decreased to 0.20 until the beginning of the ninth slug of 30/70 proppant at 0.9 lbm/gal at 15:30:26; then to 0.18 until the middle of the tenth slug of 30/70 sand at 1.0 lbm/gal at 15:42:42; further to 0.16 until the eleventh slug of 30/70 at 1.1 lbm/gal was pumped at 15:53:04; and finally to 0.13 until the end of the treatment at about 16:26:00.

The microseismic data showed a longitudinal dimension of 1,220 ft, and a height of 720 ft. As for Stage III, most of the microseismic activity occured around the perforation cluster of the previous stage, rather than around the Stage IV perforations. The height of the cloud of microseismic activity at Stage IV perforations is about 670 ft, with both upward and downward growth. The height could not be well simulated by the model, as it simulates a height of only 240 ft, which seems to be a consistent number, and probably related to the geological set-up of the model. The longitudinal stretch on

the other hand was well matched with a simulated length of 1,010 ft. Fig. 3.33 shows the final pressure match.

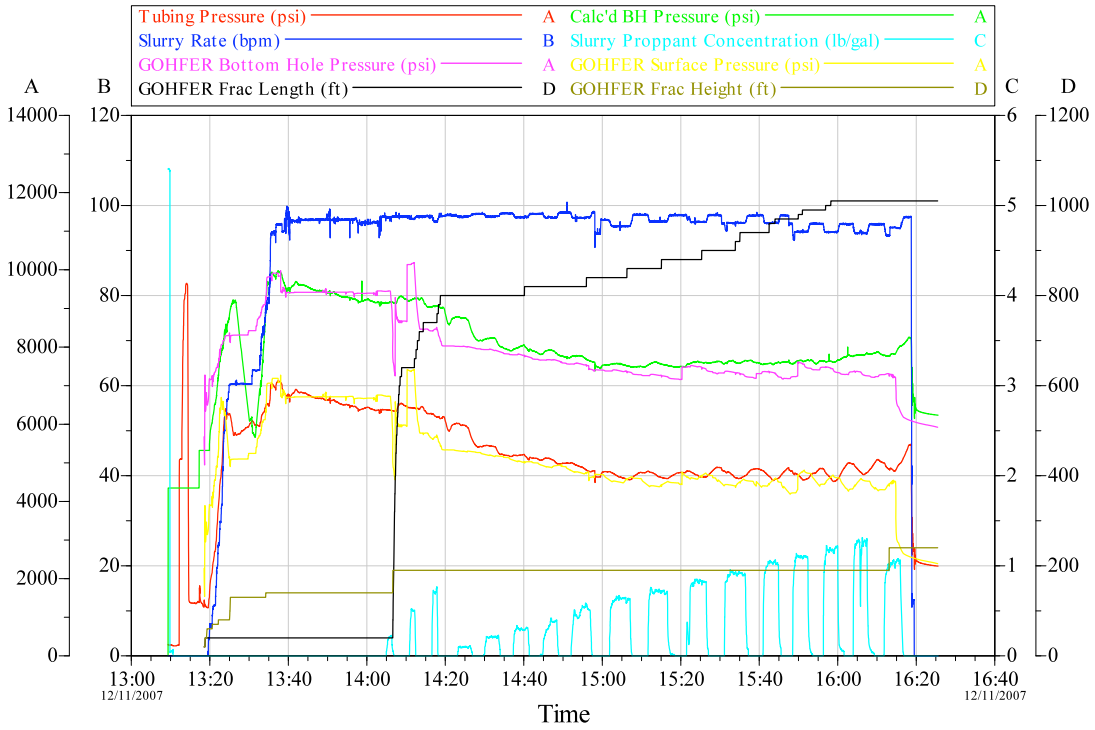

Figure 3.33: Longitudinal pressure match for Stage IV. Final fracture geometry from the model is also shown.

The time-lapse analysis showed that the fracture grew upwards first, and in the middle of the treatment it suddenly started growing downwards. After the pumps were shut off, there is almost no width in the fracture above the wellbore, as seen in Fig. 3.34, with a width around 0.1 in in the region below the wellbore.

With the downward growth and the width development below the wellbore most proppant was deposited in that part of the fracture. Time-lapse showed that it was pumped away from the perforations with almost no proppant left around the perforations at the end of the treatment, as seen in Fig. 3.35. All proppant was pumped into the outer edges of the fracture with concentrations of around 0.55 lb/ft^2 there. Fig. 3.35 shows that only very little proppant was deposited in the part of the fracture above the wellbore. When the fracture started growing downhole almost all proppant seemed to go into that part of the fracture immediately with final concentrations of up to 0.65 lb/ft^2 in that region.

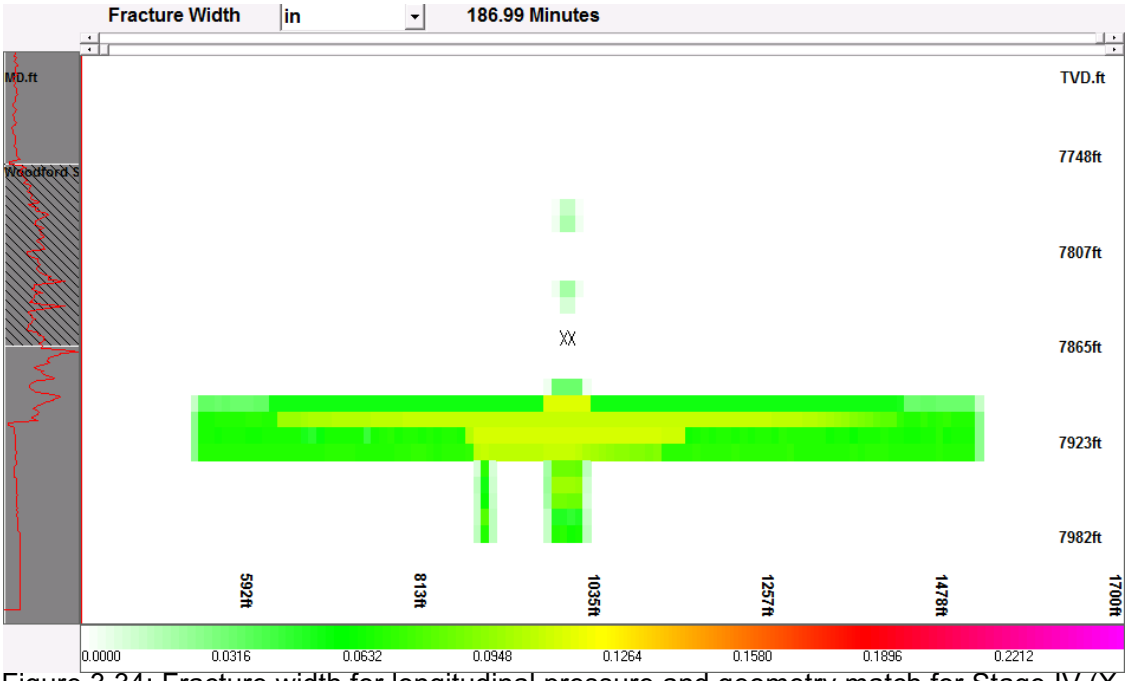

Figure 3.34: Fracture width for longitudinal pressure and geometry match for Stage IV (X represents perforations).

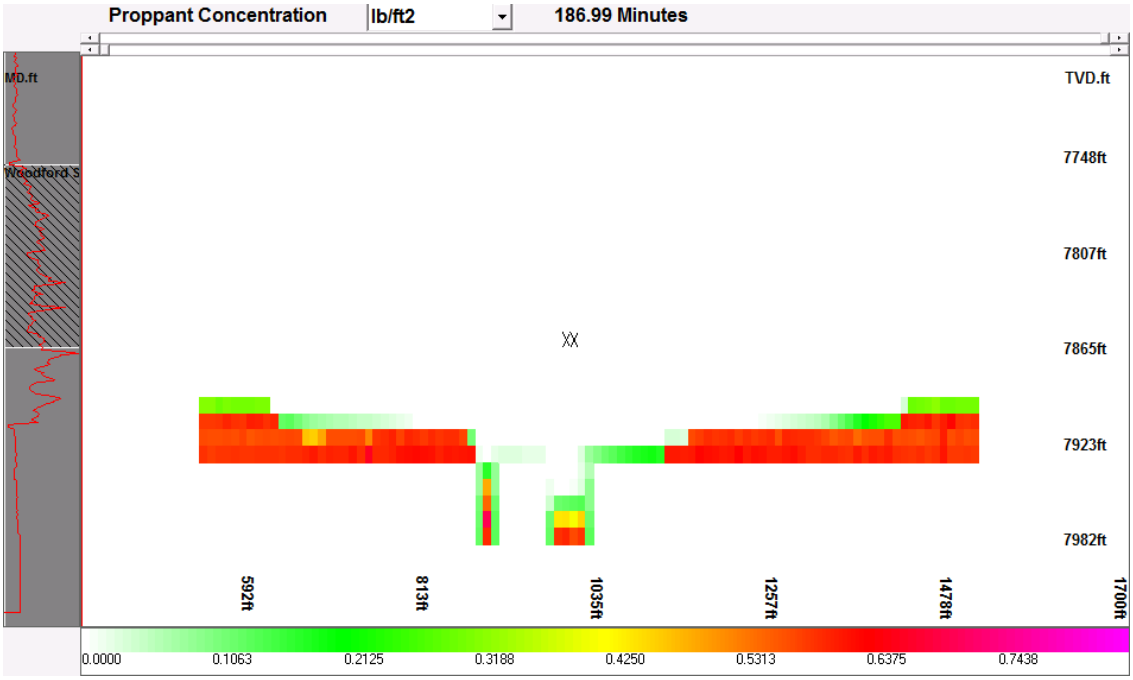

Figure 3.35: Proppant concentration for longitudinal pressure and geometry match for Stage IV (X represents perforations).

Fig. 3.36 shows the final proppant concentration overlaid with both surface and downhole microseismic data for Stage IV. After the pumps were shut-off the proppant concentration does not extend over the full height of the created fracture. Height issues are discussed in detail in Section 8.1.

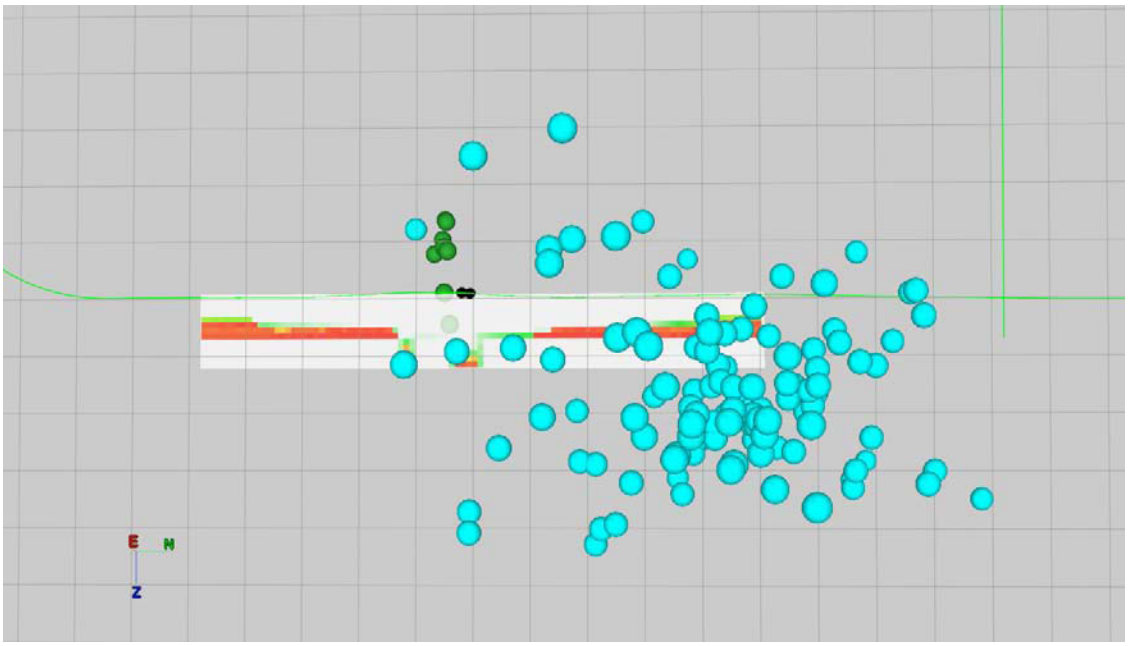

Figure 3.36: Proppant concentration and microseismic data for the longitudinal model of Stage IV shown in a south-north plane. Turquoise spheres show downhole recordings, whereas green spheres show surface recordings. Final proppant concentration does not extend over the total height of the created fracture. The perforation cluster reaches from the black dot on the left end of the proppant concentration to the black dot on the right end. The treatment wellbore can be seen in green from left to right. The grid shown is 100 by 100 ft. Most microseismic activity occurred away from the Stage IV perforation cluster in the weakened formation around the Stage III perforation cluster, which the model was not set-up to simulate.

3.5.1.5 Stage V

In order to achieve a complete match with both pressure and geometry, the model was first adjusted to match only the observed treatment pressure regardless of the fracture geometry. It was then further modified to match the obtained geometry parameters as well.

3.5.1.5.1 Pressure Match

For the final stage, PDMSF was set to 0.005 1/psi and PDL to 0.003 1/psi. The Tortuosity Pre-Factor was set to 0.15 psi/bpm^2. The perforation coefficient was only slightly decreased from the default value to 0.53, with a friction factor of 0.09 in order to achieve a pressure match. Treatment tubing length was set to the measured depth until the first perforation, which was 8,273 ft for this stage.

The final stage of the treatment turned out to be the trickiest one of all. Adjusting the perforation factor had an effect on the simulated pressure curve until about 08:15:00, whereas after that the pressure would not really respond to any changes in the factor. In order to achieve a reasonable match for both the early and later stage of the treatment, the simulated pressure during the second half of the treatment unfortunately had to be compromised.

The tectonic strain had to be slightly adjusted for this stage to 140 microstrains. Every stage sees the stress changes in the reservoir that were caused by previous fracturing stages. Since Stage V is the last one, it sees the most stress change, causing the stress regime to be slightly different from the previous stages. This effect is referred to as 'stress shadowing' and can be observed when a hydraulic fracture is generated, or propped open afterwards, causing the stress perpendicular to the fracture faces to be slightly elevated above the initial in-situ stress. Although this effect is largest at the face of the fracture it can be distributed across the reservoir for several hundred feet (Singh and Miskimins, 2010). With the increase in tectonic strain, the total stress at the perforation depth amounts to about 6,197 psi.

Since the perforation coefficient of discharge is larger the initial perforation factor has to be lower, it was set to 0.56 for the first interval from the beginning of the treatment on Dec. 12th, 2007, at about 07:09:00 until 07:36:47. As seen in Fig. 3.5 no proppant has been pumped yet. As perforations open up with continued injection the perforation factor was increased to 0.6 until 07:41:17. It was then increased further to 0.62 until after the first slug of 100-mesh sand at 0.25 lbm/gal at 07:58:46. The factor was then decreased to 0.50 in order to match the simulated pressure curve until the end of the treatment at about 10:18:00.

3.5.1.5.2 Geometry Match

For this final stage, PDMSF was set to 0.0035 1/psi, PDL to 0.0009 1/psi, and TSC to 0.0009 as well. The Tortuosity Pre-Factor was set to 0.15 psi/bpm^2. The perforation coefficient was only slightly decreased from the default value to 0.53, with a friction factor of 0.09 in order to achieve a pressure match. Treatment tubing length was set to the measured depth until the first perforation, which was 8,273 ft for this stage.

The tectonic strain was adjusted to 130 microstrains. Every stage sees the stress changes in the reservoir that were caused by previous fracturing stages. Since Stage V is the last one it sees the most stress change, causing the stress regime to be slightly different from the previous stages.

The initial perforation factor was set to 0.55 for the first interval from the beginning of the treatment on Dec. 12th, 2007, at about 07:09:00 until 07:36:47. With continued injection the perforation factor was increased to 0.58 until 07:41:17. It was then increased further to 0.60 until after the first slug of 100-mesh sand at 0.25 lbm/gal at 07:58:46. The factor was then set to 1.00 until the end of the treatment at about 10:18:00, since further adjustment of it showed no difference in pressure behavior at all.

For this stage all of the microseismic activity except for one single event occurred around Stage IV perforations. The height of the microseismic cloud is about 1,060 ft, with a longitudinal stretch of about 1,150 ft. With only one event at Stage V perforations it was difficult to assess the height of the fractured zone, so matching the height was not the primary concern for this stage. Furthermore, as is discussed in Chapter IV, surface microseismic data seems to be biased upwards, whereas downhole recordings seem to be biased downwards. However, since 240 ft seemed to be a number that the geological set-up in this model consistently produced, the parameters were adjusted in order to produce a height somewhere in this range. Again, the longitudinal dimension could be very well matched with a simulated length of 1,060 ft, and a simulated height of 240 ft. Fig. 3.37 shows the final pressure match.

Fig. 3.38 clearly shows the asymmetrical fracture growth for this stage, with almost no fracture growth occurring below the wellbore. The substantial upward growth occurred due to the higher tectonic strain, which resulted in an additional stress of about 200 psi and is discussed in detail in Section 8.1. Time-lapse analysis showed that most

fracture growth originated from the perforation cluster closest to the build of the horizontal section, with a final width of around 0.11 in. The proppant concentration, as seen in Fig. 3.39, is highest in the region above the wellbore. Almost all proppant was deposited in that part of the fracture with final concentrations around 0.45 lb/ft^2. Fig. 3.40 shows the final proppant concentration overlaid with both surface and downhole microseismic data for Stage V. After the pumps were shut-off the proppant concentration does not extend over the full height of the created fracture. Height issues are discussed in detail in Section 8.1.

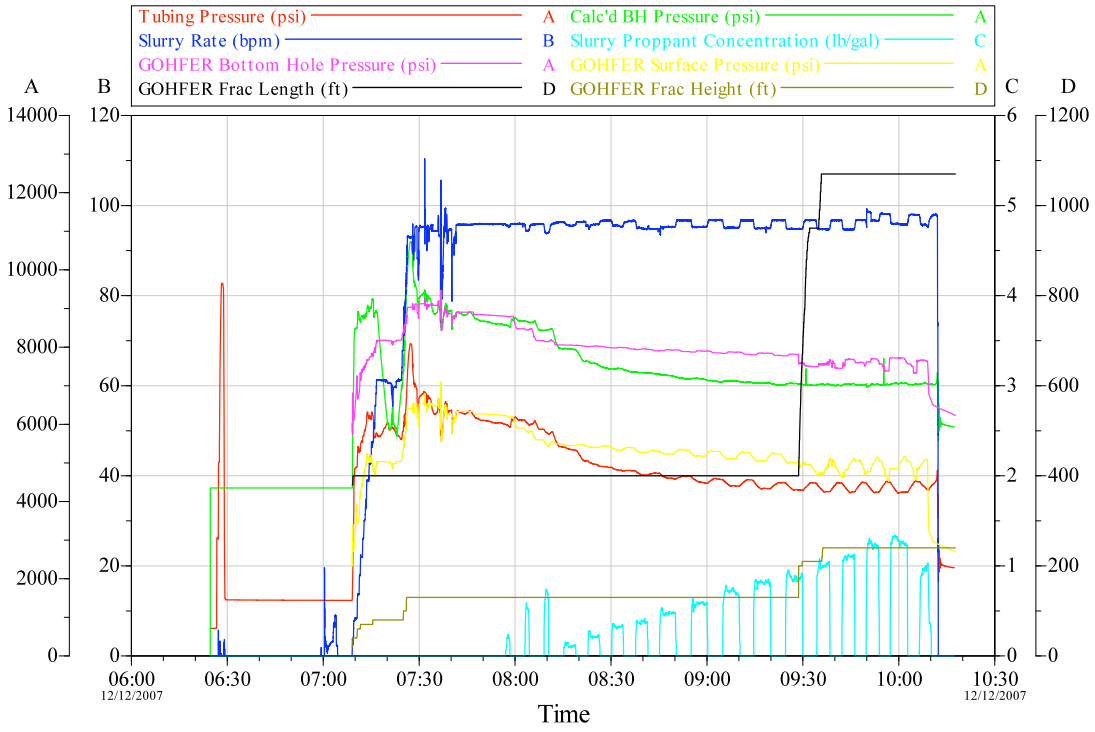

Figure 3.37: Longitudinal pressure match for Stage V. Final fracture geometry from the model is also shown.

3.5.2 Transverse Models

As mentioned before, the geometry match with the longitudinal models only gives half of the picture, i.e. the longitudinal dimension of the microseismic cloud and not the transverse fracture length. A possible way to overcome this is to build a model that is a perpendicular cross-section of the horizontal wellbore instead of a longitudinal one. For each stage there is just one grid cell in the middle of the 3,000 ft grid representing all

perforations of the whole interval. This means that the perforation cluster is simply collapsed into one point, i.e. grid cell, at the center of the perforation interval for each stage. The software now simulates fracture growth as if it were initiated from a perforation cluster of a vertical wellbore. This modification leads to a very high shot density, and does not take into account that the perforations are actually distributed longitudinally along the wellbore. Furthermore it assumes that the rock properties obtained from the available logs are uniformly distributed along each direction, since the same values that were used for the longitudinal plane were then used for the transverse plane. However, this approach helps to complete the picture and provides a simulated fracture length in the same plane as the transverse fracture length. Since symmetrical fracture growth was simulated due to laterally consistent properties, the longer half-length was doubled and used as a total length in the simulations.

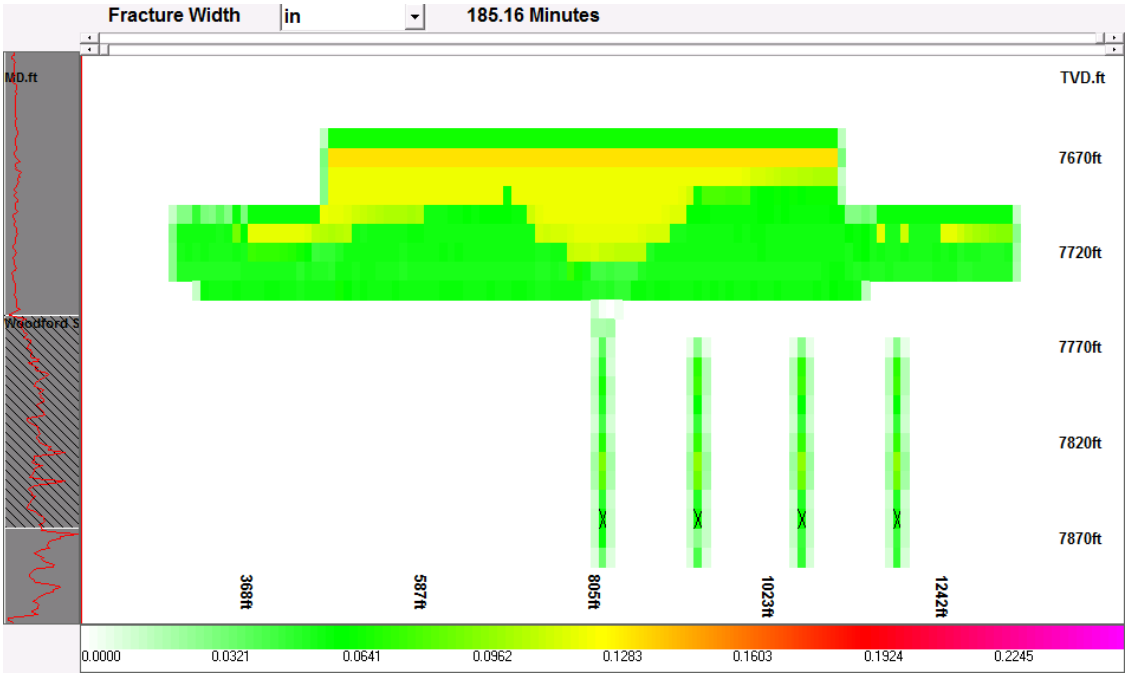

Figure 3.38: Fracture width for longitudinal pressure and geometry match for Stage V (X represents perforations).

The only property that is changed in the grid set-up is the perforation tab. Only one grid cell at the perforation depth of 7,860 – 7,870 ft (i.e. the 10 ft cell interval) in the middle of the 3,000 ft wide grid is attributed with perforations. Each stage then only one perforation interval as listed below:

- Stage I: 60 shots
- Stage II: 96 shots
- Stage III: 96 shots
- Stage IV: 90 shots
- Stage V: 66 shots

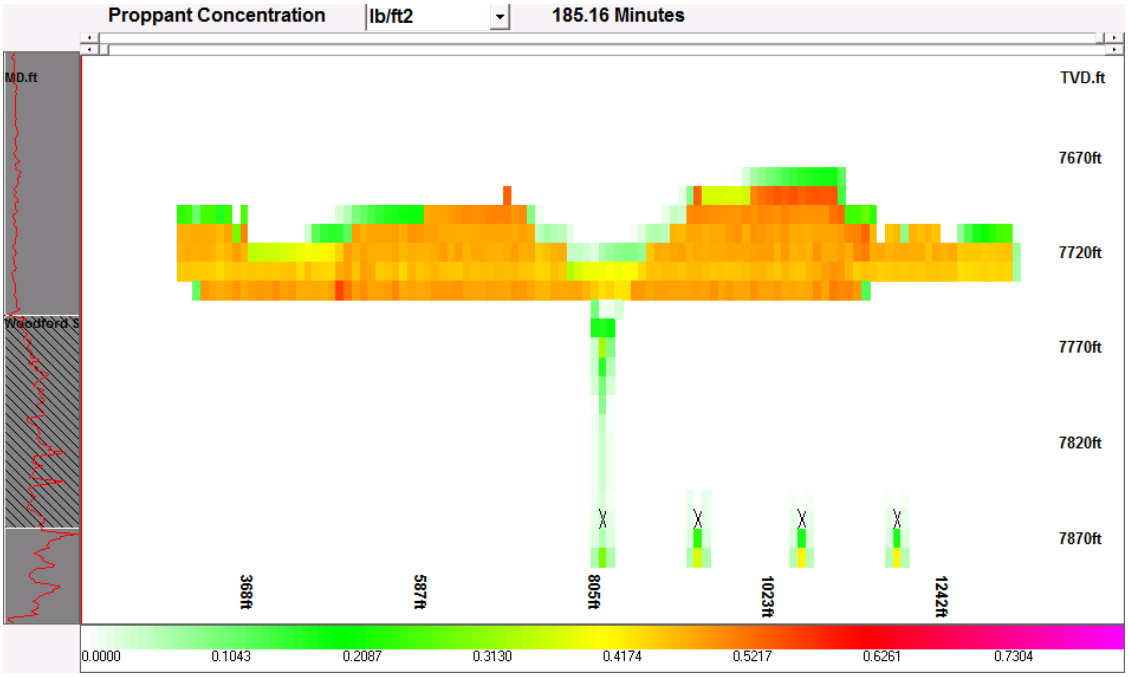

Figure 3.39: Proppant concentration for longitudinal pressure and geometry match for Stage V (X represents perforations).

As for the previous models, PDMSF, PDL, the Tortuosity Pre-Factor, the Perforation Coefficient of Discharge, the friction factor, the perforation factor and the Transverse Storage Coefficient were adjusted in order to achieve the pressure and geometry matches.

Since the simulated pressure showed the same substantial decrease during the injection of the first three sand slugs, the perforation factor was adjusted in the same pattern as for the longitudinal models. It started off at a small value, was increased after the initial pressure peak, and from then on gradually decreased throughout the treatment to match the actual treatment pressure. Due to the different configuration of the model, the perforation factor did have an influence until the very end of the treatment. Unlike for the previous models, where most adjustment occurred throughout the first half of the treatment, it had to be adjusted throughout the second half as well for the transverse

models. Since a single 10 x 10 ft grid cell, populated with up to 96 shots, was the only point for the formation to take slurry, the perforation effects were much more concentrated and the factor had to be adjusted to values well below 0.2 during the later stages of the treatment.

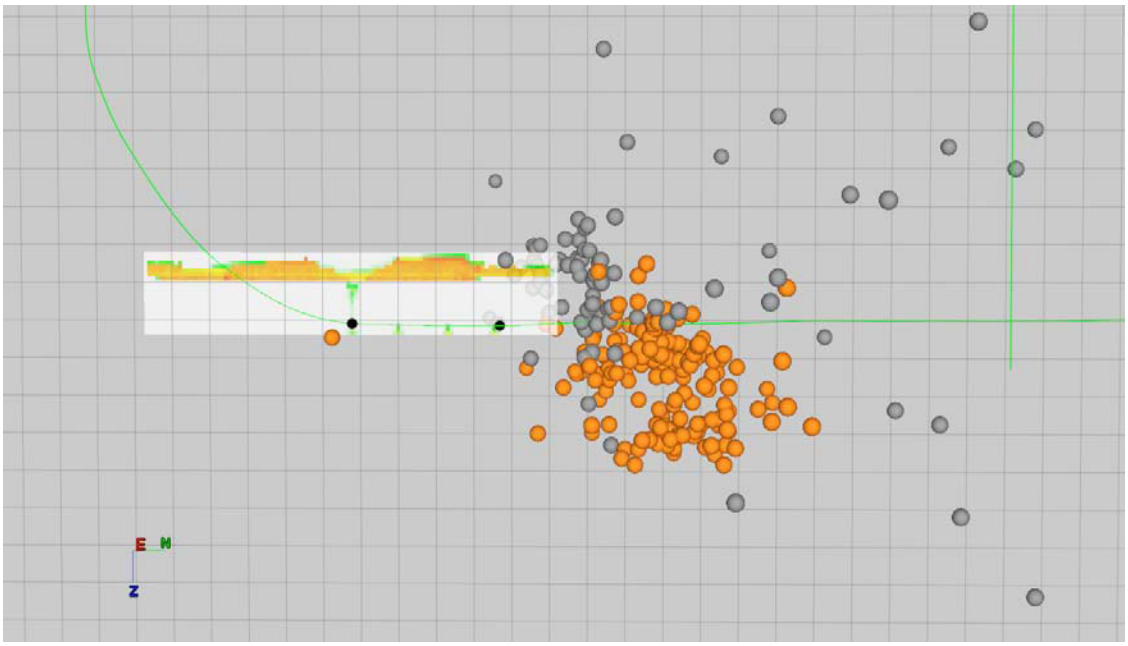

Figure 3.40: Proppant concentration and microseismic data (orange and grey spheres) for Stage V shown in a south-north plane. Orange spheres show downhole recordings, whereas grey spheres show surface recordings. Final proppant concentration does not extend over the total height of the created fracture. The perforation cluster reaches from the black dot on the left end of the proppant concentration to the black dot on the right end. The treatment wellbore can be seen in green from left to right. The grid shown is 100 by 100 ft. Most microseismic activity occurred away from the Stage V perforation cluster in the weakened formation around the Stage IV perforation cluster, which the model was not set-up to simulate.

3.5.2.1 Stage I

In order to achieve a complete match with both pressure and geometry, the model was first adjusted to match only the observed treatment pressure regardless of the fracture geometry. It was then further modified to match the obtained geometry parameters as well.

3.5.2.1.1 Pressure Match

For Stage I, PDMSF, PDL, and tectonic strain were kept at 0.005 1/psi, 0.003 1/psi, and 100 microstrains, respectively. The fairly small tectonic strained produced a very good stress profile, giving a fracture gradient that agrees with what the service company anticipated. The Tortuosity Pre-Factor was left at 0.15 psi/bpm^2 because it worked very well for the previous models, and seemed to give a reasonable picture of the pressure loss due to near wellbore tortuosity, which doesn't necessarily change just because the plane of analysis changes. The default Perforation Coefficient of Discharge of 0.55 was changed to 0.42 to reflect the initial partially plugged condition of the perforations. Even though the model looks like a vertical well to the simulator because the perforations were collapsed into one grid cell, it still represented a horizontal well. The treatment tubing length was therefore set to the measured depth of the center of the perforation cluster at 10,452 ft for this stage. The Friction Factor was adjusted to 0.03, the same value as for the longitudinal value.

As mentioned, the perforation factor reflects both perforation and near wellbore effects and therefore is not uniform throughout the treatment. It was adjusted to 0.35 from the beginning of the treatment on Dec. 10th, 2007, at about 07:16:00 until after the initial pressure peak at 07:37:56. It was then increased to 0.45 until 07:40:06. The gradual increase was continued, setting it to 0.53 until 07:49:09, and then to 0.60 until after pumping the second slug of 100 mesh sand at 0.5 lbm/gal at 08:12:56. In order to match the actual pressure, which required increasing the simulated pressure, the factor was then decreased to 0.28 until before pumping the third slug of 100 mesh sand at 0.75 lbm/gal at 08:16:31. From then on it was further gradually decreased until the end of the treatment. First to 0.24 until after pumping the sixth slug of 30/70 sand at a concentration of 0.6 lbm/gal at 0.9:07:47, then to 0.22 until the beginning of pumping the seventh slug of 30/70 sand at 0.7 lbm/gal at 09:12:28, further to 0.2 until 09:27:52 (after the eight 30/70 sand slug), to 0.18 until 09:32:33 (beginning of pumping the ninth 30/70 sand slug), to 0.15 until 09:42:41 (beginning of pumping the tenth slug of 30/70 sand), to 0.12 until 09:57:53 (beginning of pumping the twelfth slug of 30/70 sand), and finally to 0.1 until the end of the treatment at about 10:20:00.

3.5.2.1.2 Geometry Match

For the geometry match portion, PDMSF was set to 0.005 1/psi, PDL to 0.0004 1/psi, TSC to 0.00033, and tectonic strain for the Woodford Shale to 65 microstrains. The Tortuosity Pre-Factor was set to 0.15 psi/bpm^2. The perforation coefficient was decreased from the default value to 0.32, with a friction factor of 0.05 in order to achieve a pressure match. Treatment tubing length was set to the measured depth of the center of the perforation cluster, which was 9,342 ft for this stage.

The perforation factor was set to 0.45 for the first interval from the beginning of the treatment on Dec. 10th, 2007, at about 14:26:30 until 14:50:00. It was then increased to 0.6 for the next interval until 15:18:27, after the first slug of 0.25 lbm/gal 100-mesh is pumped. For the next interval until the onset of the third slug being pumped at 0.75 lbm/gal at 15:24:34 it was set to 0.25. It was then further decreased to 0.20 until after the third slug was pumped at 15:27:00, to 0.19 until 16:09:55 (beginning of pumping the sixth slug of 30/70 sand), to 0.17 until 16:19:46 (beginning of seventh slug of 30/70 sand), to 0.16 until 16:20:39 (during pumping the seventh slug of 30/70 sand), to 0.15 until 16:31:13 (during pumping the eight slug of 30/70 sand), to 0.14 until 16:39:34 (beginning of pumping the ninth slug of 30/70 sand), to 0.12 until 16:49:25 (beginning of pumping the tenth slug of 30/70 sand), to 0.11 until 17:12:08 (beginning of pumping the thirteenth slug of 30/70 sand), and finally to 0.09 until the end of the treatment at about 17:34:00.

The microseismic data showed a total fracture length of 4,200 ft. Activity was not very well contained to Stage II perforations with a height of about 630 ft. Fracture length was simulated with 3,580 ft, and height with 250 ft. Fig. 3.41 shows the final pressure match.

Time-lapse analysis showed that although the fracture started growing upward initially, after 15 minutes rapid downward growth was occurring as well. The only upward growth that could be observed was right around the perforations. Essentially all of the created fracture length came from the part of the fracture below the wellbore. Fig. 3.42 shows a final width of around 0.1 in. With the fracture extending downwards almost all of the proppant was pumped into that part of the fracture. As seen in Fig. 3.43, the final proppant concentration in the region below the Woodford Shale is about 0.7 lb/ft^2, whereas there is almost no proppant left around the perforations. Fig. 3.44 shows the

final proppant concentration overlaid with surface microseismic data for Stage I. After the pumps were shut-off the proppant concentration does not extend over the full height of the created fracture. Height issues are discussed in detail in Section 8.1.

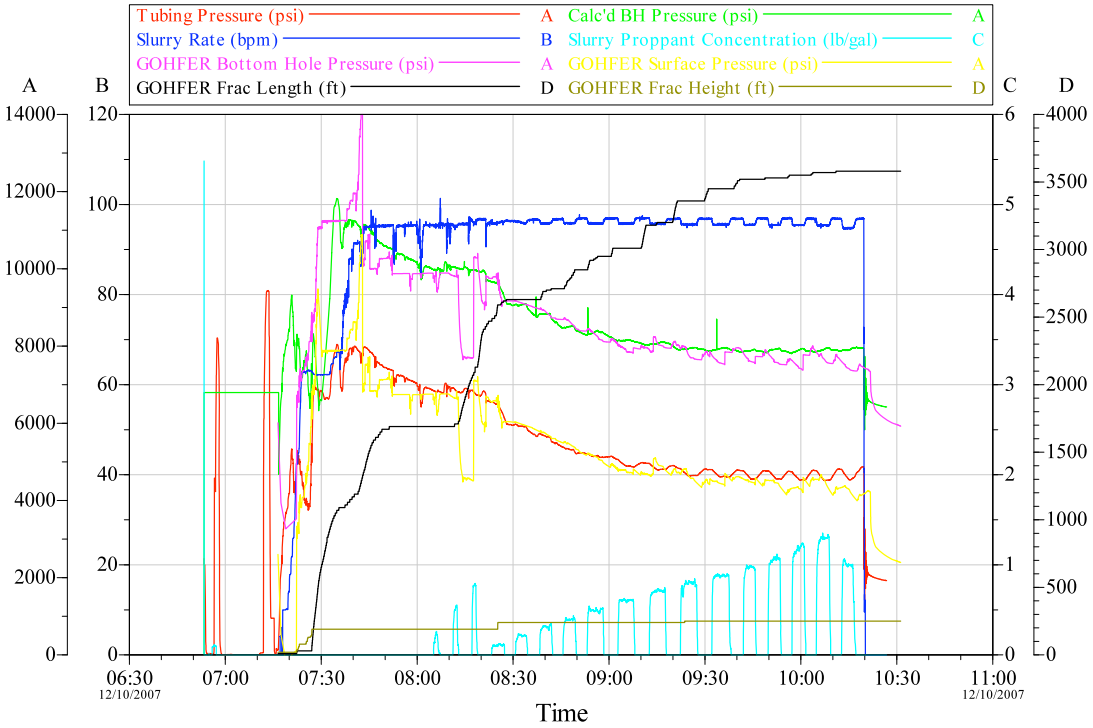

Figure 3.41: Transverse pressure match for Stage I. Final fracture geometry from the model is also shown.

3.5.2.2 Stage II

In order to achieve a complete match with both pressure and geometry, the model was first adjusted to match only the observed treatment pressure regardless of the fracture geometry. It was then further modified to match the obtained geometry parameters as well.

3.5.2.2.1 Pressure Match

As in the first stage, PDMSF was set to 0.005 1/psi, PDL to 0.003 1/psi, and tectonic strain for the Woodford Shale to 100 microstrains. The Tortuosity Pre-Factor was set to 0.15 psi/bpm^2. The perforation coefficient was decreased from the default

value to 0.32, with a friction factor of 0.05 in order to achieve a pressure match. Treatment tubing length was set to the measured depth of the center of the perforation cluster at 9,954.5 ft.

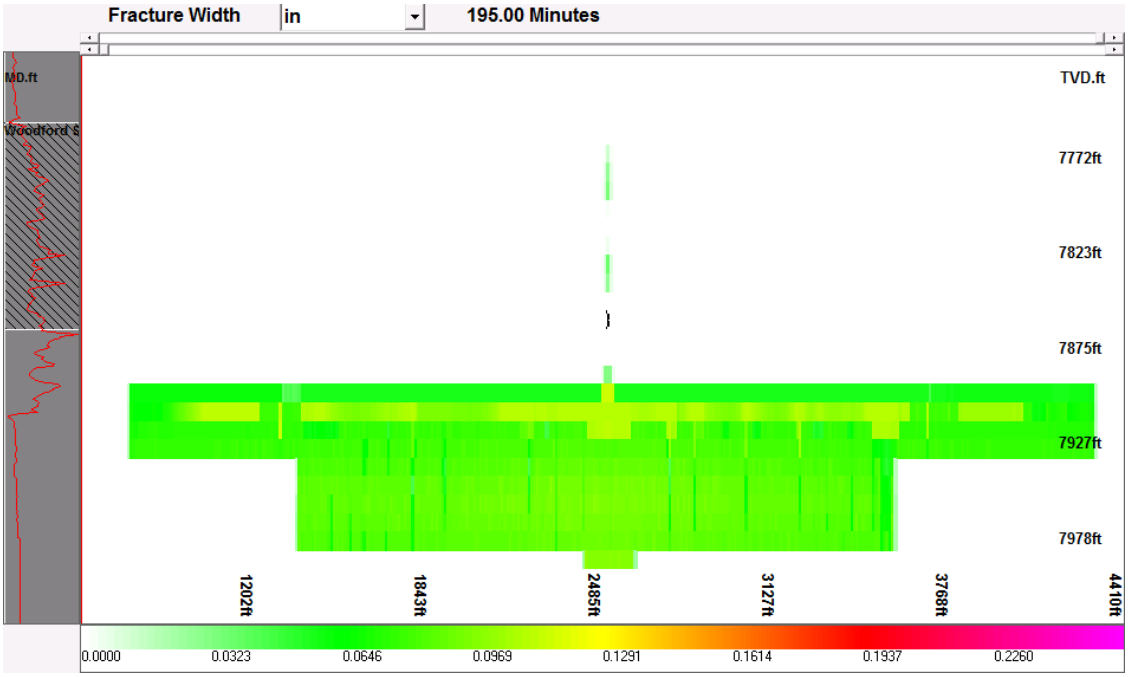

Figure 3.42: Fracture width for transverse pressure and geometry match for Stage I (X represents perforations).

The perforation factor was set to 0.45 for the first interval from the beginning of the treatment on Dec. 10th, 2007, at about 14:26:30 until 14:50:00; no proppant was pumped and the initially low value is necessary to simulate the pressure preak at the beginning of the treatment as the injection starts, as seen in Fig. 3.2. The factor was then increased to 0.6 for the next interval until 15:18:27, after the first slug of 0.25 lbm/gal 100-mesh is pumped. When the second slug of 0.50 lbm/gal is being pumped, the proppant concentration around the wellbore increases and has an effect on the treatment pressure. In order to simulate this, a gradual decrease of the perforation factor is necessary; otherwise the simulated pressure would decrease too fast. For the next interval until the onset of the third slug being pumped at 0.75 lbm/gal at 15:24:34 it was set to 0.23. It was then further decreased to 0.18 until after the third slug was pumped at 15:27:00, to 0.17 until 16:09:55 (beginning of pumping the sixth slug of 30/70 sand), to 0.15 until 16:19:46 (beginning of seventh slug of 30/70 sand), to 0.14 until 16:20:39

(during pumping the seventh slug of 30/70 sand), to 0.13 until 16:31:13 (during pumping the eight slug of 30/70 sand), to 0.12 until 16:39:34 (beginning of pumping the ninth slug of 30/70 sand), to 0.10 until 16:49:25 (beginning of pumping the tenth slug of 30/70 sand), and finally to 0.09 until the end of the treatment at about 17:34:00.

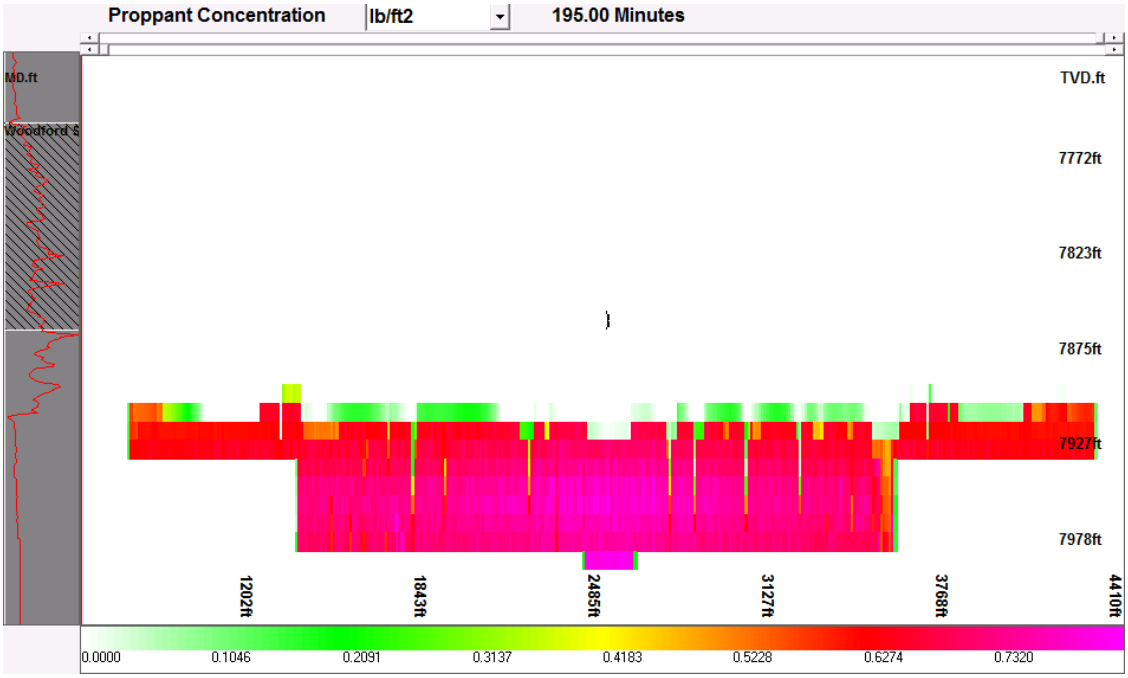

Figure 3.43: Proppant concentration for transverse pressure and geometry match for Stage I (X represents perforations).

3.5.2.2.2 Geometry Match

In Stage II, PDMSF was set to 0.005 1/psi, PDL to 0.0004 1/psi, TSC to 0.00033, and tectonic strain for the Woodford Shale to 65 microstrains. The Tortuosity Pre-Factor was set to 0.15 psi/bpm^2. The perforation coefficient was decreased from the default value to 0.32, with a friction factor of 0.05 in order to achieve a pressure match. Treatment tubing length was set to the measured depth of the center of the perforation cluster, which was 9,342 ft for this stage.

Just as for the pressure match, the perforation factor was set to 0.45 for the first interval from the beginning of the treatment on Dec. 10th, 2007, at about 14:26:30 until 14:50:00. It was then increased to 0.6 for the next interval until 15:18:27, after the first slug of 0.25 lbm/gal 100-mesh is pumped. For the next interval, until the onset of the

third slug being pumped at 0.75 lbm/gal at 15:24:34, it was set to 0.25. It was then further decreased to 0.20 until after the third slug was pumped at 15:27:00, to 0.19 until 16:09:55 (beginning of pumping the sixth slug of 30/70 sand), to 0.17 until 16:19:46 (beginning of seventh slug of 30/70 sand), to 0.16 until 16:20:39 (during pumping the seventh slug of 30/70 sand), to 0.15 until 16:31:13 (during pumping the eight slug of 30/70 sand), to 0.14 until 16:39:34 (beginning of pumping the ninth slug of 30/70 sand), to 0.12 until 16:49:25 (beginning of pumping the tenth slug of 30/70 sand), to 0.11 until 17:12:08 (beginning of pumping the thirteenth slug of 30/70 sand), and finally to 0.09 until the end of the treatment at about 17:34:00.

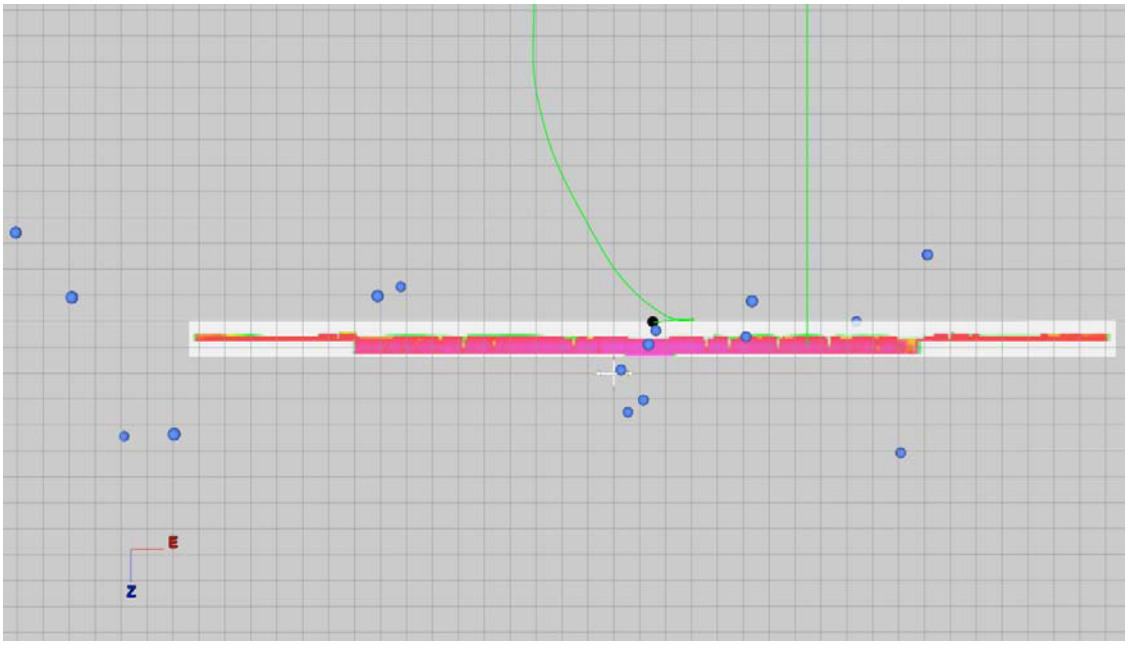

Figure 3.44: Proppant concentration and microseismic data for the transverse model of Stage I shown in a west-east plane. Blue spheres show surface recordings. Final proppant concentration does not extend over the total height of the created fracture. The perforation cluster is represented by the black dot. The directional treatment wellbore can be seen in green on the left side. The grid shown is 100 by 100 ft.

The microseismic data showed a total fracture length of 1,700 ft. Activity was well contained to the Stage II perforations with a height of about 290 ft. Fracture length was simulated with 1,350 ft, and height with 240 ft. Fig. 3.45 shows the final pressure and geometry match.

For a longer portion of this stage, only upward growth occurred with both length and height development. However, time-lapse showed that the fracture quickly grew into the region below the wellbore in the later part of the treatment developing most of the final length. Fig. 3.46 shows a final width of about 0.05 in around the perforations. Most of the proppant was deposited in the rapidly growing fracture half below the wellbore, with final concentrations of about 0.4 lb/ft^2, as seen in Fig. 3.47. Fig. 3.48 shows the final proppant concentration overlaid with both surface and downhole microseismic data for Stage II. After the pumps were shut-off the proppant concentration does not extend over the full height of the created fracture. Height issues are discussed in detail in Section 8.1.

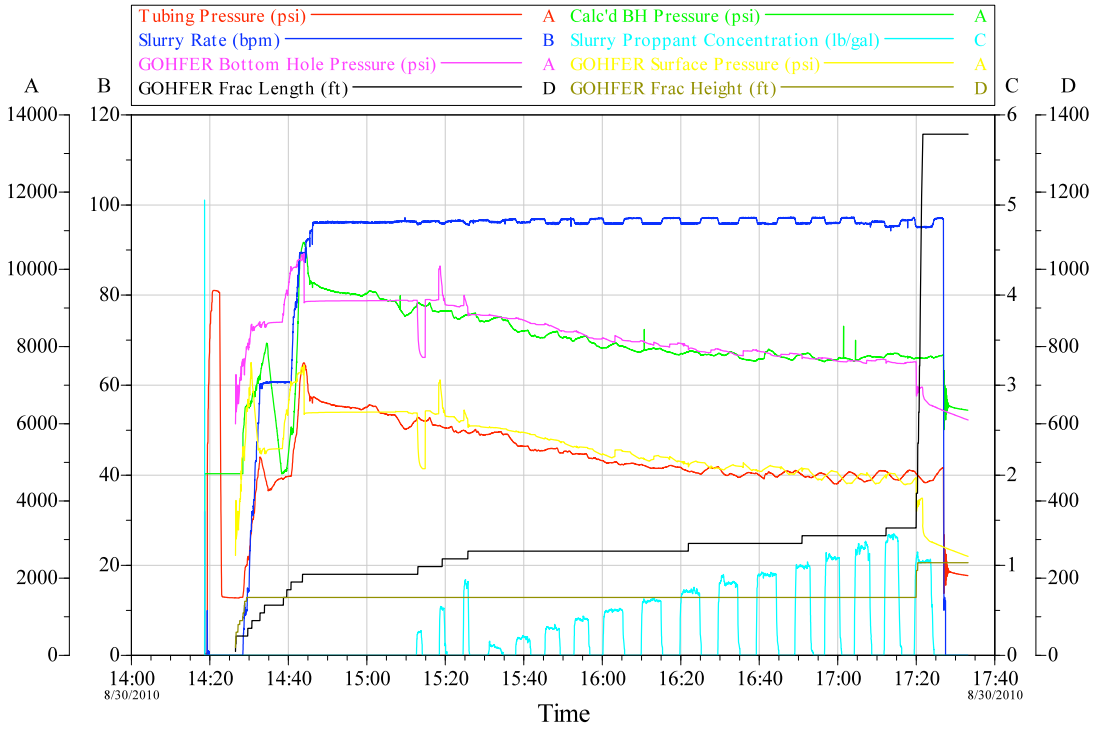

Figure 3.45: Transverse pressure match for Stage II. Final fracture geometry from the model is also shown.

3.5.2.3 Stage III

In order to achieve a complete match with both pressure and geometry, the model was first adjusted to match only the observed treatment pressure regardless of the fracture geometry. It was then further modified to match the obtained geometry parameters as well.

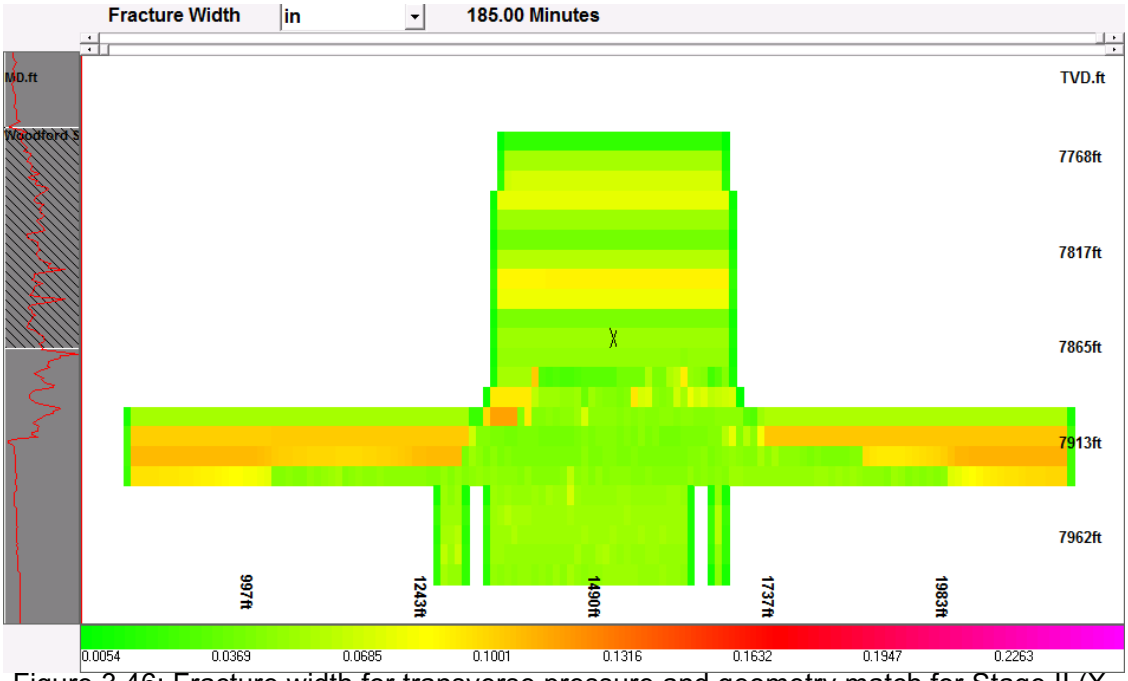

Figure 3.46: Fracture width for transverse pressure and geometry match for Stage II (X represents perforations).

3.5.2.3.1 Pressure Match

As for the previous stages, PDMSF was set to 0.005 1/psi, PDL to 0.003 1/psi, and tectonic strain for the Woodford Shale to 100 microstrains. The Tortuosity Pre-Factor was set to 0.15 psi/bpm^2. The perforation coefficient was decreased from the default value to 0.24, with a friction factor of 0.06 in order to achieve a pressure match. Treatment tubing length was set to the measured depth of the center of the perforation cluster, which was 9,342 ft for this stage.

The perforation factor for the first interval from the beginning of the job on Dec. 11th, 2007, at about 07:02:50 until 07:20:14 was set to 0.55 to reflect the pressure peak shown in Fig. 3.3 as injection begins. It is slightly higher compared to the initial perforation factor in the previous stages due to a slightly lower perforation coefficient. Increasing the first perforation factor while decreasing the perforation coefficient was found to produce the best match with the observed pressure. Until the pumping of the first slug at 0.25 lbm/gal is completed at 07:51:23, the factor was increased to 0.81 to simulate an improvement in how easily fluid is being injected. However, afterwards the perforation factor has to be modified in the same pattern as in the previous stages. The

proppant concentration around the wellbore increases and in order to keep the simulated pressure up, at the level of the observed pressure, the perforation factor has to be decreased. For this stage, a good match could be achieved without much gradual decrease. Until after the second slug with 0.50 lbm/gal is pumped at 07:57:09 it was set to 0.23, to be further lowered to 0.19 until the end of the treatment at about 10:08:00.

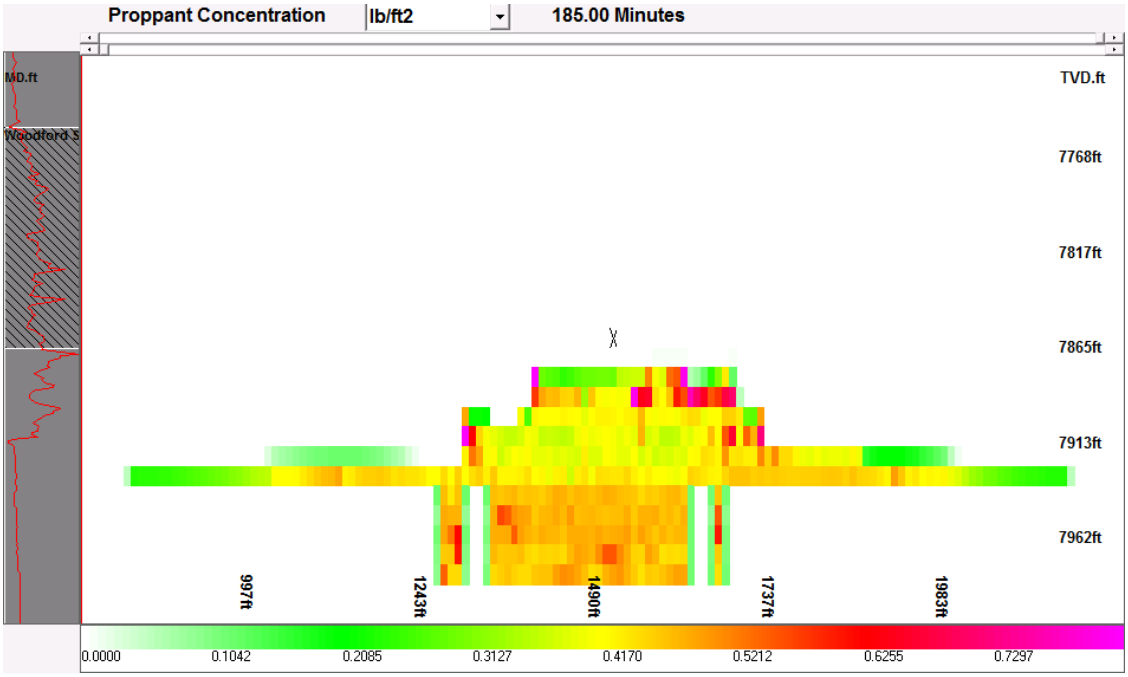

Figure 3.47: Proppant concentration for transverse pressure and geometry match for Stage II (X represents perforations).

3.5.2.3.2 Geometry Match

For the Stage II geometry match, PDMSF was set to 0.001 1/psi, PDL to 0.001 1/psi, TSC to 0.001, and tectonic strain for the Woodford Shale to 50 microstrains. The Tortuosity Pre-Factor was set to 0.10 psi/bpm^2. The perforation coefficient was decreased from the default value to 0.24, with a friction factor of 0.06 in order to achieve a pressure match. Treatment tubing length was set to the measured depth of the center of the perforation cluster, which was 9,342 ft for this stage.

The perforation factor scheme did not have to be altered much. For the first interval from the beginning of the job on Dec. 11th, 2007, at about 07:02:50 until 07:20:14, it was set to 0.55. Until the pumping of the first slug at 0.25 lbm/gal is

completed at 07:51:23 the factor was increased to 0.81, and then decreased to 0.23 until after the second slug with 0.50 lbm/gal is pumped at 07:57:09. It was then further lowered to 0.17 until the end of the treatment at about 10:08:00.

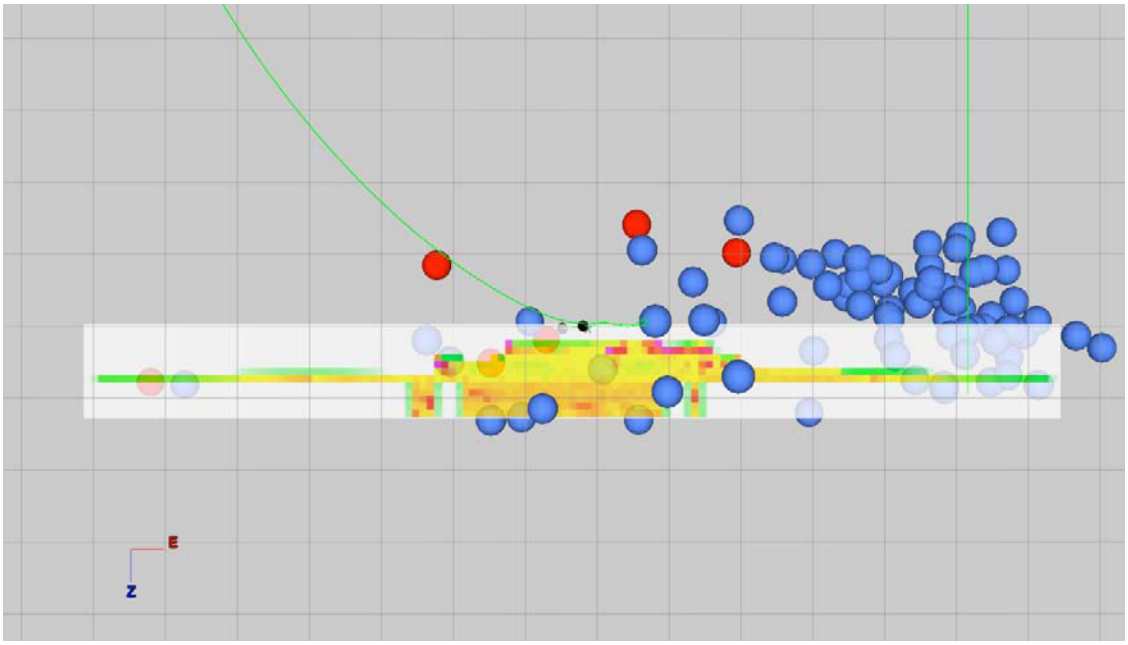

Figure 3.48: Proppant concentration and microseismic data for the transverse model of Stage II shown in a west-east plane. Blue spheres show downhole recordings, whereas red spheres show surface recordings. Final proppant concentration does not extend over the total height of the created fracture. The perforation cluster is represented by the black dot. The directional treatment wellbore can be seen in green on the left side. The grid shown is 100 by 100 ft.

The fracture length used for the match was 2,640 ft, and a fracture height of 550 ft was observed. However, the microseismic activity of Stage III mostly overlapped with the region around Stage II perforations. Looking at the Stage III perforations, it is obvious that the fracture height for this part of the reservoir was substantially lower, with about 270 ft. Since the already weakened reservoir around the Stage II perforation cluster could not be modeled accurately, this height was used for achieving the match. The fracture length was simulated for this stage with 2,260 ft with a height of 250 ft. Fig. 3.49 shows the final pressure match.

Time-lapse showed that downward growth occurred from early on in the treatment, with almost all length and height development occurring in the zone below the Woodford Shale. Fig. 3.50 shows final widths of around 0.1 in. Whereas almost no

proppant was pumped into the fracture part above the wellbore, the part below wellbore shows very high final concentrations of around 0.8 lb/ft^2, as seen in Fig. 3.51. Fig. 3.52 shows the final proppant concentration overlaid with both surface and downhole microseismic data for Stage III. After the pumps were shut-off the proppant concentration does not extend over the full height of the created fracture. Height issues are discussed in detail in Section 8.1.

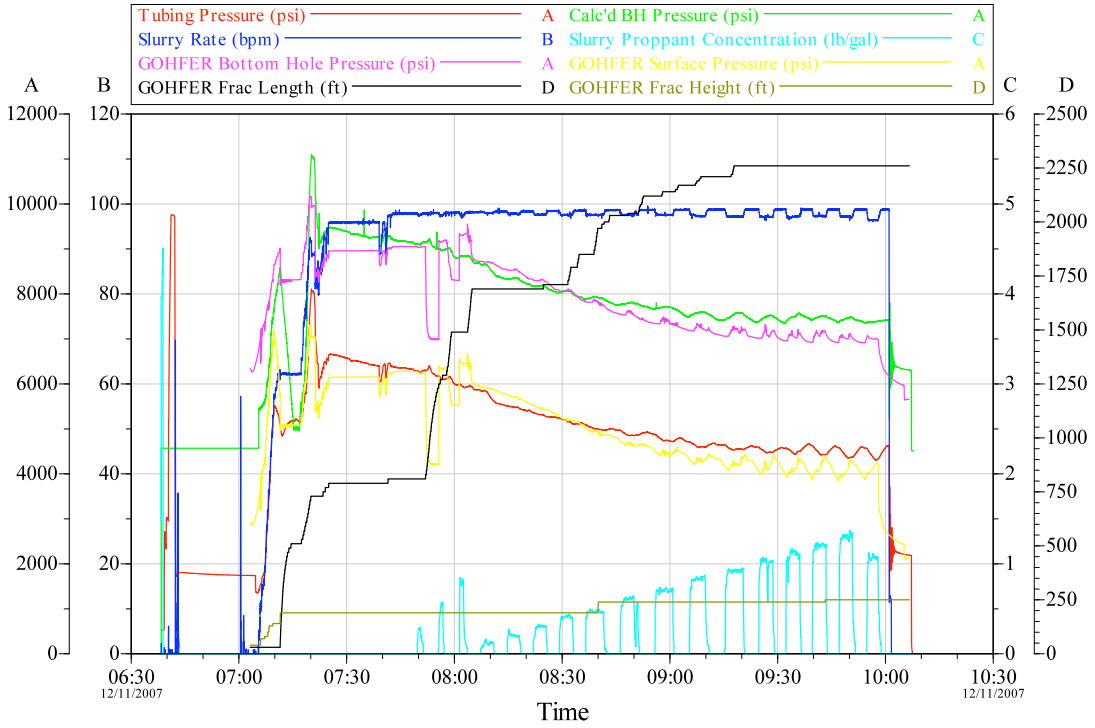

Figure 3.49: Transverse pressure match for Stage III. Final fracture geometry from the model is also shown.

3.5.2.4 Stage IV

In order to achieve a complete match with both pressure and geometry, the model was first adjusted to match only the observed treatment pressure regardless of the fracture geometry. It was then further modified to match the obtained geometry parameters as well.

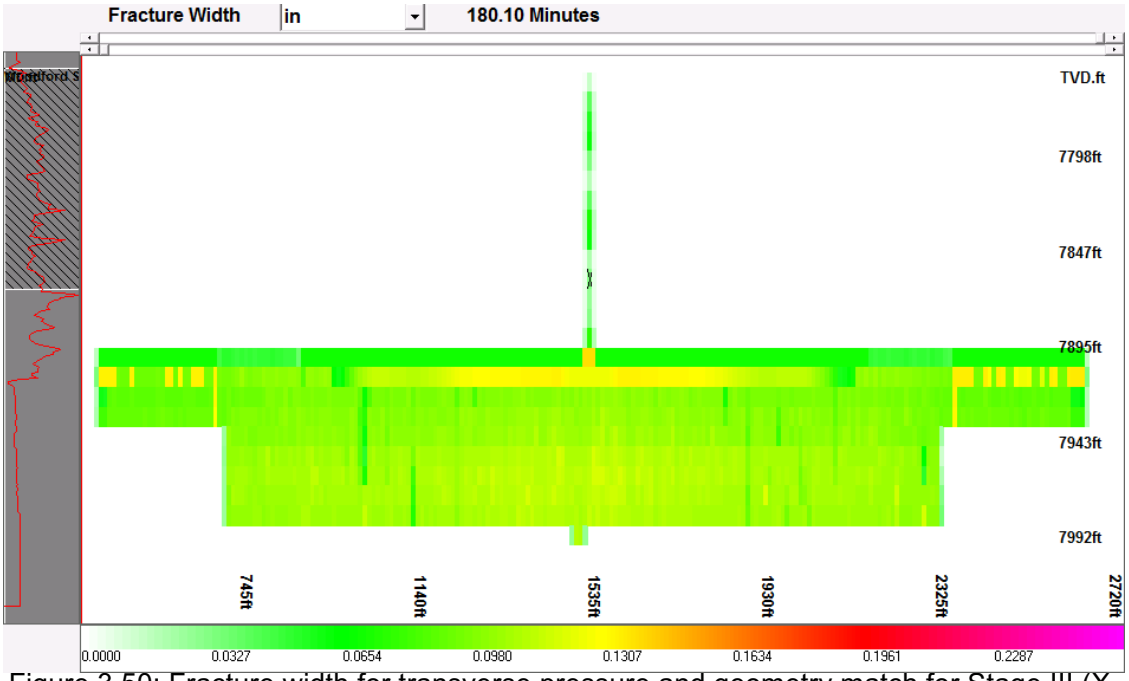

Figure 3.50: Fracture width for transverse pressure and geometry match for Stage III (X represents perforations).

3.5.2.4.1 Pressure Match

In Stage IV, PDMSF was set to 0.005 1/psi, PDL to 0.003 1/psi, and tectonic strain for the Woodford Shale to 100 microstrains. The Tortuosity Pre-Factor was set to 0.15 psi/bpm^2. The perforation coefficient was decreased from the default value to 0.25, with a friction factor of 0.07 in order to achieve a pressure match. Treatment tubing length was set to the measured depth until the first perforation, which was 8,951 ft for this stage.

In general the perforation factor for this stage showed the same pattern as for the previous stages. From the beginning of the treatment on Dec. 11th, 2007, at about 13:18:00 until right after the first pressure peak, as seen in Fig. 3.4, it was set to 0.7 until 13:39:22; no proppant was pumped yet. To reflect the opening up of perforations, the factor was increased to 0.82 until after the first slug of 100-mesh sand at 0.25 lbm/gal was pumped at 14:08:18. It was then substantially decreased to 0.27 until during pumping the second slug of 100-mesh sand at 0.5 lbm/gal at 14:12:00 to accurately match the simulated pressure to the observed one. From there on, the factor had to be gradually decreased until the end of the treatment. It was set to 0.22 until 15:11:41

(beginning of pumping the seventh slug of 30/70 sand), to 0.19 until 15:22:00 (beginning of pumping the eighth slug of 30/70 sand), to 0.15 until 15:30:26 (beginning of pumping the ninth slug of 30/70 sand), to 0.14 until 15:42:42 (during pumping the tenth slug of 30/70 sand), to 0.12 until 15:53:04 (after pumping the eleventh slug of 30/70 sand), and finally to 0.09 until the end of the treatment at about 16:26:00.

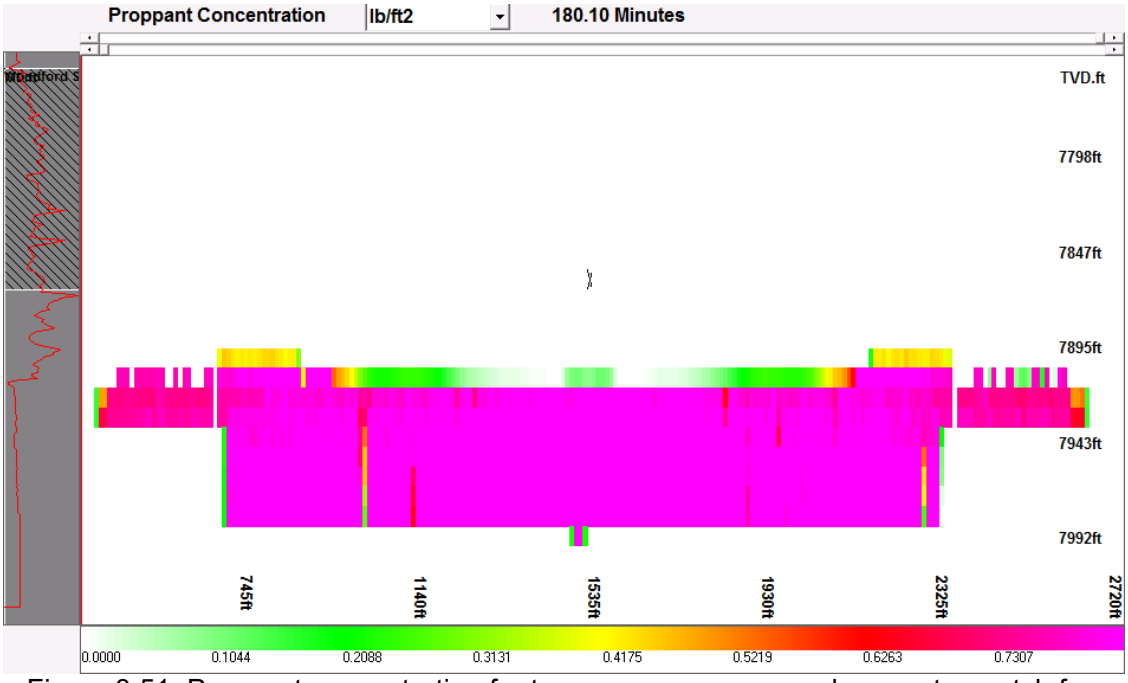

Figure 3.51: Proppant concentration for transverse pressure and geometry match for Stage III (X represents perforations).

3.5.2.4.2 Geometry Match

For the geometry match, PDMSF was set to 0.002 1/psi, PDL to 0.0005 1/psi, TSC to 0.0005, and tectonic strain for the Woodford Shale to 50 microstrains. The Tortuosity Pre-Factor was set to 0.10 psi/bpm^2. The perforation coefficient was decreased from the default value to 0.25, with a friction factor of 0.07. Treatment tubing length was set to the measured depth of the center of the perforation cluster, which was 8,958.5 ft for this stage.

From the beginning of the treatment on Dec. 11th, 2007, at about 13:18:00 until right after the first pressure peak the perforation factor was set to 0.65 until 13:39:22. It was increased to 0.72 until after the first slug of 100-mesh sand at 0.25 lbm/gal was

pumped at 14:08:18, and then substantially decreased to 0.27 until during pumping the second slug of 100-mesh sand at 0.5 lbm/gal at 14:12:00. From there on the factor had to be gradually decreased until the end of the treatment. It was set to 0.22 until 15:11:41 (beginning of pumping the seventh slug of 30/70 sand), to 0.19 until 15:22:00 (beginning of pumping the eighth slug of 30/70 sand), to 0.15 until 15:30:26 (beginning of pumping the ninth slug of 30/70 sand), to 0.14 until 15:42:42 (during pumping the tenth slug of 30/70 sand), to 0.12 until 15:53:04 (after pumping the eleventh slug of 30/70 sand), and finally to 0.09 until the end of the treatment at about 16:26:00.

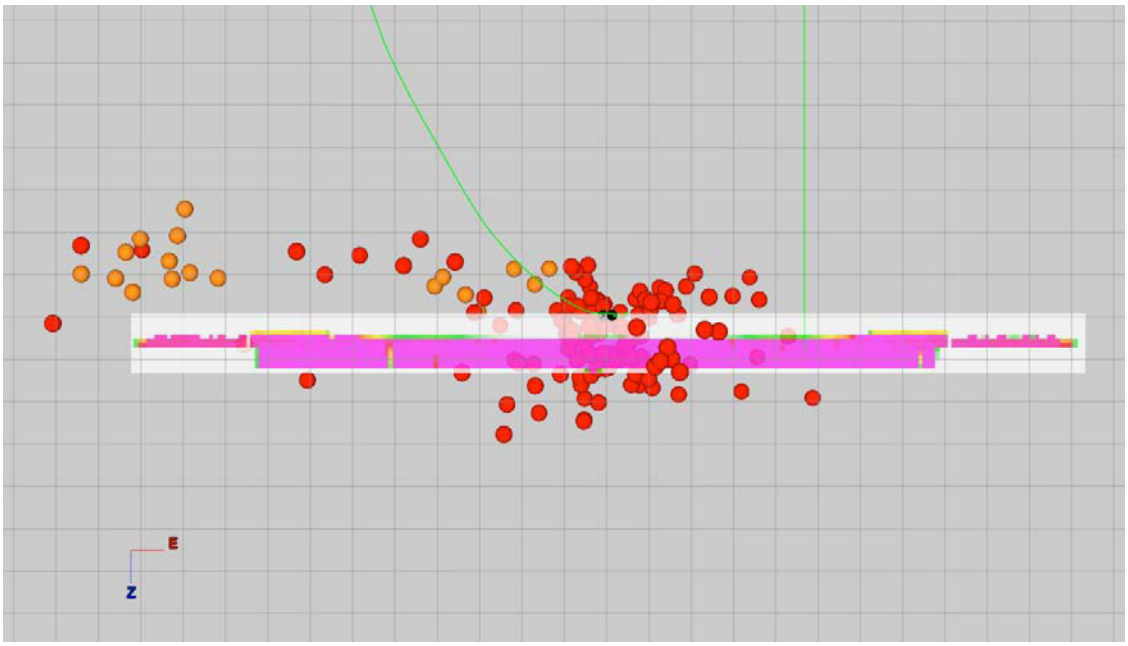

Figure 3.52: Proppant concentration and microseismic data for the transverse model of Stage III shown in a west-east plane. Red spheres show downhole recordings, whereas orange spheres show surface recordings. Final proppant concentration does not extend over the total height of the created fracture. The perforation cluster is represented by the black dot. The directional treatment wellbore can be seen in green on the left side. The grid shown is 100 by 100 ft. Most microseismic activity occurred away from the Stage III perforation cluster in the weakened formation around the Stage II perforation cluster, which the model was not set-up to simulate.

The microseismic data showed a fracture half-length of 1,950 ft extending to the west side of the treatment well only, and a height of 290 ft. The total fracture length used for the match was therefore 3,900 ft. The simulated fracture length was 3,440 ft, which is very close to the fracture length obtained from the microseismic data, with a simulated height of 250 ft. Fig. 3.53 shows the final pressure match.

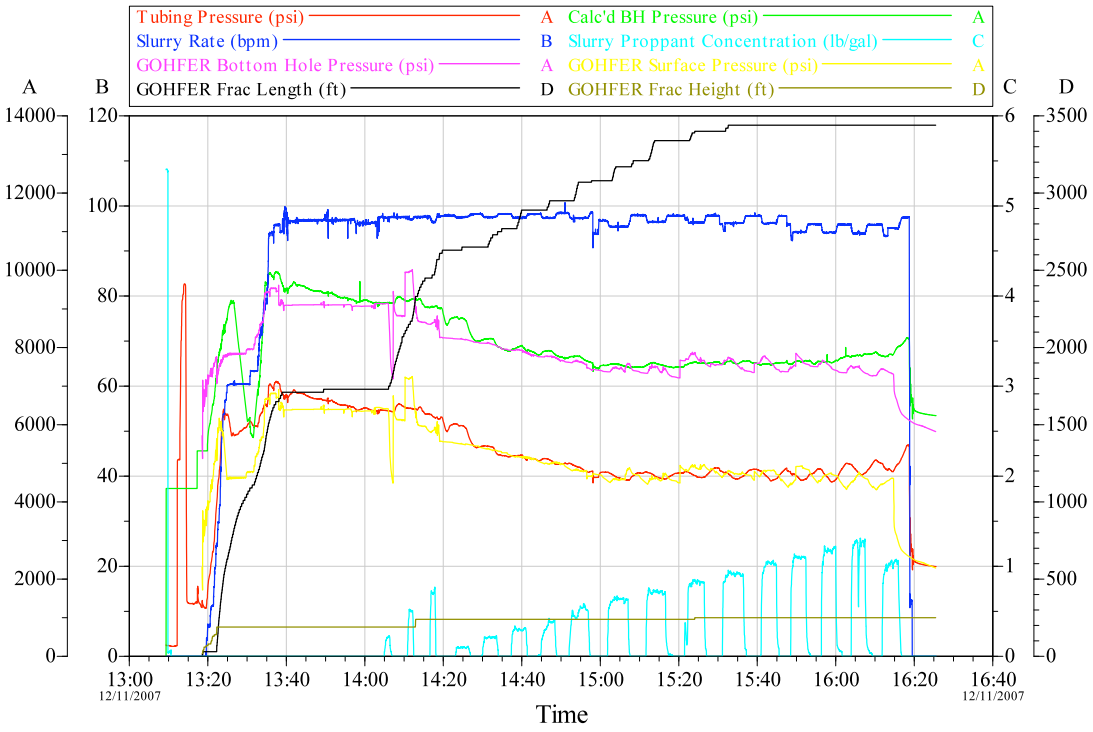

Figure 3.53: Transverse pressure match for Stage IV. Final fracture geometry from the model is also shown.

Both upward and downward growth occurred during the first couple of minutes of this stage. After this phase of initial growth, both height and length development were more focused on the region below the wellbore. After the pumps were shut off almost no fracture width remained around the perforations, as seen in Fig. 3.54, while the main fracture shows widths of around 0.07 in. Fig. 3.55 shows that proppant was deposited into the lower part of the fracture with final concentrations of around 0.7 lb/ft^2. Fig. 3.56 shows the final proppant concentration overlaid with both surface and downhole micro-seismic data for Stage III. After the pumps were shut-off, the proppant concentration does not extend over the full height of the created fracture. Height issues are discussed in detail in Section 8.1.

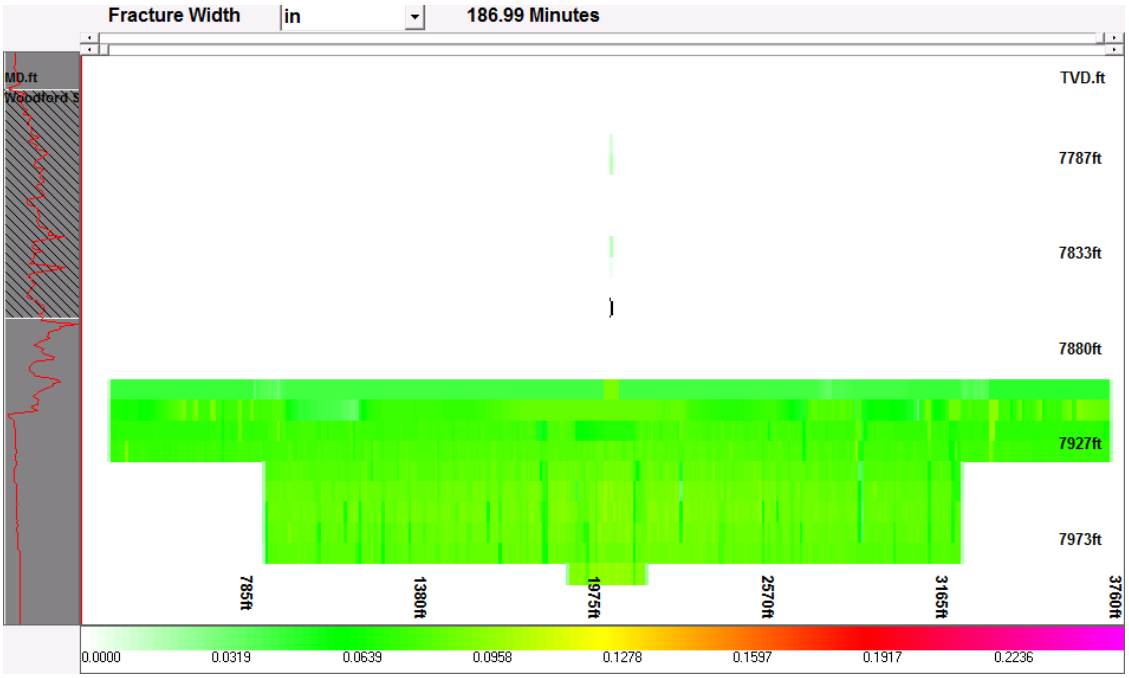

Figure 3.54: Fracture width for transverse pressure and geometry match for Stage IV (X represents perforations).

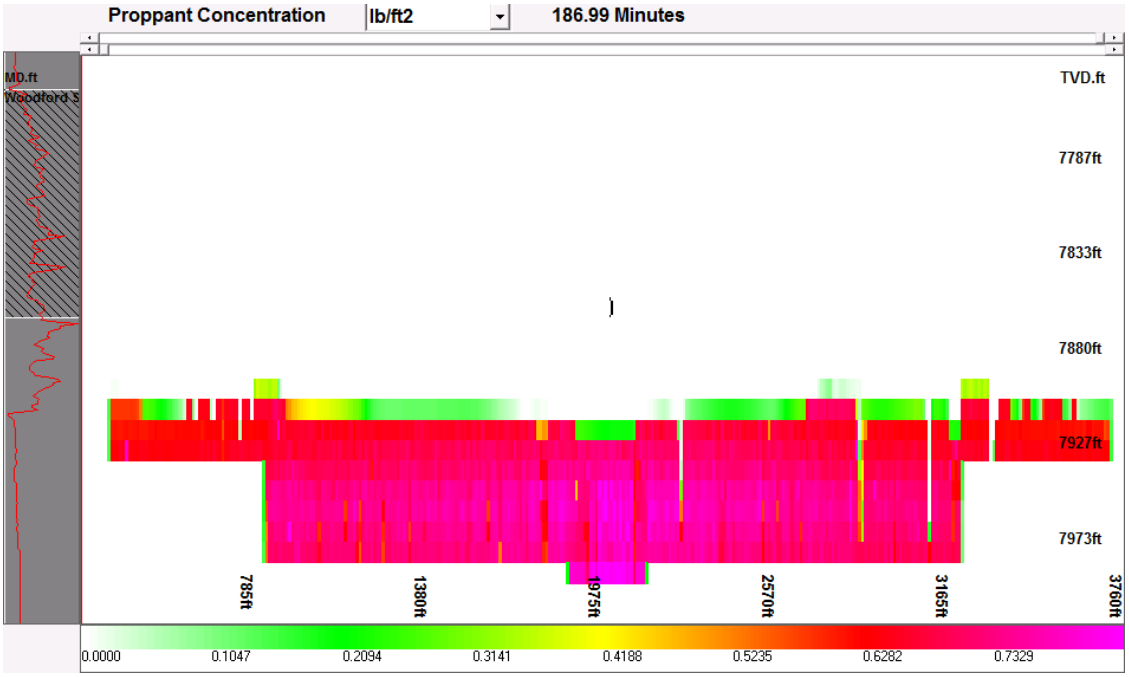

Figure 3.55: Proppant concentration for transverse pressure and geometry match for Stage IV (X represents perforations).

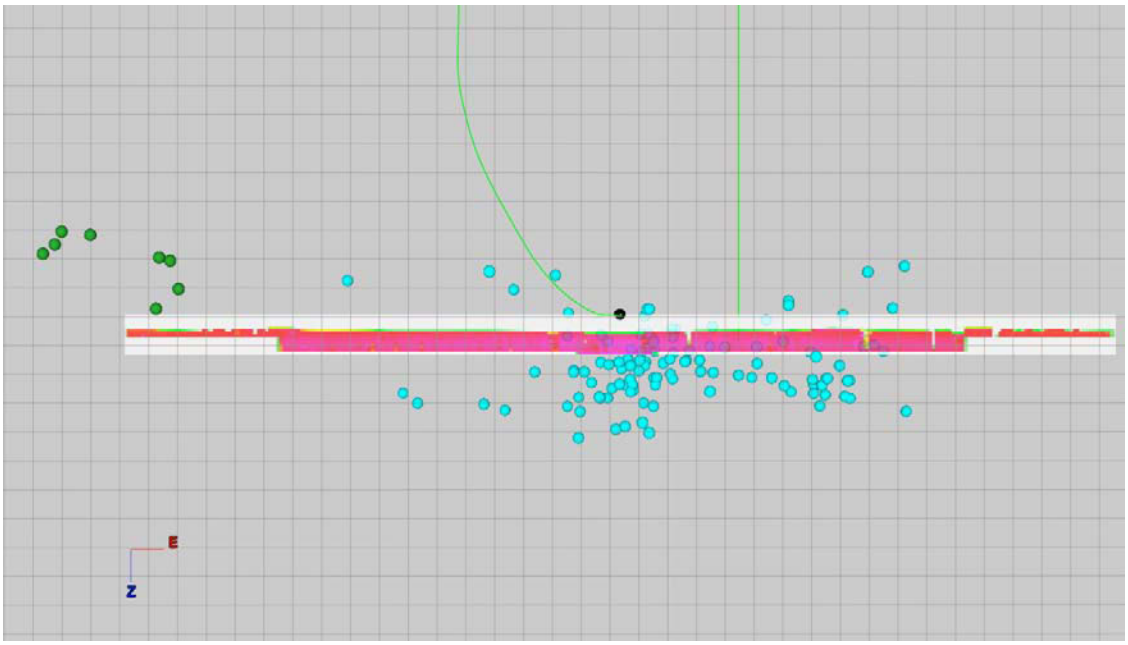

Figure 3.56: Proppant concentration and microseismic data for the transverse model of Stage IV shown in a west-east plane. Turquoise spheres show downhole recordings, whereas green spheres show surface recordings. Final proppant concentration does not extend over the total height of the created fracture. The perforation cluster is represented by the black dot. The directional treatment wellbore can be seen in green on the left side. The grid shown is 100 by 100 ft. Most microseismic activity occurred away from the Stage IV perforation cluster in the weakened formation around the Stage III perforation cluster, which the model was not set-up to simulate.

3.5.2.5 Stage V

In order to achieve a complete match with both pressure and geometry, the model was first adjusted to match only the observed treatment pressure regardless of the fracture geometry. It was then further modified to match the obtained geometry parameters as well.

3.5.2.5.1 Pressure Match

For the final stage, PDMSF was set to 0.005 1/psi and PDL to 0.0031 /psi. The Tortuosity Pre-Factor was set to 0.15 psi/bpm^2. The perforation coefficient was only slightly decreased from the default value to 0.53, with a friction factor of 0.09 in order to

achieve a pressure match. Treatment tubing length was set to the measured depth of the center of the perforation cluster, which was 8,273 ft for this stage.

As for the longitudinal model for the final stage, the tectonic strain had to be slightly increased to 140 microstrains to account for the effects of stress shadowing, resulting in a higher in-situ stress of about 6,197 psi.

Since the perforation coefficient of discharge is larger, the initial perforation factor has to be lower, and hence was set to 0.56 for the first interval from the beginning of the treatment on Dec. 12th, 2007, at about 07:09:00 until 07:36:47. As seen in Fig. 3.5, no proppant has been pumped yet. As perforations open up and the near wellbore resistance to injection decreases, the perforation factor was increased to 0.6 until 07:41:17. It was then increased further to 0.65 until after pumping the first slug of 100-mesh sand at 0.25 lbm/gal at 07:58:46. The factor was then decreased to 0.36 in order to match the simulated pressure curve until after pumping the third slug of 100-mesh sand at 0.75 lbm/gal at 08:10:28. After that the factor was set to 0.33 until 08:57:00 (during pumping the sixth slug of 30/70 sand), and finally to 0.29 until the end of the treatment at about 10:18:00.

3.5.2.5.2 Geometry Match

For the final stage, PDMSF was set to 0.002 1/psi, PDL to 0.001 1/psi, and TSC to 0.001. The Tortuosity Pre-Factor was set to 0.15 psi/bpm^2. The perforation coefficient was only slightly decreased from the default value to 0.53, with a friction factor of 0.09. Treatment tubing length was set to the measured depth of the center of the perforation cluster, which was 8,273 ft for this stage. As for the longitudinal model for the finals stage the tectonic strain had to be slightly increased to 140 microstrains to account for the effects of stress shadowing, resulting in a higher in-situ stress.

The perforation factor was adjusted to 0.45 for the first interval from the beginning of the treatment on Dec. 12th, 2007, at about 07:09:00 until 07:36:47, and was increased to 0.49 until 07:41:17. It was then increased further to 0.59 until after pumping the first slug of 100-mesh sand at 0.25 lbm/gal at 07:58:46. After this, it was decreased to 0.34 until after pumping the third slug of 100-mesh sand at 0.75 lbm/gal at 08:10:28.

After that the factor was set to 0.31 until 08:57:00 (during pumping the sixth slug of 30/70 sand), and finally to 0.27 until the end of the treatment at about 10:18:00.

As mentioned above, all of the microseismic activity for this stage occurred around Stage IV perforations. The height of the microseismic cloud is about 1,040 ft for the main fracture, with fracture half-lengths of 1,410 ft east of the wellbore, and 1,170 ft west of it, giving a total fracture length of 2,820 ft. Again, the fracture length could be very well matched with 2,140 ft. The height on the other hand, due to the fact that microseismic activity actually occurred in an already fractured part of the reservoir was not very well matched with 240 ft. Fig. 3.57 shows the final pressure match.

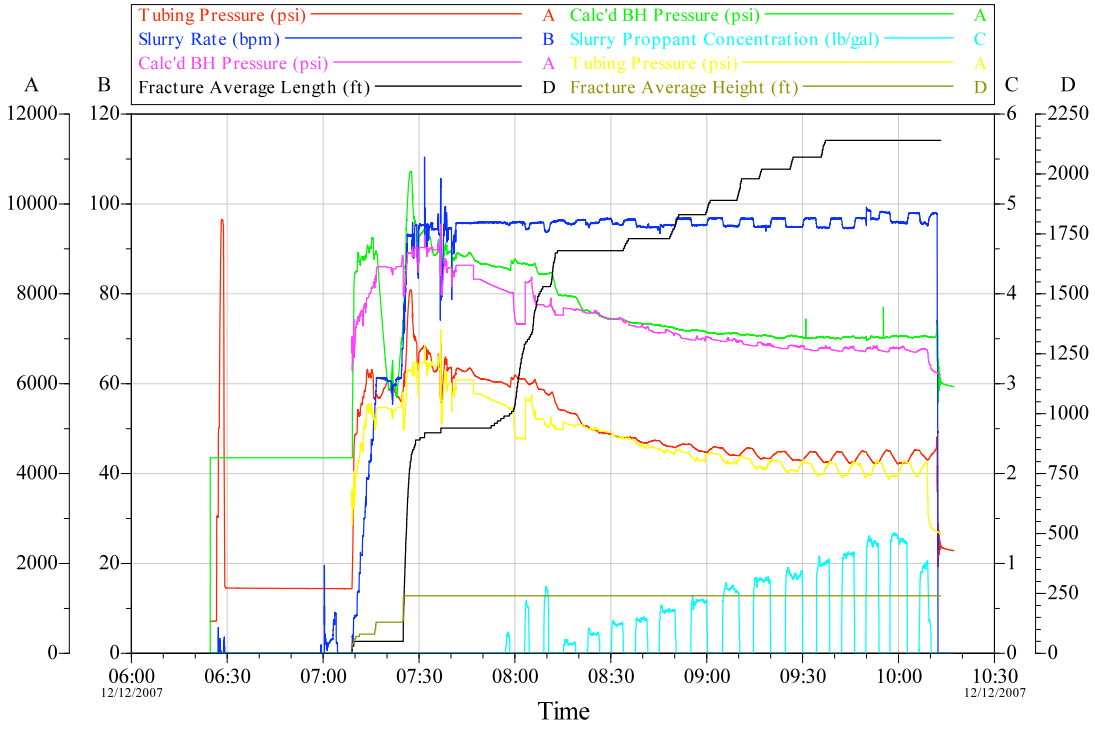

Figure 3.57: Transverse pressure match for Stage V. Final fracture geometry from the model is also shown.

Time-lapse analysis for this stage showed the same effects occurring as for the longitudinal model. Fracture growth occurred mostly above the wellbore, with clear out-of-zone growth. The substantial upward growth occurred due to the higher tectonic strain, which resulted in an additional stress of about 230 psi and is discussed in detail in Section 8.1. In this main fracture the final width was around 0.07 in, as seen in Fig. 3.58,

with almost no width around the perforations. Fig. 3.59 shows a final proppant concentration of around 0.6 lb/ft^2 in the main fracture, with only very little proppant deposition around the perforations or below the wellbore. Fig. 3.60 shows the final proppant concentration overlaid with both surface and downhole microseismic data for Stage III. After the pumps were shut-off the proppant concentration does not extend over the full height of the created fracture. Height issues are discussed in detail in Section 8.1.

Tables 3.1 and 3.2 give an overview of the model parameters for the final pressure and geometry matches of the longitudinal and the transverse model, respectively.

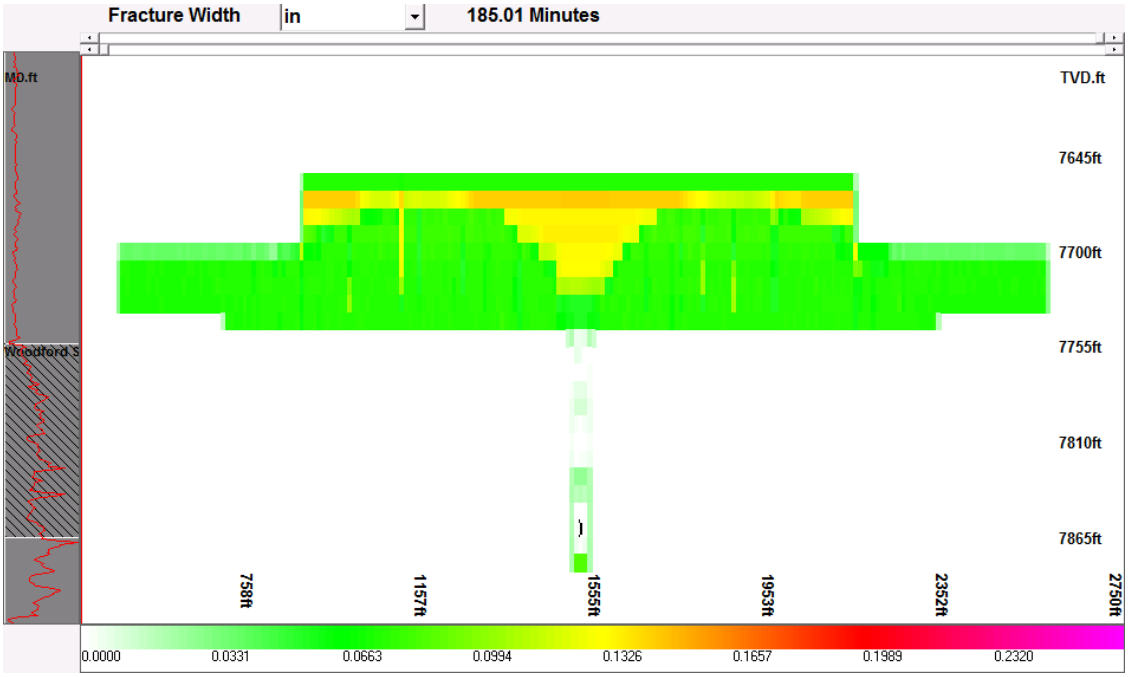

Figure 3.58: Fracture width for transverse pressure and geometry match for Stage IV (X represents perforations).

3.6 Sensitivities

Since every parameter influences the simulation on a different level it is interesting to examine which parameters have what kind of influence on the four simulated properties (pressure, fracture length, fracture height, and maximum fracture width). Each of the eight parameters summarized in Tables 3.1 and 3.2 was modified by

+/– 25%, one at a time, and the models (both longitudinal and transverse) were run again. The observed changes in the outcome were recorded and evaluated. Due to the fact that in a lot of cases the parameter variation showed no effect at all, or inconsistent trends, visualization of the changes in e.g. a tornado plot would not have produced conclusive results. Tables with the modified parameters for both longitudinal and transverse models can be found in Appendix A.

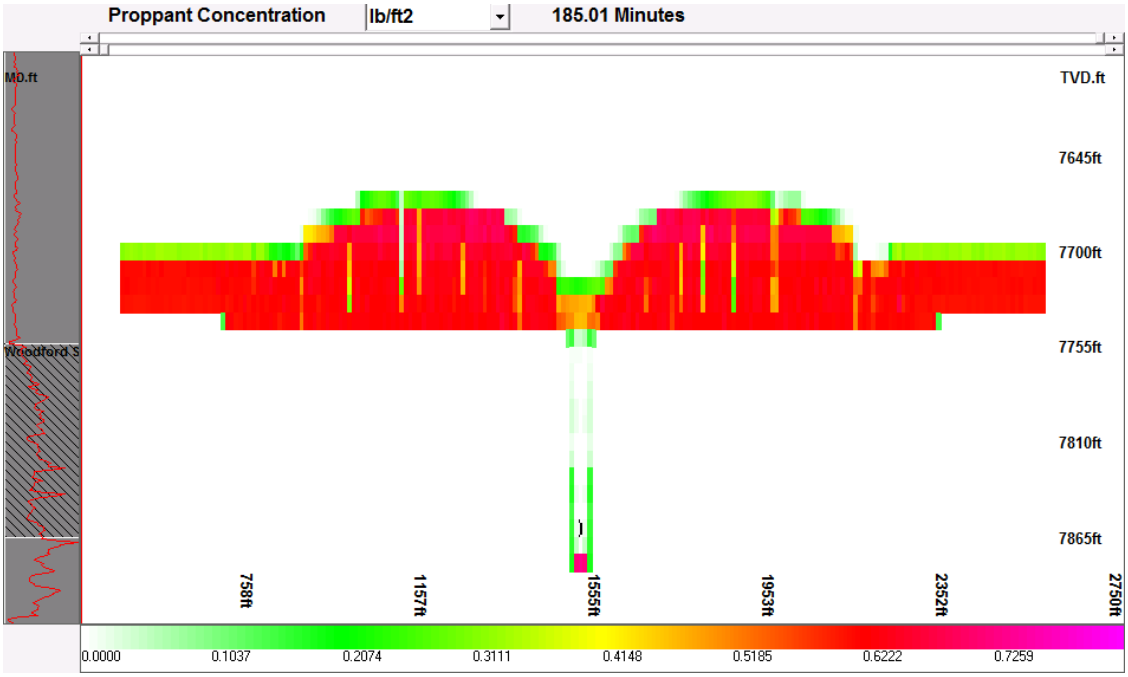

Figure 3.59: Proppant concentration for transverse pressure and geometry match for Stage V (X represents perforations).

3.6.1 Pressure

The simulated bottomhole pressure was not widely affected by changes in PDMSF, PDL, TSC, or the Tortuosity Pre-Factor. Since the first three are pressure dependent properties this does not come as much of a surprise. Near wellbore tortuosity however, which is assessed by the Tortuosity Pre-Factor and in theory has an effect on pressure behavior surprisingly shows no visible effect.

Tectonic strain, varying the stress that the rock is subjected to, has an effect on the bottomhole treatment pressure which is accounted for in the simulation as well. The decrease in tectonic strain generally lowered the BHP, and, as expected, an increase

resulted in a slight pressure increase. The 25% decrease in strain, however, showed more effect than an increase of the same percentage.

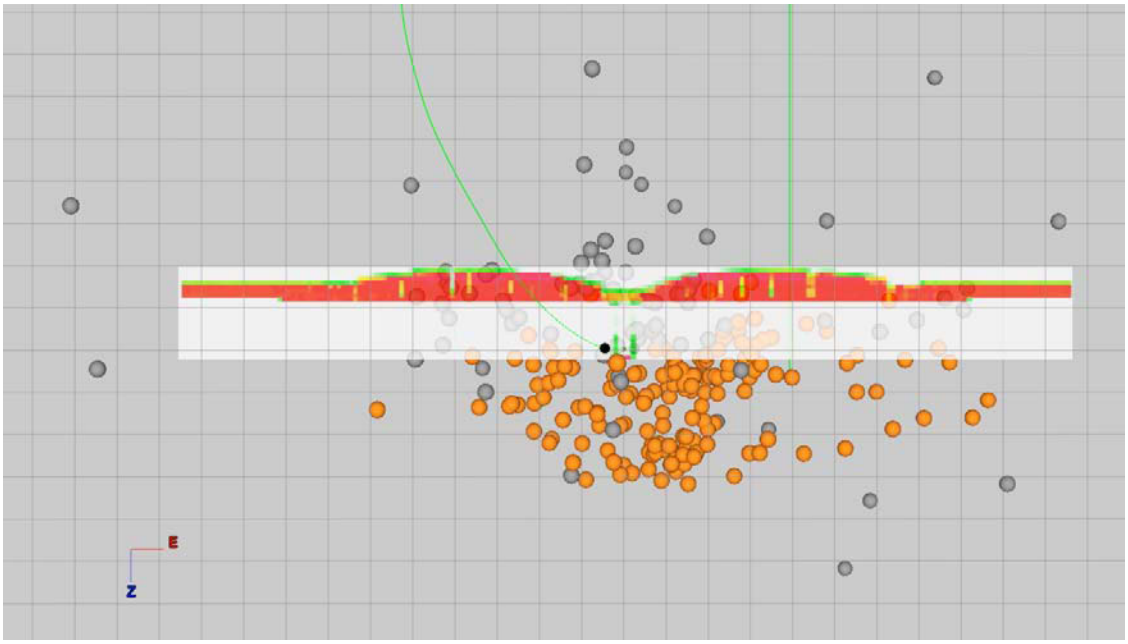

Figure 3.60: Proppant concentration and microseismic data for the transverse model of Stage V shown in a west-east plane. Orange spheres show downhole recordings, whereas grey spheres show surface recordings. Final proppant concentration does not extend over the total height of the created fracture. The perforation cluster is represented by the black dot. The directional treatment wellbore can be seen in green on the left side. The grid shown is 100 by 100 ft. Most microseismic activity occurred away from the Stage V perforation cluster in the weakened formation around the Stage IV perforation cluster, which the model was not set-up to simulate.

The change of the perforation coefficient had an effect only initially. Then this effect decreased and with the first couple of sand slugs being pumped, it diminishes and results in no pressure variation between decrease, base case, and increase in the parameter. The Perforation Factor on the other hand had a very significant effect on the BHP. Since it represents the percentage of perforations open to flow, a decrease resulted in a pressure decrease, and an increase resulted in a pressure increase.

As expected the friction factor did not have any effect on the bottomhole pressure at all, since it is a value solely accounting for pipe friction, therefore affecting the calculated surface pressure alone.

Table 3.1: Model Parameter Overview for Longitudinal Models

	Stage I	*Stage II*	*Stage III*	*Stage IV*	*Stage V*
PDMSF [1/psi]	0.0045	0.005	0.002	0.0025	0.0035
PDL [1/psi]	0.00025	0.0003	0.0015	0.0018	0.0009
TSC [-]	0.00025	0.00029	0.0015	0.0018	0.0009
Tort. Pre-Factor [psi/bpm^2]	0.15	0.15	0.10	0.10	0.15
Tectonic Strain [microstrains]	70	65	45	55	130
Perf. Coeff. [-]	0.37	0.3	0.24	0.25	0.53
Frict. Coeff. [-]	0.03	0.05	0.06	0.07	0.09
Perf. Factor [-]	0.35 *(07:15:47-07:37:56)* 0.45 *(07:37:57-07:40:06)* 0.57 *(07:40:07-07:49:09)* 0.62 *(07:49:10-08:12:56)* 0.38 *(08:12:57-08:16:31)* 0.33 *(08:16:32-10:29:00)*	0.45 *(14:26:30-14:50:00)* 0.60 *(14:50:01-15:18:27)* 0.35 *(15:18:28-15:24:34)* 0.30 *(15:24:35-15:27:00)* 0.25 *(15:27:01-17:34:00)*	0.55 *(07:02:50-07:20:14)* 0.83 *(07:20:15-07:51:23)* 0.32 *(07:51:24-07:57:09)* 0.20 *(07:57:10-10:08:00)*	0.69 *(13:18:00-13:39:22)* 0.77 *(13:39:23-14:08:18)* 0.35 *(14:08:19-14:12:00)* 0.25 *(14:12:01-15:22:20)* 0.20 *(15:22:21-15:30:26)* 0.18 *(15:30:27-15:42:42)* 0.16 *(15:42:43-15:53:04)* 0.13 *(15:53:05-16:26:00)*	0.55 *(07:09:00-07:36:47)* 0.58 *(07:36:48-07:41:17)* 0.6 *(07:41:18-07:58:46)* 1.00 *(07:58:47-10:18:00)*

3.6.2 Fracture Length

The simulated fracture length was sensitive to a change in almost all parameters, both those affecting rock properties and perforations. The sensitivity however did not always follow a clear trend. For a decrease in PDMSF and PDL the effects seemed to depend on the interaction with other parameters, resulting in both

increases and decreases, so no consistent bias could be observed. An increase in PDSMF and PDL on the other hand generally showed a slight decrease in length.

TSC as a parameter quantifying the amount of treatment fluid diversion directly affects the length of the created fracture, with a decrease resulting in a substantial increase in length, and an increase resulting in a substantial decrease in length. The decrease however seemed to have more of an effect on length than the increase. The changes of the Tortuosity Pre-Factor as well as the Friction Factor showed all effects without any observable trend, meaning that the effect on length probably depends on the values of the other parameters and how they interact with the change in tortuosity.

An increase in tectonic strain reflects an increase in total stress and therefore provides more of an obstacle to fracture growth. Fracture length expectedly decreased with an increase in tectonic strain, and increased with a decrease. For one case the opposite was found to be occurring as well. A variation in the Perforation Coefficient did not have much effect on the longitudinal models. Since there is a significantly higher number of perforations at just one grid cell for the transverse models, the effect is much more prominent in those models. However, a clear trend could not be observed since both increases and decreases can show increase, decrease, or no effect on length.

Less perforations open to flow, reflected by a decrease in the perforation factor show resulted trending towards an increase in length, which might be related to the “focusing” of treatment fluid on less open perforations. A trend towards a decrease in fracture length could be observed with an opening of perforations.

3.6.3 Fracture Height

Fracture Height did not seem to be too affected by a 25% change in parameters. Both increase and decrease in PDMSF, Tortuosity Pre-Factor, Tectonic Strain, Perforation Coefficient, Friction Factor as well as in Perforation Factor showed either no effect or a slight decrease. A change in PDL can show an increase, a decrease, or no effect at all without a consistent trend. Interestingly a decrease in TSC resulted in the same outcome, whereas an increase usually had no effect or produced a slight decrease in height.

Table 3.2: Model Parameter Overview for Transverse Models

	Stage I	*Stage II*	*Stage III*	*Stage IV*	*Stage V*
PDMSF [1/psi]	0.002	0.005	0.001	0.002	0.002
PDL [1/psi]	0.0005	0.0004	0.001	0.0005	0.001
TSC [-]	0.0005	0.00033	0.001	0.0005	0.001
Tort. Pre-Factor [psi/bpm^2]	0.10	0.15	0.10	0.10	0.15
Tectonic Strain [microstrains]	50	65	50	50	140
Perf. Coeff. [-]	0.42	0.32	0.24	0.25	0.53
Frict. Coeff. [-]	0.03	0.05	0.06	0.07	0.09
Perf. Factor [-]	0.30 *(07:15:47-07:37:56)* 0.45 *(07:37:57-07:40:06)* 0.51 *(07:40:07-07:49:09)* 0.55 *(07:49:10-08:12:56)* 0.28 *(08:12:57-08:16:31)* 0.24 *(08:16:32-09:07:47)* 0.22 *(09:07:48-09:12:28)* 0.20 *(09:12:29-09:27:52)* 0.18 *(09:27:53-09:32:33)* 0.15 *(09:32:34-09:42:41)* 0.12 *(09:42:42-09:57:53)* 0.10 *(09:57:54-10:29:00)*	0.45 *(14:26:30-14:50:00)* 0.60 *(14:50:01-15:18:27)* 0.25 *(15:18:28-15:24:34)* 0.20 *(15:24:35-15:27:00)* 0.19 *(15:27:01-16:09:55)* 0.17 *(16:09:56-16:19:46)* 0.16 *(16:19:47-16:20:39)* 0.15 *(16:20:40-16:31:13)* 0.14 *(16:31:14-16:39:34)* 0.12 *(16:39:35-16:49:25)* 0.11 *(16:49:26-17:12:08)* 0.09 *(17:12:09-17:34:00)*	0.55 *(07:02:50-07:20:14)* 0.81 *(07:20:15-07:51:23)* 0.23 *(07:51:24-07:57:09)* 0.17 *(07:57:10-10:08:00)*	0.65 *(13:18:00-13:39:22)* 0.72 *(13:39:23-14:08:18)* 0.27 *(14:08:19-14:12:00)* 0.22 *(14:12:01-15:11:41)* 0.19 *(15:11:42-15:22:00)* 0.13 *(15:22:01-15:30:26)* 0.12 *(15:30:27-15:42:42)* 0.10 *(15:42:43-15:53:04)* 0.07 *(15:53:05-16:26:00)*	0.45 *(07:09:00-07:36:47)* 0.49 *(07:36:48-07:41:17)* 0.54 *(07:41:18-07:58:46)* 0.34 *(07:58:47-08:10:28)* 0.31 *(08:10:29-08:57:00)* 0.27 *(08:57:01-10:18:00)*

3.6.4 Maximum Fracture Width

The sensitivity of the maximum fracture width to the change in parameters seemed to be limited to PDMSF only. A decrease in that parameter clearly resulted in an increase in width, whereas an increase clearly resulted in a decrease. Tortuosity Pre-Factor, Perforation Coefficient of Discharge, friction factor, and perforation factor have no effect on fracture width, with only two exceptions where a decrease in width was observed for both an increase and a decrease in Friction Factor and Perforation Factor. Variation in PDL and TSC produced very inconclusive results implying that the effect of a change in this parameter might depend more on the values of and the interaction with the other parameters. A decrease in tectonic strain showed the same results, whereas an increase showed either no effect at all, or a slight increase in maximum fracture width.

CHAPTER 4

MICROSEISMIC ANALYSIS

The availability of both surface and downhole microseismic recordings for a multi-stage treatment in one well provides the opportunity to directly compare the two data sets on different levels. In order to evaluate how reliable and accurate the individual technologies are, and to determine advantages and disadvantages, this chapter investigates the congruency between the surface and downhole data, as well as attempts to estimate how many events are actually necessary to produce a good and fairly accurate match with a hydraulic fracture model. In Chapter V, the recorded data are then analyzed in terms of fracture complexity, as well as in terms of the relationship between the magnitude of events, time and location of occurrence, and seismic deformation in conjunction with reservoir characterization.

It should be noted that microseismic events are not necessarily generated at the fracture itself but rather in a region surrounding the actual fracture. The envelope the data produces therefore not only depends on measuring and processing accuracy but also on mechanisms that can influence the generation of events, such as very high stress at the fracture tip, and leak-off effects (Warpinski et al., 1999). Nevertheless, the microseismic recordings for the treatment in this project should give an accurate picture of fracture growth and geometry, because, as mentioned in Chapter II, gas reservoirs usually have a more narrow cloud of events due to the high compressibility of the fluid.

The recorded microseismic data was visualized and analyzed with the Transform^{TM} Software and Pinnacle's PinnVision^{TM}. The available data set included a well trajectory survey of the treatment well, location of the vertical observation well, and microseismic recordings for each stage.

4.1 General Analysis

This chapter is structured in three parts. The first part is a general analysis of the microseismic data in terms of fracture azimuth, time and location of occurrence of the events, as well as the magnitude that is associated with them. Fracture azimuths were first visually obtained and then compared with the final report that the service company provided. This compares downhole and surface recordings and looks at differences in event distribution throughout the reservoir.

4.1.1 Surface Data

In order to monitor the treatment from the surface, an array was laid out with straight lines of geophones (with discontinuities due to local surface restrictions) extending from a central location near the surface location of the treatment well. One of the arms was almost parallel to the horizontal interval of the well (Gertson, 2011).

Altogether, 617 events were recorded, most of a very small magnitude. Due to the accuracy of determining the event location, especially of smaller events, it is useful to look at a plot of cumulative number of events vs. event magnitude in order to find out how reliable the data set is, and whether all events should be considered for the analysis (Gertson, 2011).

Sorting all events from largest to smallest magnitude and plotting them against the cumulative number of events, a plot such as Fig. 4.1 can be generated. A clear change of slope can be observed at a magnitude of about -2.75. This magnitude should therefore be used as a cut-off criterion. For the analysis of surface microseismic in this work, only events with a magnitude of -2.75 or larger were considered, in total 222. (It should be noted that an obvious change in slope also occurs at a magnitude of about -1.9, which would have left very few events for analysis had it been applied as a cut-off value.)

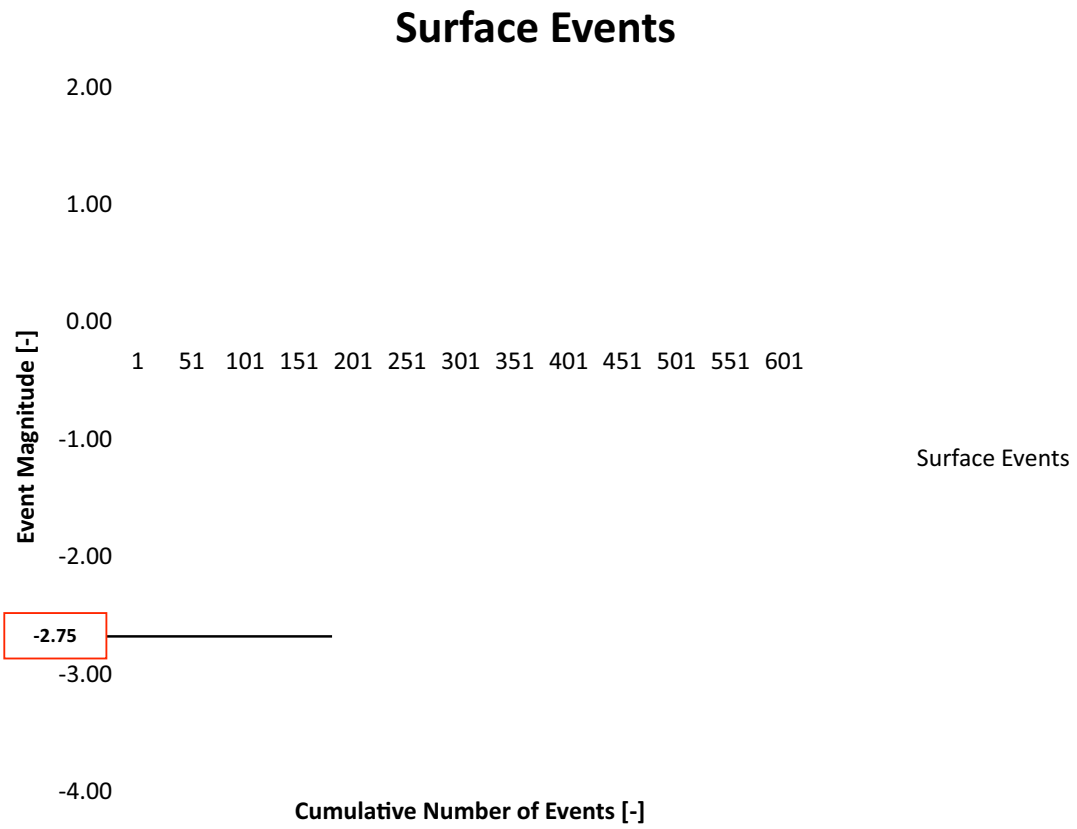

Figure 4.1: Surface event cut-off criterion. Only events above -2.75 are considered in this analysis.

4.1.1.1 Stage I

In total, 121 events were recorded during Stage I, with 16 events left after the magnitude cut-off was applied. However, the recorded events do not give a complete picture of microseismic activity because the first 64 minutes of Stage I were not recorded. As seen in Fig. 4.2, the events are rather scattered, with one apparent fracture growing from Stage I perforations, and other fractures seemingly extending from Stage II and Stage III perforation clusters.

Time-lapse playback showed that events started to occur near the wellbore, growing from Stage I perforations, and then fractures originating from Stage II and Stage III perforations followed up. Fractures grew outwards with distinct downward growth at first, but after some time, upward growth and downward growth occurred simultaneously.

Microseismic activity showed a fracture azimuth of about 77 degrees, with a longitudinal stretch of 1,700 ft along the wellbore. The cloud is distributed asymmetrically with about 2,300 ft of activity west of the treatment well, and about 960 ft east of it. Fracture height can be observed with 300 ft above the wellbore, and 500 ft below it. Looking at only the main fracture originating from Stage I perforations, a longitudinal stretch of 630 ft, and a height of 130 ft above, and 500 ft below the wellbore was observed. The main fracture had only slightly shorter half lengths with 2,100 ft west of the wellbore and 960 ft east of it.

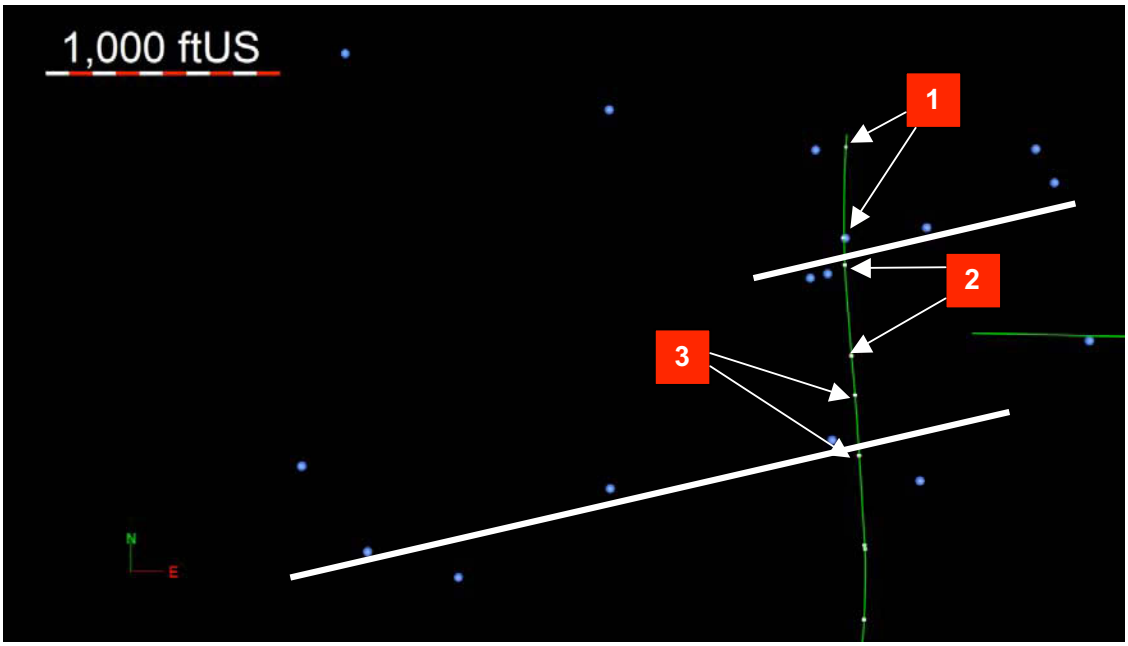

Figure 4.2: Surface microseismic recordings (blue spheres) for Stage I. The horizontal well trajectory of the treatment wellbore can be seen in green from south to north. The monitoring well can be seen in green east of the treatment well. White solid lines indicate perceived fracture planes. Numbers mark stage perforation clusters.

4.1.1.2 Stage II

During Stage II, 134 events were recorded in total, although the first 20 minutes of the treatment were not recorded. After applying the magnitude cut-off, six events are left for analysis. Microseismic activity clearly overlaps with Stage I perforations, as seen in Fig. 4.3, with the fracture seemingly growing from the end of the Stage II perforation cluster into the direction of the already weakened region around the Stage I perforations.

Although six events restrict analysis to some extent, it was observed in the time- lapse playback that events started occurring near the wellbore, of both smaller and larger magnitude, and then extended outwards. Downward and upward growth appeared to occur simultaneously.

The fracture seems to be fairly contained to the Woodford Shale with a height of 150 ft above, and 90 ft below the wellbore. A fracture azimuth of 78 degrees was observed with microseismic activity stretching around 300 ft along the wellbore. The cloud of events was clearly asymmetric with 610 ft west of the wellbore and 260 ft east of it.

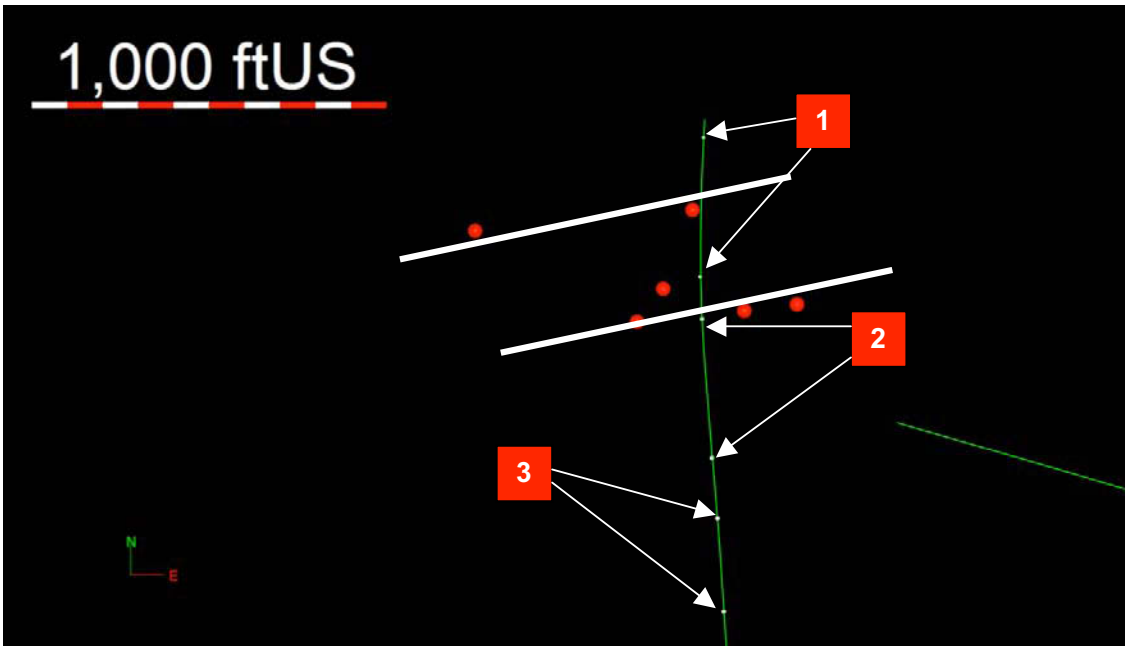

Figure 4.3: Surface microseismic recordings (red spheres) for Stage II. The horizontal well trajectory of the treatment wellbore can be seen in green from south to north. The monitoring well can be seen in green east of the treatment well. White solid lines indicate perceived fracture planes. Numbers mark stage perforation clusters.

4.1.1.3 Stage III

In total, 141 events were recorded during Stage III, with 19 events left after the cut-off was applied. The generated fracture network seems to be overlapping with the area around Stage II perforations, as seen in Fig. 4.4. Time-lapse playback showed that the fracture grew outwards from the perforations into the reservoir, with smaller and

larger events occurring simultaneously. Fracture growth along the fracture azimuth occurred mostly upwards, with only one event recorded below the wellbore. Microseismic activity stretched about 360 ft along the wellbore, with a height of 260 ft above the wellbore, and 60 ft below it. No events were recorded east of the wellbore, showing fracture growth exclusively west of the wellbore with a length of 1,270 ft and a fracture azimuth of 77 degrees.

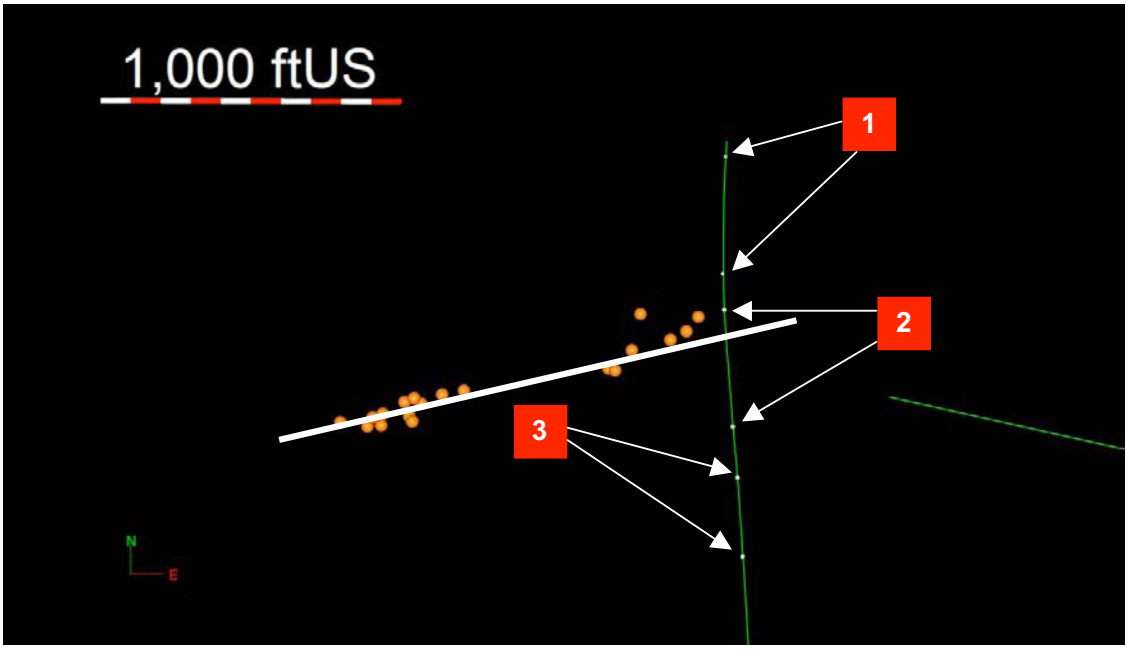

Figure 4.4: Surface microseismic recordings (orange spheres) for Stage III. The horizontal well trajectory of the treatment wellbore can be seen in green from south to north. The monitoring well can be seen in green east of the treatment well. White solid lines indicate perceived fracture planes. Numbers mark stage perforation clusters.

4.1.1.4 Stage III ½

The operating company decided to continue recording microseismicity for a couple of hours after Stage III of the treatment was pumped. Microseismic activity was observed even without injection because the rock was still under stress. Whether this activity can be interpreted as continued fracture growth is arguable (Gertson, 2011). The reservoir equalized some of the additional stress that it has been put under due to the previous stages, and therefore generated microseismic events when stress is released at certain locations.

Fifteen events were recorded during this stage, with four events left after applying the cut-off. About one and a half hours after Stage III was completed generally larger events were recorded. Although only four events can be used for the analysis, three of them occurred along the fracture azimuth seemingly extending the fracture generated by Stage III, as seen in Fig. 4.5. One event was recorded between Stage III and Stage IV perforations. When viewed in time lapse playback the fracture appeared to continue growing further into the reservoir.

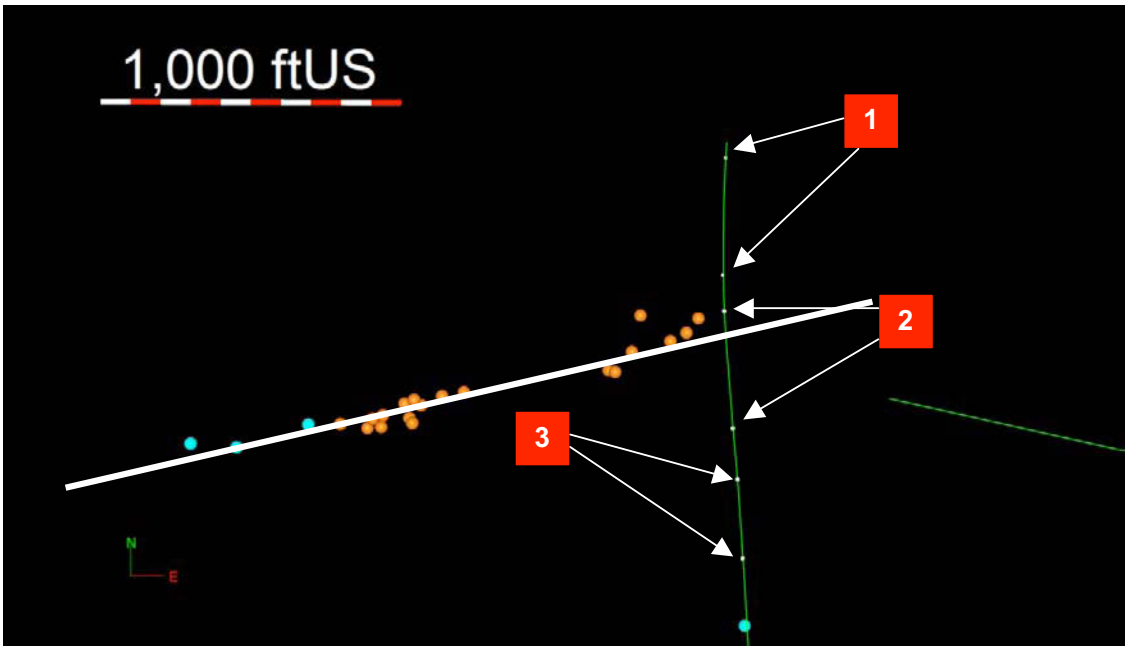

Figure 4.5: Surface microseismic recordings for Stage III (orange spheres) and Stage III ½ (turquoise spheres). The horizontal well trajectory of the treatment wellbore can be seen in green from south to north. The monitoring well can be seen in green east of the treatment well. White solid lines indicate perceived fracture planes. Numbers mark stage perforation clusters.

4.1.1.5 Stage IV

Although the first ten minutes of this stage were not recorded, 84 events were recorded in total, with eight remaining after the application of the magnitude cut-off. Fig. 4.6 shows that the events were contained to Stage IV perforations. It can be seen that all events occurred far out in the reservoir west of the wellbore. Time-lapse playback shows that event occurrence as focused on the beginning, the middle, and the end of the treatment, with periods in between where no events were recorded. The fracture seems

to be growing outwards into the reservoir along the fracture azimuth of about 78 degrees. A fracture half-length of 1,950 ft west of the wellbore was observed, with no recorded microseismic activity east of it. Events are very contained to what appears to be a single fracture, giving a longitudinal stretch of only 90 ft. No events were observed at depths below the wellbore, but up to 290 ft above it.

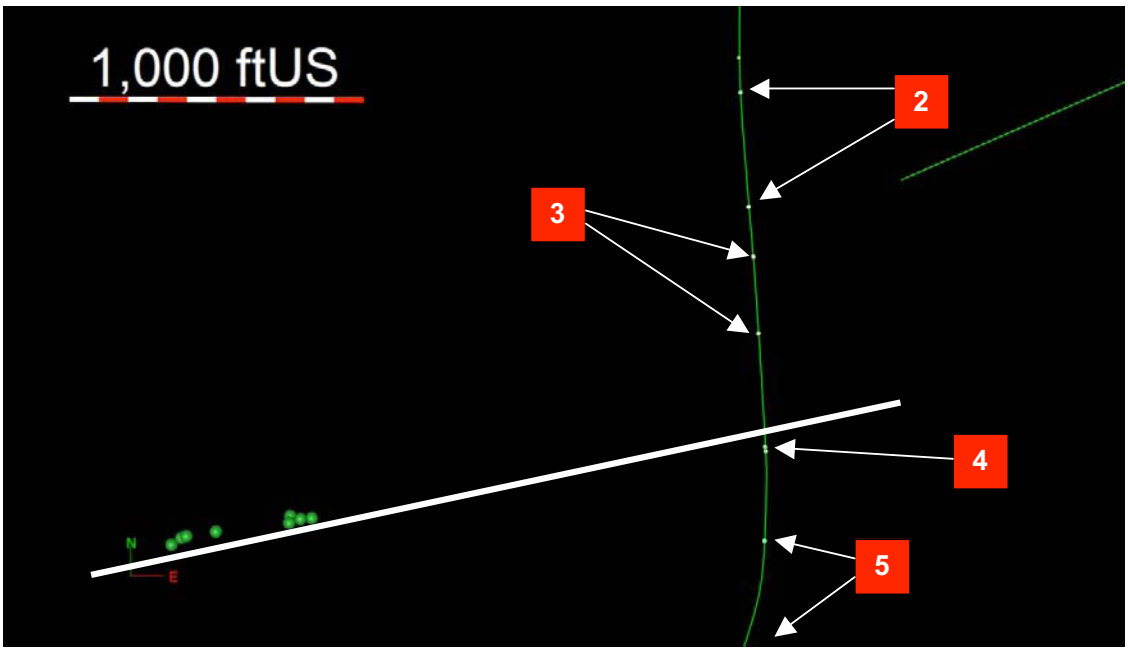

Figure 4.6: Surface microseismic recordings (green spheres) for Stage IV. The horizontal well trajectory of the treatment wellbore can be seen in green from south to north. The monitoring well can be seen in green east of the treatment well. White solid lines indicate perceived fracture planes. Numbers mark stage perforation clusters.

4.1.1.6 Stage V

The last stage of the treatment is also the stage with the most events recorded. In total, 122 events were recorded, with 83 remaining after the cut-off was applied. Generally, microseismic events were of a larger magnitude than during previous stages. However, they were very scattered, with locations from around Stage II perforations all the way to Stage IV perforations. Looking at the data points, as shown in Fig. 4.7, a main fracture can be observed, originating from the Stage IV perforation cluster. Events along this main fracture also show the largest magnitude of all events that were recorded.

The time-lapse playback showed that the first events occurring are the ones outlining the main fractures, with generally overall larger magnitudes. Next, events overlapping with the area around Stage II and Stage III perforations began to occur. During later stages of the treatment, microseismic activity occurred simultaneously in that region as well as outlining growth of the main fracture along the fracture azimuth. In general more events above the wellbore were recorded, with initially upward growth only, and simultaneous upward and downward growth later on.

The microseismic activity observed during this stage was of fairly large dimensions. A total longitudinal stretch of about 1,420 ft along the wellbore was observed, with fracture half-lengths of 1,410 ft west of the wellbore, and 1,170 ft east of it, at a fracture azimuth of 78 degrees. Events were recorded up to 750 ft above the wellbore, and up to 630 ft below it. Looking at the main fracture only, fracture dimensions are slightly smaller. Microseismic activity around it had a longitudinal stretch of 500 ft along the wellbore, 1,410 ft of half-length west of the wellbore, and 940 ft east of it. Fracture height was observed with 710 ft above the wellbore and 330 ft below it.

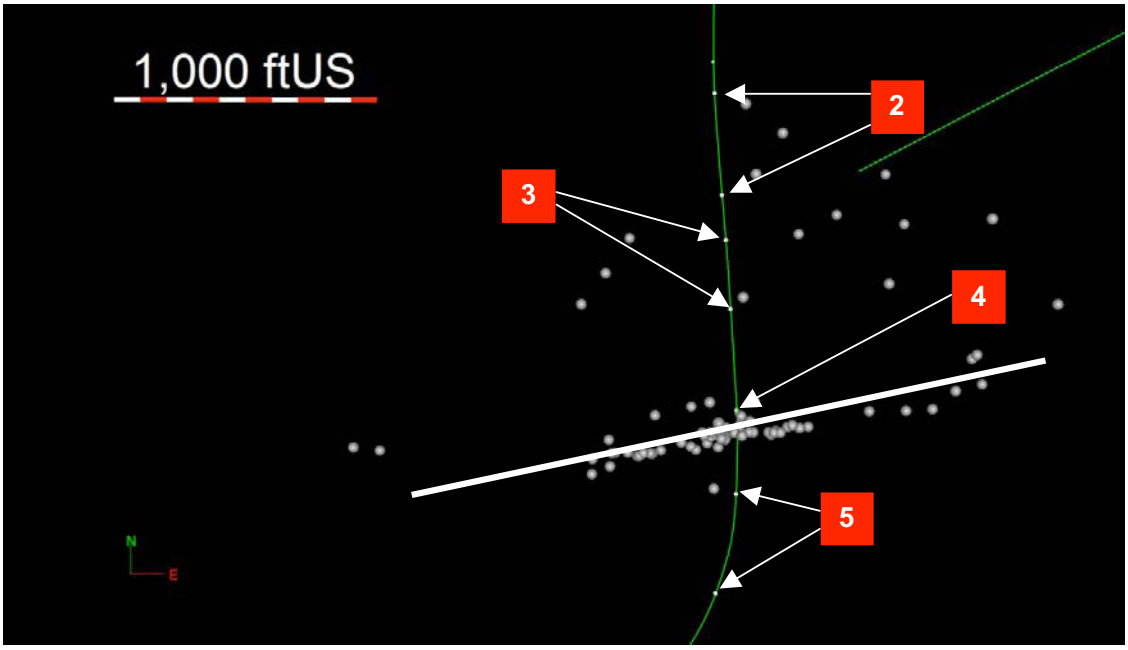

Figure 4.7: Surface microseismic recordings (grey spheres) for Stage V. The horizontal well trajectory of the treatment wellbore can be seen in green from south to north. The monitoring well can be seen in green east of the treatment well. White solid lines indicate perceived fracture planes. Numbers mark stage perforation clusters.

4.1.1.7 Summary

Table 4.1 gives an overview of fracture dimensions obtained from surface microseismic. It can be seen that surface recordings for this treatment show a substantially asymmetrical fracture growth to the west side of the wellbore. Furthermore, except for Stage I, there was more upward growth than downward growth recorded. Fig. 4.8 shows all stages that were recorded by surface receivers. The observed fracture azimuths were in good agreement with the azimuths determined by the service company.

Table 4.1: Microseismic Activity from Surface Recordings

Stage	*Perforation Interval [ft MD]*	*Number of Recorded Events [-]*	*Microseismic Activity*			
			Length (W/E of wellbore) [ft]	*Longitudinal Stretch [ft]*	*Height (above/below wellbore) [ft]*	*Fracture Azimuth [degrees]*
I	10,262 - 10,642	16	2,300 / 950	1,700	300 / 500	77
II	9,764 - 10,145	6	610 / 260	300	150 / 90	78
III	9,342 - 9,598	19	1,270 / 0	360	260 / 60	77
IV	8,951 - 8,966	8	1,950 / 0	90	290 / 0	78
V	8,273 - 8,653	83	1,410 / 1,170	1,420	750 / 630	78

4.1.2 Downhole Data

The treatment was monitored with an array of twelve downhole geophones that were lowered into a vertical observation well at a depth from 7,519 ft to 7,774 ft. The distance from the sensors to the various perforation intervals ranged from about 630 ft to about 1,540 ft. Stage I was not recorded due to equipment complications.

It is generally acknowledged that the best results can be obtained when the sensors are positioned across the interval of interest. However, in this particular case, the geophones were positioned above the Woodford Shale and not across it. The Woodford Shale shows a substantially lower seismic velocity than the Mayan Shale above it, and the Hunton Limestone, and the Sylvan Shale below it, so the seismic

energy that would be recorded by sensors straddling the Woodford Shale would arrive refracted rather than direct, leading to more difficulty in calculating the event location (Gertson, 2011).

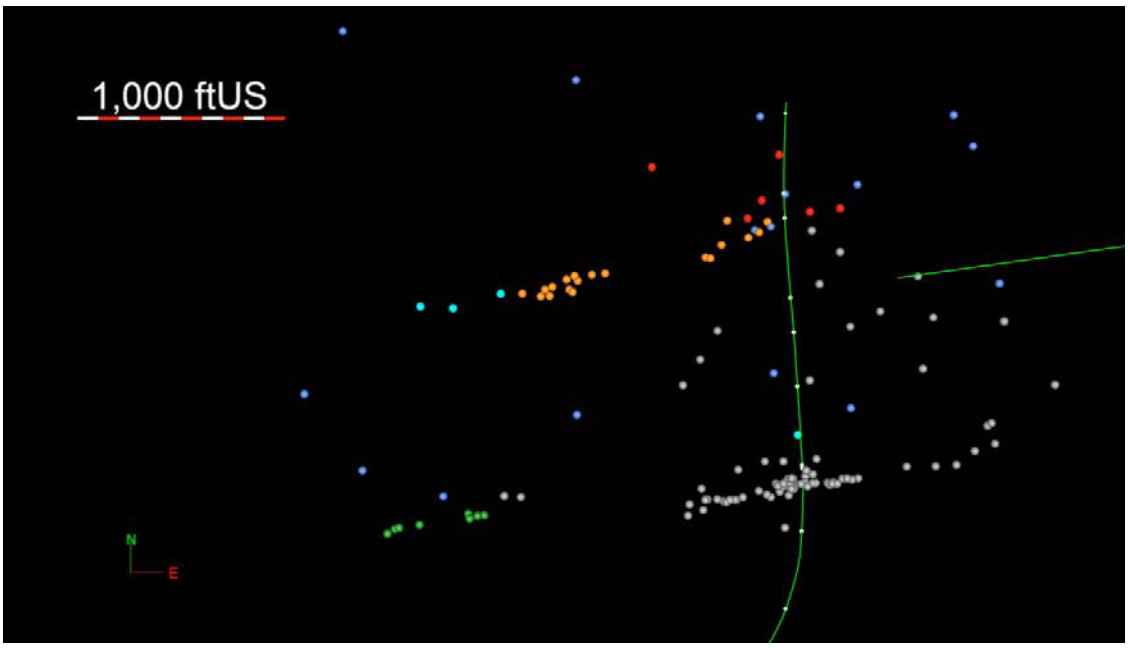

Figure 4.8: Surface microseismic recordings for all stages. The respective events and perforation intervals are shown in Figs. 4.2 through 4.7. The horizontal well trajectory of the treatment wellbore can be seen in green from south to north. The monitoring well can be seen in green east of the treatment well.

4.1.2.1 Stage II

In total, 81 events were recorded by the sensors during Stage II. Fracture growth seems to be contained to the Stage II perforations, as seen in Fig. 4.9, and most events occur within the Woodford Shale. What can also be seen is that more events are recorded in the vicinity of the observation well, as opposed to the 'far' side of the treatment wellbore. This may have two reasons: asymmetrical fracture growth, and location bias of the observation well. Most likely the latter makes up the largest portion of this effect in this situation.

In the time-lapse playback it could be seen that events began to occur near the treatment wellbore on the "near" side, i.e. east of the treatment well, which was closer to the observation well. Events near the treatment wellbore were of a larger magnitude

than events near the observation wellbore. This might mean that a lot of rock deformation was occurring in the region closer to the perforation, but it might also be due to the fact that the closer events are to the sensors, the smaller their magnitude can be in order for them to be recorded. The earlier events seemed to outline the fractured zone, whereas later events mostly filled in the space between these outlines.

The fracture has an azimuth of about 78 degrees, and a height of about 280 ft, which seems to be symmetrically distributed between above and below the treatment wellbore. The zone of microseismic activity has a longitudinal stretch of about 810 ft along the wellbore, and shows asymmetrical half-lengths, with 550 ft west of the treatment wellbore and 850 ft east of it.

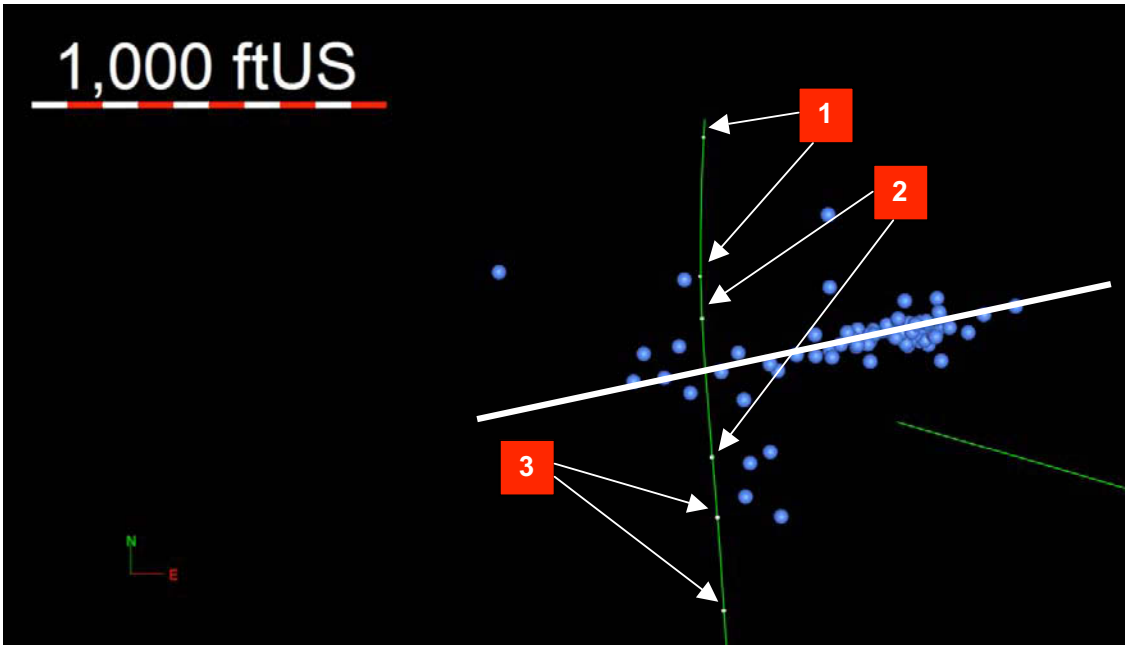

Figure 4.9: Downhole microseismic recordings (blue spheres) for Stage II. The horizontal well trajectory of the treatment wellbore can be seen in green from south to north. The monitoring well can be seen in green east of the treatment well. White solid lines indicate perceived fracture planes. Numbers mark stage perforation clusters.

4.1.2.2 Stage III

During the third stage of the treatment, 132 events were recorded. As seen in Fig. 4.10, microseismic activity seems to be occurring at two different locations: most events overlap with Stage II perforations with only two fractures originating from the

Stage III perforation cluster. Since the formation has already been fractured and therefore weakened around Stage II perforations, it is easier for the fracturing fluid to take the way of less resistance and further deform the reservoir at Stage II, than to exclusively initiate fractures that grow from Stage III perforations. It is believed to be more an effect of “taking the path of least resistance” than a problem of stage isolation (Gertson, 2011). It can also be seen that there is substantial downward growth into formations below the Woodford Shale. Microseismic activity was observed up to about 190 ft above the treatment wellbore, and up to 290 ft below it, giving a total fracture height of about 480 ft.

Time-lapse playback of the data showed that most events, of both small and large magnitude, occurred in the vicinity of the treatment wellbore, within the first hour of the treatment. Events farther away from the wellbore were observed to have a larger magnitude, which ties back into the fact that the farther events are away from the sensors, the larger they have to be in order to be recorded. During the two-and-a-half hours after the first 60 minutes of the treatment, substantially fewer events were recorded. Upward and downward growth appeared to occur simultaneously.

The zone of microseismic activity has a longitudinal stretch of about 1,100 ft along the wellbore, with a fracture azimuth of about 76 degrees. Half-lengths are asymmetrical, with about 1,300 ft west of the treatment wellbore and 560 ft east of it.

4.1.2.3 Stage IV

A total number of 113 events were recorded throughout the fourth stage of this hydraulic fracturing treatment. Fig. 4.11 shows that most events overlap with Stage III perforations, with one fracture even seemingly originating from Stage II perforations, and one distinct fracture growing from the Stage IV perforation cluster. The overlap is due to effects explained above in the Stage III analysis. More events were recorded close to the observation well, with most events occurring in the beginning and the end of the treatment, and less in the middle. There is substantial downward growth of about 430 ft below the treatment well, with about 190 ft of upward growth, giving a total height of 620 ft.

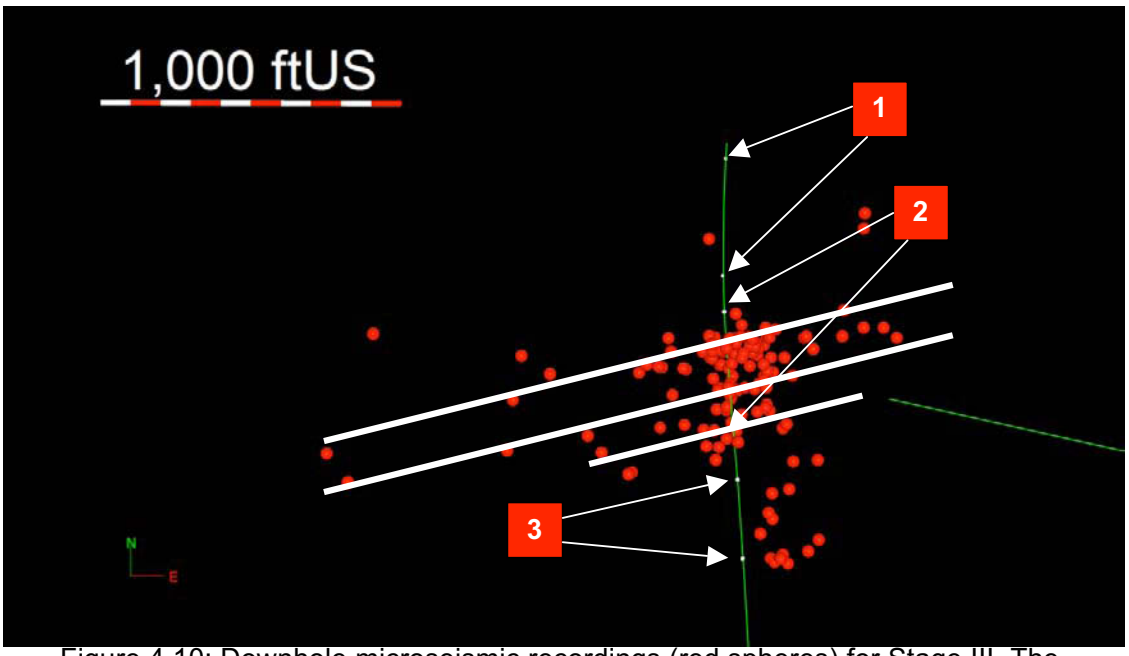

Figure 4.10: Downhole microseismic recordings (red spheres) for Stage III. The horizontal well trajectory of the treatment wellbore can be seen in green from south to north. The monitoring well can be seen in green east of the treatment well. White solid lines indicate perceived fracture planes. Numbers mark stage perforations.

Events of all magnitudes first occurred in the near wellbore region, with the fracture growing east towards the location of the observation well. A possible reason for this asymmetry is again the location bias of the recording sensors. The fracture initially started growing downwards, whereas upward growth only occurred during the later part of the treatment. Stage IV shows the least asymmetry of all stages, with about 920 ft of microseismic activity east of the treatment wellbore, and about 1,080 ft west of it, with a fracture azimuth of about 77 degrees. The longitudinal stretch of activity along the wellbore is about 1,060 ft.

4.1.2.4 Stage V

During the last stage of this hydraulic fracturing treatment a total number of 171 events were recorded. This stage seems to have events of a generally larger magnitude than previous stages. As can be seen in Fig. 4.12, most events overlap with Stage IV perforations. One fracture, however, seems to be originating from a Stage III perforation

interval, and one distinctly from Stage V perforations. Stage V, too, shows substantially more downward growth than upward growth, with a total height of about 510 ft, of which only 350 ft are below the treatment wellbore, and only about 160 ft above it. The zone of microseismic activity has a longitudinal stretch of about 1,150 ft, and a length of about 640 ft east of the treatment well, and about 930 ft west of it. Fracture azimuth is about 75 degrees.

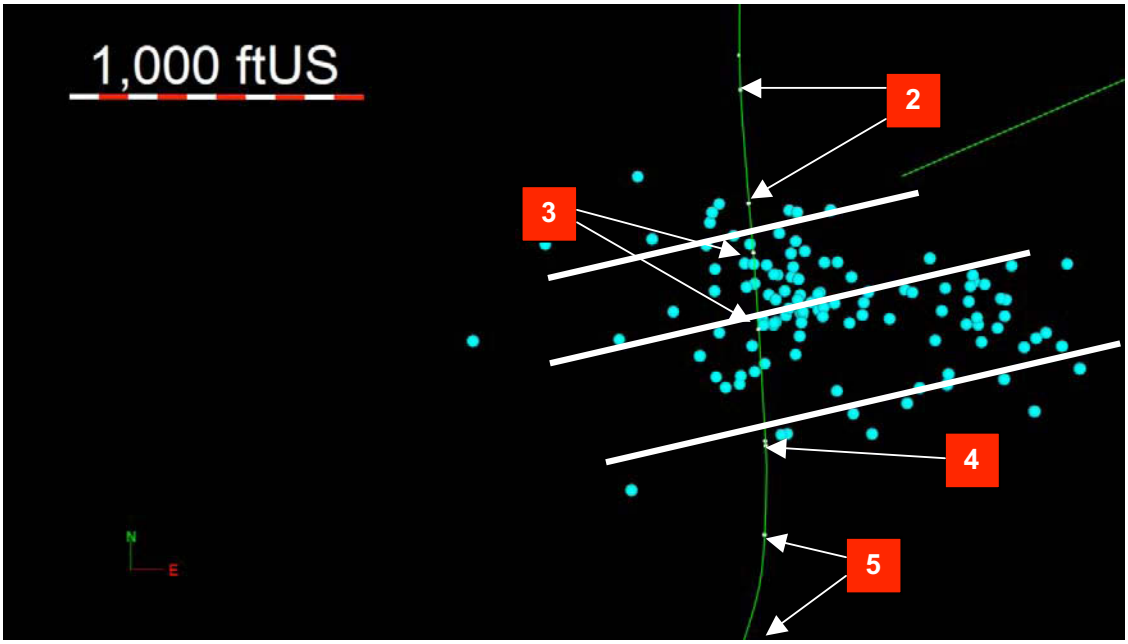

Figure 4.11: Downhole microseismic recordings (turquoise spheres) for Stage IV. The horizontal well trajectory of the treatment wellbore can be seen in green from south to north. The monitoring well can be seen in green east of the treatment well. White solid lines indicate perceived fracture planes. Numbers mark stage perforations.

Time-lapse playback showed that most events occurred during the beginning of the stage within the first hour. Fracture growth could easily be observed, growing from the perforations out into the reservoir. Even though most events occurred around Stage IV perforations, the one event that could be observed at a Stage V perforation set was one of the first to be recorded. Upward and downward growth appeared to occur simultaneously.

4.1.2.5 Summary

Table 4.2 gives an overview of fracture dimensions obtained from downhole microseismic. Except for Stage II, the sensors recorded more activity east of the treatment wellbore, which is probably related to the eastern location of the observation well. Unlike the surface data, the downhole set generally shows more downward fracture growth. Fig. 4.13 shows all stages that were recorded by the downhole receivers. The observed fracture azimuths were in good agreement with the azimuths determined by the service company.

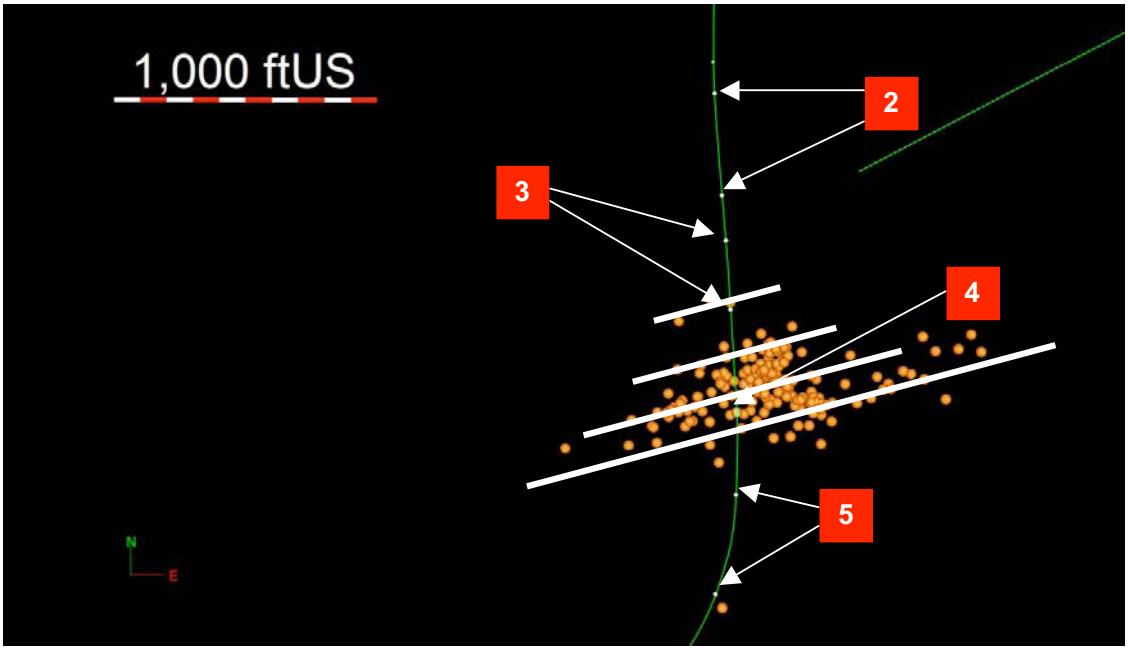

Figure 4.12: Downhole microseismic recordings (orange spheres) for Stage V. The horizontal well trajectory of the treatment wellbore can be seen in green from south to north. The monitoring well can be seen in green east of the treatment well. White solid lines indicate perceived fracture planes. Numbers mark stage perforations.

4.1.3 Combined Data Sets

Merging both data sets into one complete data set was the basis for the models developed in Chapter III. Since both surface and downhole sensors do not necessarily record the same events, combining them should give the most complete picture of fracture growth and microseismic activity.

Table 4.2: Microseismic Activity from Downhole Recordings

Stage	*Perforation Interval [ft MD]*	*Number of Recorded Events [-]*	*Microseismic Activity*			
			Length (W/E of wellbore) [ft]	*Longitudinal Stretch [ft]*	*Height (above/below wellbore) [ft]*	*Fracture Azimuth [degrees]*
II	9,764 - 10,145	81	550 / 850	810	140 / 140	78
III	9,342 - 9,598	132	1,320 / 560	1,100	190 / 290	76
IV	8,951 - 8,966	113	920 / 1,080	1,060	190 / 430	77
V	8,273 - 8,653	171	640 / 930	1,150	160 / 350	75

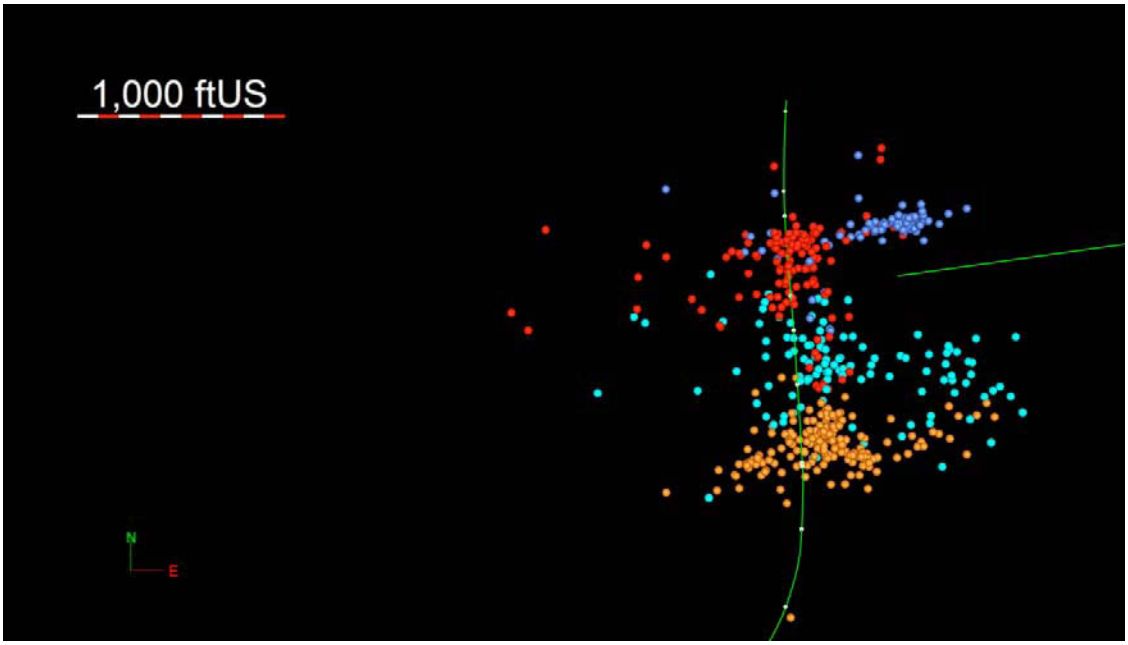

Figure 4.13: Downhole microseismic recordings for all stages. The respective events and perforation intervals are shown in Figs. 4.9 through 4.12. The horizontal well trajectory of the treatment wellbore can be seen in green from south to north. The monitoring well can be seen in green east of the treatment well.

4.1.3.1 Stage I

Only surface data was available for the first stage of the treatment, since the downhole sensors did not record due to equipment issues. Detailed information about the fracture geometry solely based on surface microseismic is found in Section 4.1.1.1.

4.1.3.2 Stage II

Downhole recordings show confinement to Stage II perforations, whereas surface data shows a slight overlap with Stage I perforations, as seen in Fig. 4.14. Surface events are also of a larger magnitude than the downhole events. Generally downhole and surface recordings seem to be in good agreement, though. Both data sets show a fracture azimuth of 78 degrees. The combined geometry gives a longitudinal stretch of 830 ft, and half-lengths of 610 ft west of the wellbore, and 850 ft east of it. The height was observed with 150 ft above the wellbore, and 140 ft below it, which can be seen in Fig. 4.15.

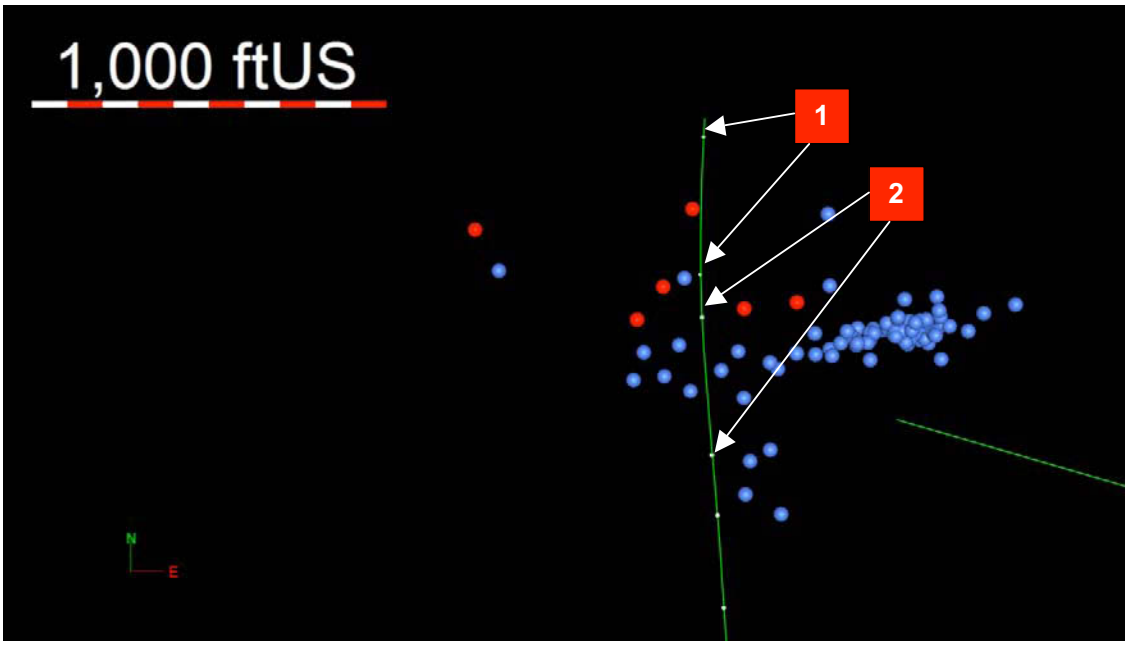

Figure 4.14: Downhole (blue spheres) and surface (red spheres) microseismic recordings for Stage II. The horizontal well trajectory of the treatment wellbore can be seen in green from south to north. The monitoring well can be seen in green east of the treatment well. Numbers mark stage perforation clusters.

4.1.3.3 Stage III

Both downhole and surface microseismic show an overlap with Stage II perforations. The surface data seems to fit in well with the downhole data, as the events are located inside of the microseismic cloud outlined by the downhole data, which can be seen in Fig. 4.16. Fracture azimuths seem to be in good agreement, with 76 degrees

from the downhole recordings, and 77 degrees from the surface data. Time lapse playback gives a good picture of fracture growth from the wellbore out into the reservoir. Combined geometry gave a longitudinal stretch of about 1,100 ft, and half-lengths of 1,320 ft west of the wellbore, and 560 ft east of it. Fracture height was observed with 260 ft above the wellbore and 290 ft below it. As seen in Fig. 4.17, most height development is depicted by microseismic activity occurring around Stage II perforations.

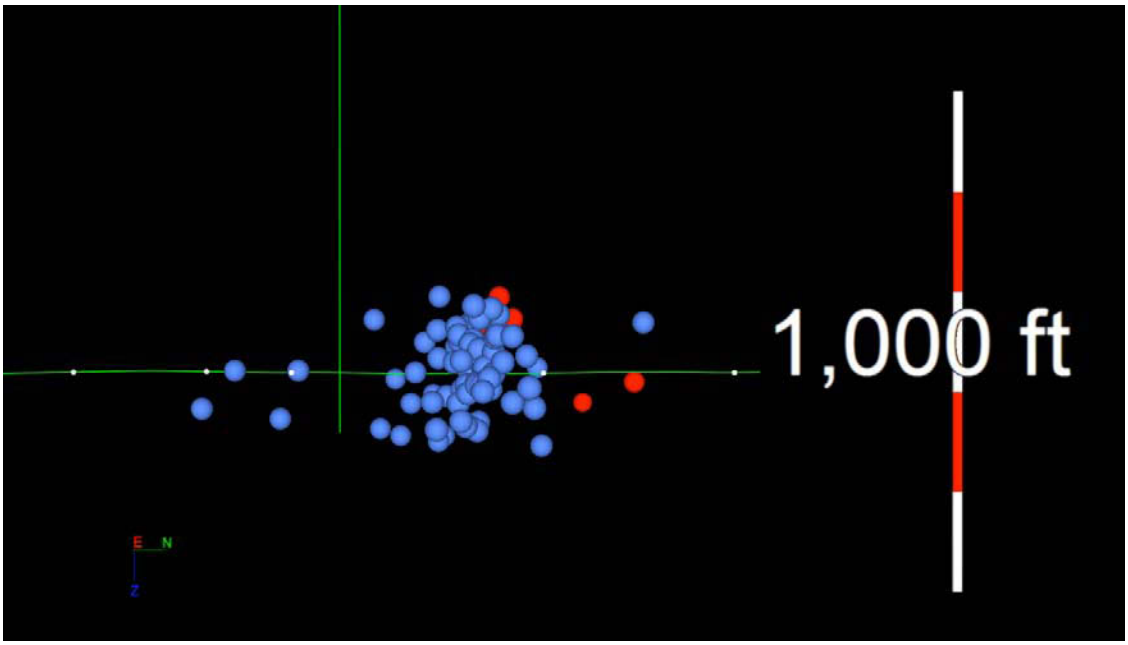

Figure 4.15: Side view of downhole (blue spheres) and surface (red spheres) microseismic recordings for Stage II. Microseismic activity above and below the horizontal treatment wellbore (in green) can be seen. The monitoring well is shown vertically in green.

4.1.3.4 Stage IV

The surface data shows events that are far west of the wellbore in a region where the downhole sensors did not record any events at all, as seen in Fig. 4.18. In combination, both data sets seem to give a more complete picture of microseismic activity and therefore fracture growth. The far surface events are expected to occur later than the downhole events that were closer to the wellbore, which is clearly proven by the time lapse playback. The surface data seems to be contained to Stage IV perforations, whereas most downhole events occur in an area that overlaps with the Stage III perforation cluster. The combined data gives a fracture height of 290 ft above the

wellbore, and 430 ft below it. As seen in Fig. 4.19 most height development occurs around the perforation cluster of the previous stage. The longitudinal stretch along the wellbore of the microseismic cloud can be observed at 1,220 ft. Half-lengths were observed with 1,950 ft west of the wellbore, and 1,080 ft east of it. The fracture azimuths of both data sets seem to be in good agreement, with 77 degrees from the downhole recordings, and 78 degrees from the surface data.

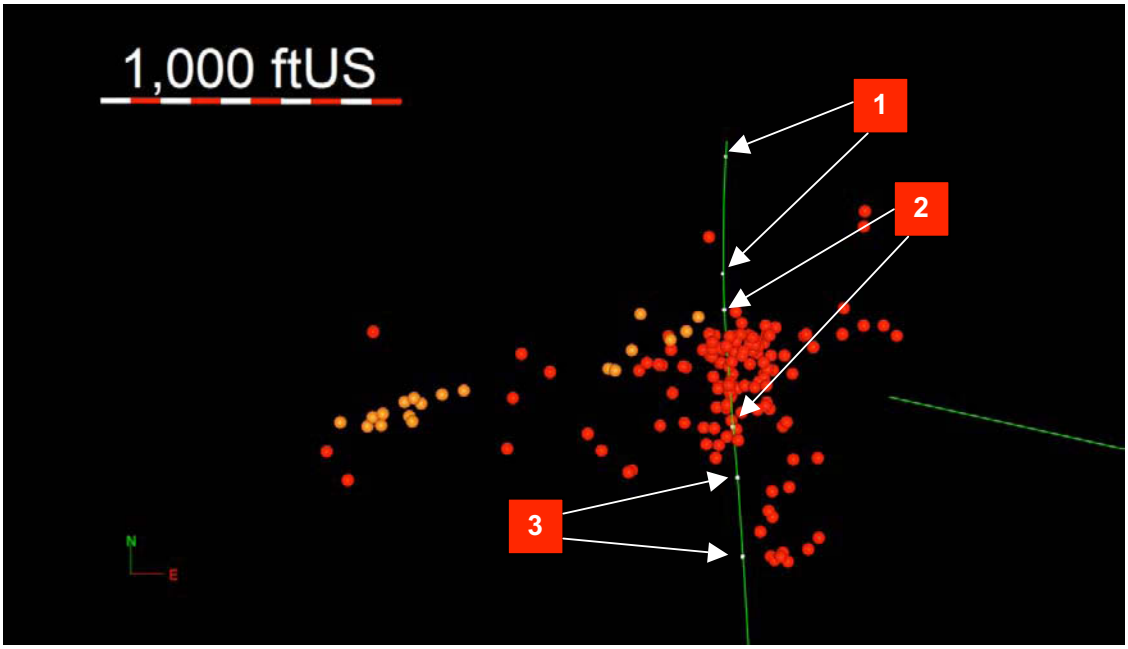

Figure 4.16: Downhole (red spheres) and surface (orange spheres) microseismic recordings for Stage III. The horizontal well trajectory of the treatment wellbore can be seen in green from south to north. The monitoring well can be seen in green east of the treatment well. Numbers mark stage perforation clusters.

4.1.3.5 Stage V

The surface data seems to be a lot more scattered for this stage than the downhole data. However, the main fracture that was observed from the surface microseismic seems to be in very good agreement with the fracture that is outlined by the downhole data in terms of fracture azimuth, as seen in Fig. 4.20. Both downhole and surface recordings show substantial microseismic activity in parts of the reservoir that have been fractured during the previous stages of the treatment. The fracture azimuths of both data sets seem to be matching well, with 75 degrees from the downhole microseismic and 78 degrees from the surface recordings. The dimensions of the

complete microseismic activity were clearly larger than the dimensions of just the main fracture. Overall fracture height was found to be 750 ft above the wellbore, and 630 below it, with a longitudinal stretch of 1,420 ft along the wellbore, as seen in Fig. 4.21. It can also be seen that most height development away from the Stage V perforation cluster. The western half-length was observed at 1,410 ft, with the eastern half-length being 1,170 ft. Considering only events associated with the main fracture gives a longitudinal stretch of 1,150 ft, with a fracture height of 710 ft above the wellbore, and 350 ft below it. Half-lengths were observed at 1,410 ft west of the wellbore, and 940 ft east of it.

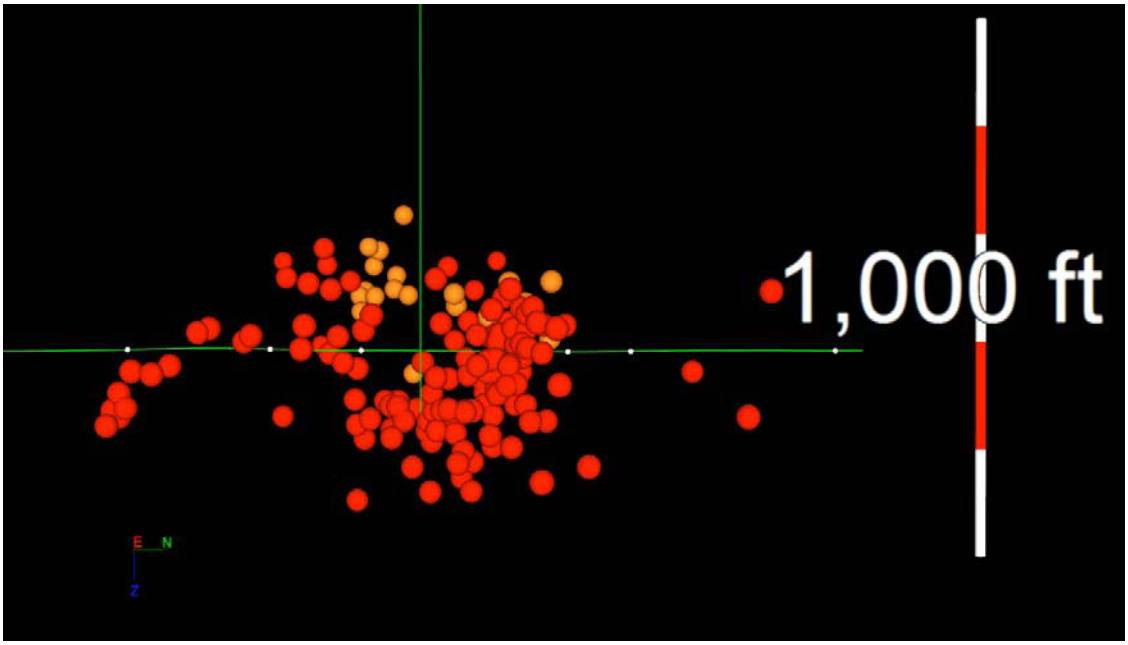

Figure 4.17: Side view of downhole (red spheres) and surface (orange spheres) microseismic recordings for Stage III. Microseismic activity above and below the horizontal treatment wellbore (in green) can be seen. The monitoring well is shown vertically in green.

4.1.3.6 Summary

In general, the surface data shows more upward growth than downward growth, which is contrary to the downhole recordings that show substantially more downward than upward growth. The models from Chapter III tend to agree with the downward growth depicted by the events recorded by the downhole sensors. Instead of assuming that either upward or downward growth has not been accurately captured by

the surface or downhole sensors, it might be more reasonable to expect a certain depth error associated with the data sets to be the reason for this. Looking at the data one might observe that the surface events have depth components, i.e. z-coordinates, that are too small, whereas the downhole events have depth components that are too large. It should be noted, though, that it is entirely possible that, even though both data sets have errors associated with them, the vertical location error can be larger for one data set than for the other.

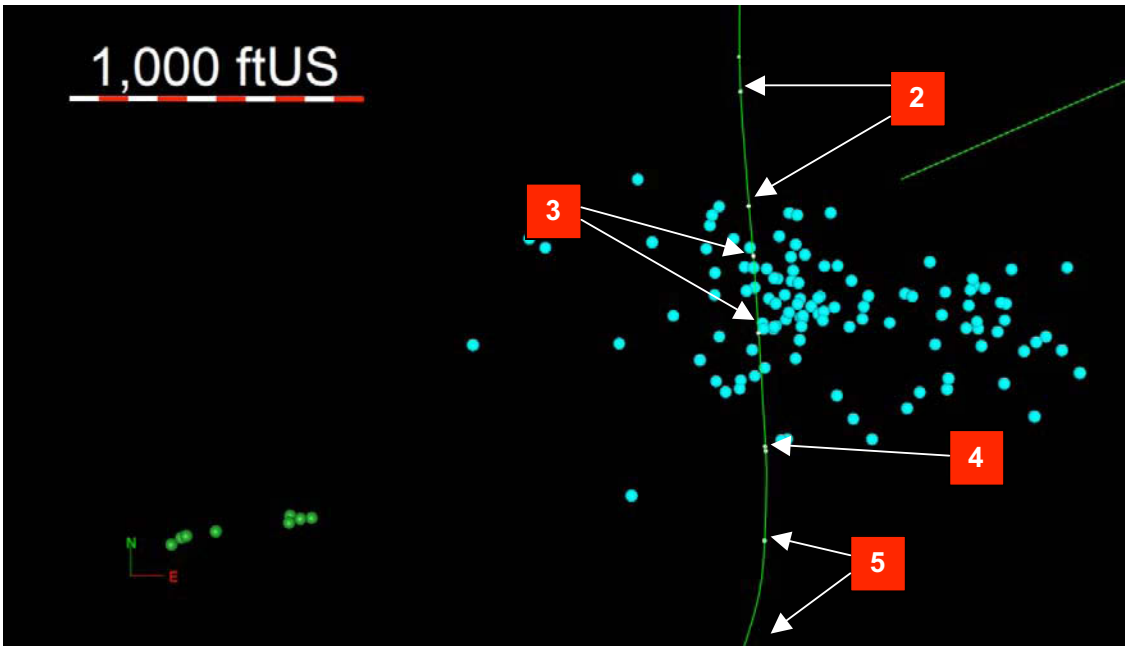

Figure 4.18: Downhole (turquoise spheres) and surface (green spheres) microseismic recordings for Stage IV. The horizontal well trajectory of the treatment wellbore can be seen in green from south to north. The monitoring well can be seen in green east of the treatment well. Numbers mark stage perforation clusters.

Events recorded by the surface sensors are of a generally larger magnitude than events included in the downhole data set. Time-lapse playback shows good agreement between surface and downhole data in terms of where large magnitude events occur, if visualized in a map view. Comparing the maximum distance between events and sensors, which is about 8,500 ft of vertical distance between the deepest event of the surface recordings and the surface, and about 1,900 ft between the observation wellbore and the farthest event of the downhole data set, this is no surprise.

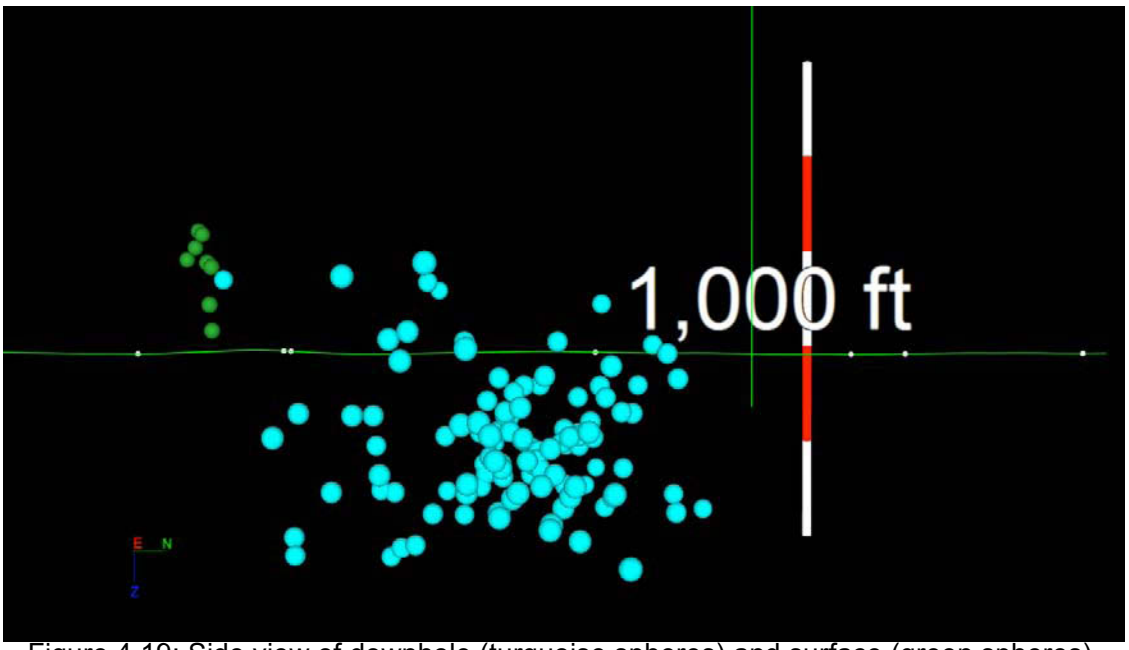

Figure 4.19: Side view of downhole (turquoise spheres) and surface (green spheres) microseismic recordings for Stage IV. Microseismic activity above and below the horizontal treatment wellbore (in green) can be seen. The monitoring well is shown vertically in green.

Table 4.3 gives an overview of fracture dimensions obtained from the combination of surface and downhole data, and Fig. 4.22 shows all microseismic events for all stages, including recordings from Stage III ½. Together with Table 4.4 depicting the difference in fracture geometry obtained from surface and downhole recordings, it is clear that each data set if analyzed on its own gives a fairly different picture of fracture growth, with average differences of hundreds of feet. If used together, as shown in Fig. 4.22, it can be seen that they overlap in certain regions and pick up on different things in others. However, it can also be seen that they complement each other very well and together give a more complete picture of fracture growth and stimulated reservoir volume.

4.2 Model Calibration

The second part of this chapter focuses on the difference in model calibration if the downhole or the surface data set is used exclusively. Two additional models were

built for each stage, one using the downhole data, and one using the surface data, which are then compared to each other as well as to the base case models that were calibrated using both data sets in Chapter III. Each data set in general has different inherent errors and will produce different results if used for the same purpose. Using either surface or downhole recordings exclusively to achieve a match with a simulation model will therefore result in a different calibration. The match achieved with surface data will have a different bias than the match achieved with downhole data. Assuming that the most accurate representation of reality can be achieved incorporating both data sets, the calibrated models will not only differ from each other but also from the base case. All pressure matches for both surface and downhole models can be found in Appendix B.

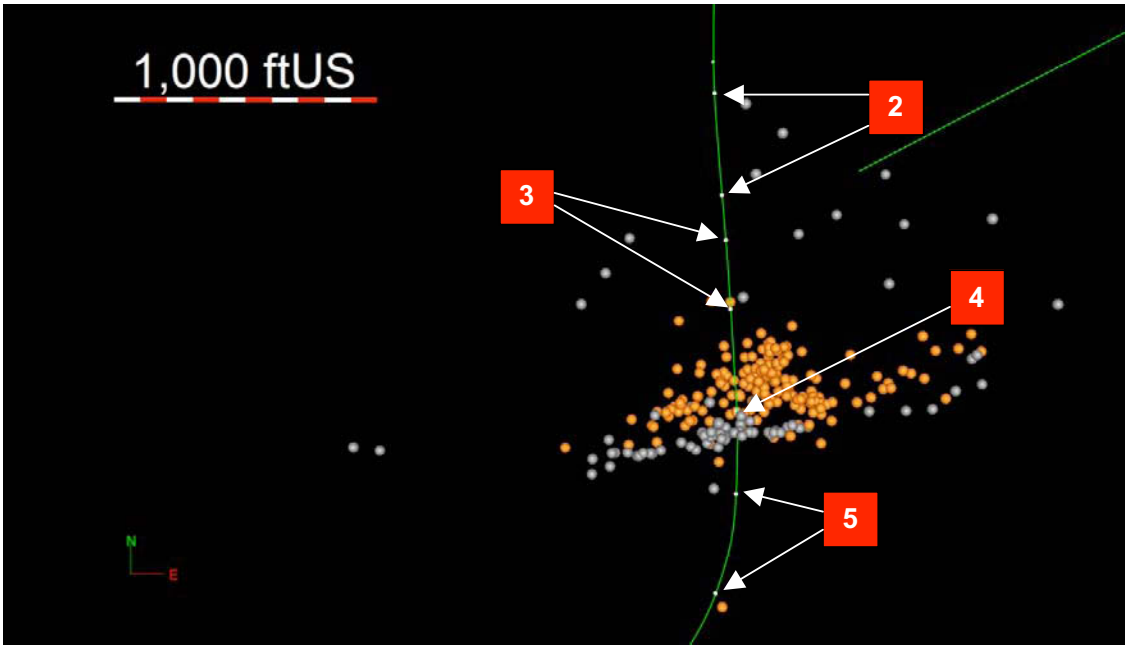

Figure 4.20: Downhole (orange spheres) and surface (grey spheres) microseismic recordings for Stage V. The horizontal well trajectory of the treatment wellbore can be seen in green from south to north. The monitoring well can be seen in green east of the treatment well. Numbers mark stage perforation clusters.

4.2.1 Surface

In order to match the fracture geometry that was obtained from surface microseismic data, models were built with GOHFER™ for each of the five monitored stages.

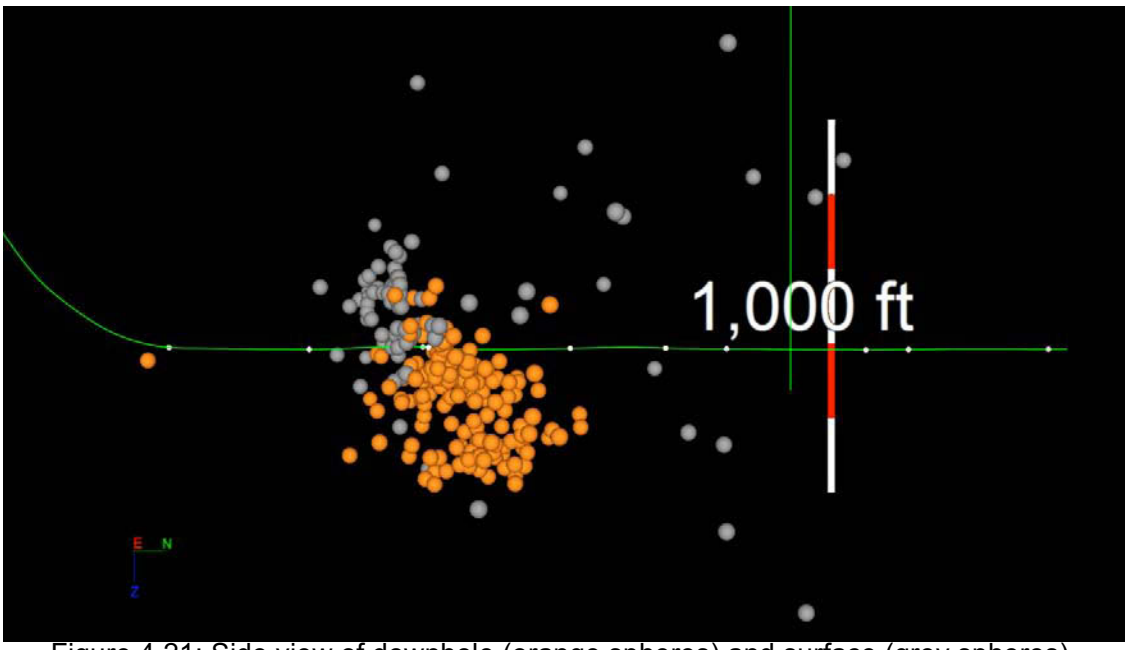

Figure 4.21: Side view of downhole (orange spheres) and surface (grey spheres) microseismic recordings for Stage V. Microseismic activity above and below the horizontal treatment wellbore (in green) can be seen. The monitoring well is shown vertically in green.

Table 4.3: Microseismic Activity from Surface and Downhole Recordings

Stage	*Perforation Interval [ft MD]*	*Number of Recorded Events [-]*	*Microseismic Activity*				
			Length (W/E of wellbore) [ft]	*Longitudinal Stretch [ft]*	*Height (above/below wellbore) [ft]*	*Fracture Azimuth [degrees]*	
						S	*D*
I	10,262 - 10,642	16	2,300 / 950	1,700	300 / 500	77	-
II	9,764 - 10,145	87	610 / 850	830	150 / 140	78	78
III	9,342 - 9,598	151	1,320 / 560	1,100	260 / 290	77	76
IV	8,951 - 8,966	121	1,950 / 1,080	1,220	290 / 430	78	77
V	8,273 - 8,653	254	1,410 / 1,170	1,420	750 / 630	78	75

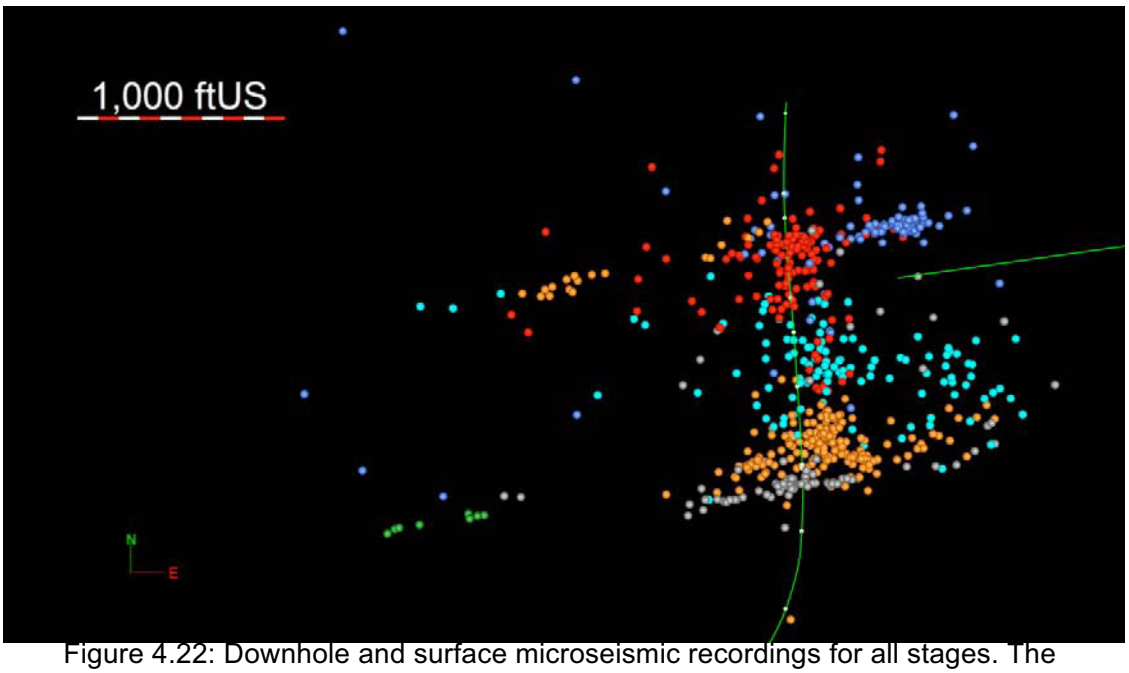

Figure 4.22: Downhole and surface microseismic recordings for all stages. The respective events and perforation intervals are shown in Figs. 4.2 through 4.7 and Figs. 4.9 through 4.12.The horizontal well trajectory of the treatment wellbore can be seen from south to north. The monitoring well can be seen east of the treatment well.

4.2.1.1 Longitudinal Models

As discussed in Section 3.5, matching is done with two types of models: a longitudinal and a transverse representation of the wellbore. The longitudinal direction allows for modeling the longitudinal stretch along the wellbore of the fracture network.

4.2.1.1.1 Stage I

PDMSF was set to 0.0045 1/psi, PDL to 0.00025 1/psi, and tectonic strain for the Woodford Shale to 70 microstrains. The Tortuosity Pre-Factor was set to 0.15 psi/bpm^2. The perforation coefficient was decreased from the default value to 0.37, with a friction factor of 0.03 in order to achieve a match. TSC was adjusted to 0.00025. Treatment tubing length was set to the measured depth until the first perforation, which was 10,262 ft for this stage.

Table 4.4: Difference between Surface and Downhole Data Set Regarding Fracture Geometry Parameters

Stage	*Total Length [ft]*			*Longitudinal Stretch [ft]*			*Height [ft]*		
	S	*D*	*Difference*	*S*	*D*	*Difference*	*S*	*D*	*Difference*
I	3,250	-	-	1,700	-	-	800	-	-
II	870	1,400	530	300	810	510	240	280	40
III	1,270	1,880	610	360	1,100	740	320	480	160
IV	1,950	2,000	50	90	1,060	970	290	620	330
V	2,580	1,570	1,010	1,420	1,150	270	1,380	510	870

Average Difference:	550	*Average Difference:*	623	*Average Difference:*	350

The perforation factor was set to 0.35 for the interval from the beginning of the treatment on Dec. 10th, 2007, at 07:15:47 to 07:37:56. For the next interval until 07:40:06 the perforation factor was increased to 0.45 as the resistance to fluid injection decreases. It was then further increased to 0.57 until 07:47:09 to make the increase more gradual. During the injection of the first two slugs of 100-mesh sand it was increased to 0.62 until 08:12:56. Between the second and the third slug of proppant with a concentration of 0.75 lbm/gal, the factor was set to 0.38 until 08:16:31 and then further decreased to 0.35 until the end of the treatment at about 10:29:00.

The surface microseismic data showed that the main fracture has a longitudinal dimension of about 630 ft, and a height of about 630 ft. Microseismic activity was not well contained to Stage I perforations. The above parameters led to a simulated longitudinal stretch of fracturing activity of 500 ft, and a simulated height of 150 ft.

4.2.1.1.2 Stage II

PDMSF was set to 0.0014 1/psi, PDL to 0.0019 1/psi, and tectonic strain for the Woodford Shale to 75 microstrains. The Tortuosity Pre-Factor was set to 0.15 psi/bpm^2. The perforation coefficient was decreased from the default value to 0.3, with a friction factor of 0.05 in order to achieve a match. TSC was set to 0.0019. Treatment tubing length was set to the measured depth until the first perforation, which was 9,764 ft for this stage.

The perforation factor was set to 0.45 for the first interval from the beginning of the treatment on Dec. 10th, 2007, at about 14:26:30 until 14:50:00. It was then increased to 0.6 for the next interval until 15:18:27, after the first slug of 0.25 lbm/gal 100-mesh is pumped. For the next interval until the onset of the third slug being pumped at 0.75 lbm/gal at 15:24:34 it was set to 0.25. It was then further decreased to 0.20 until after the third slug was pumped at 15:27:00, to 0.19 until 16:09:55 (beginning of pumping the sixth slug of 30/70 sand), to 0.17 until 16:19:46 (beginning of seventh slug of 30/70 sand), to 0.16 until 16:20:39 (during pumping the seventh slug of 30/70 sand), to 0.15 until 16:31:13 (during pumping the eight slug of 30/70 sand), to 0.14 until 16:39:34 (beginning of pumping the ninth slug of 30/70 sand), to 0.12 until 16:49:25 (beginning of pumping the tenth slug of 30/70 sand), to 0.11 until 17:12:08 (beginning of pumping the thirteenth slug of 30/70 sand), and finally to 0.09 until the end of the treatment at about 17:34:00.

From the surface microseismic data it could be seen that the microseismic cloud has a longitudinal dimension of about 300 ft, and a height of about 240 ft. The longitudinal stretch along the wellbore was simulated for this stage with 400 ft with a height of 150 ft.

4.2.1.1.3 Stage III

PDMSF was set to 0.002 1/psi, PDL to 0.0015 1/psi, and tectonic strain for the Woodford Shale to 70 microstrains. The Tortuosity Pre-Factor was set to 0.10 psi/bpm^2. The perforation coefficient was decreased from the default value to 0.24, with a friction factor of 0.06 in order to achieve a match. TSC was set to 0.0015. Treatment tubing length was set to the measured depth until the first perforation, which was 9,342 ft for this stage.

The perforation factor for the first interval from the beginning of the job on Dec. 11th, 2007, at about 07:02:50 until 07:20:14 was set to 0.55. Until the pumping of the first slug at 0.25 lbm/gal is completed at 07:51:23 the factor was increased to 0.83. Until after the second slug with 0.50 lbm/gal is pumped at 07:57:09 it was set to 0.32, to be further lowered to 0.20 until the end of the treatment at about 10:08:00.

From the surface microseismic data, it could be seen that the microseismic cloud has a longitudinal dimension of about 360 ft, and a height of about 320 ft. As explained in the analysis of the surface data, the microseismic activity of Stage III of this treatment mostly overlapped with the region around Stage II perforations. Since the already weakened reservoir around the Stage II perforation cluster could not be modeled accurately, the height could only be simulated with 150 ft. Longitudinal stretch however was modeled more accurately at 300 ft.

4.2.1.1.4 Stage IV

PDMSF was set to 0.002 1/psi, PDL to 0.0015 1/psi, and tectonic strain for the Woodford Shale to 80 microstrains. The Tortuosity Pre-Factor was set to 0.10 psi/bpm^2. TSC was adjusted to 0.0015. The perforation coefficient was decreased from the default value to 0.25, with a friction factor of 0.07 in order to achieve a pressure match. Treatment tubing length was set to the measured depth until the first perforation, which was 8,951 ft for this stage.

From the beginning of the treatment on Dec. 11th, 2007, at about 13:18:00 until right after the first pressure peak, the perforation factor was set to 0.69. The factor was increased to 0.77 until after the first slug of 100-mesh sand at 0.25 lbm/gal was pumped at 14:08:18. It was then substantially decreased to 0.0.40 until the middle of pumping the second slug of 100-mesh sand at 0.5 lbm/gal at 14:12:00 to accurately match the simulated pressure to the observed one. From there on the factor had to be gradually decreased until the end of the treatment. Until the beginning of the eighth slug of 30/70 proppant at 0.8 lbm/gal at 15:22:20 it was set to 0.30. It was then further decreased to 0.22 until the end of the treatment at about 16:26:00.

Microseismic activity for this stage was confined along a single growing fracture, leading to a very small longitudinal stretch of about 90 ft with a height of 290 ft. The longitudinal dimension was simulated at 80 ft, and the height at 150 ft.

4.2.1.1.5 Stage V

PDMSF was set to 0.0032 1/psi, PDL to 0.001 1/psi, and TSC to 0.001 as well. The Tortuosity Pre-Factor was set to 0.15 psi/bpm^2. The perforation coefficient was only slightly decreased from the default value to 0.53, with a friction factor of 0.09 in order to achieve a pressure match. Treatment tubing length was set to the measured depth until the first perforation, which was 8,273 ft for this stage.

The tectonic strain was adjusted to 120 microstrains. Every stage sees the stress changes in the reservoir that were caused by previous fracturing stages. Since Stage V is the last one it sees the most stress change, causing the stress regime to be slightly different from the previous stages.

The initial perforation factor was set to 0.55 for the first interval from the beginning of the treatment on Dec. 12th, 2007, at about 07:09:00 until 07:36:47. With continued injection the perforation factor was increased to 0.58 until 07:41:17. It was then increased further to 0.60 until after the first slug of 100-mesh sand at 0.25 lbm/gal at 07:58:46. The factor was then set to 1.00 until the end of the treatment at about 10:18:00, since further adjustment of it showed no difference in pressure behavior at all.

For this stage all of the microseismic activity except for one single event occurred around Stage IV perforations. The height of the main fracture is about 1,040 ft, with a longitudinal stretch of about 500 ft. The dimensions could be matched with a simulated length of 700 ft, and a simulated height of 240 ft.

4.2.1.2 Transverse Models

As discussed in Section 3.5, matching is done with two types of models: a longitudinal and a transverse representation of the wellbore. The perpendicular direction allows for modeling the length of the transverse fractures. Since GOHFER^{TM} simulates symmetrical fracture growth in this situation, the longer half-length was doubled and used as a total length in the simulations.

4.2.1.2.1 Stage I

PDMSF was set to 0.002 1/psi, PDL to 0.0005 1/psi, and tectonic strain for the Woodford Shale to 50 microstrains. The Tortuosity Pre-Factor was set to 0.10 psi/bpm^2. The perforation coefficient was decreased from the default value to 0.42, with a friction factor of 0.03 in order to achieve a match. TSC was adjusted to 0.0005. Treatment tubing length was set to the measured depth of the center of the perforation cluster, which was 10,452 ft for this stage.

The perforation factor for this stage needed a lot of fine-tuning. From the beginning of the treatment on Dec. 10th, 2007, at 07:15:47 until 07:37:56 it was set to 0.30, and then further increased to 0.45 until 07:40:06, to 0.51 until 07:49:09, and to 0.55 until 08:12:56. From then on the factor was decreased. First to 0.28 until 08:16:31, and then in a more gradual fashion to 0.24 until 09:07:47, to 0.22 until 09:12:28, to 0.20 until 09:27:52, to 0.18 until 09:32:33, to 0.15 until 09:42:41, to 0.12 until 09:57:53, and finally to 0.10 until the end of the treatment at about 10:29:00.

The microseismic activity for this stage was very scattered, and therefore a main fracture with a height of 630 ft, and a half-length of 2,100 ft west of the wellbore, and 960 ft east of it was identified. To model the complete length of 4,200 ft, 1,000 ft of additional grid were added left and right of the end of initial grid. Fracture length was simulated with 3,580 ft and height with 250 ft.

4.2.1.2.2 Stage II

PDMSF was set to 0.005 /psi, PDL to 0.0004 /psi, TSC to 0.00033, and tectonic strain for the Woodford Shale to 65 microstrains. The Tortuosity Pre-Factor was set to 0.15 psi/bpm^2. The perforation coefficient was decreased from the default value to 0.32, with a friction factor of 0.05 in order to achieve a pressure match. Treatment tubing length was set to the measured depth of the center of the perforation cluster, which was 9,342 ft for this stage.

The perforation factor was set to 0.45 for the first interval from the beginning of the treatment on Dec. 10th, 2007, at about 14:26:30 until 14:50:00. It was then increased to 0.6 for the next interval until 15:18:27, after the first slug of 0.25 lbm/gal 100-mesh is

pumped. For the next interval until the onset of the third slug being pumped at 0.75 lbm/gal at 15:24:34 it was set to 0.25. It was then further decreased to 0.20 until after the third slug was pumped at 15:27:00, to 0.19 until 16:09:55 (beginning of pumping the sixth slug of 30/70 sand), to 0.17 until 16:19:46 (beginning of seventh slug of 30/70 sand), to 0.16 until 16:20:39 (during pumping the seventh slug of 30/70 sand), to 0.15 until 16:31:13 (during pumping the eight slug of 30/70 sand), to 0.14 until 16:39:34 (beginning of pumping the ninth slug of 30/70 sand), to 0.12 until 16:49:25 (beginning of pumping the tenth slug of 30/70 sand), to 0.11 until 17:12:08 (beginning of pumping the thirteenth slug of 30/70 sand), and finally to 0.09 until the end of the treatment at about 17:34:00.

The surface microseismic data showed a fracture half-length of 610 ft east of the wellbore, and 260 ft west of it. The total modeled fracture length that was used in the match was 1,220 ft. Activity was well contained to Stage II perforations with a height of about 240 ft. Fracture length was simulated with 1,350 ft, and height with 240 ft.

4.2.1.2.3 Stage III

PDMSF was set to 0.001 1/psi, PDL to 0.001 1/psi, TSC to 0.001, and tectonic strain for the Woodford Shale to 50 microstrains. The Tortuosity Pre-Factor was set to 0.10 psi/bpm^2. The perforation coefficient was decreased from the default value to 0.24, with a friction factor of 0.06 in order to achieve a pressure match. Treatment tubing length was set to the measured depth of the center of the perforation cluster, which was 9,342 ft for this stage.

The perforation factor for the first interval from the beginning of the job on Dec. 11th, 2007, at about 07:02:50 until 07:20:14 was set to 0.55. Until the pumping of the first slug at 0.25 lbm/gal is completed at 07:51:23 the factor was increased to 0.81, and then decreased to 0.23 until after the second slug with 0.50 lbm/gal is pumped at 07:57:09. It was then further lowered to 0.17 until the end of the treatment at about 10:08:00.

The microseismic cloud showed fracture half-lengths of 1,270 ft west of the wellbore, without any activity east of it, giving a total fracture length to simulate of 2,540

ft, and a height of 320 ft. Whereas the height seemed to be inaccurately modeled at 250 ft like for all the other models, the length was simulated with 2,260 ft.

4.2.1.2.4 Stage IV

PDMSF was set to 0.002 1/psi, PDL to 0.0005 1/psi, TSC to 0.0005, and tectonic strain for the Woodford Shale to 50 microstrains. The Tortuosity Pre-Factor was set to 0.10 psi/bpm^2. The perforation coefficient was decreased from the default value to 0.25, with a friction factor of 0.07. Treatment tubing length was set to the measured depth of the center of the perforation cluster, which was 8,958.5 ft for this stage.

From the beginning of the treatment on Dec. 11th, 2007, at about 13:18:00 until right after the first pressure peak the perforation factor was set to 0.65 until 13:39:22. It was increased to 0.72 until after the first slug of 100-mesh sand at 0.25 lbm/gal was pumped at 14:08:18, and then substantially decreased to 0.27 until during pumping the second slug of 100-mesh sand at 0.5 lbm/gal at 14:12:00. From there on the factor had to be gradually decreased until the end of the treatment. It was set to 0.22 until 15:11:41 (beginning of pumping the seventh slug of 30/70 sand), to 0.19 until 15:22:00 (beginning of pumping the eighth slug of 30/70 sand), to 0.15 until 15:30:26 (beginning of pumping the ninth slug of 30/70 sand), to 0.14 until 15:42:42 (during pumping the tenth slug of 30/70 sand), to 0.12 until 15:53:04 (after pumping the eleventh slug of 30/70 sand), and finally to 0.09 until the end of the treatment at about 16:26:00.

The surface microseismic data showed a fracture half-length of 1,950 ft extending to the west side of the treatment well only, and a height of 290 ft. The total fracture length used for the match was therefore 3,900 ft. The simulated fracture length was 3,440 ft, which is very close to the fracture length obtained from the microseismic data, with a simulated height of 250 ft.

4.2.1.2.5 Stage V

PDMSF was set to 0.002 1/psi, PDL to 0.001 1/psi, and TSC to 0.001. The Tortuosity Pre-Factor was set to 0.15 psi/bpm^2. The perforation coefficient was only

slightly decreased from the default value to 0.53, with a friction factor of 0.09. Treatment tubing length was set to the measured depth of the center of the perforation cluster, which was 8,273 ft for this stage. As for the longitudinal model for the finals stage the tectonic strain had to be slightly increased to 140 microstrains to account for the effects of stress shadowing, resulting in a higher in-situ stress.

The perforation factor was adjusted to 0.45 for the first interval from the beginning of the treatment on Dec. 12th, 2007, at about 07:09:00 until 07:36:47, and was increased to 0.49 until 07:41:17. It was then increased further to 0.59 until after pumping the first slug of 100-mesh sand at 0.25 lbm/gal at 07:58:46. After this it was decreased to 0.34 until after pumping the third slug of 100-mesh sand at 0.75 lbm/gal at 08:10:28. After that the factor was set to 0.31 until 08:57:00 (during pumping the sixth slug of 30/70 sand), and finally to 0.27 until the end of the treatment at about 10:18:00.

As mentioned above, all of the microseismic activity for this stage occurred around Stage IV perforations with a height of the main fracture of about 1,040 ft, and fracture half-lengths of 1,410 ft east of the wellbore, and 1,170 ft west of it, giving a total fracture length of 2,820 ft. Again, the fracture length could be very well matched with 2,140 ft. The height on the other hand, due to the fact that microseismic activity actually occurred in an already fractured part of the reservoir was not very well matched with 240 ft.

4.2.1.3 Summary

Tables 4.5 and 4.6 give an overview of the model parameters for the surface matches of the longitudinal and the transverse model, respectively.

Mohammad reports in her thesis from 2009 a fairly large difference between the microseismic and the simulated fracture dimensions, both over- and under-estimating geometry components, with average values of about 32% for the fracture length and about 54% for fracture height, for a surface monitored well. Simulated parameters deviate up to -67% for length, and up to -203% for height.

Table 4.7 gives an overview of the microseismic and simulated fracture dimensions. Both data sets clearly show that the microseismic activity recorded during

one stage usually overlaps with the region around the perforations of the previous stage. Fracture growth for each stage, and therefore microseismicity seem to be dominated by pre-existing structures, i.e. the fracture network from the previous stage as well as natural fractures. Modeling cannot accurately account for the already fractured and therefore weakened reservoir around the previous stage.

Table 4.5: Model Parameter Overview for Longitudinal Surface Microseismic Models

	Stage I	*Stage II*	*Stage III*	*Stage IV*	*Stage V*
PDMSF [1/psi]	0.004	0.0014	0.002	0.002	0.0032
PDL [1/psi]	0.0003	0.0019	0.0015	0.0015	0.001
TSC [-]	0.0003	0.0019	0.0015	0.0015	0.001
Tort. Pre-Factor [psi/bpm^2]	0.15	0.15	0.10	0.10	0.15
Tectonic Strain [microstrains]	70	75	70	80	120
Perf. Coeff. [-]	0.37	0.3	0.24	0.25	0.53
Frict. Coeff. [-]	0.03	0.05	0.06	0.07	0.09
Perf. Factor [-]	0.35 *(07:15:47-07:37:56)* 0.45 *(07:37:57-07:40:06)* 0.57 *(07:40:07-07:49:09)* 0.62 *(07:49:10-08:12:56)* 0.39 *(08:12:57-08:16:31)* 0.35 *(08:16:32-10:29:00)*	0.45 *(14:26:30-14:50:00)* 0.60 *(14:50:01-15:18:27)* 0.35 *(15:18:28-15:24:34)* 0.30 *(15:24:35-15:27:00)* 0.25 *(15:27:01-17:34:00)*	0.55 *(07:02:50-07:20:14)* 0.83 *(07:20:15-07:51:23)* 0.32 *(07:51:24-07:57:09)* 0.20 *(07:57:10-10:08:00)*	0.69 *(13:18:00-13:39:22)* 0.77 *(13:39:23-14:08:18)* 0.40 *(14:08:19-14:12:00)* 0.30 *(14:12:01-15:22:20)* 0.22 *(15:22:21-16:26:00)*	0.55 *(07:09:00-07:36:47)* 0.58 *(07:36:48-07:41:17)* 0.6 *(07:41:18-07:58:46)* 1.00 *(07:58:47-10:18:00)*

It should be noted that due to symmetry reasons for the hydraulic fracture models, the total length is double the longest half-length, like it was used as matching parameter in the models. It can be seen that both length and longitudinal stretch could be very well matched for all stages with average deviations of only -10% and -5%, respectively. Height on the other hand could not successfully be matched for all stages,

as seen with the average deviations of -59% for the longitudinal models, and -35% for the transverse models. Except for Stage II which was very well contained to Stage II perforations, every stage fractured into the region of the formation that has already been stimulated by the previous stage, which the specific models used in this thesis could not accurately account for. This is discussed more in detail in Section 8.1. The fracture height that was obtained from Stage II can be used as a representative value for the un-stimulated reservoir. Since this height could be very well matched with the model, it shows that the geological set-up of the model was fairly accurate.

4.2.2 Downhole

In order to match the fracture geometry that was obtained from downhole microseismic data, models were built with GOHFER^{TM} for each of the four monitored stages.

4.2.2.1 Longitudinal Models

As discussed in Section 3.5, matching is done with two types of models: a longitudinal and a transverse representation of the wellbore. The longitudinal direction allows for modeling the longitudinal stretch along the wellbore of the fracture network.

4.2.2.1.1 Stage II

PDMSF was set to 0.005 1/psi, PDL to 0.0003 1/psi, and tectonic strain for the Woodford Shale to 65 microstrains. The Tortuosity Pre-Factor was set to 0.15 psi/bpm^2. The perforation coefficient was decreased from the default value to 0.3, with a friction factor of 0.05 in order to achieve a match. TSC was adjusted to 0.00029. Treatment tubing length was set to the measured depth until the first perforation, which was 9,764 ft for this stage.

The perforation factor was set to 0.45 for the first interval from the beginning of the treatment on Dec. 10th, 2007, at about 14:26:30 until 14:50:00. The factor was then

increased to 0.6 for the next interval until 15:18:27, after the first slug of 0.25 lbm/gal 100-mesh is pumped, as seen in Fig. 3.2. For the next interval until the onset of the third slug being pumped at 0.75 lbm/gal at 15:24:34 it was set to 0.35. It was then further decreased to 0.3 until after the third slug was pumped at 15:27:00. From then on until the end of the treatment at about 17:34:00 it was set to 0.25.

The downhole microseismic data showed that the microseismic cloud has a longitudinal dimension of about 810 ft, and a height of about 280 ft. Microseismic activity was well contained to Stage II perforations. Above parameters led to a simulated longitudinal stretch of fracturing activity of about 790 ft, and a simulated height of about 240 ft.

4.2.2.1.2 Stage III

PDMSF was set to 0.002 1/psi, PDL to 0.0015 1/psi, and tectonic strain for the Woodford Shale to 45 microstrains. The Tortuosity Pre-Factor was set to 0.10 psi/bpm^2. The perforation coefficient was decreased from the default value to 0.24, with a friction factor of 0.06 in order to achieve a match. TSC was set to 0.0015. Treatment tubing length was set to the measured depth until the first perforation, which was 9,342 ft for this stage.

The perforation factor for the first interval from the beginning of the job on Dec. 11th, 2007, at about 07:02:50 until 07:20:14 was set to 0.55. Until the pumping of the first slug at 0.25 lbm/gal is completed at 07:51:23 the factor was increased to 0.83. Until after the second slug with 0.50 lbm/gal is pumped at 07:57:09 it was set to 0.32, to be further lowered to 0.20 until the end of the treatment at about 10:08:00.

From the downhole microseismic data, it could be seen that the microseismic cloud has a longitudinal dimension of about 1,100 ft, and a height of about 480 ft. As explained above in the analysis of the downhole data, the microseismic activity of Stage III of this treatment mostly overlaps with the region around Stage II perforations. Looking at the Stage III perforations, as seen in Fig. 4.23, it is obvious that the fracture height for this part of the reservoir is substantially lower, with about 270 ft. Since the already weakened reservoir around the Stage II perforation cluster could not be modeled

accurately, this height was used for achieving the match. The longitudinal stretch along the wellbore was simulated for this stage with 1,100 ft with a height of 240 ft.

4.2.2.1.3 Stage IV

PDMSF was set to 0.0025 1/psi, PDL to 0.0018 1/psi, and tectonic strain for the Woodford Shale to 55 microstrains. The Tortuosity Pre-Factor was set to 0.10 psi/bpm^2. TSC was adjusted to 0.0018. The perforation coefficient was decreased from the default value to 0.25, with a friction factor of 0.07 in order to achieve a pressure match. Treatment tubing length was set to the measured depth until the first perforation, which was 8,951 ft for this stage.

In general, the perforation factor for this stage shows the same pattern as for the previous stages. From the beginning of the treatment on Dec. 11th, 2007, at about 13:18:00 until right after the first pressure peak, as seen in Fig. 3.4, it was set to 0.69. The factor was increased to 0.77 until after the first slug of 100-mesh sand at 0.25 lbm/gal was pumped at 14:08:18. It was then substantially decreased to 0.35 until the middle of pumping the second slug of 100-mesh sand at 0.5 lbm/gal at 14:12:00 to accurately match the simulated pressure to the observed one. From there on the factor had to be gradually decreased until the end of the treatment. Until the beginning of the eighth slug of 30/70 proppant at 0.8 lbm/gal at 15:22:20 it was set to 0.25. It was then further decreased to 0.20 until the beginning of the ninth slug of 30/70 proppant at 0.9 lbm/gal at 15:30:26; then to 0.18 until the middle of the tenth slug of 30/70 sand at 1.0 lbm/gal at 15:42:42; further to 0.16 until the eleventh slug of 30/70 at 1.1 lbm/gal was pumped at 15:53:04; and finally to 0.13 until the end of the treatment at about 16:26:00.

The downhole microseismic data showed a longitudinal dimension of 1,060 ft and a height of 620 ft. As for Stage III, most of the microseismic activity occurs around the perforation cluster of the previous stage, rather than around Stage IV perforations. The height of the cloud of microseismic activity at Stage IV perforations is about 570 ft, with a substantial amount of apparent downward growth. This downward growth could not be well simulated by the model, as it only simulates a height of 240 ft, which seems to be a consistent number, and probably related to the geological set-up of the model.

The longitudinal stretch on the other hand was very well matched with a simulated length of 1,010 ft.

4.2.2.1.4 Stage V

For the final stage, PDMSF was set to 0.0035 1/psi, PDL to 0.0009 1/psi, and TSC to 0.0009 as well. The Tortuosity Pre-Factor was set to 0.15 psi/bpm^2. The perforation coefficient was only slightly decreased from the default value to 0.53, with a friction factor of 0.09 in order to achieve a pressure match. Treatment tubing length was set to the measured depth until the first perforation, which was 8,273 ft for this stage.

The tectonic strain was adjusted to 130 microstrains. Every stage sees the stress changes in the reservoir that were caused by previous fracturing stages. Since Stage V is the last one it sees the most stress change, causing the stress regime to be slightly different from the previous stages.

The initial perforation factor was set to 0.55 for the first interval from the beginning of the treatment on Dec. 12th, 2007, at about 07:09:00 until 07:36:47. With continued injection the perforation factor was increased to 0.58 until 07:41:17. It was then increased further to 0.60 until after the first slug of 100-mesh sand at 0.25 lbm/gal at 07:58:46. The factor was then set to 1.00 until the end of the treatment at about 10:18:00, since further adjustment of it showed no difference in pressure behavior at all.

For this stage, all of the microseismic activity except for one single event occurred around Stage IV perforations. The height of the microseismic cloud is about 510 ft, with a longitudinal stretch of about 1,150 ft. With only one event at Stage V perforations it was difficult to assess the height of the fractured zone, so matching the height was not the primary concern for this stage. However, since 240 ft seemed to be a number that geological set-up in this model produced a lot, the parameters were adjusted in order to produce a height somewhere in this range. Again, the longitudinal dimension could be very well matched with a simulated length of 1,060 ft, and a simulated height of 240 ft.

Table 4.6: Model Parameter Overview for Transverse Surface Microseismic Models

	Stage I	*Stage II*	*Stage III*	*Stage IV*	*Stage V*
PDMSF [1/psi]	0.002	0.005	0.001	0.002	0.002
PDL [1/psi]	0.0005	0.0004	0.001	0.0005	0.001
TSC [-]	0.0005	0.00033	0.001	0.0005	0.001
Tort. Pre-Factor [psi/bpm^2]	0.10	0.15	0.10	0.10	0.15
Tectonic Strain [microstrains]	50	65	50	50	140
Perf. Coeff. [-]	0.42	0.32	0.24	0.25	0.53
Frict. Coeff. [-]	0.03	0.05	0.06	0.07	0.09
Perf. Factor [-]	0.30 *(07:15:47-07:37:56)* 0.45 *(07:37:57-07:40:06)* 0.51 *(07:40:07-07:49:09)* 0.55 *(07:49:10-08:12:56)* 0.28 *(08:12:57-08:16:31)* 0.24 *(08:16:32-09:07:47)* 0.22 *(09:07:48-09:12:28)* 0.20 *(09:12:29-09:27:52)* 0.18 *(09:27:53-09:32:33)* 0.15 *(09:32:34-09:42:41)* 0.12 *(09:42:42-09:57:53)* 0.10 *(09:57:54-10:29:00)*	0.45 *(14:26:30-14:50:00)* 0.60 *(14:50:01-15:18:27)* 0.25 *(15:18:28-15:24:34)* 0.20 *(15:24:35-15:27:00)* 0.19 *(15:27:01-16:09:55)* 0.17 *(16:09:56-16:19:46)* 0.16 *(16:19:47-16:20:39)* 0.15 *(16:20:40-16:31:13)* 0.14 *(16:31:14-16:39:34)* 0.12 *(16:39:35-16:49:25)* 0.11 *(16:49:26-17:12:08)* 0.09 *(17:12:09-17:34:00)*	0.55 *(07:02:50-07:20:14)* 0.81 *(07:20:15-07:51:23)* 0.23 *(07:51:24-07:57:09)* 0.17 *(07:57:10-10:08:00)*	0.65 *(13:18:00-13:39:22)* 0.72 *(13:39:23-14:08:18)* 0.27 *(14:08:19-14:12:00)* 0.22 *(14:12:01-15:11:41)* 0.19 *(15:11:42-15:22:00)* 0.13 *(15:22:01-15:30:26)* 0.12 *(15:30:27-15:42:42)* 0.10 *(15:42:43-15:53:04)* 0.07 *(15:53:05-16:26:00)*	0.45 *(07:09:00-07:36:47)* 0.49 *(07:36:48-07:41:17)* 0.54 *(07:41:18-07:58:46)* 0.34 *(07:58:47-08:10:28)* 0.31 *(08:10:29-08:57:00)* 0.27 *(08:57:01-10:18:00)*

Table 4.7: Comparison of Fracture Dimensions for Surface Microseismic Models

Stage	*Fracture Length [ft]*			*Longitudinal Stretch of Fractured Zone [ft]*		
	Microseismic	*Simulated*	*Difference*	*Microseismic*	*Simulated*	*Difference*
I	4,200	3,580	-15%	630	500	-21%
II	1,220	1,350	11%	300	400	33%
III	2,540	2,260	-11%	360	300	-17%
IV	3,900	3,440	-12%	90	80	-11%
V	2,820	2,140	-24%	500	700	40%
	Average Difference:		-10%	*Average Difference:*		5%

Stage	*Height from longitudinal models [ft]*			*Height from transverse models [ft]*		
	Microseismic	*Simulated*	*Difference*	*Microseismic*	*Simulated*	*Difference*
I	630	150	-76%	630	250	-60%
II	240	150	-38%	240	240	0%
III	320	150	-53%	320	250	-22%
IV	290	150	-48%	290	250	-14%
V	1,040	210	-80%	1,040	240	-77%
	Average Difference:		-59%	*Average Difference:*		-35%

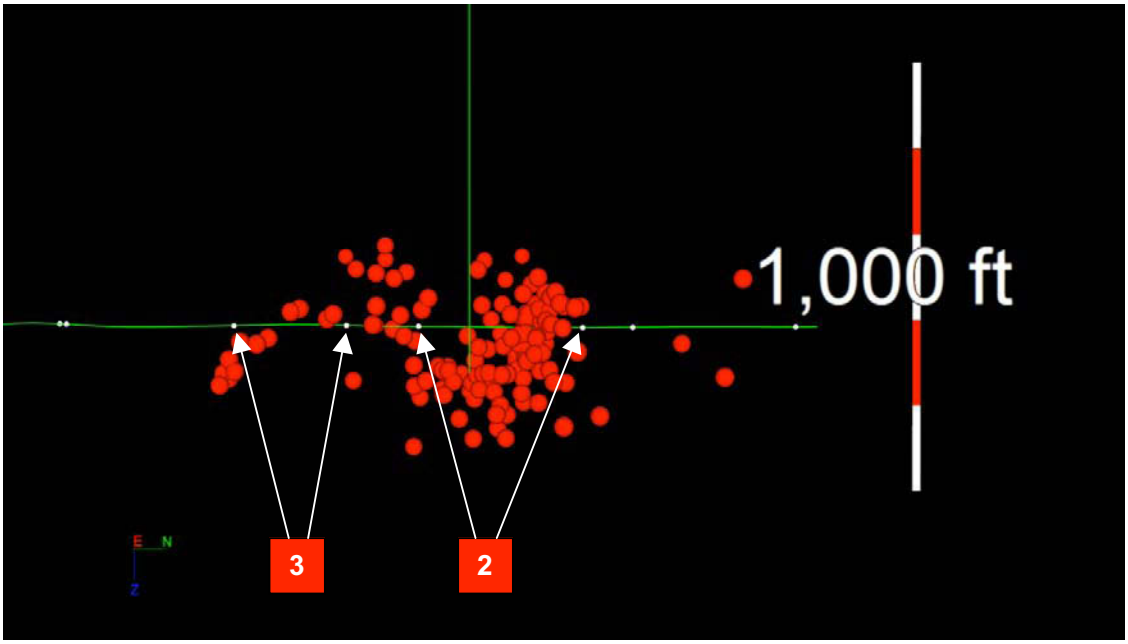

Figure 4.23: Side view of downhole microseismic recordings (red spheres) for Stage III. The treatment wellbore is shown in green from left to right. The monitoring wellbore is shown vertically in green. Numbers mark stage perforation clusters.

4.2.2.2 Transverse Models

As discussed in Section 3.5, matching is done with two types of models: a longitudinal and a transverse representation of the wellbore. The perpendicular direction allows for modeling the length of the transverse fractures.

4.2.2.2.1 Stage II

PDMSF was set to 0.005 1/psi, PDL to 0.0004 1/psi, TSC to 0.00033, and tectonic strain for the Woodford Shale to 65 microstrains. The Tortuosity Pre-Factor was set to 0.15 psi/bpm^2. The perforation coefficient was decreased from the default value to 0.32, with a friction factor of 0.05 in order to achieve a pressure match. Treatment tubing length was set to the measured depth of the center of the perforation cluster, which was 9,342 ft for this stage.

The perforation factor was set to 0.45 for the first interval from the beginning of the treatment on Dec. 10th, 2007, at about 14:26:30 until 14:50:00. It was then increased to 0.6 for the next interval until 15:18:27, after the first slug of 0.25 lbm/gal 100-mesh is pumped. For the next interval until the onset of the third slug being pumped at 0.75 lbm/gal at 15:24:34 it was set to 0.25. It was then further decreased to 0.20 until after the third slug was pumped at 15:27:00, to 0.19 until 16:09:55 (beginning of pumping the sixth slug of 30/70 sand), to 0.17 until 16:19:46 (beginning of seventh slug of 30/70 sand), to 0.16 until 16:20:39 (during pumping the seventh slug of 30/70 sand), to 0.15 until 16:31:13 (during pumping the eight slug of 30/70 sand), to 0.14 until 16:39:34 (beginning of pumping the ninth slug of 30/70 sand), to 0.12 until 16:49:25 (beginning of pumping the tenth slug of 30/70 sand), to 0.11 until 17:12:08 (beginning of pumping the thirteenth slug of 30/70 sand), and finally to 0.09 until the end of the treatment at about 17:34:00.

The downhole microseismic data showed a fracture half-length of 550 ft east of the wellbore, and 850 ft west of it. The modeled total fracture length that was used in the match was 1,700 ft. Activity was well contained to Stage II perforations with a height of about 280 ft. Fracture length was simulated with 1,350 ft, and height with 240 ft.

4.2.2.2.2 Stage III

PDMSF was set to 0.001 1/psi, PDL to 0.001 1/psi, TSC to 0.001, and tectonic strain for the Woodford Shale to 50 microstrains. The Tortuosity Pre-Factor was set to 0.10 psi/bpm^2. The perforation coefficient was decreased from the default value to 0.24, with a friction factor of 0.06 in order to achieve a pressure match. Treatment tubing length was set to the measured depth of the center of the perforation cluster, which was 9,342 ft for this stage.

The perforation factor for the first interval from the beginning of the job on Dec. 11th, 2007, at about 07:02:50 until 07:20:14 was set to 0.55. Until the pumping of the first slug at 0.25 lbm/gal is completed at 07:51:23 the factor was increased to 0.81, and then decreased to 0.23 until after the second slug with 0.50 lbm/gal is pumped at 07:57:09. It was then further lowered to 0.17 until the end of the treatment at about 10:08:00.

The fracture half-lengths were observed with 1,320 ft east of the treatment wellbore and 560 ft west of it. For symmetry reasons the total fracture length was assumed with 2,640 ft. The observed fracture height was 480 ft. As explained above in the analysis of the downhole data, the microseismic activity of Stage III of this treatment mostly overlaps with the region around Stage II perforations. Looking at the Stage III perforations in Fig. 4.19, it is obvious that the fracture height for this part of the reservoir is substantially lower, with about 270 ft. Since the already weakened reservoir around the Stage II perforation cluster could not be modeled accurately, this height was used for achieving the match. The fracture length was simulated for this stage with 2,260 ft with a height of 250 ft.

4.2.2.2.3 Stage IV

PDMSF was set to 0.002 1/psi, PDL to 0.001 1/psi, TSC to 0.001, and tectonic strain for the Woodford Shale to 50 microstrains. The Tortuosity Pre-Factor was set to 0.10 psi/bpm^2. The perforation coefficient was decreased from the default value to 0.25, with a friction factor of 0.07. Treatment tubing length was set to the measured depth until the center of the perforation cluster, which was 8,958.5 ft for this stage.

From the beginning of the treatment on Dec. 11th, 2007, at about 13:18:00 until right after the first pressure peak the perforation factor was set to 0.65 until 13:39:22. It was increased to 0.72 until after the first slug of 100-mesh sand at 0.25 lbm/gal was pumped at 14:08:18, and then substantially decreased to 0.27 until during pumping the second slug of 100-mesh sand at 0.5 lbm/gal at 14:12:00. From there on the factor had to be gradually decreased until the end of the treatment. It was set to 0.22 until 15:11:41 (beginning of pumping the seventh slug of 30/70 sand), to 0.19 until 15:22:00 (beginning of pumping the eighth slug of 30/70 sand), to 0.15 until 15:30:26 (beginning of pumping the ninth slug of 30/70 sand), to 0.14 until 15:42:42 (during pumping the tenth slug of 30/70 sand), to 0.12 until 15:53:04 (after pumping the eleventh slug of 30/70 sand), and finally to 0.09 until the end of the treatment at about 16:26:00.

The downhole microseismic data showed fracture half-lengths of 920 ft east of the treatment wellbore, 1,080 ft west of it, and a height of 620 ft. The total fracture length used for the match was therefore 2,160 ft. As for Stage III, most of the microseismic activity occurs around the perforation cluster of the previous stage, rather than around Stage IV perforations. The height of the cloud of microseismic activity at Stage IV perforations is about 570 ft, with a substantial amount of apparent downward growth. This downward growth could not be well simulated by the model, as it only simulates a height of 240 ft. The simulated fracture length was 2,120 ft, which is very close to the fracture length obtained from the microseismic data.

4.2.2.2.4 Stage V

PDMSF was set to 0.004 1/psi, PDL to 0.001 1/psi, and TSC to 0.001. The Tortuosity Pre-Factor was set to 0.15 psi/bpm^2. The perforation coefficient was only slightly decreased from the default value to 0.53, with a friction factor of 0.09. Treatment tubing length was set to the measured depth of the center of the perforation cluster, which was 8,273 ft for this stage. As for the longitudinal model for the finals stage the tectonic strain had to be slightly increased to 140 microstrains to account for the effects of stress shadowing, resulting in a higher in-situ stress.

The perforation factor was adjusted to 0.47 for the first interval from the beginning of the treatment on Dec. 12th, 2007, at about 07:09:00 until 07:36:47, and was

increased to 0.51 until 07:41:17. It was then increased further to 0.56 until after pumping the first slug of 100-mesh sand at 0.25 lbm/gal at 07:58:46. After this it was decreased to 0.36 until after pumping the third slug of 100-mesh sand at 0.75 lbm/gal at 08:10:28. After that the factor was set to 0.33 until 08:57:00 (during pumping the sixth slug of 30/70 sand), and finally to 0.29 until the end of the treatment at about 10:18:00.

As mentioned, all of the microseismic activity for this stage occurred around Stage IV perforations, except for one single event. The height of the microseismic cloud is about 510 ft, with fracture half-lengths of 640 ft east of the wellbore, and 930 ft west of it, giving a total fracture length of 1,860 ft.. With only one event at Stage V perforations it was difficult to assess the height of the fractured zone, so matching the height was not the primary concern for this stage. However, since 240 ft seemed to be a number that geological set-up in this model produced a lot, the parameters were adjusted in order to produce a height somewhere in this range. Again, the fracture length could be very well matched with 1,710 ft, and a simulated height of 240 ft.

4.2.2.3 Summary

Tables 4.8 and 4.9 give an overview of the model parameters for the downhole matches of the longitudinal and the transverse model, respectively. What can clearly be seen is that the tectonic strain for Stage V was substantially larger than for the previous stages in order to model the stress that was generated by those previous stages.

Table 4.10 gives an overview of the microseismic and simulated fracture dimensions. As mentioned in Section 4.1.3.6, both data sets clearly show that the microseismic activity recorded during one stage usually overlaps with the region around the perforations of the previous stage. Fracture growth for each stage, and therefore microseismicity seem to be dominated by pre-existing structures, i.e. the fracture network from the previous stage as well as natural fractures. Modeling cannot accurately account for the already fractured and therefore weakened reservoir around the previous stage.

Mohammad reports in her thesis from 2009 a fairly large difference between the microseismic and the simulated fracture dimensions, both over- and under-

estimating geometry components, with average values of about 34% for the fracture length and about 27% for fracture height, for a downhole monitored well. Simulated parameters deviate up to -56% for length, and up to 59% for height.

Table 4.8: Model Parameter Overview for Longitudinal Downhole Microseismic Models

	Stage II	*Stage III*	*Stage IV*	*Stage V*
PDMSF [1/psi]	0.005	0.002	0.0025	0.0035
PDL [1/psi]	0.0003	0.0015	0.0018	0.0009
TSC [-]	0.00029	0.0015	0.0018	0.0009
Tort. Pre-Factor [psi/bpm^2]	0.15	0.10	0.10	0.15
Tectonic Strain [microstrains]	65	45	55	130
Perf. Coeff. [-]	0.3	0.24	0.25	0.53
Frict. Coeff. [-]	0.05	0.06	0.07	0.09
Perf. Factor [-]	0.45 *(14:26:30-14:50:00)* 0.60 *(14:50:01-15:18:27)* 0.35 *(15:18:28-15:24:34)* 0.30 *(15:24:35-15:27:00)* 0.25 *(15:27:01-17:34:00)*	0.55 *(07:02:50-07:20:14)* 0.83 *(07:20:15-07:51:23)* 0.32 *(07:51:24-07:57:09)* 0.20 *(07:57:10-10:08:00)*	0.69 *(13:18:00-13:39:22)* 0.77 *(13:39:23-14:08:18)* 0.35 *(14:08:19-14:12:00)* 0.25 *(14:12:01-15:22:20)* 0.20 *(15:22:21-15:30:26)* 0.18 *(15:30:27-15:42:42)* 0.16 *(15:42:43-15:53:04)* 0.13 *(15:53:05-16:26:00)*	0.55 *(07:09:00-07:36:47)* 0.58 *(07:36:48-07:41:17)* 0.6 *(07:41:18-07:58:46)* 1.00 *(07:58:47-10:18:00)*

Table 4.10 shows an overview of the microseismic and simulated fracture geometry components. It should be noted that due to symmetry reasons for the hydraulic fracture models, the total length is double the longest half-length, like it was used as

matching parameter in the models. It can be seen that like for the surface models both length and longitudinal stretch could be very well matched for all stages with average deviations of only -11% and -4%, respectively. Height on the other hand could not successfully be matched for all stages, as seen with the average deviations of -45% for the longitudinal models, and -43% for the transverse models. Except for Stage II which was very well contained to Stage II perforations, every stage fractured into the region of the formation that was already stimulated by the previous stage, which the specific models used in this thesis could not accurately account for. This is discussed more in detail in Section 8.1. The fracture height that was obtained from Stage II can be used as a representative value for the un-stimulated reservoir. Since this height could be very well matched with the model, it shows that the geological set-up of the model was fairly accurate.

4.2.3 Combined Models

A base case model for each stage was created by incorporating both downhole and surface microseismic in the analysis. The fracture dimensions that were observed analyzing both available data sets were used for the models in the 'Pressure and Geometry Matching' part of Chapter III, where detailed information regarding the adjustment of parameters can be found. Tables 4.11 and 4.12 show a summary of parameters used to achieve pressure and geometry matches for the combined models.

Mohammad reports in her thesis from 2009 a fairly large difference between the microseismic and the simulated fracture dimensions, both over- and under-estimating geometry components, with average values of about 32% for the fracture length and about 54% for fracture height, for a surface monitored well. Simulated parameters deviate up to -67% for length, and up to -203% for height. For the downhole monitored well analyzed in the thesis, the average deviation was 34% for the fracture length, and about 27% for the fracture height, with maximum differences of -56% for length, and 59% for height.

Table 4.13 shows an overview of the microseismic and simulated fracture geometry components using both sets of microseismic data. It should be noted that due to symmetry reasons for the hydraulic fracture models, the total length is double the

longest half-length, like it was used as matching parameter in the models. It can be seen that both length and longitudinal stretch could be very well matched for all stages with average deviations of only -17% and -10%, respectively. Height on the other hand could not successfully be matched for all stages, as seen with the average deviations of -59% for the longitudinal models, and -55% for the transverse models. Except for Stage II which was very well contained to the Stage II perforations, every stage fractured into the region of the formation that has already been stimulated by the previous stage. The specific models used in this thesis could not accurately account for the already fractured and therefore weakened reservoir around the respective previous stage, which is discussed more in detail in Section 8.1. The fracture height that was obtained from Stage II can be used as a representative value for the un-stimulated reservoir. Since this height could be very well matched with the model, it shows that the geological set-up of the model was fairly accurate.

4.3 Number of Events

The third part of this chapter evaluates the problem of determining how many microseismic events are necessary in order to achieve a reasonable estimate of fracture geometry. There is a variety of factors that influence how well fracture geometry can be obtained from microseismic data. Regarding the microseismic data, the accuracy of the event location and the number of events are the two major parameters. While Chapter VII examines the accuracy of the recorded data, this section evaluates the role of the number of events. Since the surface data set includes only few data points and is therefore basically addressed in the matches obtained in Section 4.2.1, only the downhole set was used in this analysis.

In order to quantify the influence of the number of recorded events, fracture geometry was obtained from data sets and truncated in two different ways. The first three variations were generated by assigning a random number between one and the total number of events for a particular stage to each event, and sorting the data sets by these random numbers, from smallest to largest. The upper half, two thirds, or three quarters respectively, were then deleted, and the remaining data points loaded into Transform^{TM}, from which the fracture geometry was obtained. It should be noted that in

order to maintain the randomness, a new random number was assigned before a data set was truncated. This method represents a completely random selection of every second, third, or fourth event that was not based on a characterizing property. The second method to crop the data set used the confidence number that the service company assigned to each event as a characterizing parameter. The event confidence is a value that indicates the overall quality of all variables that go into calculating the event location and ranges from zero, signalizing a very low confidence, to five, implying a very high confidence. It takes into account various quality parameters that Section 7.2 discusses in more detail. Since a confidence number of three generally defines the event location as accurate, all events with a value of less than 3.0 were not considered in this analysis. As opposed to the random elimination of data points in the first method used in this section, this methodology represents a qualitative selection of events.

4.3.1 Stage II

The original data set includes 81 events that were trimmed down to 41 for half of the total number of events, to 27 for a third, and to 20 for a quarter, respectively. Out of those 81 events, 47 had a confidence number above three, indicating that about 60% of the original data set is considered accurate.

The random elimination of events seems to give a random result. It can be seen in Table 4.14, that all components of the fracture geometry show a fairly narrow range, except for the half length west of the wellbore and the longitudinal stretch along the wellbore.

Fig. 4.24 shows all events with a confidence higher than three. It can be seen that the high confidence events seem to outline the main fracture. Events farther away from the main fracture generally seem to have a lower confidence, but all fracture dimensions seem to be accurately obtained from the original data set as can be seen in Table 4.14. The truncated data set shows an average confidence number of 3.48.

Table 4.9: Model Parameter Overview for Transverse Downhole Microseismic Models

	Stage II	*Stage III*	*Stage IV*	*Stage V*
PDMSF [1/psi]	0.005	0.001	0.002	0.004
PDL [1/psi]	0.0004	0.001	0.001	0.001
TSC [-]	0.00033	0.001	0.001	0.001
Tort. Pre-Factor [psi/bpm^2]	0.15	0.10	0.10	0.15
Tectonic Strain [microstrains]	65	50	50	140
Perf. Coeff. [-]	0.32	0.24	0.25	0.53
Frict. Coeff. [-]	0.05	0.06	0.07	0.09
Perf. Factor [-]	0.45 *(14:26:30-14:50:00)* 0.60 *(14:50:01-15:18:27)* 0.25 *(15:18:28-15:24:34)* 0.20 *(15:24:35-15:27:00)* 0.19 *(15:27:01-16:09:55)* 0.17 *(16:09:56-16:19:46)* 0.16 *(16:19:47-16:20:39)* 0.15 *(16:20:40-16:31:13)* 0.14 *(16:31:14-16:39:34)* 0.12 *(16:39:35-16:49:25)* 0.11 *(16:49:26-17:12:08)* 0.09 *(17:12:09-17:34:00)*	0.55 *(07:02:50-07:20:14)* 0.81 *(07:20:15-07:51:23)* 0.23 *(07:51:24-07:57:09)* 0.17 *(07:57:10-10:08:00)*	0.65 (13:18:00-13:39:22) 0.72 (13:39:23-14:08:18) 0.27 (14:08:19-14:12:00) 0.22 (14:12:01-15:11:41) 0.19 (15:11:42-15:22:00) 0.15 (15:22:01-15:30:26) 0.14 *(15:30:27-15:42:42)* 0.12 (15:42:43-15:53:04) 0.09 *(15:53:05-16:26:00)*	0.47 *(07:09:00-07:36:47)* 0.51 *(07:36:48-07:41:17)* 0.56 *(07:41:18-07:58:46)* 0.36 *(07:58:47-08:10:28)* 0.33 *(08:10:29-08:57:00)* 0.29 *(08:57:01-10:18:00)*

4.3.2 Stage III

A total number of 132 events was included in the original data set, which was truncated to 66 events for half of the total number, to 44 for a third, and to 33 for a quarter. In total 89 events had a confidence value of three or above, representing about 70% of the original data set.

As for the previous stage the random selection of events results in a random distribution of fracture geometry between the various trimmed data sets. Table 4.15 shows that the various components of the fracture geometry have a fair amount of variation. The fracture azimuth seems not be influenced by the number of events.

Fig. 4.25 shows all events with a confidence higher than three. Again, it can be seen that the high confidence events seem to outline the main fracture. The fracture length and height seem to be accurately obtained from the original data set. The longitudinal stretch however shows a lower confidence on the outer ends. Altogether the events have an average confidence number of 3.76 making it the most accurate data set together with Stage V.

Table 4.10: Comparison of Fracture Dimensions for Downhole Microseismic Models

Stage	*Fracture Length [ft]*			*Longitudinal Stretch of Fractured Zone [ft]*		
	Microseismic	*Simulated*	*Difference*	*Microseismic*	*Simulated*	*Difference*
II	1,700	1,350	-21%	810	790	-2%
III	2,600	2,260	-13%	1,100	1,100	0%
IV	2,160	2,120	-2%	1,060	1,010	-5%
V	1,860	1,710	-8%	1,150	1,060	-8%
	Average Difference:		-11%	*Average Difference:*		-4%

Stage	*Height from longitudinal models [ft]*			*Height from transverse models [ft]*		
	Microseismic	*Simulated*	*Difference*	*Microseismic*	*Simulated*	*Difference*
II	280	240	-14%	280	240	-14%
III	480	240	-50%	480	250	-48%
IV	620	240	-61%	620	250	-60%
V	510	240	-53%	510	250	-51%
	Average Difference:		-45%	*Average Difference:*		-43%

Table 4.11: Model Parameter Overview for Longitudinal Combined Microseismic Models

	Stage I	*Stage II*	*Stage III*	*Stage IV*	*Stage V*
PDMSF [1/psi]	0.0045	0.005	0.002	0.0025	0.0035
PDL [1/psi]	0.00025	0.0003	0.0015	0.0018	0.0009
TSC [-]	0.00025	0.00029	0.0015	0.0018	0.0009
Tort. Pre-Factor [psi/bpm^2]	0.15	0.15	0.10	0.10	0.15
Tectonic Strain [microstrains]	70	65	45	55	130
Perf. Coeff. [-]	0.37	0.3	0.24	0.25	0.53
Frict. Coeff. [-]	0.03	0.05	0.06	0.07	0.09
Perf. Factor [-]	0.35 *(07:15:47-07:37:56)* 0.45 *(07:37:57-07:40:06)* 0.57 *(07:40:07-07:49:09)* 0.62 *(07:49:10-08:12:56)* 0.38 *(08:12:57-08:16:31)* 0.33 *(08:16:32-10:29:00)*	0.45 *(14:26:30-14:50:00)* 0.60 *(14:50:01-15:18:27)* 0.35 *(15:18:28-15:24:34)* 0.30 *(15:24:35-15:27:00)* 0.25 *(15:27:01-17:34:00)*	0.55 *(07:02:50-07:20:14)* 0.83 *(07:20:15-07:51:23)* 0.32 *(07:51:24-07:57:09)* 0.20 *(07:57:10-10:08:00)*	0.69 *(13:18:00-13:39:22)* 0.77 *(13:39:23-14:08:18)* 0.35 *(14:08:19-14:12:00)* 0.25 *(14:12:01-15:22:20)* 0.20 *(15:22:21-15:30:26)* 0.18 *(15:30:27-15:42:42)* 0.16 *(15:42:43-15:53:04)* 0.13 *(15:53:05-16:26:00)*	0.55 *(07:09:00-07:36:47)* 0.58 *(07:36:48-07:41:17)* 0.6 *(07:41:18-07:58:46)* 1.00 *(07:58:47-10:18:00)*

4.3.3 Stage IV

The original data set includes 113 events that were trimmed down to 57 for half of the total number of events, to 38 for a third, and to 29 for a quarter, respectively. Out of those 113 events 53 had a confidence number above three, indicating that about 50% of the original data set is considered accurate, which is the lowest percentage of all stages that were recorded.

Again, the random elimination of events seems to give a random result. It can be seen in Table 4.16 that all components of the fracture geometry are affected by the random event selection. It should be noted that the variation in azimuth at about 5 degrees is greater for Stage IV than for the previous stages.

Fig. 4.26 shows all events with a confidence higher than three. It can be seen that the high confidence events seem to outline the main fracture. The fracture half length on the west side of the wellbore seems to be the only component that has a rather low confidence, while all other dimensions were accurately depicted by the original data set, reflected by a solid confidence value of 3.49 for the trimmed data set.

4.3.4 Stage V

A total number of 171 events was included in the original data set, which was truncated to 86 events for half of the total number, to 57 for a third, and to 43 for a quarter. In total, 125 events had a confidence value of three or above, representing over 70% of the original data set.

As for the previous stages the random selection of events results in a random distribution of fracture geometry between the various trimmed data sets. Table 4.17 shows that especially the longitudinal stretch has a large amount of variation. However, the azimuth seems to be fairly constant. It should be noted that for the first case analyzing half of the original data set the complete fracture length and the length of the apparent main fracture are different, with 1,050 ft for the complete length, and 550 ft for the main fracture length. This is due to a single event at the Stage V perforations.

Fig. 4.27 shows all events with a confidence higher than three. As for the previous stages it can be seen that the high confidence events seem to outline the main fracture. The single event that occurred at the Stage V perforations interestingly has a high confidence, and is therefore included in the data set. The longitudinal stretch can be obtained at 1,050 ft for the complete length of the microseismic cloud, or at 500 ft for just the main fracture. The events that were recorded during Stage III and V show the highest confidence of all stages, with a value of 3.76, leading to almost no difference between the original data set and the truncated one, especially for Stage V.

Table 4.12: Model Parameter Overview for Transverse Combined Microseismic Models

	Stage I	*Stage II*	*Stage III*	*Stage IV*	*Stage V*
PDMSF [1/psi]	0.002	0.005	0.001	0.002	0.002
PDL [1/psi]	0.0005	0.0004	0.001	0.0005	0.001
TSC [-]	0.0005	0.00033	0.001	0.0005	0.001
Tort. Pre-Factor [psi/bpm^2]	0.10	0.15	0.10	0.10	0.15
Tectonic Strain [microstrains]	50	65	50	50	140
Perf. Coeff. [-]	0.42	0.32	0.24	0.25	0.53
Frict. Coeff. [-]	0.03	0.05	0.06	0.07	0.09
Perf. Factor [-]	0.30 *(07:15:47-07:37:56)* 0.45 *(07:37:57-07:40:06)* 0.51 *(07:40:07-07:49:09)* 0.55 *(07:49:10-08:12:56)* 0.28 *(08:12:57-08:16:31)* 0.24 *(08:16:32-09:07:47)* 0.22 *(09:07:48-09:12:28)* 0.20 *(09:12:29-09:27:52)* 0.18 *(09:27:53-09:32:33)* 0.15 *(09:32:34-09:42:41)* 0.12 *(09:42:42-09:57:53)* 0.10 *(09:57:54-10:29:00)*	0.45 *(14:26:30-14:50:00)* 0.60 *(14:50:01-15:18:27)* 0.25 *(15:18:28-15:24:34)* 0.20 *(15:24:35-15:27:00)* 0.19 *(15:27:01-16:09:55)* 0.17 *(16:09:56-16:19:46)* 0.16 *(16:19:47-16:20:39)* 0.15 *(16:20:40-16:31:13)* 0.14 *(16:31:14-16:39:34)* 0.12 *(16:39:35-16:49:25)* 0.11 *(16:49:26-17:12:08)* 0.09 *(17:12:09-17:34:00)*	0.55 *(07:02:50-07:20:14)* 0.81 *(07:20:15-07:51:23)* 0.23 *(07:51:24-07:57:09)* 0.17 *(07:57:10-10:08:00)*	0.65 *(13:18:00-13:39:22)* 0.72 *(13:39:23-14:08:18)* 0.27 *(14:08:19-14:12:00)* 0.22 *(14:12:01-15:11:41)* 0.19 *(15:11:42-15:22:00)* 0.13 *(15:22:01-15:30:26)* 0.12 *(15:30:27-15:42:42)* 0.10 *(15:42:43-15:53:04)* 0.07 *(15:53:05-16:26:00)*	0.45 *(07:09:00-07:36:47)* 0.49 *(07:36:48-07:41:17)* 0.54 *(07:41:18-07:58:46)* 0.34 *(07:58:47-08:10:28)* 0.31 *(08:10:29-08:57:00)* 0.27 *(08:57:01-10:18:00)*

Table 4.13: Comparison of Fracture Dimensions for Combined Microseismic Models

Stage	*Fracture Length [ft]*			*Longitudinal Stretch of the Fractured Zone [ft]*		
	Microseismic	*Simulated*	*Difference*	*Microseismic*	*Simulated*	*Difference*
I	4,200	3,580	-15%	630	500	-21%
II	1,700	1,350	-21%	830	790	-5%
III	2,640	2,260	-14%	1,100	1,100	0%
IV	3,900	3,440	-12%	1,220	1,010	-17%
V	2,820	2,140	-24%	1,150	1,070	-7%
	Average Difference:		-17%	*Average Difference:*		-10%

Stage	*Height from longitudinal models [ft]*			*Height from transverse models [ft]*		
	Microseismic	*Simulated*	*Difference*	*Microseismic*	*Simulated*	*Difference*
I	630	150	-76%	630	250	-60%
II	290	240	-17%	290	240	-17%
III	550	240	-56%	550	250	-55%
IV	720	240	-67%	720	250	-65%
V	1,060	240	-77%	1,060	240	-77%
	Average Difference:		-59%	*Average Difference:*		-55%

Table 4.14: Summary of Fracture Geometry for Stage II

	Original Data Set	*Every Second Event (i.e. Half of the Original Data Set)*	*Every Third Event (i.e. One Third of the Original Dat Set)*	*Every Fourth Event (i.e. One Quarter of the Original Data Set)*	*Confidence >3.0*
Length (W/E of wellbore) [ft]	550/850	50/850	550/660	0/610	550/850
Longitudinal Stretch [ft]	810	770	680	350	630
Height (above/below wellbore) [ft]	140/140	140/110	100/90	130/130	110/130
Fracture Azimuth [degrees]	78	78	79	80	78

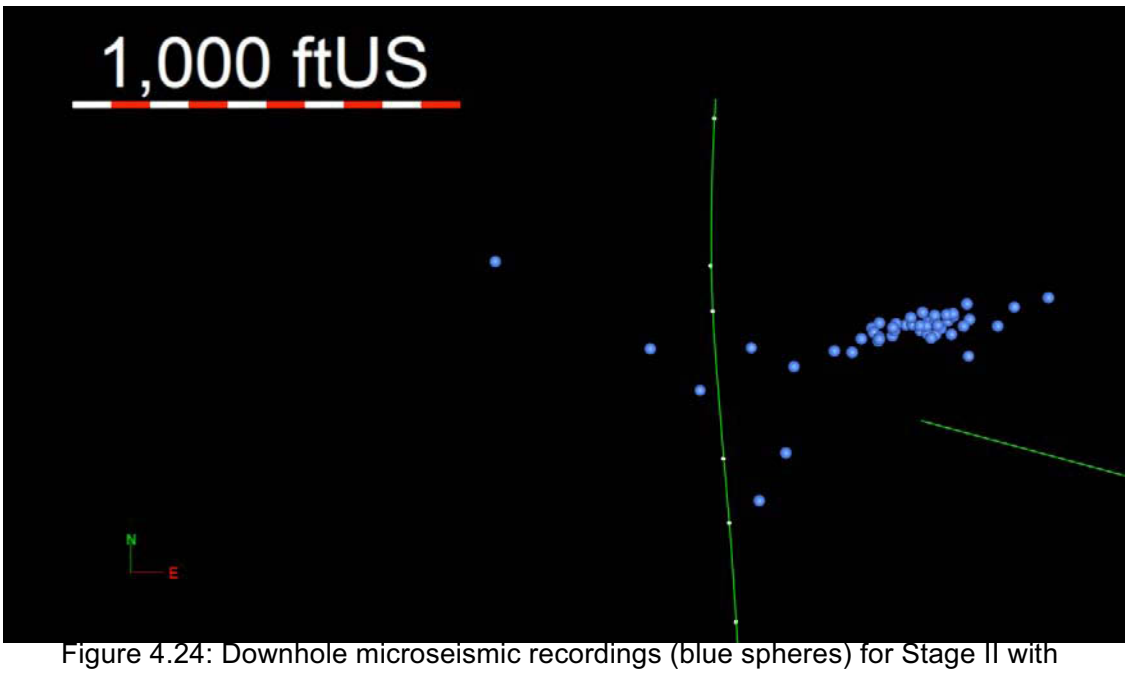

Figure 4.24: Downhole microseismic recordings (blue spheres) for Stage II with confidence number above 3.0. The horizontal well trajectory of the treatment wellbore can be seen in green from south to north. The monitoring well can be seen in green east of the treatment well.

Table 4.15: Summary of Fracture Geometry for Stage III

	Original Data Set	*Every Second Event (i.e. Half of the Original Data Set)*	*Every Third Event (i.e. One Third of the Original Dat Set)*	*Every Fourth Event (i.e. One Quarter of the Original Data Set)*	*Confidence >3.0*
Length (W/E of wellbore) [ft]	1,320/560	1,270/480	1,320/250	1,250/470	1,260/560
Longitudinal Stretch [ft]	1,100	1,100	750	1,080	820
Height (above/below wellbore) [ft]	190/290	190/240	190/250	180/240	180/270
Fracture Azimuth [degrees]	76	76	75	75	75

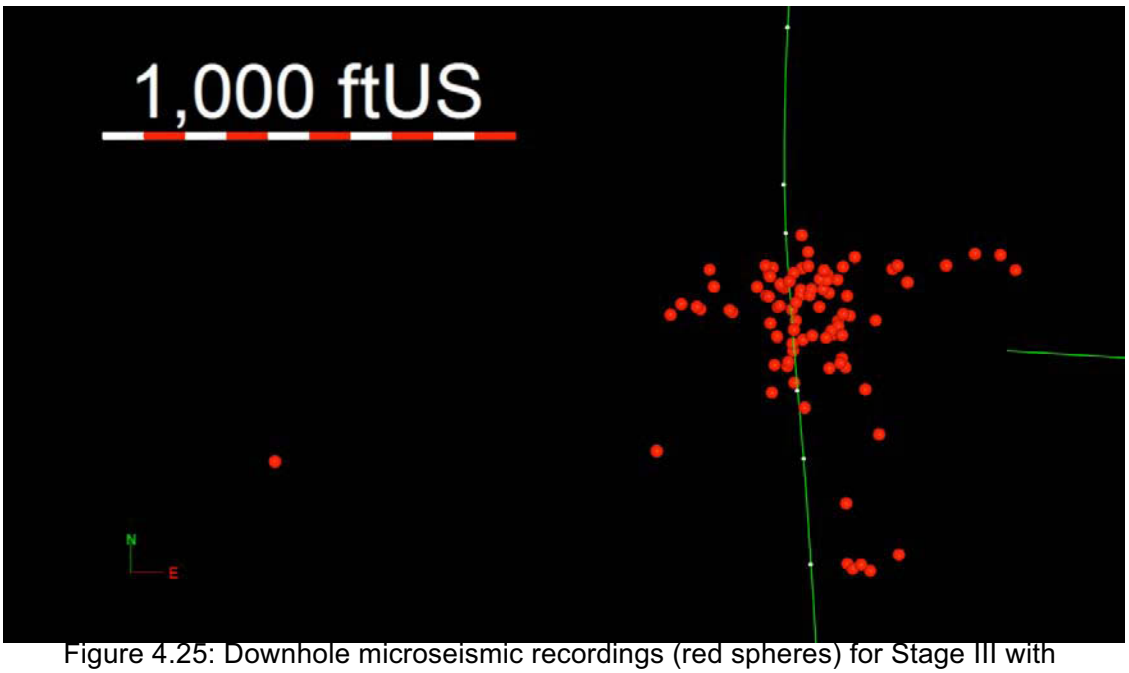

Figure 4.25: Downhole microseismic recordings (red spheres) for Stage III with confidence number above 3.0. The horizontal well trajectory of the treatment wellbore can be seen in green from south to north. The monitoring well can be seen in green east of the treatment well.

Table 4.16: Summary of Fracture Geometry for Stage IV

	Original Data Set	*Every Second Event (i.e. Half of the Original Data Set)*	*Every Third Event (i.e. One Third of the Original Dat Set)*	*Every Fourth Event (i.e. One Quarter of the Original Data Set)*	*Confidence >3.0*
Length (W/E of wellbore) [ft]	920/1,080	670/1,060	920/970	750/1,040	450/1,080
Longitudinal Stretch [ft]	1,060	1,050	880	860	920
Height (above/below wellbore) [ft]	190/430	190/370	130/380	180/420	180/350
Fracture Azimuth [degrees]	77	80	75	80	80

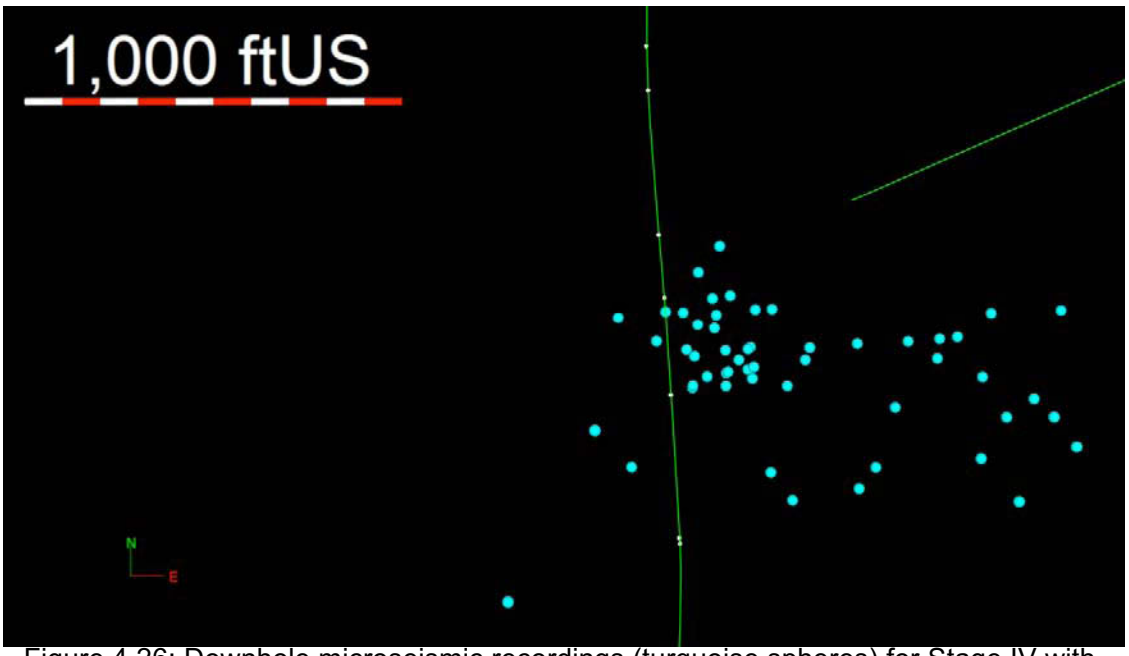

Figure 4.26: Downhole microseismic recordings (turquoise spheres) for Stage IV with confidence number above 3.0. The horizontal well trajectory of the treatment wellbore can be seen in green from south to north. The monitoring well can be seen in green east of the treatment well.

Table 4.17: Summary of Fracture Geometry for Stage V

	Original Data Set	*Every Second Event (i.e. Half of the Original Data Set)*	*Every Third Event (i.e. One Third of the Original Dat Set)*	*Every Fourth Event (i.e. One Quarter of the Original Data Set)*	*Confidence >3.0*
Length (W/E of wellbore) [ft]	640/930	400/850	640/930	620/920	640/930
Longitudinal Stretch [ft]	1,150	1,050	540	430	1,050
Height (above/below wellbore) [ft]	160/350	160/320	140/340	90/330	150/350
Fracture Azimuth [degrees]	75	76	75	75	76

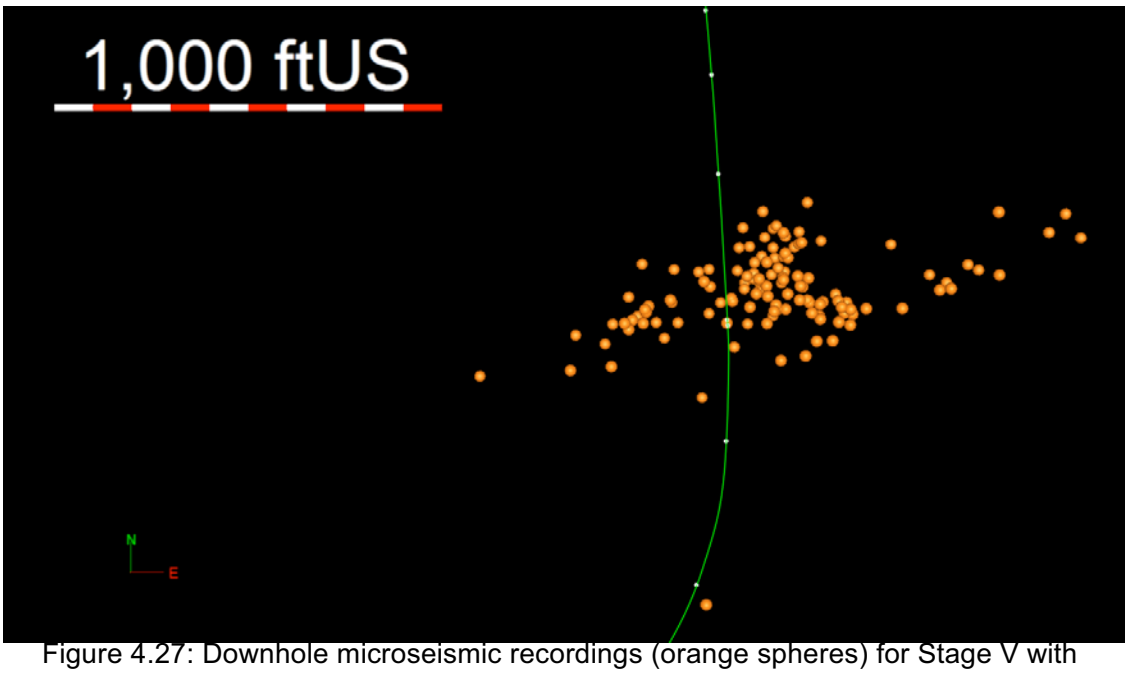

Figure 4.27: Downhole microseismic recordings (orange spheres) for Stage V with confidence number above 3.0. The horizontal well trajectory of the treatment wellbore can be seen in green from south to north.

4.3.5 Summary

All components of the fracture geometry were affected by the number of events for the random elimination of events. The confidence number, however, seems to be a better parameter in evaluating the quality of a data set than just looking at how many events were recorded. Table 4.18 gives an overview of the deviation of the cropped data sets. It can be seen that the random elimination of events affects all geometry components. The results for the data set that was modified excluding all events with a confidence number below 3.0 implies that the events that outline the fracture generally seem to be fairly confident. Therefore the dimensions of the fracture do not deviate very much from the original data set including events with a less accurate location, as seen in Fig. 4.28.

Table 4.18: Deviation between Fracture Geometry Obtained from Truncated Data Sets and Original Dimensions

		Every Second Event (i.e. Half of the Original Data Set)	*Every Third Event (i.e. One Third of the Original Dat Set)*	*Every Fourth Event (i.e. One Quarter of the Original Data Set)*	*Confidence >3.0*
Stage II	*Length (W/E of wellbore)*	-91% / 0%	0% / -22%	-100% / -28%	0% / 0 %
	Longitudinal Stretch	-5%	-16%	-57%	-22%
	Height (above/below wellbore)	0% / -21%	-29% / -36%	-7% / -7%	-21% / -7%
	Fracture Azimuth [degrees]	0	+1	+2	0
Stage III	*Length (W/E of wellbore)*	-4% / -14%	0% / -55%	-5% / -16%	-5% / 0%
	Longitudinal Stretch	0%	-31%	-2%	-25%
	Height (above/below wellbore)	0% / -17%	0% / -14%	-5% / -17%	-5% / -7%
	Fracture Azimuth [degrees]	0	-1	-1	-1
Stage IV	*Length (W/E of wellbore)*	-27% / -2%	0% / -10%	-18% / -4%	-51% / 0%
	Longitudinal Stretch	-1%	-17%	-19%	-13%
	Height (above/below wellbore)	0% / -14%	-32% / -12%	-5% / -2%	-5% / -19%
	Fracture Azimuth [degrees]	+3	-5	+3	+3
Stage V	*Length (W/E of wellbore)*	-38% / -9%	0% / 0%	-3% / -1%	0% / 0%
	Longitudinal Stretch	-9%	-53%	-63%	-9%
	Height (above/below wellbore)	0% / -9%	-13% / -3%	-44% / -6%	-6% / 0%
	Fracture Azimuth [degrees]	+1	0	0	+1

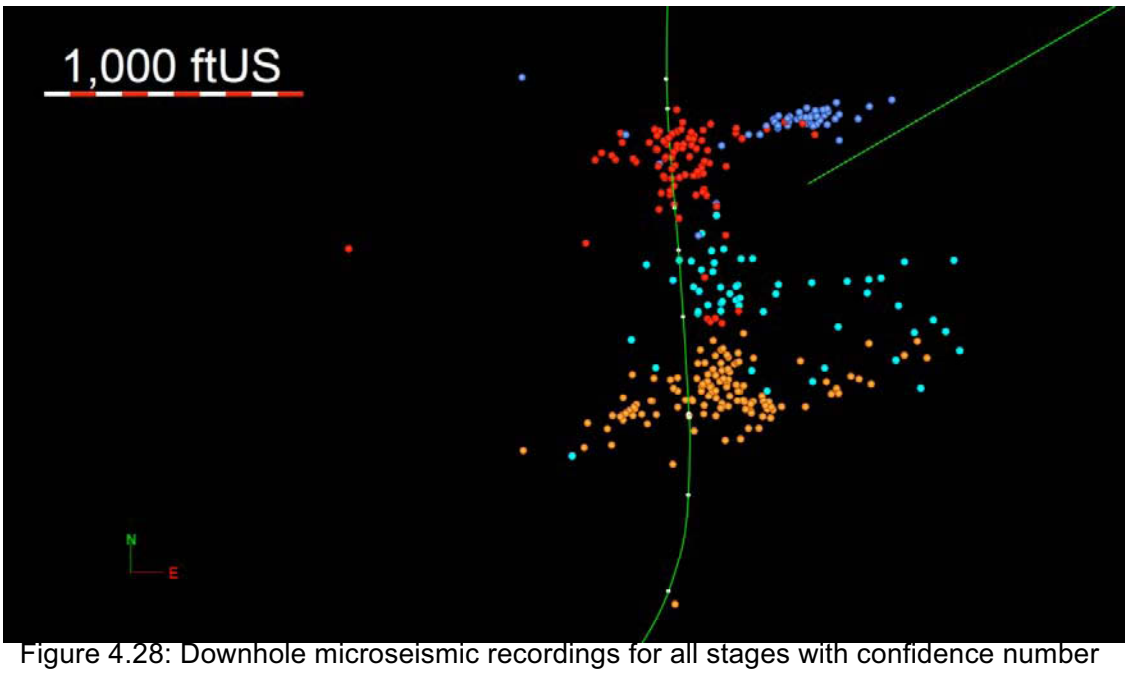

Figure 4.28: Downhole microseismic recordings for all stages with confidence number above 3.0. Stage II is shown in blue, Stage III is shown in red, Stage IV is shown in turquoise, and Stage V is shown in orange. The horizontal well trajectory of the treatment wellbore can be seen in green from south to north. The monitoring well can be seen in green east of the treatment well.

CHAPTER 5

EVENT MAGNITUDE

Earthquake magnitude is expressed in the moment magnitude scale, which is an extension of the earlier developed Richter scale. Microseismic events created by hydraulic stimulation, generally with magnitudes of -4 to -2, are usually five to seven orders of magnitude smaller than seismic events that can be perceived on the surface (+3 or higher) (Warpinski, 2009b). Eq. 2.6 showed that the seismic moment of an event depends on the amount of shear displacement along the fault plane, the area of the fault plane, and the shear modulus. Table 5.1 gives an overview of moment magnitudes and corresponding seismic moment, amount of displacement, area of displacement, and the equivalent explosive charge.

Table 5.1: Event Magnitude and Corresponding Parameters (from Maxwell et al., 2009)

Event Magnitude [-]	*Seismic Moment [dyne-cm]*	*Displacement [cm]*	*Area of Displacement [cm^2]*	*Equivalent Explosive Charge*
0	$1 \cdot 10^{13}$	0.1	300,000	1 kg
-1	$4 \cdot 10^{11}$	0.04	30,000	30 g
-2	$1 \cdot 10^{10}$	0.01	3,000	1 g
-3	$4 \cdot 10^{8}$	0.004	300	30 mg
-4	$1 \cdot 10^{7}$	0.001	30	1 mg

A very useful tool in the analysis of microseismic data is a cumulative moment plot. Various changes of the seismic moment can be observed throughout the treatment. Consecutive stages can show an increase in seismic moment, depicting the effect of previous stages. In other cases, such increases might be followed by an unexpected decrease, i.e. a stage that shows a smaller cumulative moment than the previous one, indicating interaction with faults, natural fractures, or extension of the fracture into a part of the reservoir with deviating properties. If the hydraulic fracture intersects a fault, the cumulative moment curve is usually shifted upwards due to the generation of very 'loud' microseisms. Some stages may also come to a plateau after some time, implying that

even though more volume is injected, not much shearing related to that additional volume is occurring (Warpinski, 2009b). However, increase in seismic moment can be controlled by a few large events, as there is about a 32-fold difference in moment between microseismic events that are just one magnitude apart (Vermylen and Zoback, 2011). The quality of the information that can be obtained from such plots should therefore be carefully evaluated.

The seismic moment for each event can easily be calculated when re-arranging Eq. 2.7 to:

$$M_0 = 10^{1.5M+16.1} \qquad \text{(Eq. 5.1)}$$

M_0 … seismic moment [dyne-cm]
M … moment magnitude[log scale]

Fig. 5.1 shows a cumulative seismic moment plot for events recorded by the surface receivers during all five stages of the hydraulic fracturing treatment that were analyzed for this work. It can be seen that the stages monitored from the surface show both small and relatively large events. Stage III and V have a cumulative seismic moment that is about five orders of magnitude larger than the other stages. The plot also shows that both Stage III and V reach a plateau after some time, meaning that even though more fluid and proppant are injected into the reservoir, not much additional shearing due to fracture growth is occurring. Stage III reaches this plateau rather early after about an hour of pumping.

The event magnitude for the surface data set ranges from -2.75 to 0.86 therefore producing a very wide range of cumulative seismic moment. The plot for the surface data is clearly dominated by large magnitude events. Considering the maximum vertical distance between events of the surface data set and the surface sensors of about 8,500 ft, as opposed to the maximum distance from an event to the observation well for the downhole monitoring of about 1,900 ft, it is no surprise. Modifying the data set by excluding events recorded during Stages III and V leads to the plot that can be seen in Fig. 5.2. Due to low number of events in the surface data set this plot unfortunately does not provide any quality information either.

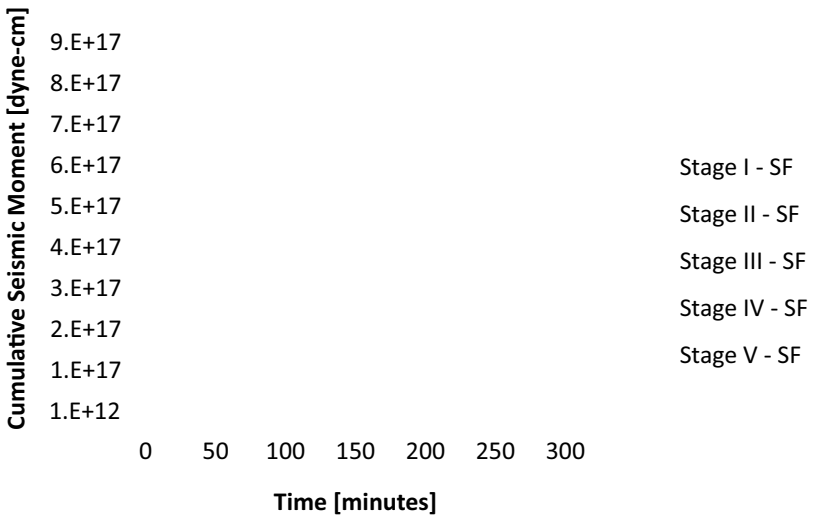

Figure 5.1: Cumulative seismic moment plot for surface recordings. The cumulative seismic moment scale is truncated towards the lower end. This indicates a large difference in magnitude between Stages V and III and Stages I, II, and IV, resulting in a 100,000-fold increase from a cumulative seismic moment of 1E+12 to 1E+17 dyne-cm.

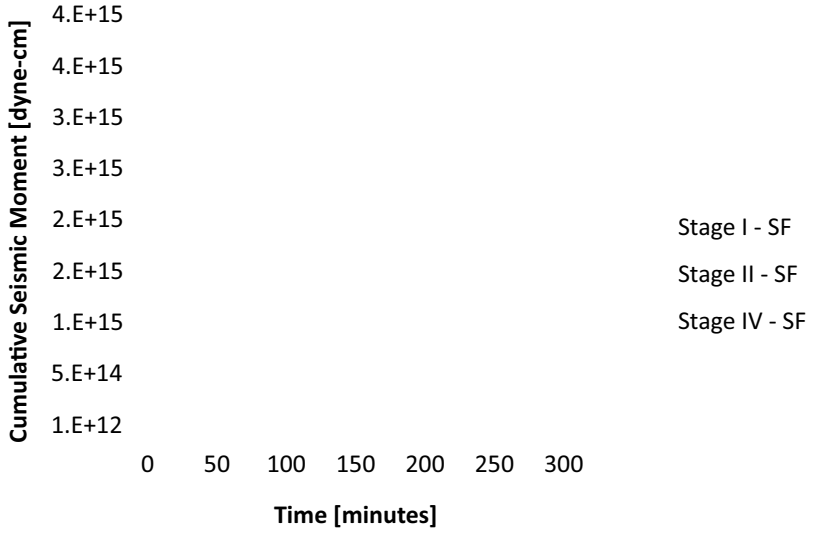

Figure 5.2: Cumulative seismic moment plot for surface recordings without Stages III and V. The cumulative seismic moment scale is truncated towards the lower end. This indicates a large difference in magnitude resulting in a 500-fold increase from a cumulative seismic moment of 1E+12 to 5E+14 dyne-cm.

Having recorded substantially more events, a cumulative seismic moment plot generated from the downhole data gives a better picture of the treatment. The curves seen in Figure 5.3 are a lot more significant than those for the surface recordings. Since Stage II was the earliest stage to be recorded with downhole sensors it has the smallest cumulative seismic moment. For Stage III a substantial increase can be observed. However, the cumulative moment generated during Stage IV is lower than for the previous stage, indicating that the microseismic activity was of lower intensity, as, according to Equation 2.6, the seismic moment depends on the amount of shear displacement along the fault plane and the area of the fault plane. Stage V shows the highest cumulative moment, which is in good agreement with the surface data. For all stages the curves reach a plateau after a certain time, reflecting that although additional volume is being injected, it does not generate much additional microseismicity.

Due to the large cumulative seismic moment of Stages III and V from the surface recordings with an order of magnitude of almost up to 10^{18}, a plot including both surface and downhole data would be just as distorted as Figure 5.1.

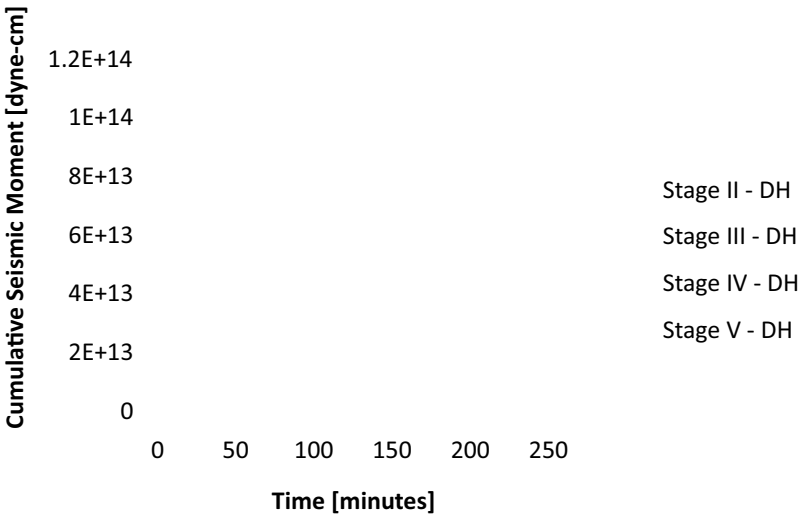

Figure 5.3: Cumulative seismic moment plot for downhole recordings.

Microseismic events that are recorded during hydraulic fracturing treatment can be analyzed with a magnitude scaling technique that Gutenberg and Richter applied to

regular seismic events (i.e. earthquakes) for the first time in 1944. Plotting the cumulative number of events greater than or equal to a certain magnitude on a logarithmic scale versus the magnitude of the events, a log-linear relationship can be observed for events that were accurately detected by the microseismic sensors (Vermylen and Zoback, 2011). This relationship is determined by the following equation:

$$\log_{10}(N \geq M) = a - b \cdot M \qquad \text{(Eq. 5.2)}$$

N≥M … Cum. number of events larger or equal to a certain magnitude [-]
a … log. of total number of events larger or equal to a magnitude of 0 [-]
b … slope [-]
M … seismic event magnitude [-]

For earthquakes, a general b-value of 1 was found in the analysis of Gutenberg and Richter. A b-value that is significantly larger than 1 indicates a large amount of small events, i.e. the generation of microseisms (Vermylen and Zoback, 2011). Since earthquakes represent seismic events that are related to fault activity, it can be inferred that fault related seismicity has a b-value of 1. Non-fault related seismic activity on the other hand, which is generated due to shear failure occurring during fracturing of the rock, usually has a b-value that is greater than 1 (Downie et al., 2010).

When plotting all stages of a certain fracturing treatment and all of them show identical values for b, the a-value can be used as a parameter to compare the activity level of each stage. It can be "used to quantify the rate of seismicity and thus the density of fractures created in the reservoir" (Vermylen and Zoback, 2011). Fig. 5.4 shows such a plot for one stage that was monitored by both a near and a far array. The magnitude threshold above which events were recorded without much sensor effects is clearly visible where the curves deviate from being parallel to the x-axis into the log-linear shape. The threshold for the two arrays is different, however, the slope of the curve, as well as the intercept, or the activity level, are both the same, meaning that both arrays have monitored the stage accurately, or at least with the same intrinsic error. Fig. 5.5 shows a magnitude scaling plot for two stages monitored by one array of sensors. It can be seen that more events were recorded during the stage closer to the sensors. The activity level (i.e. the intercept) for the near stage is larger than that of the far stage though. Since the a-value is the theoretical number of events with a magnitude larger or equal to zero it shows that the far stage in fact was more successful than the near stage

in terms of generating microseismicity (i.e. hydraulically fracturing the formation). However, this can only be inferred about a particular treatment if the b-values are more or less equal (Vermylen and Zoback, 2011).

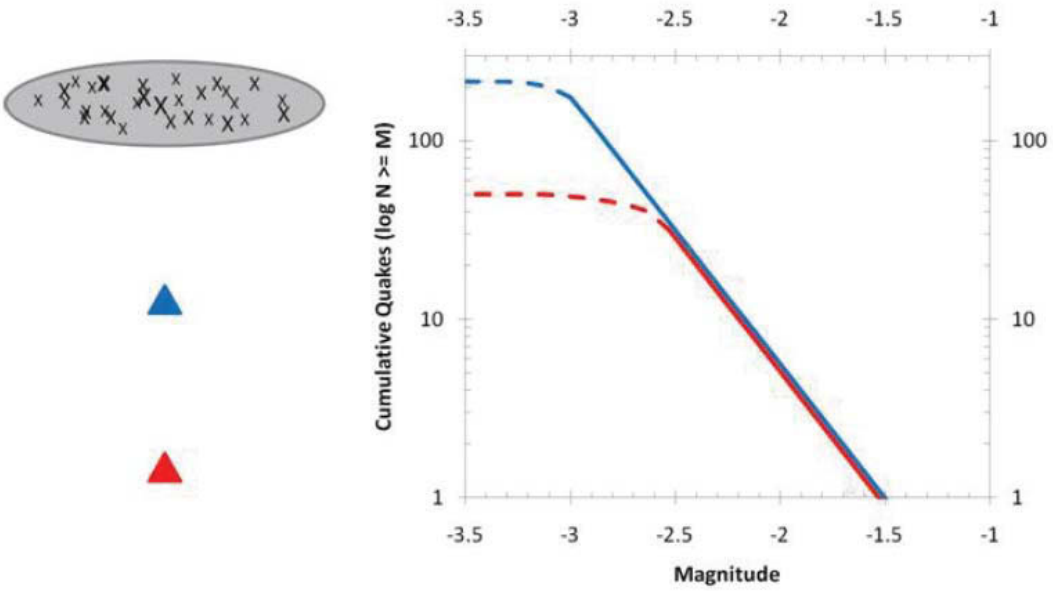

Figure 5.4: Magnitude distribution for a hydraulic fracturing stage monitored by two arrays (from Vermylen and Zoback, 2011).

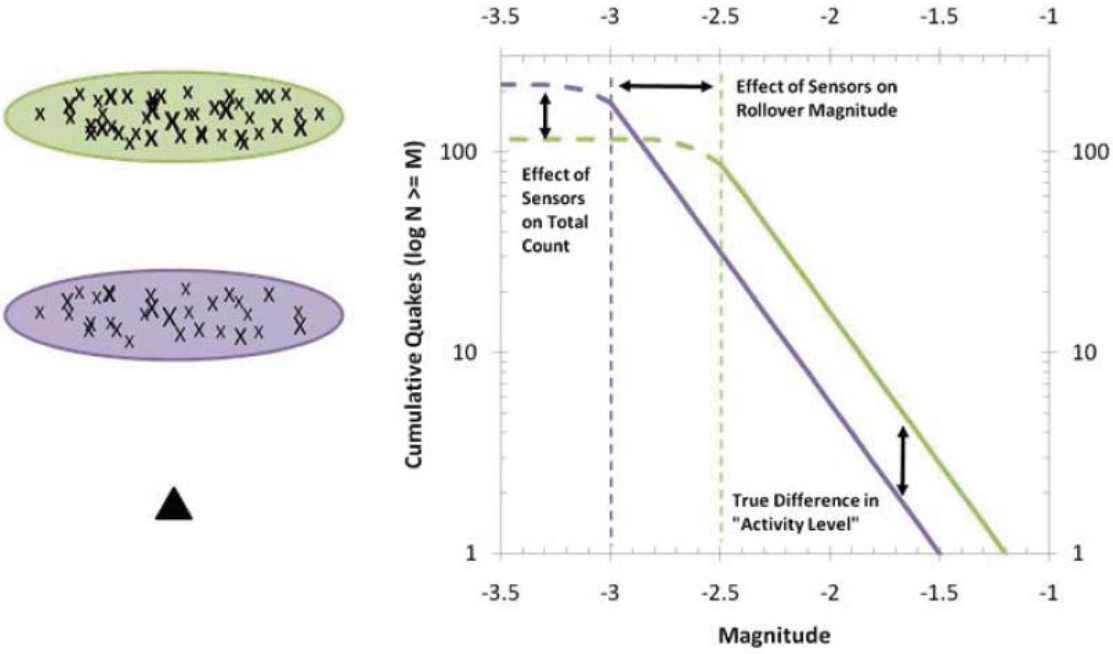

Figure 5.5: Magnitude distribution for two hydraulic fracturing stages monitored by a single array (from Vermylen and Zoback, 2011).

Looking at a magnitude scaling plot for the downhole recordings of the treatment that is being analyzed in this thesis in Fig. 5.6, it can be seen that all stages show different slopes for the log-linear part of the curve. Furthermore, the "linear" behavior of the curve clearly deviates from the theoretical ideal straight line.

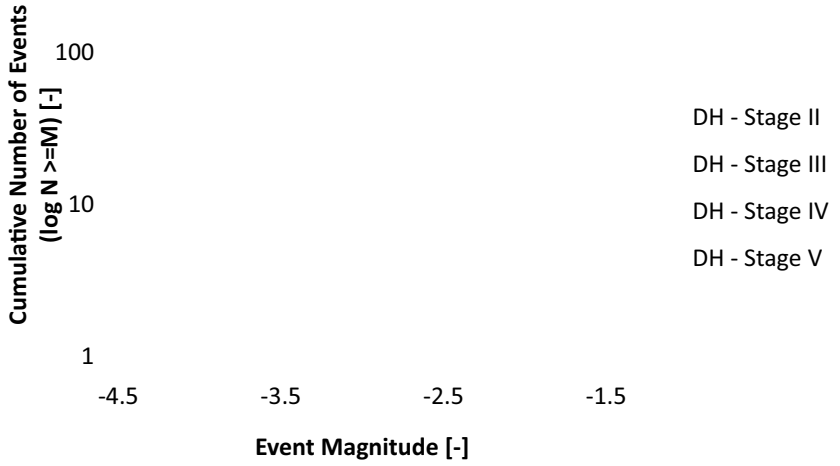

Figure 5.6: Magnitude distribution plot for downhole recordings of five stage hydraulic fracturing treatment in the Woodford Shale.

In order to more accurately compare the activity level for all stages, a threshold value of -3.4 was applied, as seen in Fig. 5.7. The b-values for the stages are 1.36 for Stage II, 1.75 for Stage III, 1.62 for Stage IV, and 1.29 for Stage V, respectively. a-values were observed with -3.52 for Stage II, -4.15 for Stage III, -3.52 for Stage IV, and -2.06 for Stage V, respectively. (The trendlines showed R^2 values of 0.9281 for Stage II, 0.9526 for Stage III, 0.9729 for Stage IV, and 0.9457 for Stage V.) Since the slopes are significantly different, the activity levels cannot be compared in a meaningful way. What can be seen though is that Stage II generates the least amount of microseismic events, which is not surprising since it is the earliest stage of all stages recorded. Stage V, being the last stage of the treatment, shows the most recorded events. Generating a magnitude scaling plot for the surface recordings of the treatment that is being analyzed, as seen in Fig. 5.8, is substantially less useful. With less than 20 events recorded for each of the first four stages, the curves clearly deviate from the theoretical behavior,

minimizing the qualitative information that can be obtained. Although more than 80 events were recorded for the last stage, the curve is not significant either.

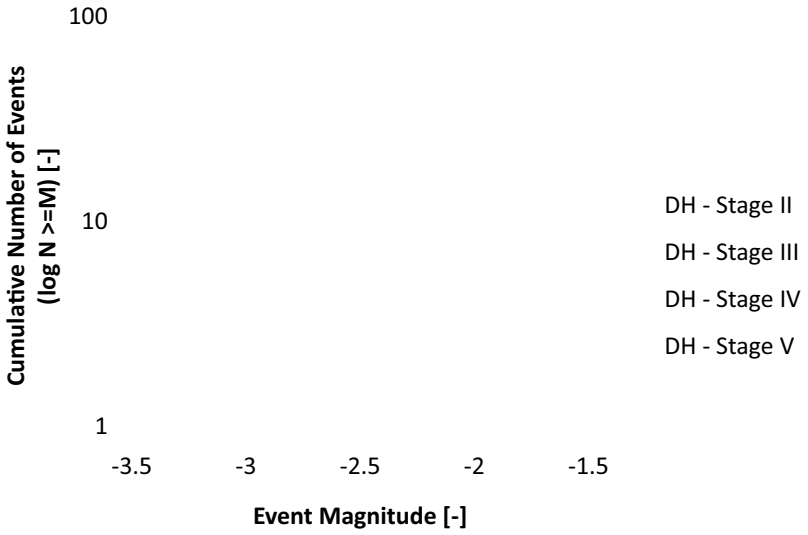

Figure 5.7: Magnitude distribution plot for downhole recordings of five stage hydraulic fracturing treatment in the Woodford Shale after application of magnitude threshold (trendlines can be seen in black for each stage).

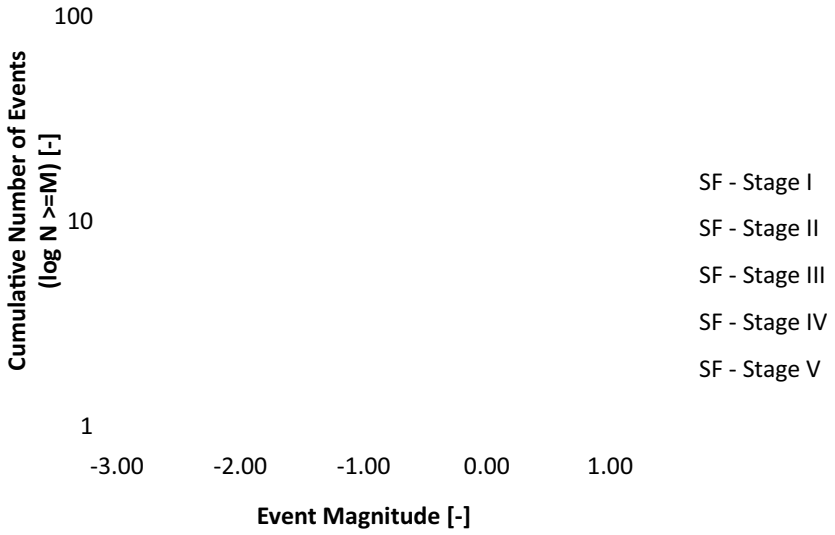

Figure 5.8: Magnitude distribution plot for surface recordings of five stage hydraulic fracturing treatment in the Woodford Shale

Comparing the plots for downhole and surface recordings, the effect of receiver-to-event distance can again be observed. While the downhole data includes substantially more events with a smaller magnitude the surface receivers have recorded more large magnitude events. Therefore, a combined plot generated from a data set that includes both surface and downhole events looks distorted and is of no practical use.

CHAPTER 6

FRACTURE COMPLEXITY AND INTERACTION WITH NATURAL FRACTURES

Communication between the hydraulic fracture network and natural fractures and faults can affect the efficiency of a stimulation treatment. By activating pre-existing structures, the hydraulic fracturing fluid is able to utilize them and possibly reach farther out into the reservoir, creating hydraulic connectivity between the artificially created network and the network that was already present but could not be fully utilized for flow of hydrocarbons.

However, communication with pre-existing structures can also have negative effects. The reservoir's leak-off behavior changes as natural fractures open up because matrix leak-off is no longer the only effect occurring. Additional flow-paths of potentially higher conductivity have an effect on proppant transport and may eventually lead to screen-outs in certain locations if leak-off is very high. Also, fracture (half-) lengths will generally be shortened by increased leak-off due to natural fractures. Another effect that is referred to as shear decoupling occurs when the treatment damages the rock. Separate 'pieces' of rock are no longer elastically coupled and therefore deform as discrete units, resulting in a reduction of fracture width as well as an increase in friction pressure, which ultimately complicates the placement of proppant (Barree and Winterfeld, 1998).

If the locations of the microseisms are prominent enough for a trend to be observed, they can indicate a hydraulic path. This association between microseismic connectivity and hydraulic connectivity can also be used to improve understanding of the reservoir in terms of pre-existing structures (Jupe et al., 1998).

The Woodford Shale in the subject area shows a west-east dip with a strike that is almost north-south. The treatment well was drilled almost parallel to the strike, from south to north, with the formation showing very little dip along the wellbore, resulting in a fairly 'flat' horizontal section. In the north part of a one square mile region, with the treatment well running in the middle of it, a fault-related structure can be found.

In the south-west corner of this parcel the fault structure shows almost 1,000 ft of displacement. This major fault with an east-west strike splinters into smaller fault structures having more north-south strikes. Since the perforation intervals for the earlier stages of the treatment are closer to these fault splinters, they might see more effects caused by their presence (Gertson, 2011).

The information obtained from the cumulative seismic moment plots in the previous chapter can be linked to faults or pre-existing natural fractures. During Stage V both surface and downhole sensors recorded the most events of large magnitude of all stages that were monitored. The surface data set even includes ten events with a magnitude larger than zero. For all stages, the observed microseismic activity overlapped with the region that was stimulated from the perforation cluster of the previous stage, which means that almost every stage fractured into the fracture network that was created by the previous stage. Stage V is not an exception, and, as mentioned in Chapter IV, in fact almost all of the microseismic activity occurred away from Stage V perforations. However, events of this magnitude might not only be related to the fracturing network of the previous stage, but also to faults providing large enough slip surfaces to produce such large events. A large slip area and a large distance of slip demonstrate the presence of such pre-existing structures (Gertson, 2011).

Another indication for interaction with pre-existing structures is the speed of fracture propagation (Gertson, 2011). However, the speed of propagation, which is linked to the speed of event generation, can also be influenced by 'pre-existing' structures such as a fracture network that was created during a previous stage. Examining the time-lapse playback for Stages III and V of both surface and downhole data, it can be seen that events are generated more than twice as fast than during previous stages, implying the utilization of pre-existing faults and fractures. Fig. 6.1 shows a plot of the cumulative number of recorded events against time for the downhole data. The x-axis shows negative values for events recorded west of the treatment well and positive values for events recorded east of the treatment well. The y-axis shows the time in minutes and is truncated to a 30 minute difference between each stage instead of showing the full time difference between pumping consecutive stages. It can be seen that the smaller the angle between x-axis and a particular curve is, the faster events were generated for that stage. Steeper curves with a larger angle to the x-axis indicate slower event generation. The plot visualizes how fast events were generated better than

the time-lapse playback and clearly depicts that Stages III and V are the stages with the highest speed of event generation.

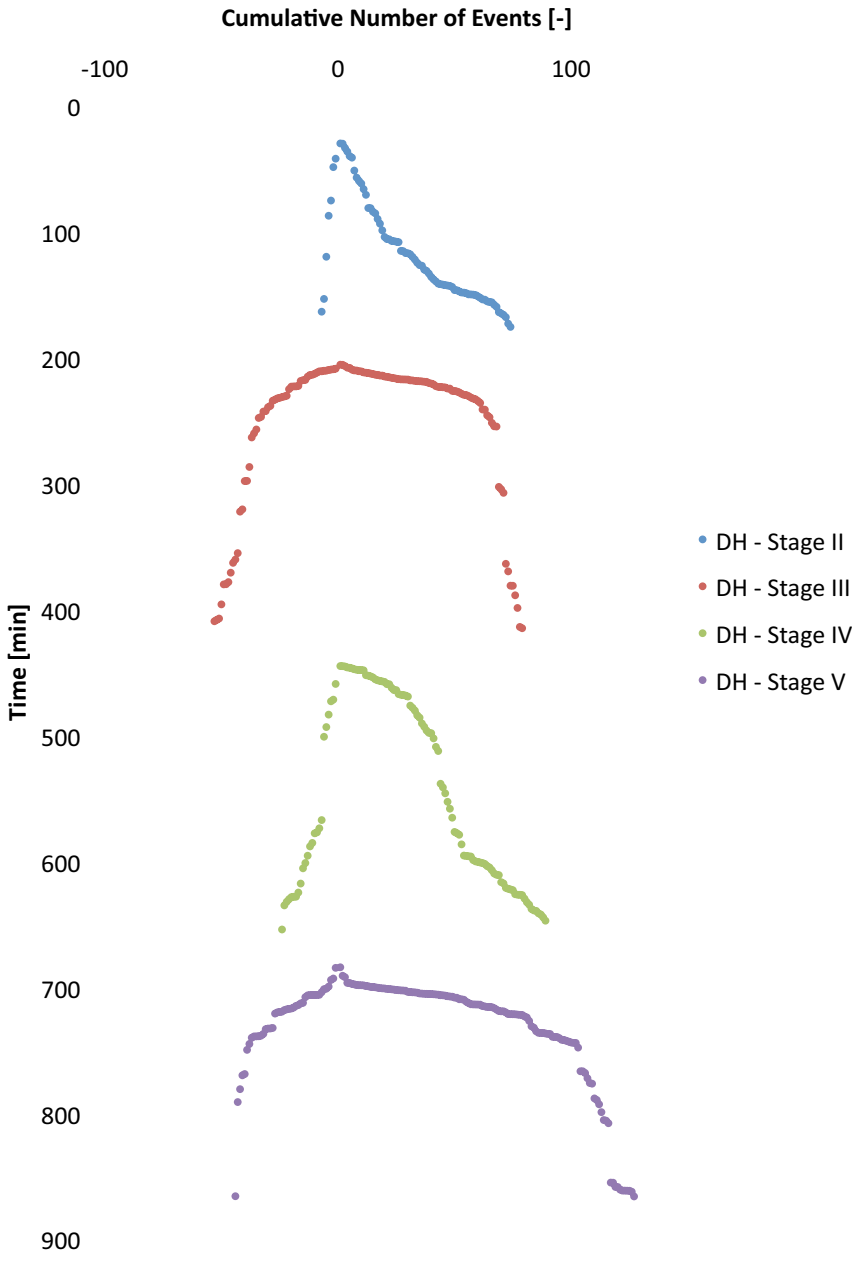

Figure 6.1: Cumulative number of events versus time for downhole microseismic data. Events generated west of the wellbore are shown on the negative x-axis, whereas events generated east of the wellbore are shown on the positive x-axis. The speed of event generation is indicated by the slopes of the curves.

The paleo-stress direction in this area of the Arkoma Basin was south-east to north-west, which changed to west-east, plus-minus about ten degrees, in present days (Gertson, 2011). Looking at the fractures in Fig. 6.2, they generally seem to follow the maximum present day stress.

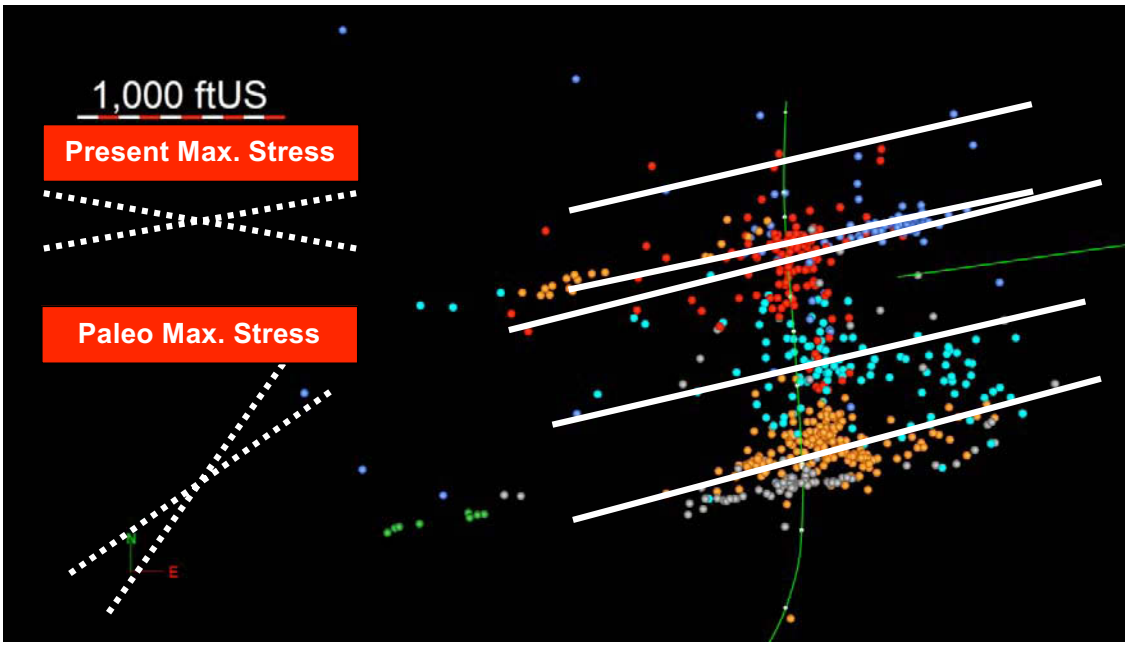

Figure 6.2: Microseismic recordings from both surface and downhole receivers. White solid lines show fracture azimuths. The respective downhole and surface events are shown in Figs. 6.3 and 6.4. The horizontal well trajectory of the treatment wellbore can be seen in green from south to north. The monitoring well can be seen in green east of the treatment well.

Fig. 6.3 shows the microseismic events that were recorded by surface receivers during all five stages of the treatment. Comparing Fig. 6.3 to Fig. 6.4, which shows the downhole recordings, it is obvious that the complexity of the created fracture network can be better observed from the downhole recordings, due to the simple fact that a lot more events were recorded. However, it can be seen that the downhole sensors did not fully record any microseismic activity far to the west of the treatment wellbore, most likely because of the viewing limit of the geophones. Due to the superior areal coverage of surface monitoring compared to monitoring from an offset well, it was able to pick up more microseismic activity occurring far away from the treatment wellbore. Whether this activity far out in the reservoir is truly related to the activation of natural fractures and faults, though, is arguable.

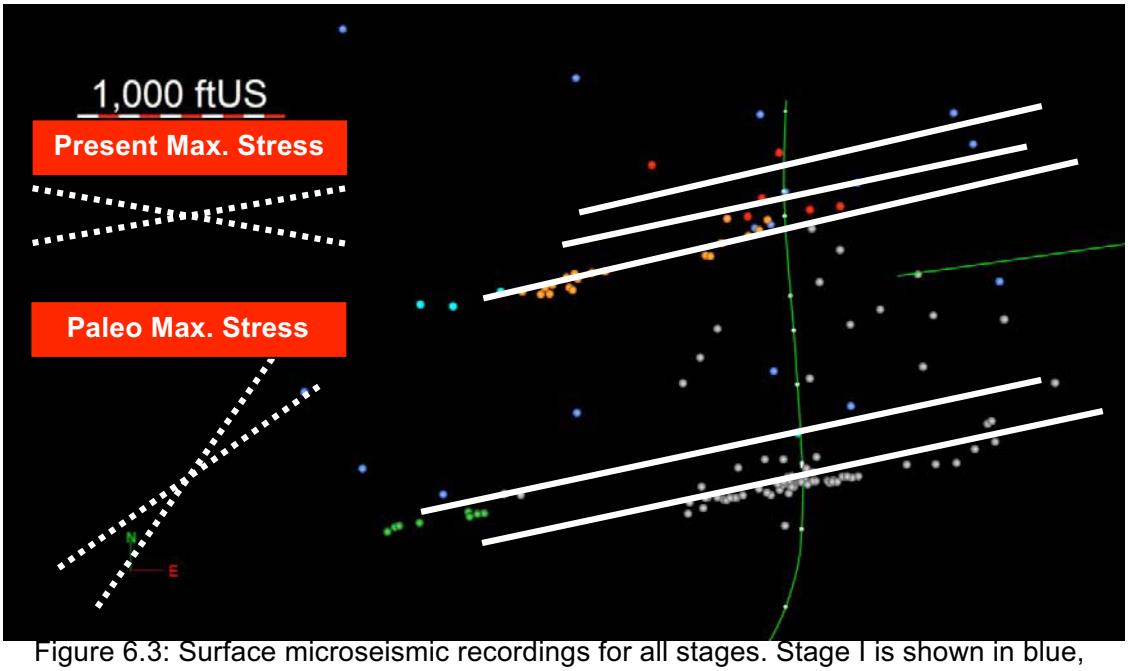

Figure 6.3: Surface microseismic recordings for all stages. Stage I is shown in blue, Stage II in red, Stage III in orange, Stage III ½ in turquoise, Stage IV in green, and Stage V in grey . White solid lines show fracture azimuths. The horizontal well trajectory of the treatment wellbore can be seen in green from south to north. The monitoring well can be seen in green east of the treatment well.

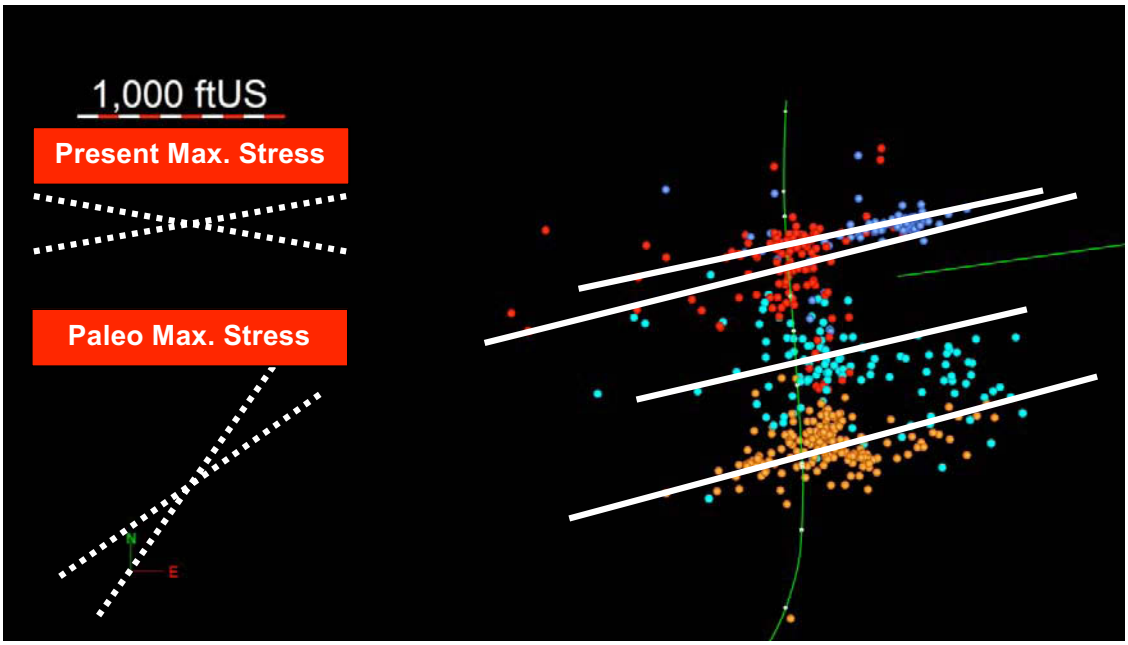

Figure 6.4: Downhole microseismic recordings for all stages. Stage II is shown in blue, Stage III in red, Stage IV in turquoise, and Stage V in orange. White solid lines show fracture azimuths. The horizontal well trajectory of the treatment wellbore can be seen in green from south to north. The monitoring well can be seen in green east of the treatment well.

Evaluating the stages that were monitored by downhole sensors, as seen in Figures 6.5 through 6.8, it is obvious that the created hydraulic fractures highly deviate from the idealistic planar single-fracture model. It can be seen that although the general fracture azimuth follows the present day stress in E-W direction, features related to structures following the SE-NW paleo stress could also be observed. Time-lapse playback visualized event generation along both of those features, although the behavior was more pronounced for the main fracture azimuth following the present day stress. It can be inferred that the stimulation treatment was successful in creating a fairly complex hydraulic fracture network for all stages. It should be noted that influencing the downhole stress regime by drilling a long horizontal interval also has an effect on the complexity of the created fracture network, although it is not known to what extent.

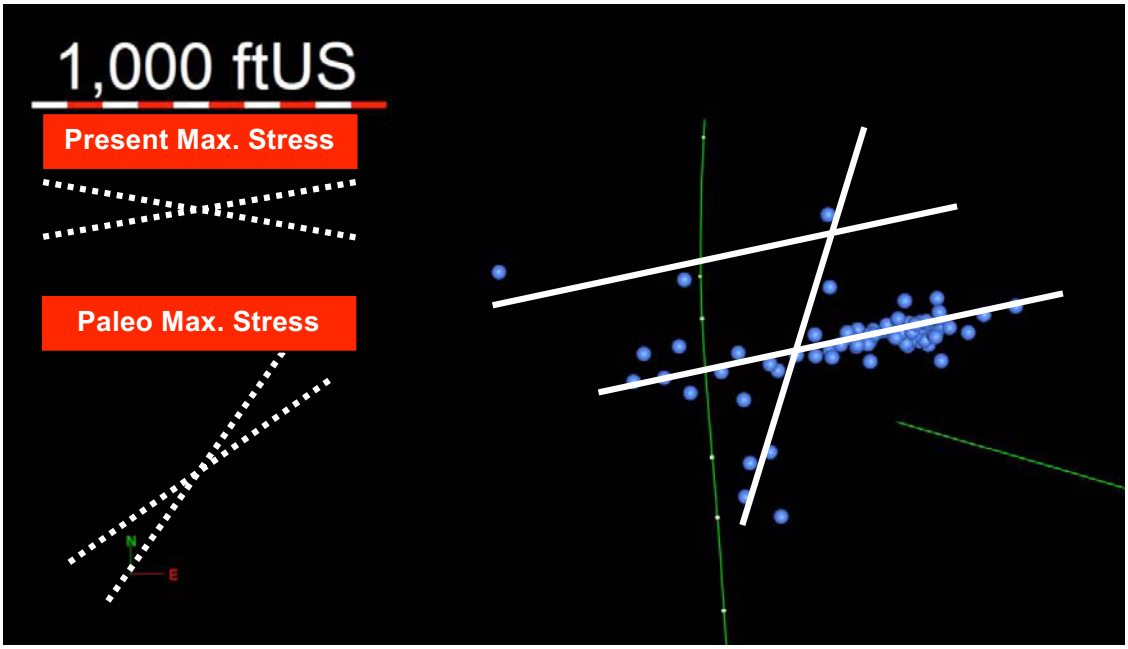

Figure 6.5: Microseismic downhole recordings (blue spheres) for Stage II. White solid lines indicate the complexity of the created fracture network. The horizontal well trajectory of the treatment wellbore can be seen in green from south to north. The monitoring well can be seen in green east of the treatment well.

In the Viola limestone below the Woodford Shale karsts were developed when it was on the surface during the Ordovician. This karst system can be found all over the Arkoma Basin and is clearly visible on seismic maps. Most of the karsts collapsed at some point causing a localized downward shift of the overlying geology indirectly adding

complexity to the Woodford Shale. In the vicinity of the treatment well, karsts can be found west of the horizontal interval close to the Stage IV and Stage V perforation clusters. In Fig. 6.9 only showing events recorded during these stages such a karst can be seen where no microseisms have been recorded. Although it is unclear what kind of effect these structures have on hydraulic fracturing treatments, it is assumed that the fracturing fluids are transported around the karst, along fractures that were created during the formation of the karst, rather than through the geology filling the karst (Gertson, 2011).

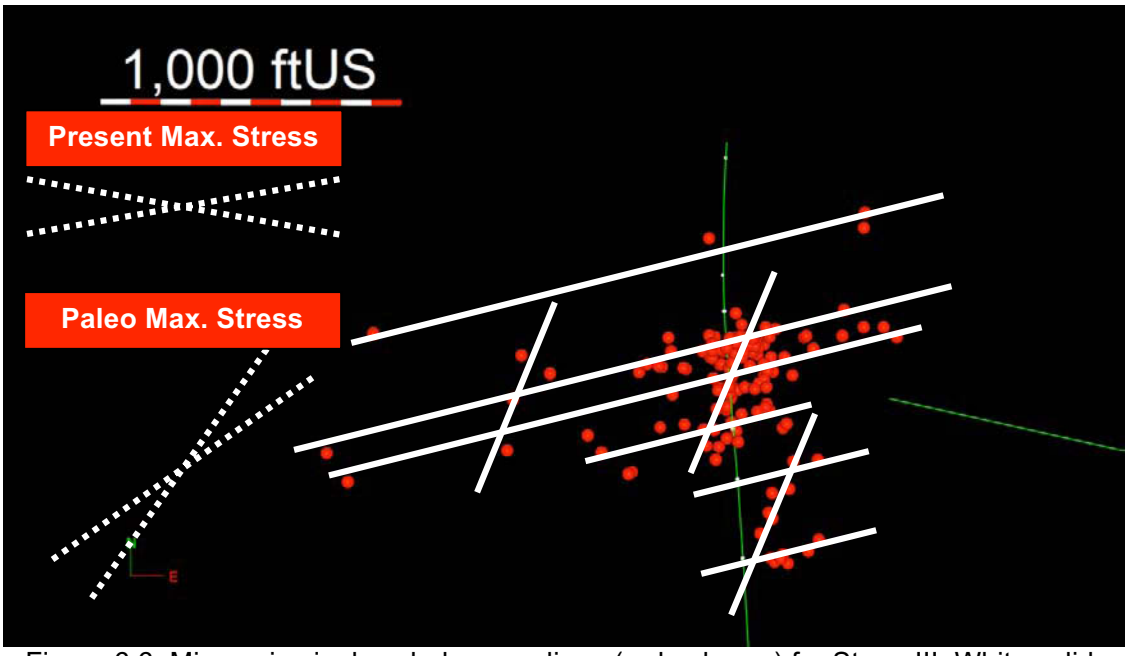

Figure 6.6: Microseismic downhole recordings (red spheres) for Stage III. White solid lines indicate the complexity of the created fracture network. The horizontal well trajectory of the treatment wellbore can be seen in green from south to north. The monitoring well can be seen in green east of the treatment well.

In the case where faults are present and in contact with the injected fracturing fluid, they can shift the microseismic picture and lead to misinterpretation and incorrect analysis of the treatment. However, they can usually be identified by examining the recorded data. Microseismic activity occurring after the job has been executed can be explained as 'aftermath' shear deformation on the one hand due to the treatment, but if the events are of an unusually large magnitude on the other hand, they can be attributed to activation of and interaction with existing faults. Also, large magnitude events

throughout the treatment can identify involvement of a fault when looking at a plot of event magnitude versus distance from the receiver (Downie et al., 2010).

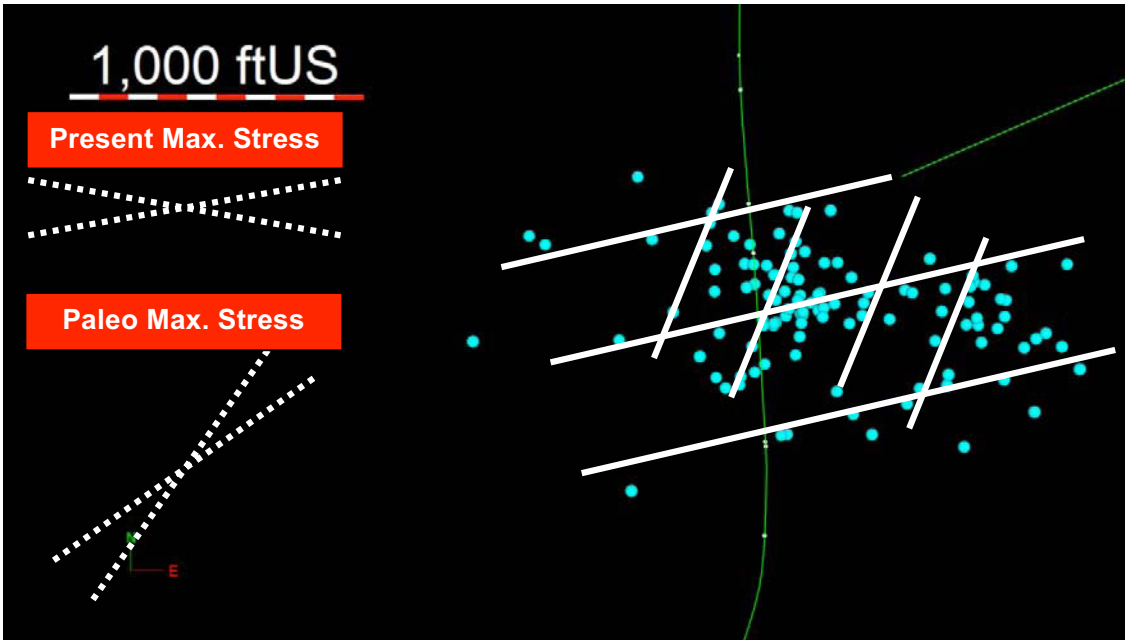

Figure 6.7: Microseismic downhole recordings (turquoise spheres) for Stage IV. White solid lines indicate the complexity of the created fracture network. The horizontal well trajectory of the treatment wellbore can be seen in green from south to north. The monitoring well can be seen in green east of the treatment well.

A fairly easy technique to evaluate the interaction with faults is plotting the magnitude of events against the distance to the receivers (Warpinski, 2009). Since the strength of a microseismic event, i.e. the seismic moment, and consecutively the event magnitude, depend on the amount of shear displacement along the fault plane and the area of the fault plane, as seen in Eq. 2.6, events generated along pre-existing fault structures are very likely to produce events of larger magnitude. A magnitude versus distance plot therefore makes it easy to identify these events, and relate them to the interaction with faults. Additionally the viewing limit for a certain formation can be obtained.

When generating the magnitude-distance plot for the data set, the location to which the distance from an event was calculated was set to the center of the receiver string at 7,646.5 ft. Without any information about which event was recorded by which

receiver, the exact receiver-to-event distance was unobtainable making the plot slightly less accurate. However, this is the practice commonly used in the industry.

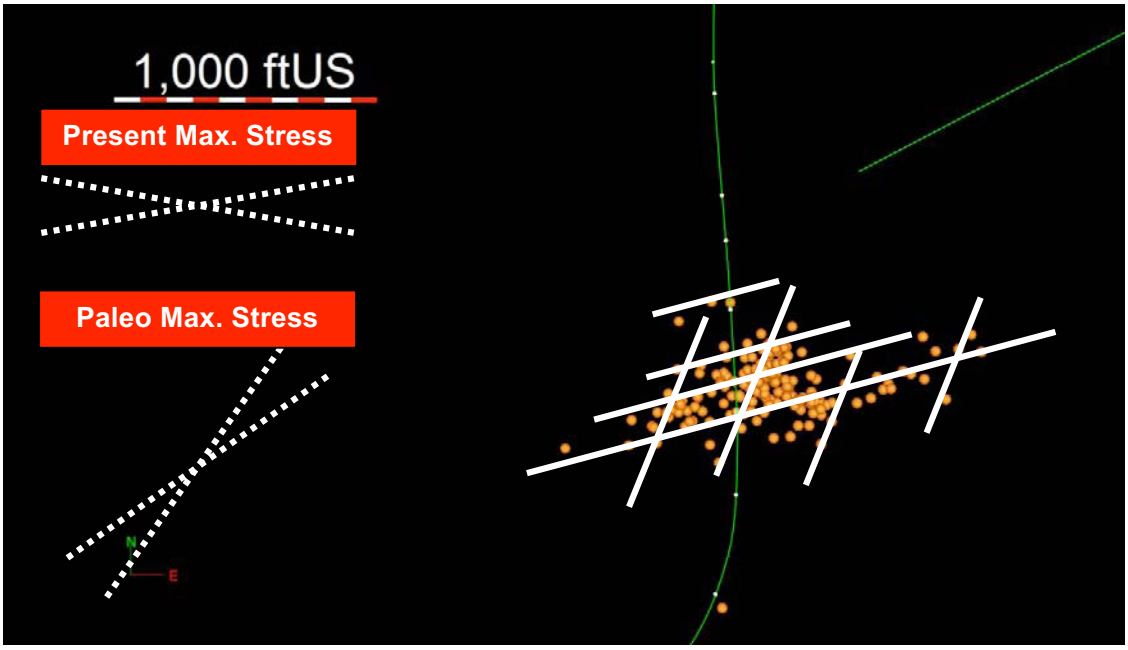

Figure 6.8: Microseismic downhole recordings (orange spheres) for Stage V. White solid lines indicate the complexity of the created fracture network. The horizontal well trajectory of the treatment wellbore can be seen in green from south to north. The monitoring well can be seen in green east of the treatment well.

Fig. 6.10 shows what the cumulative seismic moment plots already visualized: Stages III and V show the most events of large magnitude. An upper limit for the typical event magnitude can be established at about -3.1 giving a viewing limit of about 1,900 ft for the Woodford Shale in this region. The link between 'loud' events and intersecting faults leads to the assumption that the fracture network generated during Stage V most likely communicated with a fault. Stage III and even Stage IV, although with fewer events of larger magnitude, show a similar behavior. However, it is not as clearly pronounced as for Stage V. Only minor communication with a fault occurred during Stages III and IV, if at all.

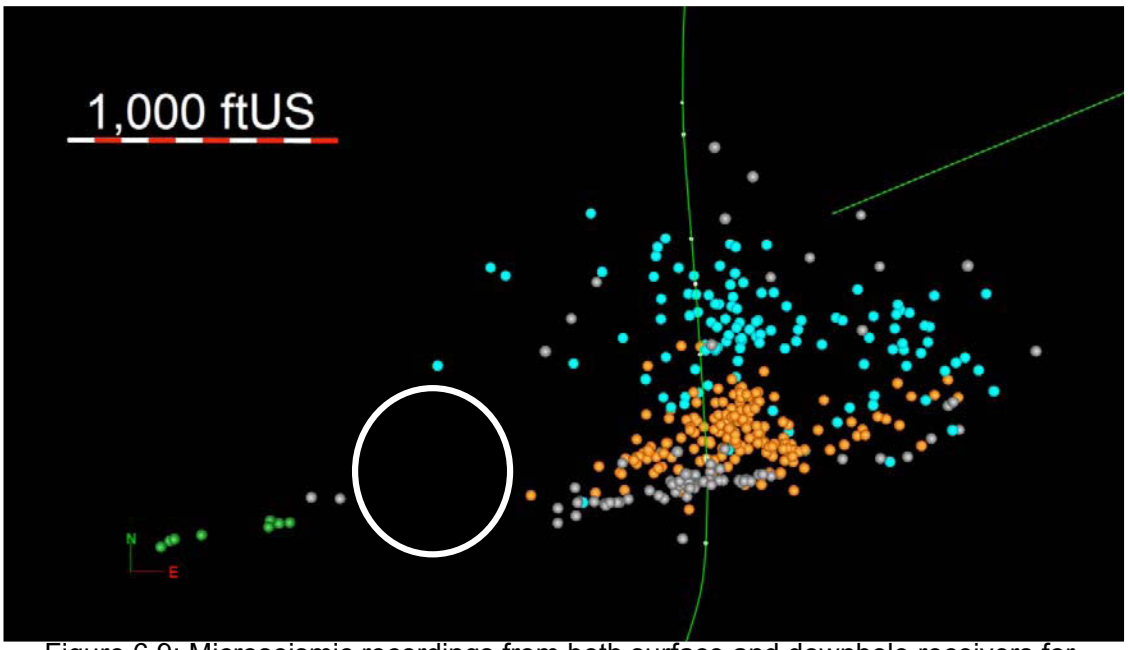

Figure 6.9: Microseismic recordings from both surface and downhole receivers for Stages IV and V. Location of the karst is marked by the white solid circle.

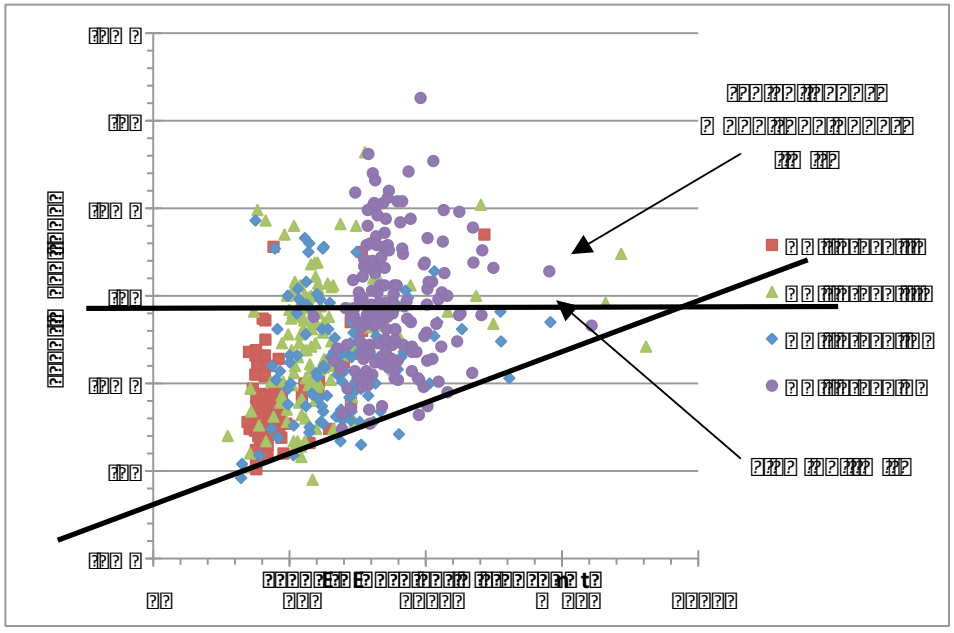

Figure 6.10: Magnitude-distance plot for downhole data.

CHAPTER 7

ERROR ANALYSIS

Two things are crucial in determining the actual position of the microseismic event in the reservoir: the geological velocity structure, and the carefulness of picking the direct arrivals of the acoustic wave. The accuracy of the event location is therefore limited, with restraints being related not only to signal processing but also due to the tool itself (Le Calvez et al., 2005).

There are advantages and disadvantages related to both surface and downhole monitoring. Surface receivers usually have a higher threshold for detecting events and are only able to record lower frequency signals. Furthermore the distances between sensors and events are generally fairly high, so it can be more difficult to detect microseisms on the surface if they have to travel through a couple of thousand feet of formation. Due to the geometry and extent of the array however, they provide a broader and more uniform coverage. Downhole receivers on the other hand are usually closer to the part of the reservoir that is being stimulated, and can also be in the treatment well itself. Being able to record more signals, it should be noted that they may be biased due to the location of the monitoring well (Abbott et al., 2007). Surface receivers are subjected to more environmental noise than downhole sensors, which allows consistent imaging of P-wave arrival times only. Downhole receivers on the other hand can record both P- and S-wave arrivals accurately (Eisner et al., 2009). According to general observations by Eisner et al. (2009) for surface monitoring with a 1:1 depth to offset ratio the error in the vertical position can be several tens of meters, with over 40 m for most common scenarios. Whereas the vertical position is very sensitive to the velocity model, the horizontal position seems a lot more robust, with no specific bias in any direction and an error of usually below 10 m. Downhole sensors on the other hand show very low error in the vertical position of under 10 m for most common scenarios, but can have an azimuthal uncertainty in the range of tens of meters. However, this depends on the location of the event in conjunction with the tool location.

Considering all of the above it is obvious that every single event occurring and recorded during a stimulation treatment has an accuracy level of its own, which is basically a combination of travel time tagging, the geological velocity model and event signal strength. A plot showing all events can therefore be misleading because it does not include a tool to display how accurately each location was determined (Zimmer et al., 2009). A study with synthetically generated microseismic events done by Maxwell in 2009 clearly shows the errors associated with obtaining fracture dimensions from microseismic data. Usually the outlines of the cloud of events are used to gather the fracture dimensions, which unfortunately have a higher level of inaccuracy associated with them than events closer to the receivers and could potentially be statistical outliers as well. It is therefore important to evaluate the location error of each event.

Probably the biggest factor that creates difficulties even when everything else was optimized is noise. Microseismic events have very low amplitude and can therefore easily be out-drowned by environmental noise. This can be as small of a signal as is generated by gas bubbles traveling past the sensors. Common sources of noise are drilling activity that is undertaken in the same field and production through artificial lift, which can influence both downhole and surface sensors, as well as roadwork, flow behind the casing due to poor cement integrity, leaking bridge plugs, and fluid flow in nearby wells (Weijers, 2011). Surface receivers are especially affected by noise generated on the surface, such as trains or cattle. While noise cannot always be avoided, it should be kept at a minimum, since filtering can be complicated by the fact that microseisms and noise often show a similar range of frequency (Warpinski, 2009a).

The core piece of microseismic processing is the velocity model. It is the basis on which the distance between the event and the receiver is calculated, once an event has been detected. An inaccurate velocity structure can result in an error of a couple of hundred feet, rendering the recorded data useless. The easiest way to build a reliable model is a dipole sonic log that records both compressional and shear velocities. While the vertical velocities can be used to calibrate the velocity model for the surface sensors, they have to be converted to horizontal velocities for processing the downhole data, which is achieved with perforation shots. This is an important step, as horizontal velocities can deviate up to 20% from the vertical velocities (Warpinski, 2009a). In case sonic data has not been collected when running a log it can be synthetically generated from Gamma Ray, neutron porosity, average porosity, and from resistivity. Naturally the

four curves will not be the same due to the different input parameters. They especially deviate from each other in areas of higher gas saturation due to the individual behavior of each parameter the curves are based on (GOHFER^{TM} LAS User Manual). As sonic data was not available for this project, synthetic DTC curves were used to generate further parameters such as Poisson's Ratio and Young's modulus. The most reasonable results were achieved with a DTC curve that was generated with correlations based on volume fraction weighted lithology.

In order to orient the sensors in an earlier step a calibration shot or perforation shot in a known position at a known time is used. This calibration shot can also be used to calibrate the velocity model. It should be noted that although the acoustic waves use the same travel part to the receivers that the microseisms will use, "it generally does not generate a wide enough array of ray paths to characterize all of the layers needed" (Warpinski, 2009a). Deliberately leaving the time of the shot as an unknown, the velocity structure can be further refined. With the location as a given variable the model can be adjusted to accurately locate the event while minimizing the residuals for each tool in the array at the same time (i.e. the difference between the theoretical or calculated travel time and the actually picked travel time) (Warpinski, 2009a).

7.1 Surface

In this project, the surface array was laid out in a star shaped fashion with straight lines of geophones originating from a central location that was near the surface location of the treatment well. The velocity model that was used in determining the event locations recorded by surface receivers was based on the operating company's 3D seismic profile for that region, and was adjusted based on perforation shots (Gertson, 2011). As mentioned in Section 4.1.1, the data set contained a large number of events, which were unfortunately too scattered to give a clear picture. After the application of a cut-off value that was determined at a point where a significant change in slope occurred on a plot of cumulative number of events versus event magnitude, the data set delivered a more reliable picture of fracture growth. With the aforementioned plot, it was determined that a fairly large amount of events occurred within a very small range of very small magnitude (-2.75 to -3.75). Considering the higher detection threshold of

surface receivers as well as the vertical depth of about 8,000 ft, events of such a small magnitude should be treated with caution in general, and were therefore not considered for this analysis. Unfortunately there was no quality report available for the surface imaging. However, taking into account the good agreement between surface and downhole data as well as the sophisticated velocity model available, it can be assumed that the surface data set has a very high level of confidence, and event location can be considered as accurate as possible.

7.2 Downhole

It is generally acknowledged that the best results can be obtained when downhole sensors are positioned across the interval of interest. This delivers events of the highest amplitude, that show the least possible effect of the velocity structure, and most accurately monitor activity above, in, and below the zone of interest (Warpinski, 2009a). However, in this particular case, the geophones were positioned above the Woodford Shale, and not across it. As mentioned in Section 4.1.2, the Woodford Shale shows a substantially lower seismic velocity than the Mayan Shale above it, and the Hunton Limestone and the Sylvan Shale below it, so the seismic energy that would be recorded by sensors straddling the Woodford Shale would arrive refracted rather than direct, leading to possible incorrect calculation of the event location (Gertson, 2011).

The velocity model used in determining the event locations recorded by downhole receivers was derived from a dipole sonic log from an offset well that was depth-corrected to match the treatment well. This initial velocity structure was then further calibrated with perforation shots representing both a known event location and a known time of event generation. The respective service company was able to calculate the perforation locations very close to their known locations, making the velocity model accurate.

Chapter VI has already evaluated a quality control parameter that is easily obtainable: a plot of event magnitude versus receiver-to-event distance. The farther away an event occurs from the tool, the larger its moment magnitude has to be in order to be distinguished from environmental noise and accurately detected. The so-called ‘viewing limit’ of a receiver, which was determined at about 1,900 ft in this situation, is a

characteristic of the formation and the project set-up, and determines how accurate microseismic imaging will be in the first place, considering location of events, location of monitoring tools, noise, and specific geology (Zimmer et al., 2009).

More quality control parameters, such as the average noise level vs. time, sensor specific noise levels, signal-to-noise ratio (SNR) statistics, time-residual statistics, data and event confidence, and location error could be found in the quality report that was issued by the respective company that monitored the treatment.

The noise levels that were identified from the recorded data were calculated with the average RMS amplitude over all tools that were employed. When each sensor is evaluated separately, it can be observed that the noise levels are similar for every sensor and show the same behavior for each stage. Examining the average background noise levels for each stage it can be seen that all sensors recorded noise at levels between $5 \cdot 10^2$ nV and $1 \cdot 10^3$ nV. For Stage II the noise level starts out at about $1 \cdot 10^3$ - $2 \cdot 10^3$ nV in the beginning and drop to about $5 \cdot 10^2$ - $1 \cdot 10^3$ nV in the end. Stage III shows more fluctuation at levels of about $6 \cdot 10^2$ nV to $2 \cdot 10^3$ nV. Stage IV shows similar fluctuations between $6 \cdot 10^2$ and $3 \cdot 10^3$ nV, with a spike of $8 \cdot 10^3$ nV towards the end. During Stage V more noise was recorded at the beginning at up to $1 \cdot 10^4$ nV leveling off towards the end within a range of $6 \cdot 10^2$ to $2 \cdot 10^3$ nV.

An important value used to rate the quality of the recorded data is the signal-to-noise ratio. It determines the accuracy of the arrival times and is calculated by comparing the RMS amplitude of the signal before and past the travel time pick. The SNR can sometimes better indicate the location error for a particular event than the event magnitude, since a distant event can be of a large magnitude, falsely implying accuracy, but have a poor SNR. The calculated location of this event is therefore more inaccurate as the travel times are badly picked, which is implied by the low SNR (Zimmer et al., 2009). Events should have a SNR of above 1, representing the lower end of the acceptable range, while a SNR of above 3 characterizes high quality signals. The sensors generally show most events with a SNR of above 1, with more than half of them having a SNR of above 3.

In order to evaluate the accuracy of the calculated azimuth, the difference between the azimuth observed by a specific sensor and the average azimuth for all

events is visualized in a hodogram variation plot. An average variation over all tools of as close to zero as possible is desirable. For this data set the hodogram consistency for all receivers is found to be between – and + 18 degrees.

As mentioned, the time residual is the difference between the theoretical or calculated travel time and the actually picked travel time. This residual characterizes the accuracy of both the arrival time picks and the velocity model and should be minimized at values close to zero. Most sensors show a very narrow range of time residuals between -3 and +3 ms. The deepest sensor however shows a wider distribution indicating poor travel time accuracy.

The event confidence is a value that indicates the overall quality of all variables that go into calculating the event location and ranges from zero, signalizing a very low confidence, to five, implying a very high confidence. It takes into account information of the number of sensors, the average time residual for both P- and S-wave, the signal-to-noise ratio for both P- and S-wave, as well as the hodogram variation. Most events, especially the ones outlining the main fracture have a confidence of 3 and above. The farther away from the main fracture and from the monitoring wellbore, the lower the confidence. The closer to the center lines of the main fracture the higher the confidence, although there are some low confidence events as well. The average confidence for all events of all stages was 3.12, with individual average confidence values of 3.07 for Stage II, 3.27 for Stage III, 2.60 for Stage IV, and 3.38 for Stage V, respectively.

The event location error is made up of three parts: error in azimuth, error in radius from the receiver, and error in vertical depth. While the azimuth error is derived from the variation of the azimuth estimates for each tool and increases with distance from the sensors, the depth and radial errors are determined by the effect of arrival time residuals on the event location. The azimuth error was found to be between zero and eight feet, with a radial error between six and 34 feet; most events were found between nine and 26 feet of radial error though. The vertical error also shows a wide range of eight to 34 feet, although for events recorded during Stage V it can be up to 76 ft. Figures 7.1 through 7.4 show the radial and azimuth error for each stage.

The azimuthal error can be up to several hundred feet for some events, and the radial error is in the range of multiple tens of feet. It should be noted that the error bars

do not represent an equally distributed probability along the bar. The depicted event location is far more probable than the event being located at the edges of the error bars (Zimmer et al., 2009).

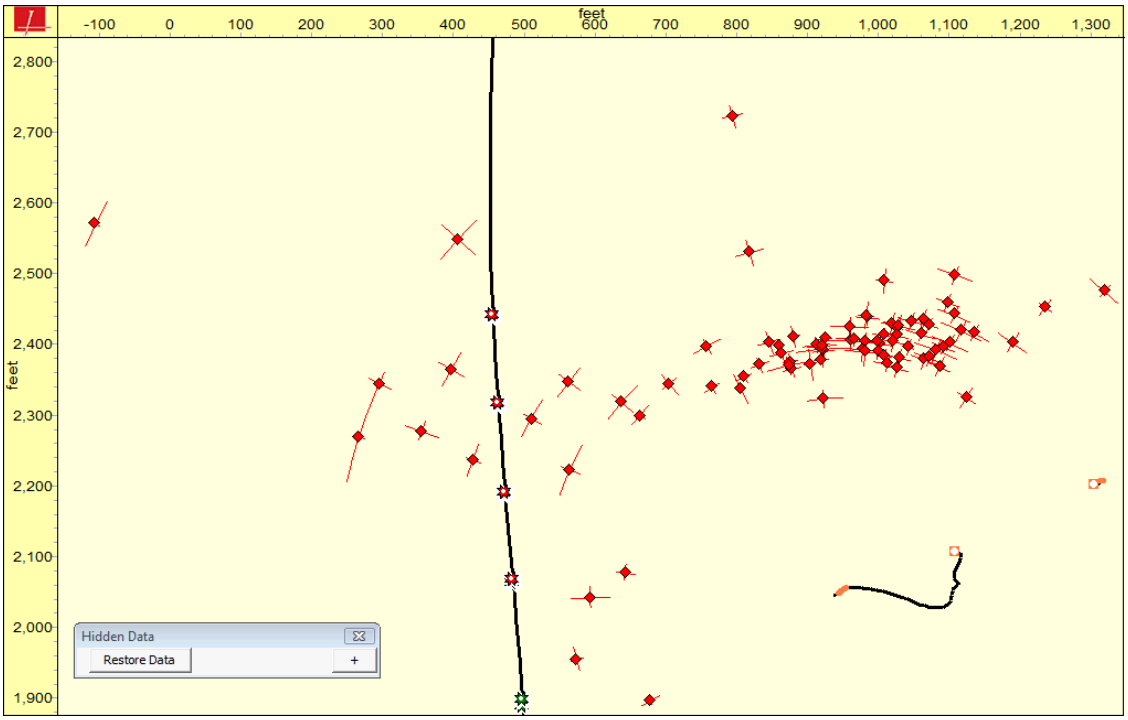

Figure 7.1: Radial and azimuth error for downhole recordings of Stage II. The horizontal well trajectory of the treatment wellbore can be seen in black from south to north. The monitoring well can be seen in black east of the treatment well.

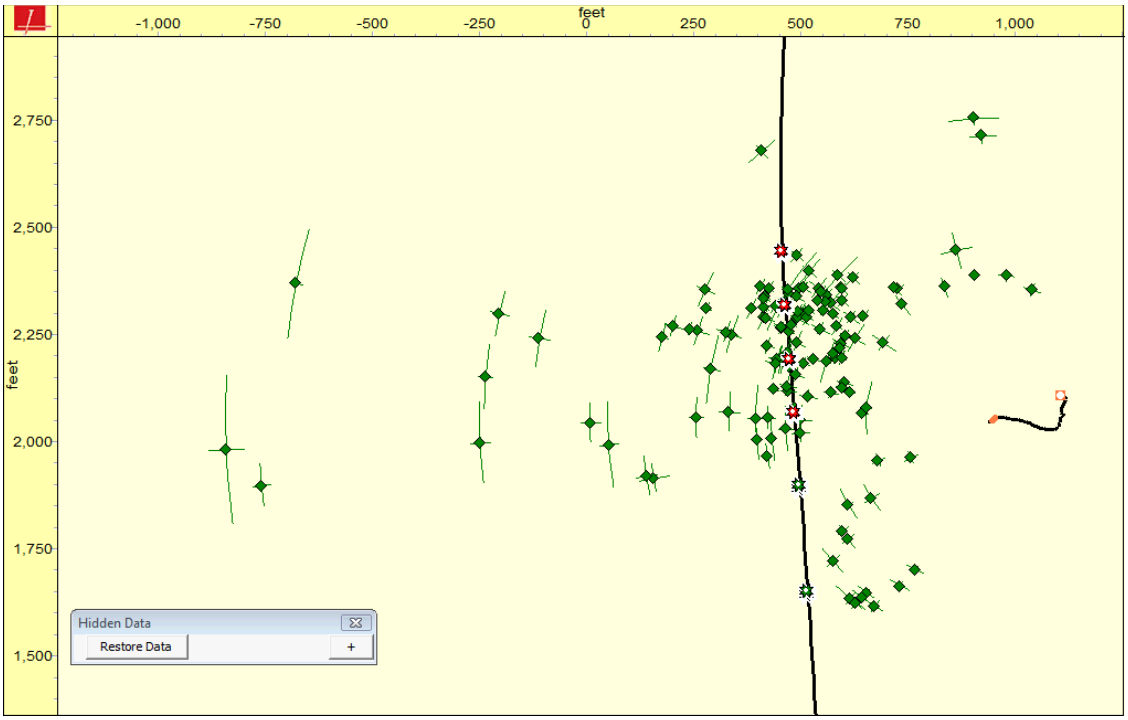

Figure 7.2: Radial and azimuth error for downhole recordings of Stage III. The horizontal well trajectory of the treatment wellbore can be seen in black from south to north. The monitoring well can be seen in black east of the treatment well.

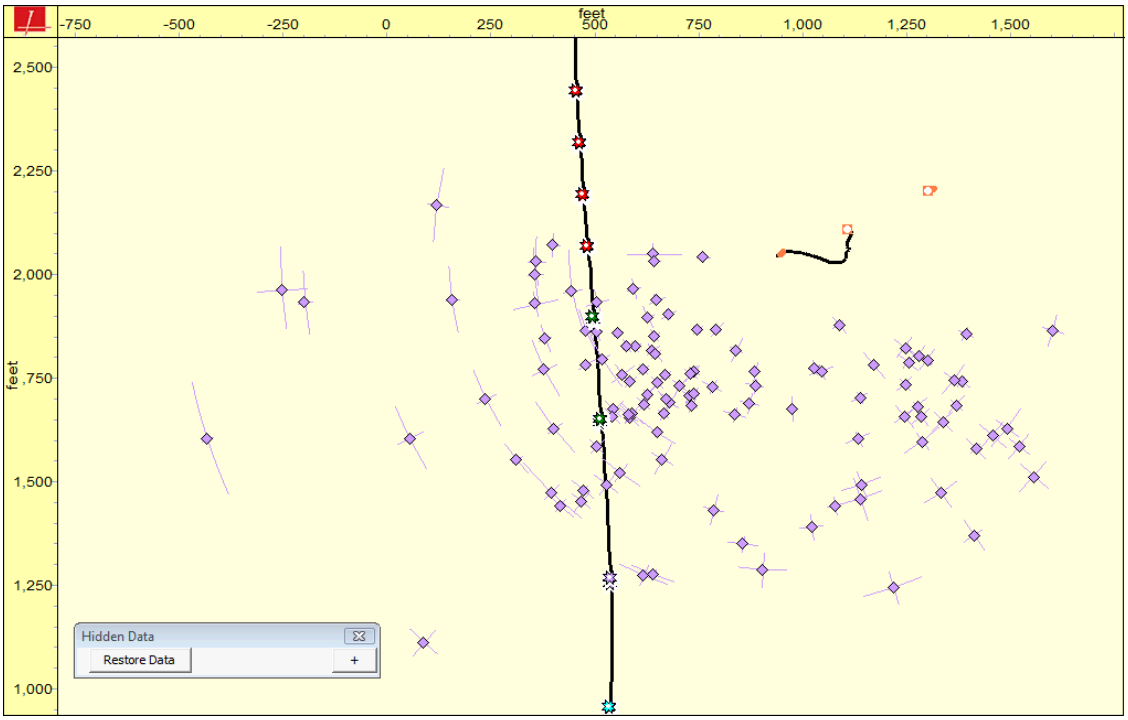

Figure 7.3: Radial and azimuth error for downhole recordings of Stage IV. The horizontal well trajectory of the treatment wellbore can be seen in black from south to north. The monitoring well can be seen in black east of the treatment well.

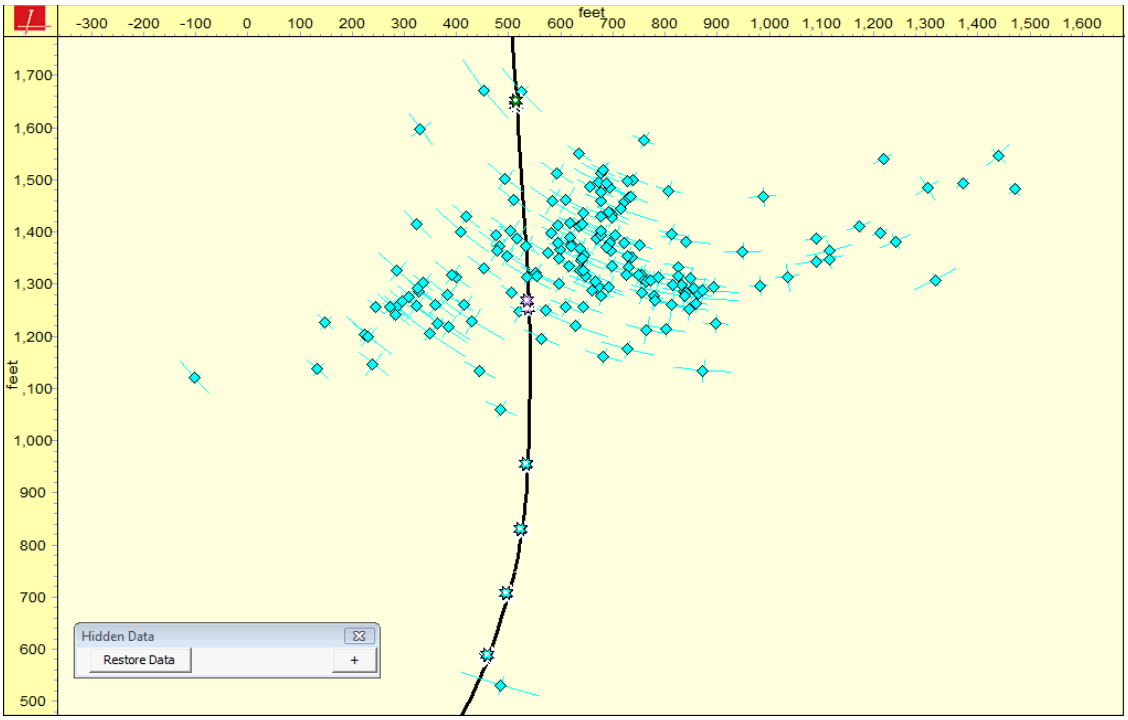

Figure 7.4: Radial and azimuth error for downhole recordings of Stage V. The horizontal well trajectory of the treatment wellbore can be seen in black from south to north. The monitoring well can be seen in black east of the treatment well.

CHAPTER 8

DISCUSSION

This chapter discusses the results obtained from the hydraulic fracture models that were developed for each stage, as well as, the congruency between surface and downhole microseismic data. Furthermore, it summarizes the findings in terms of reservoir characterization, and discusses the results of the error analysis.

8.1 Hydraulic Fracture Models

One of the core pieces of this thesis were the hydraulic fracture models for each stage. Modeling in combination with fracture diagnostic technologies is able to produce results that improve our knowledge of the fracture propagation processes, which is especially of importance in regions with complex geological structures and for unconventional reservoirs, such as shales. Populating a hydraulic fracture model with known petrophysical properties and modifying it consecutively in order to mirror microseismic recordings provides a calibrated model for a specific area to more accurately characterize the reservoir. The information gained from such an analysis helps to improve future treatments as well as reservoir management in the long run (Warpinski et al., 2006).

Two models were built for each of five fracturing stages in the subject well, one in the longitudinal direction of the wellbore, simulating the longitudinal dimension of the fracture network, and one perpendicular to the well, simulating the length of the transverse fractures. Although GOHFER^{TM} simulates fracture growth in 3D, the third dimension is the fracture width. For a planar fracture, this gives a fairly complete, although simple, representation of fracture growth. For complex fracturing, however, it does not. There are two components of a transverse fracture, the longitudinal stretch of the fracture network along the wellbore, and the actual, transverse, fracture length. A geometry match with the longitudinal models only gives half of the picture, i.e. the

longitudinal dimension of the microseismic cloud and not the transverse fracture length. A possible way to overcome this is to build a model that is a perpendicular cross-section of the horizontal wellbore instead of a longitudinal one. For the subject models, there is just one grid cell in the middle of the 3,000 ft grid representing all perforations of the whole interval. The perforation cluster is simply collapsed into one point, i.e. a grid cell, at the center of the perforation interval for each stage. The software then simulates fracture growth as if it were initiated from a perforation cluster of a vertical wellbore. This modification leads to a very high shot density, and does not take into account that the perforations are actually distributed longitudinally along the wellbore. Furthermore, it assumes that the rock properties obtained from the available logs are uniformly distributed along each direction, since the same values used for the longitudinal plane were then used for the transverse plane. However, this approach helps to complete the picture and provides a simulated fracture length in the same plane as the transverse fracture length. Since GOHFER™ simulates symmetrical fracture growth for the subject models, the longer half-length was doubled and used as a total length in the simulations.

The geological set-up of the models was based on a log suite from the monitoring well, to which a depth shift of -18 ft was applied, in accordance with stratigraphy correlations. Since there were no measurements of acoustic velocities available, the compressional travel time curve was artificially generated from GOHFER™'s built-in log calculation module, based on the average porosity. Important properties such as Young's modulus and Poisson's ratio were found to be within the range of usual values for the Woodford Shale, with Young's modulus on the lower end of the spectrum, and Poisson's ratio on the higher side. Tectonic strain was used to match the pressure curves, as it increased the simulated pressure in a way that a modification of other parameters could not achieve, or where adjustment of other parameters was not found to be reasonable. The calculated fracture gradient with a default tectonic strain of 100 microstrains matched the one that was anticipated by the service company very well. Additional feedback for the geological set-up was provided by a second log suite from an offset well located about three miles south of the treatment well. The Young's modulus used in the model was slightly lower than the one calculated from the tracks of the second log suite, while the Poisson's ratio was found to be on the high side. Since the values used in the models were still within the range of usual values for the Woodford Shale, they were not changed from the initial set-up using the log from the

monitoring well. The only real discrepancy between the model and the additional log suite was found to be permeability. The log showed matrix permeability, which is usually very low and in the nano-Darcy range. The values used in the models however, were about one order of magnitude greater for the zone of interest and represented a combined permeability, rather than the matrix permeability only. Since the overall permeability taking into account pre-existing structures such as natural fractures or smaller fissures can be substantially higher than the matrix permeability, the permeability values that populated the grid cells were assumed to be as accurate as possible.

A couple of key parameters were adjusted in order to achieve the matches. PDMSF is a pressure dependent value that reflects the increase of Young's modulus, i.e. stiffening of the formation, throughout the treatment if a positive value is used, such as in the subject models. PDL, another pressure dependent parameter, accounts for the increase of leak-off due to the opening of natural fractures. Modification of TSC represents the diversion of fracturing fluid into transverse fractures, which ultimately results in shorter (half-) lengths. Proppant, pumping rate, and even the stimulation fluid have an effect on how easily the slurry moves through the perforations and through the near wellbore area. Although the Tortuosity Pre-Factor accounts for near wellbore tortuosity, a perforation factor reflects both perforation and near wellbore effects and had to be constantly adjusted throughout the treatment. Representing the ease with which fluid moves through the perforations it accounts for (partially) plugged perforations as well as resistance to injection exhibited by the formation. It could be varied between 0.0 and 1.0, representing either 0% or 100% of the cross-sectional area of the perforations, i.e. contact area with the formation that is open to flow. Perforations taking fluid may also modify the stress regime around the perforations that are not taking fluid, potentially leading to these perforations opening up. This factor was adjusted in a pattern that was the same for all stages. Starting at a low value it simulated the pressure peak at the beginning of the treatment, due to fluid injection into the reservoir and the resistance as it was forced into the formation, as well as probably partially plugged perforations. After the fracture was initiated, the factor was gradually increased as the resistance to fluid injection decreased. This might have been due to the fact that debris was pumped away and partially plugged perforations open up a little, or because the near wellbore area was altered because of the created hydraulic fractures. When fractures are generated

the stress regime in the near wellbore area changes which can also lead to the opening of previously plugged perforations.

The perforation factor was a single number to account for all of the above effects, regardless which of them was more prominent than others and affected the injection behavior more. It should be noted that it is therefore not completely correct to say that a perforation factor of 0.50 means that 50% of the perforations are open. The combination of the occurring effects rather leads to a condition that can be represented by a perforation factor of 0.50. As more and more proppant and fluid was pumped into the reservoir, the proppant concentration at the perforations and in the near wellbore area increased, so the perforation factor had to be gradually lowered until the end of the treatment in order for the simulated pressure to match the actual data.

The simulation results for the longitudinal model of Stage I show that upward and downward growth occurred simultaneously with almost twice as much height development in the zone above the wellbore than below. The transverse model however, gave a contradictory picture, with almost no activity above the wellbore. From the microseismic data, for this stage only surface recordings, it could be seen that activity below and above the wellbore did occur simultaneously. The height of the fractured zone below the wellbore was larger than above the wellbore though. Unfortunately, the surface data was very scattered, which made the observation of fracture growth and geometry difficult.

The longitudinal model for Stage II showed that fracture growth occurred first upward and downward only towards the very end of the stage. The height of the fractured zones above and below the wellbore seemed to be fairly equal, with slightly more downward growth than upward. The transverse model was in good agreement with that, but showed that most length development came from the zone below the wellbore. While downhole microseismic data gave a similar picture, surface data showed more height growth above the wellbore than below.

For Stage III both the longitudinal and the transverse model showed simultaneous upward and downward growth, with most activity, i.e. length development, occurring in the zone below the wellbore. The downhole recordings seemed to agree

with that, whereas the surface data showed an opposite picture of substantial upward growth with only one event occurring below the wellbore.

Also for Stage IV, both models showed substantial downward growth with almost all length development occurring below the wellbore. As for the previous stages, downhole and surface microseismic recordings pointed into different directions in terms of upward and downward growth. Surface data showed no height development below the wellbore at all, while downhole data showed substantial downward growth.

The longitudinal and transverse models for Stage V agreed very well with each other and both showed substantial upward growth. Downhole data on the other hand showed a lot more activity below the wellbore, whereas surface data depicted almost equal height development below and above the wellbore. The significant difference between the models for Stage V and the models for the previous stages is the amount of tectonic strain. For Stage V, a higher tectonic strain had to be used in order to account for the stress state changes caused by the previous stages. A tectonic strain of 130 microstrains for the longitudinal model and 140 microstrains for the transverse model resulted in an additional stress of 208 psi and 234 psi, respectively. This produced the desired matches, but at the same time enabled the simulation of fracture growth into the zone above the Woodford Shale. Applying a lower tectonic strain similar to the values used for the other stages showed different results for the longitudinal and the transverse models. For the longitudinal model, a tectonic strain in the range of 50 microstrains produced matches that were not as good as the original one, but probably still acceptable. For the transverse model, however, no match could be achieved with a tectonic strain of 50 microstrains. However, considering the E-W orientation of the maximum stress and the S-N orientation of the wellbore, the different response to a variation in stress in the longitudinal direction compared to the transverse direction is no surprise.

In general, both length and longitudinal stretch could be very well matched for all stages with average deviations of only -17% and -10%, respectively. Height on the other hand could not successfully be matched for all stages, as seen with the average deviations of -59% for the longitudinal models, and -55% for the transverse models. This bias toward more accurately matching the length than the height agrees with the findings of Mohammad in her thesis from 2009. Microseismic data showed that except for Stage

II, no stage was contained to the respective stage perforation cluster and most microseismic activity overlapped with the zone around the perforations of the previous stage. The region of the formation of the previous stage was already fractured and therefore weakened, which made it easier for the fracturing fluid to take the way of less resistance and further deform the already stimulated part of the formation than to exclusively initiate fractures that grow from the actual stage's perforations. It is believed to be more an effect of "taking the path of least resistance" than a problem of stage isolation (Gertson, 2011). The fracture network from the previous stage seemed to have dominated fracture growth and microseismicity. It should be noted, though, that microseismicity generated in an already fractured part of the reservoir can also be related to leak-off, which can occur for a long time after a stage was pumped, as it was shown by surface microseismic data for Stage III½. However, modeling could not accurately account for the already fractured, and therefore weakened, reservoir around a previous stage.

Fracturing regions of a reservoir that were already fractured in a previous stage however, is a phenomenon that is frequently detected in a variety of hydraulic stimulations. Especially in complex formations with pre-existing natural fractures, such as shales, this hydraulic connectivity can divert the fracturing fluid into parts of the reservoir that have already been weakened. The closer the spacing of the stages of a multistage fracturing treatment, the higher the chances this will occur (Eisner et al., 2006).

Although the formation around the Stage I perforations was the first part of the reservoir to be fractured, the few data points of the surface data set were too scattered to make a significant observation. Downhole data for Stage II showed that microseismic activity for this stage was confined to the region around the stage's perforations. The fracture height obtained from the downhole data for this stage can therefore be used as a representative value for the un-stimulated reservoir. The particular fracturing fluid and proppant combination for the studied treatment in the subject well produced a height of 290 ft in the case where no re-fracturing occurred, which was very accurately simulated for all models of all stages. Since re-fracturing could not be accounted for in the subject models, they simulated fracture growth in the un-stimulated reservoir. Even though the actual fracture height, which was influenced by re-fracturing into already weakened formation, could not be very well matched, the fact that the a height of 240 ft was

produced by almost all hydraulic fracture models supports the accuracy of the geological set-up.

Although a model, on the one hand, is able to calculate fracture growth and to anticipate properties, the results are often questionable and "suffer from a tenuous and generally unknown relationship with reality" (Weijers et al., 2005). The danger of fracture modeling lies in non-unique solutions that produce the desired outcome but are detached and not representative of the processes occurring in a particular reservoir (Cipolla et al., 2009). An important measure to guarantee the validity of the models was the geological set-up, as discussed above. A log suite from the monitoring well was used to populate the simulation grid with geological properties, which could be justified by average values for the Woodford Shale, as well as by an additional log suite from an offset well showing the same stratigraphy. For the key parameters in the models, it was generally attempted to keep the range of variation from stage to stage to a minimum and rather find some that work well for all stages within a certain range, in order to provide some consistency. However, they did change a little throughout the reservoir and along the wellbore. Another aspect that validated the models, apart from the geological set-up, was the pressure behavior after the pumps were shut off. Unfortunately, only between five and ten minutes of data were recorded after the treatment, but the pressure behavior could be very well matched, as seen in Figures 3.21 through 3.49. Additionally, a sensitivity analysis was performed to examine which parameters have what kind of influence on the simulated properties, as well as to evaluate the uniqueness of the models. If an increase or a decrease in a certain parameter resulted in a clearly observable trend it would facilitate non-unique solutions, as parameters could be combined in more than one way to produce the same result. If no clear trend can be observed however, it is substantially more unlikely for parameters to be adjusted in ways that result in the same outcome. The eight parameters that were modified in the models used in this work (PDMSF, PDL, TSC, Tortuosity Pre-Factor, Tectonic Strain, Perforation Coefficient of Discharge, Friction Coefficient, and Perforation Factor) were modified by +/– 25%, one at a time, and both the longitudinal and the transverse models were run again. The observed changes in the simulated fracture properties (pressure, fracture length, fracture height, and maximum width) were then recorded and evaluated. No general observation could be made for either of the parameters and simulated properties. Trends, if observed at all, were very inconsistent, so that no clear statement

could be made. Often times both increase and decrease in one parameter would have the same effect, sometimes no effect at all, or only one modification would lead to a change in the simulated properties. The effects seemed to be governed not only by the change in a particular parameter, but rather by the way how parameters interacted with each other. The fact that the results of the models were obviously not dependent on certain parameters only, together with the fact that a lot of parameters only produced the desired outcome at a particular value, and not at values lower or higher than the one used, leads to the assumption that the outcome of the models, i.e. the simulated properties, were fairly unique.

8.2 Microseismic Analysis

Although microseismic monitoring is a valuable technology to match actual treatment data to a simulation model providing a calibrated model for a specific region, it is sensitive to, and dependent on, the number of recorded microseisms, as well as the accuracy of these events. Since there are different errors associated with surface and downhole monitoring, using one technology exclusively to match and calibrate the model can produce skewed results. The match achieved with surface data will have a different bias than the match achieved with downhole data. Assuming that a monitoring well is somewhat close to the treatment well, i.e. smaller event-to-receiver distance, downhole sensors are able to detect more events than surface sensors and can therefore give a more accurate match. Surface receivers can have a higher sensitivity to the velocity model which may decrease the accuracy in determining the vertical position of an event. They also often record fewer events because of the higher distance. It is therefore important to understand how many microseismic events are actually necessary to produce a good match with a model from a software package, as well as, if and what the difference between the match with surface data and the match with downhole data is able to tell us about data recording and the reservoir in general.

The availability of both surface and downhole microseismic recordings for a multi-stage treatment in one well provides the opportunity to directly compare the two data sets on different levels. In order to evaluate how reliable and accurate the individual technologies are, and to determine advantages and disadvantages, this work

investigated the congruency between the surface and downhole data, as well as attempted to estimate how many events were actually necessary to produce a good and fairly accurate match with a hydraulic fracture model.

For the surface data set, 617 events were recorded, most of a very small magnitude. Due to the accuracy of determining the event location, especially of smaller events, a plot of cumulative number of events versus event magnitude is a useful tool in order to find out how reliable the data set is, and whether all events should be considered for the analysis (Gertson, 2011). With the information obtained from that plot a cut-off value of -2.75 was applied to the data set, meaning that only events with a magnitude of -2.75 or greater were considered, which left 222 events for the analysis.

Downhole sensors recorded 497 events in total, but due to technical issues did not monitor the first stage of the treatment. Therefore, Stage I was not included in the comparative analysis of surface and downhole data. Although it is generally acknowledged that the best results can be obtained when the sensors are positioned across the interval of interest, for the treatment studied in this thesis, the geophones were positioned above the Woodford Shale, and not across it. The Woodford Shale shows a substantially lower seismic velocity than the Mayan Shale above it, and the Hunton Limestone, and the Sylvan Shale below it, so the seismic energy that would be recorded by sensors straddling the Woodford Shale would arrive refracted rather than direct, leading to more difficulty in calculating the event location (Gertson, 2011).

Surface recordings for Stage II showed that microseismic activity clearly overlapped with Stage I perforations, with the fracture network seemingly growing from the end of the Stage II perforation cluster into the direction of the already weakened region around the Stage I perforations. Downward and upward growth appeared to occur simultaneously, with slightly more upward than downward growth. Downhole data, on the other hand, showed that fracture growth was very well contained to the Stage II perforations, as well as symmetrical height development above and below the wellbore.

For Stage III surface and downhole recordings agreed in terms of overlapping of activity with the area around the Stage II perforations. They diverged on the matter of height development though. While surface data showed substantially more upward growth than downward growth with only one event recorded below the wellbore,

downhole data showed significant downward growth, exceeding height development above the wellbore.

Evaluation of microseismic data for Stage IV showed that surface and downhole data did not agree very well. Surface recordings showed events contained to what appeared to be a single fracture growing from the Stage IV perforations, whereas downhole data showed events that were more scattered and mostly overlapped with the region around Stage III perforations. As for the previous stage the two data sets also showed different height development. While surface data showed no downward growth at all without a single event recorded below the wellbore, downhole recordings showed significantly more downward than upward growth.

For the last stage of the treatment, both surface and downhole data sets generally contained events of a larger magnitude than were recorded during previous stages. Downhole recordings showed that most events overlapped with the Stage IV perforations and only one event was observed at the Stage V perforations. Surface data on the other hand was far more scattered, ranging from the region around the Stage II perforations to the formation around the Stage IV perforations, with no event recorded at the Stage V perforations. Whereas surface data showed slightly more upward than downward growth, downhole data showed the opposite and substantial activity in the zone below the wellbore.

In general, the surface data showed more upward growth than downward growth, which is contrary to the downhole recordings that showed substantially more downward than upward growth. The models from Chapter III tend to agree with the downward growth depicted by the events recorded by the downhole sensors. Instead of assuming that either upward or downward growth has not been accurately captured by the surface or the downhole sensors, it might be more reasonable to expect a certain depth error associated with the data sets to be the reason for this. Looking at the data, one might observe that the surface events have depth components, i.e. z-coordinates, that are too small, whereas the downhole events have depth components that are too large. It should be noted, though, that it is entirely possible that, even though both data sets have errors associated with them, the vertical location error can be larger for one data set than for the other. Considering the fact that the models with a geological set-up that matches up well to two sets of logs, simulate fracture growth as it is shown by the

downhole data, it can be assumed that downhole microseismic monitoring gave a more accurate picture of fracture growth for the subject well. Although both data sets provided similar fracture azimuths, they did not provide the same fracture lengths and heights.

Events recorded by the surface sensors were of a generally larger magnitude than events included in the downhole data set. Comparing the maximum distance between events and sensors, which is about 8,500 ft of vertical distance between the deepest event of the surface recordings and the surface, and about 1,900 ft between the observation wellbore and the farthest event of the downhole data set, as well as the applied cut-off value, this is no surprise.

It could be observed that the surface and downhole data set, if used together, overlapped in certain regions and picked up on different things in others. However, they complemented each other very well and in general gave a more complete picture of fracture growth and stimulated reservoir volume, if combined.

Using either surface or downhole recordings exclusively to achieve a match with a simulation model will result in a different calibration. In order to evaluate this difference, two additional models were built for each stage, one using the downhole data, and one using the surface data. Each data set in general has different inherent errors and will produce different results if used for the same purpose. The models were governed by the fracture geometry that was obtained from the data sets. Fracture length and longitudinal stretch of the fracture network along the wellbore could be very well matched for each stage for both the models based on surface and the ones based on downhole data. Height, however, could not be well matched with differences of up to 60%, based on the re-fracturing of formation that has already been fractured by a previous stage, as discussed in Section 8.1.

The bottom line is that if an engineer had to calibrate models for a particular field using either surface or downhole data exclusively, the outcome would not be a complete representation of potential realities. Both technologies have advantages and disadvantages over the other one in terms of event location accuracy, viewing limit, and costs. The most important thing to remember is that any model is only as good as the input that goes into it. It therefore depends on the individual situation and geological circumstances, as well as well on the availability of wellbores for monitoring purposes

which technology is a 'better' option to use. Using both surface and downhole sensors to monitor a hydraulic fracturing treatment is clearly the most costly option but also gives the most accurate representation of reality.

8.3 Reservoir Characterization

The microseismic data recorded during the treatment analyzed in this thesis was also used for reservoir characterization to obtain more information about pre-existing structures. Reservoir dynamics can be monitored by microseismic mapping to some extent. Since microseismic connectivity can be linked to hydraulic connectivity, flow channels such as natural fractures and faults can be identified from the data (Jupe et al., 1998; Jupe et al., 2000). In the Woodford Shale hydraulic stimulation seems to create complex fracture networks showing various orientations comparable to treatments in the Barnett Shale, although with a higher degree of communication with pre-existing fractures and faults (Vulgamore et al., 2007).

Natural fractures and how well stimulation treatments can utilize, i.e. open, them are important factors in gas production from shale reservoirs (King, 2010). The efficiency of hydraulic fracturing can be affected by this communication. Pre-existing structures can be beneficial by providing additional flow-paths for hydrocarbon production and fracturing fluid diversion, but can also have negative effects by taking too much fluid, decreasing the efficiency of fluid injection. Due to the simple fact that significantly more events were recorded by downhole sensors, the complexity of the created fracture network could be better observed from the downhole data set. However, due to the superior areal coverage of surface monitoring it can pick up a lot more interaction with pre-existing structures. Whether the microseismic activity far out in the reservoir monitored by surface sensors is truly related the activation of natural fractures and faults is arguable though.

In the case where faults are present and in contact with the injected fracturing fluid, they can shift the microseismic picture and lead to misinterpretation and incorrect analysis of the treatment (Downie et al., 2010). The strength of a microseismic event, i.e. the seismic moment, and consequently the event magnitude, depend on the amount of shear displacement along the fault plane and the area of the fault plane. This means that

events generated along pre-existing fault structures are very likely to produce events of larger magnitude, and therefore make them easy to identify. Plotting the event magnitude versus the event-to-receiver distance identified Stages III and V as the stages with the most events of larger magnitude. Since every stage fractured into a region of the reservoir that was already fractured by a previous stage, these 'loud' events can also be influenced by the already weakened reservoir providing larger slip surfaces than the unstimulated formation.

An additional observation supporting the interaction with pre-existing structure is the speed of fracture propagation (Gertson, 2011). Events were generated more than twice as fast during Stage V than during previous stages, implying the utilization of pre-existing faults and fractures. It should be noted though, that 'pre-existing' structures such as a fracture network that was created during a previous stage might also facilitate an increase in the speed of event generation. Overall the link between 'loud' events and intersecting faults leads to the assumption that the fracture network generated during Stage V most likely communicated with a fault. Stage III and even Stage IV, although with fewer events of larger magnitude, showed a similar behavior that is not as clearly pronounced as for Stage V though.

In general, the microseismic data showed that the stimulation treatment was successful in creating a fairly complex hydraulic fracture network for all stages. Most of this information was obtained from the downhole data set. The significance of the information that could be obtained from the surface data set was limited because it included fewer data points and showed events that were generally more scattered. Although fractures mostly follow the present day east-west stress, microseismic activity along features following the southeast-northwest paleo-stress could also be observed.

Additional information about the treatment and interaction with faults could be obtained from a cumulative seismic moment plot showing the changes of the seismic moment throughout the treatment. The plot generated from the surface data did not provide very much information due to the fact that the surface data set contained only a few events for each stage. Furthermore, it was governed by a few large events, as there is about a 32-fold difference in moment between microseismic events that are just one magnitude apart (Vermylen and Zoback, 2011). The downhole recordings on the other hand produced a very informative plot. As for the surface plot, it showed that Stages III

and V had the highest cumulative moment of all stages. Interestingly, the large cumulative moment of Stage III was followed by microseismic activity of significantly lower intensity during Stage IV, possibly indicating interaction with natural fractures, or an extension of the fracture into a part of the reservoir with deviating properties (Warpinski, 2009b). Stage V showed the highest cumulative moment, which is in good agreement with the surface data and ties back into the intersection of a fault or the interaction with the fracture network created during previous stages, both possibly providing large enough slip surfaces for large magnitude events. For all stages, the curves reached a plateau after a certain time, indicating that although additional volume was injected, it did not generate much additional microseismicity.

To further evaluate the microseismic data the magnitude scaling technique of Gutenberg and Richter was applied to it. When plotting the cumulative number of events greater than or equal to a certain magnitude on a logarithmic scale versus the magnitude of the events, a log-linear relationship can be observed for events that were accurately detected by the microseismic sensors. In case all stages show close to identical slopes, the intercept of the straight line represents a parameter to compare the activity level of each stage. It can be “used to quantify the rate of seismicity and thus the density of fractures created in the reservoir” (Vermylen and Zoback, 2011). Due to the small surface data set this technique was only applied to the downhole recordings. Since all stages showed different slopes for the log-linear part of the curve, the activity levels could not be compared in a meaningful way, unfortunately. Furthermore, the ‘linear’ behavior of the curve clearly deviated from the theoretical ideal straight line.

Another important property that can be attributed to interaction with faults is seismic deformation. Although a variety of factors are contributing to the seismic deformation caused by a hydraulic fracturing treatment, the most dominant ones being the pumping energy, the state of stress in the formation, as well as formation brittleness, the intersection of a fault or interaction with other pre-existing structures may produce more deformation. Knowing the fault systems and the natural fractures that are present is therefore important to eventually increase the efficiency of a treatment (Maxwell et al., 2008). However, the actual seismic energy appears to be a minor component of the total injected energy that creates the fracture. It is therefore questionable how big the effect of seismic deformation is on the overall deformation that is occurring. A large part of it

might actually occur aseismically, limiting the information that can be obtained from microseismic data (Maxwell et al., 2008).

8.4 Error Analysis

The two most crucial things in determining the accurate position of a microseismic event are the velocity model and the arrival time picks. The accuracy of the event location is therefore limited, with restraints related not only to signal processing but also to the tool itself (Le Calvez et al., 2005). Fracture geometry that is obtained from microseismic data is consequently governed by the quality of the microseismic data, and is further influenced by the fact that microseismic events are not necessarily generated at the fracture itself but rather in a region surrounding the actual fracture. The envelope the data produces therefore not only depends on measuring and processing accuracy, but also on mechanisms that can influence the generation of events, such as very high stress at the fracture tip and leak-off effects (Warpinski et al., 1999).

As discussed in Section 8.2, there are advantages and disadvantages related to both surface and downhole monitoring. The core piece governing the accuracy of both technologies however is the velocity model. It builds the basis on which the distance between an event and a receiver is calculated once an event has been detected (Warpinski, 2009a). The velocity model for the surface data acquisition was based on the operating company's 3D seismic profile for that specific region and was adjusted based on perforation shots (Gertson, 2011). For the downhole microseismic monitoring, the velocity structure was derived from a dipole sonic log from an offset well that was depth corrected and further calibrated with perforation shots. Since the perforations were calculated correctly, the downhole velocity model was considered accurate.

The available quality report for the downhole microseismic recordings discussed quality control parameters such as average noise levels, signal-to-noise ratios, time-residuals, confidence levels, and location errors. With background noise being a potentially serious issue for downhole sensors, it was satisfactory to see that the noise levels for each sensor were relatively low.

A very important value determining the accuracy of the travel time picks is the signal-to-noise ratio, which can even better indicate the location error for a particular event than the event magnitude sometimes. As the lower end of the acceptable range of SNR values for an event is 1.0, all events should have values above that. The sensors generally showed most events with a SNR of above 1.0, with more than half of them having a SNR of above 3.0, characterizing high quality signals.

The time residual characterizes the accuracy of both the arrival time picks and the velocity model and should be minimized at values close to zero. It is the difference between the theoretical travel time and the picked travel time. Most sensors showed a very narrow range of time residuals between -3 and +3 ms. The deepest sensor however showed a wider distribution indicating poor travel time accuracy.

A parameter to evaluate the accuracy of the calculated azimuth for an event is the hodogram consistency. It shows the difference between the observed azimuth for an event and the average azimuth for all events for each sensor, with desirable values being as close to zero as possible. For the data set analyzed in this thesis, the average variation was found to be between –18 and +18 degrees, which is fairly good.

Taking into account all quality parameters mentioned above, as well as the number of sensors, a confidence value for each event was calculated. It indicates the overall quality of all variables that go into calculating an event and ranges from 0.0, signalizing a very low confidence, to 5.0, implying a very high confidence. Most events, especially the ones outlining the main fracture, had a confidence of 3.0 and above. The average confidence for all events of all stages was 3.12.

Also discussed in the quality report were the three parts of the location error, namely the azimuth error, radial error, and vertical error. The error in azimuth was found to be between 0.0 and 8.0 ft, indicating a high accuracy of event location in terms of azimuth. The error in radius from the receiver, however, was found to be between 9.0 and 26.0 ft, which can still be considered fairly accurate but with less confidence than the event azimuth. An even wider range of error was found for the depth component of an event. The vertical error was estimated between 8.0 and 34.0 ft, although for events recorded during Stage V it was up to 76.0 ft.

Unfortunately, no quality report was available for the surface imaging. As discussed in Section 8.2, surface and downhole data deviated in terms of the vertical position of an event. Since depth accuracy is usually an issue for surface data considering the thousands of feet of formation a seismic signal has to travel through, one might assume that the surface data is more inaccurate than the downhole data. However, taking into account the fracture barrier below the Woodford Shale, it was expected for the fracture to develop more height above the wellbore than below it, which agrees with what the surface data showed. The hydraulic fracture models on the other hand simulated substantial downward growth for all stages, with the exception of Stage V, which was based on the fairly accurate geological set-up of the models and agrees with the downhole microseismic recordings. For Stage V the downhole data showed more downward growth, whereas both the longitudinal and the transverse model showed substantial upward growth. This discrepancy is possibly related to the larger vertical location error of up to 76 ft for this Stage V events.

Taking into account the quality parameters discussed above, the confidence in the downhole data is generally very high. Surface and downhole recordings, alone and combined, gave a reasonable picture of fracture growth if viewed from above, and all indicators point toward a fairly high accuracy of the data in terms of x and y components. However, both data sets probably had a higher inaccuracy associated with the vertical dimension, producing the different results in terms of height development. Considering what the results of the models showed, it can be assumed that downhole monitoring more accurately recorded fracture growth for the subject well, though.

Additional to the accuracy of the event locations, the number of recorded events and its influence on the obtained fracture geometry was also evaluated. Since the surface data set included only few data points, only the downhole set was used in this analysis. In order to qualify and quantify the influence of the number of events, fracture geometry was obtained from data sets that were truncated in two different ways. The first three variations were generated by selecting only every second, third, or fourth data point for geometry analysis by eliminating data based on a random number between one and the total number of events for a particular stage. This method represents a completely random elimination of half, two thirds, or three quarters of the original data set, and was not based on a characterizing property. The fourth data set was generated by eliminating all events with an event confidence below 3.0. Since the confidence value

indicates the overall quality of all variables that go into calculating the event location, it represents a systematic truncation increasing the accuracy of the data set.

All components of the fracture geometry were affected by the number of events for the random elimination of events. As the methodology was random, so were the effects on fracture dimensions. The random technique of eliminating a substantial part of the total events compared to the qualitative approach of systematically truncating the data set showed that the number of events did play a role in obtaining the fracture geometry. However, it did not seem to be a large determining factor. Even with just a quarter of the original data set, the various components of the fracture geometry did not dramatically deviate from the one that the full data set gave, and still produced a fairly decent picture. There were some exceptions where a 100% difference between data sets for one geometry parameter was observed. This could be attributed to the randomness of the data point elimination and the consequently random outcomes though. In reality, event detection is usually not subjected to such random factors. The confidence number therefore is a parameter that is better suited for evaluating the quality of a data set and is able to make a more significant statement about how reliable the information obtained from microseismic data is. As most events outlining the fracture network had an associated confidence value of greater than 3.0, the fracture geometry did not deviate much from the one obtained from the original data set, although up to 50% of the data were excluded from analysis.

CHAPTER 9

CONCLUSIONS

This chapter provides conclusions that can be drawn from the results discussed in the previous chapters, as well as gives recommendations for future research work. Hydrocarbon production from shale reservoirs, such as the formation studied in this thesis, would not be economically successful without the employment of two technologies: horizontal drilling and well stimulation (Arthur et al., 2009). The Woodford Shale shows the highest drilling activity in the Arkoma Basin in Oklahoma, with most wells being horizontal and multi-stage hydraulically fractured (Vulgamore et al., 2007; and Waters et al., 2009). This project showed the importance of microseismic monitoring of hydraulic fracturing treatments and the information that can be gained by thoroughly analyzing the recorded data in conjunction with hydraulic fracture modeling. The outcomes and findings promote an understanding of which technique leads to an accurate picture of the hydraulic fracturing treatment. Matching simulation models with microseismic data enhances the accuracy of such models for a particular region as well as their predictive qualities.

9.1 Conclusions

The development of a hydraulic fracture model for each stage that matches both recorded pressure and observed fracture geometry, and the analysis of both surface and downhole microseismic data on various levels, lead to the following conclusions and observations:

- In general, both length and longitudinal stretch could be very well matched to combined surface and downhole microseismic data for all stages with average deviations of only -17% and -10%, respectively. Height on the other hand could not successfully be matched for all stages, as seen with the average deviations of -59% for the longitudinal models, and -55% for the transverse models. This

bias toward more accurately matching the length than the height agrees with the findings of Mohammad in her thesis from 2009.

- Overall, the surface data showed more upward growth than downward growth, which was contrary to the downhole recordings that showed substantially more downward than upward growth. Considering the fact that the hydraulic fracture models simulated fracture growth as it was shown by the downhole data, it can be assumed that downhole microseismic monitoring gave a more accurate picture of fracture growth for the subject well.
- An evaluation of the influence of the number of recorded events on the fracture geometry showed that although it did play a role, it did not seem to be a factor that exclusively determines the quality of a data set. A data set containing few events can provide reliable information, if the confidence in the event locations is high. Random elimination of data points lead to random results, whereas the systematic truncation of the data set based on the event confidence values as a characterizing property was able to make a more significant statement about the quality of the information obtained from microseismic data than just the mere number of recorded events.
- In general, the downhole microseismic data showed that the stimulation treatment was successful in creating a fairly complex hydraulic fracture network for all stages. Surface data was less significant due to fewer data points and events that were more scattered. Although fractures mostly follow the present day east-west stress, microseismic activity along features following the southeast-northwest paleo-stress could also be observed. Furthermore, the speed of event generation, which was more than twice as high for Stage V than for previous stages, could also be used to indicate interaction with pre-existing structures. This agrees with a cumulative moment plot identifying Stage V as the stage with the highest cumulative moment of all stages, which further pointed out the interaction with a fault or a pre-existing fracture network.
- Model calibration based on either surface or downhole microseismic data exclusively produces different results because the obtained fracture geometry is governed by the data sets. Using both surface and downhole sensors to monitor a hydraulic fracturing treatment is clearly the most costly option but also gives the most accurate representation of possible realities.

- The accuracy and reliability of the recorded surface microseismic data was enhanced by applying a magnitude cut-off value and considering only events with magnitude equal to or greater than the cut-off value. The cut-off value was determined from a plot of the cumulative number of events versus the event magnitude.
- A plot of event magnitude versus event-to-receiver distance identified Stages III and V as the stages with the most events of larger magnitude, and showed a viewing limit of about 1,900 ft for the Woodford Shale. Both stages could therefore be associated with pre-existing fault structures or natural fractures, as such structures can usually facilitate the generation of large magnitude events. However, since re-fracturing of previous stages was observed, these 'loud' events could have been also influenced by the already weakened reservoir providing larger slip surfaces than the un-stimulated formation. Overall, the link between 'loud' events and the intersection of faults leads to the assumption that the fracture network generated during Stage V most likely communicated with a fault.
- The fracture height of 290 ft obtained from the downhole data for Stage II, where microseismic activity was confined to the region around the stage's perforations and no re-fracturing occurred, was used as a representative value for the un-stimulated reservoir that the particular fracturing fluid and proppant combination for the studied treatment in the subject well produced. Even though the subject models could not account for re-fracturing and did not match the microseismic fracture heights, the fact that a height of 240 ft was produced by almost all models supports the accuracy of the geological set-up.
- Although the fracture network created during previous stages seemed to have dominated fracture growth and microseismicity for each stage, modeling could not accurately account for the already fractured, and therefore weakened, reservoir. It should be noted that microseismicity generated in an already fractured part of the reservoir can also be related to leak-off, which can occur for a long time after a stage was pumped.

9.2 Recommendations

This section summarizes the recommendations for future research work in order to improve the calibration of hydraulic fracture models, as well as the analysis of microseismic data:

- In order to populate the hydraulic fracture model with properties of the highest possible accuracy, the wellbore log that is used as the basis for the geological set-up should include measurements of both compressional and shear acoustic velocities. Although the compressional travel time curve can be generated from other values, it would be beneficial to have actual measurements as a reference.
- To further improve the accuracy of the geological set-up, a mini-frac analysis or DFIT should be performed, from which important properties such as effective permeability and closure stress can be obtained through a simple G-function analysis.
- As both microseismicity and fracture growth for a particular stage seemed to be dominated by the fracture network that was created during a previous stage, hydraulic fracture models should be consequently modified and adjusted for the following stage. The geological properties of a model for a particular stage should reflect the already weakened reservoir with altered properties from the previous stage, if re-fracturing of that part of the reservoir can be observed from microseismic data as it was the case for this project.
- Since re-fracturing of a region of the reservoir that was already stimulated during a previous stage proved to be a major issue, it would be beneficial to have both surface and downhole data for the first stage of the treatment in order to obtain a representative fracture height for the un-stimulated reservoir.
- In order to perform a comparative error analysis and qualify the accuracy of both surface and downhole data in regards to each other, a quality control report for the surface data would have been beneficial and should be included in future projects.

NOMENCLATURE

A	…	area of the fault plane [cm^2]
a	…	log. of total number of events larger or equal to a magnitude of 0 [-]
a_1	…	shale fraction multiplier [psi]
a_2	…	measured difference between ISIP and closure pressure [psi]
α_H	…	horizontal Biot's Constant [-]
α_V	…	vertical Biot's Constant [-]
b	…	slope [-]
c_0	…	wave velocity [cm/sec]
C_D	…	perforation coefficient of discharge [-]
CSV	…	Comma-Separated Value, file format [-]
d	…	amount of shear displacement along the fault plane [cm]
d_p	…	diameter of perforations [in]
DTC	…	compressional sonic travel time
D_{TV}	…	true vertical depth [ft]
E	…	Young's modulus [MMpsi]
E_{dyn}	…	dynamic Young's modulus [MMpsi]
E_{static}	…	static Young's modulus [MMpsi]
ε_x	…	tectonic strain [microstrains]
F_c	…	radiation pattern coefficient [1/sec^2-cm]
Φ	…	effective porosity [-]
G	…	shear modulus [g/cm-sec^2]
GOHFER™	…	Grid Oriented Hydraulic Fracture Extension Replicator
γ_{ob}	…	overburden stress gradient [psi/ft]
γ_P	…	pore fluid gradient [psi/ft]
ID	…	inner diameter [in]
ISIP	…	instantaneous shut-in pressure [psi]
k_1	…	adjustable coefficient [mD]
k_2	…	adjustable coefficient [-]
LAS	…	Log ASCII Standard, file format [-]
M	…	seismic event magnitude or moment magnitude [log scale]
M_0	…	seismic moment [g-cm^2/sec^2, i.e. dyne-cm]
MD	…	measured depth [ft]
μ	…	permeability [mD]
$N \geq M$	…	Cum. number of events larger or equal to a certain magnitude [-]
N_p	…	number of open perforations [-]
v	…	Poisson's ratio [-]
OGIP	…	original gas in place [tcf]
Ω_0	…	low frequency level of a displacement seismogram [1/sec]
p_{BH}	…	bottomhole (or net) pressure [psi]
p_c	…	closure pressure [psi]
PDL	…	Pressure Dependent Leak-off Factor [1/psi]
PDMSF	…	Pressure Dependent Modulus Stiffness Factor [1/psi]
$p_{friction}$	…	pressure loss due to friction [psi]

$p_{hydrostatic}$	…	hydrostatic pressure [psi]
p_{nwb}	…	pressure loss due to near wellbore effect [psi]
P_{off}	…	pore pressure offset [psi]
p_{perf}	…	pressure loss at perforations [psi]
P_{pf}	…	friction pressure at the perforations [psi]
$p_{surface}$	…	surface pressure [psi]
p_{tort}	…	pressure loss due to tortuosity [psi]
PZS	…	process zone stress [psi]
q	…	total pump rate [bpm]
R	…	source-receiver distance [cm]
RMS	…	root mean square
ρ_0	…	density [g/cm^3]
ρ_{bulk}	…	bulk density [g/cm^3]
ρ_f	…	slurry density [g/cm^3]
SNR	…	signal-to-noise ratio
spf	…	shots per foot
σ_t	…	tectonic stress [psi]
t	…	time [sec]
t_0	…	time of event generation [sec]
t_a	…	tagged arrival time [sec]
t_{Pan}	…	arrival time of P-wave at n-th receiver [sec]
t_{San}	…	arrival time of S-wave at the n-th receiver [sec]
TSC	…	Transverse Storage Coefficient [1/psi]
TVD	…	true vertical depth [ft]
v	…	velocity [ft/sec]
v_P	…	compressional velocity [ft/sec]
v_S	…	shear velocity [ft/sec]
V_{SH}	…	shale fraction [-]
VSP	…	vertical seismic profile
x	…	distance [ft]
x_n	…	distance of event from n-th receiver [ft]

REFERENCES

Abbott D., Neale C., Lakings J., Wilson L., Close J.C. and Richardson E., *"Hydraulic Fracture Diagnostics in the Williams Fork Formation, Piceance Basin, Colorado, Using Surface Microseismic Monitoring Technology"* SPE 108142, SPE Rocky Mountain Oil & Gas Technology Symposium, Denver, CO, April 16-18, 2007.

Arthur J.D., Bohm B., Coughlin B.J. and Layne M, *"Evaluating Implications of Hydraulic Fracturing in Shale Gas Reservoirs"* SPE 121038, SPE Americas E&P Environmental Safety Conference, San Antonio, TX, March 23-25, 2009.

Barree R.D., Gilbert J.V. and Conway M.W., *"An Effective Model for Pipe Friction Estimation in Hydraulic Fracturing Treatments"* SPE 122917, SPE Rocky Mountain Petroleum Technology Conference, Denver, CO, April 14-16, 2009b.

Barree R.D., Gilbert J.V. and Conway M.W., *"Stress and Rock Property Profiling for Unconventional Reservoir Stimulation"* SPE 118703, SPE Hydraulic Fracturing Technology Conference, The Woodlands, TX, January 19-21, 2009a.

Barree R.D. and Winterfeld P.H., *"Effects of Shear Planes and Interfacial Slippage on Fracture Grwoth and Treating Pressures"* SPE 48926, SPE Annual Technical Conference and Exhibition, New Orleans, LA, September 27-30, 1998.

Cipolla C.L., Lolon E.P. and Mayerhofer M.J., *"Resolving Created, Propped, and Effective Hydraulic Fracture Length"*, SPE Production & Operations, Vol. 24, p. 620, November 2009.

Cipolla C.L., Warpinski N.R. and Mayerhofer M.J., *"Hydraulic Fracture Complexity: Diagnosis, Remediation, and Exploitation"* SPE 115771, SPE Asia Pacific Oil & Gas Conference and Exhibition, Perth, Australia, October 20-22, 2008.

Cipolla C.L. and Wright C.A., *"State-of-the-Art in Hydraulic Fracture Diagnostics"* SPE 64434, SPE Asia Pacific Oil & Gas Conference and Exhibition, Brisbane, Australia, October 16-18, 2000.

Downie R.C., Kronenberger E. and Maxwell S.C., *"Using Microseismic Source Parameters to Evaluate the Influence of Faults on Fracture Treatments – A Geophysical Approach to Interpretation"* SPE 134772, SPE Annual Technical Conference and Exhibition, Florence, Italy, September 19-22, 2010.

Eisner L., Duncan P.M., Heigl W.M. and Keller W.R., *"Uncertainties in passive seismic monitoring"*, The Leading Edge, Vol. 28, pp. 648-655, June 2009.

Eisner L., Fischer T. and Le Calvez J.H., *"Detection of repeated hydraulic fracturing (out-of-zone growth) by microseismic monitoring"*, The Leading Edge, Vol. 25, pp. 548-554, May 2006.

Gertson R., personal communication, 2011.

Groenenboom J., van Dam D.B. and de Pater C.J., *"Time-Lapse Ultrasonic Measurements of Laboratory Hydraulic-Fracture Growth: Tip Behavior and Width Profile"*, SPE Journal, Vol. 6, pp. 14-24, March 2001.

Jacobi D., Breig J., LeCompte B., Kopal M., Hursan., Mendez F., Bliven S. and Longo J., *"Effective Geochemical and Geomechanical Characterization of Shale Gas Reservoirs from the Wellbore Environment: Caney and the Woodford Shale"* SPE 124231, SPE Annual Technical Conference and Exhibition, New Orleans, LA, October 4-7, 2009.

Jupe A., Jones R., Dyer B. and Wilson S., *"Monitoring and Management of Fractured Reservoirs Using Induced Microearthquake Activity"* SPE/ISRM 47315, SPE/ISRM Eurock '98, Trondheim, Norway, July 8-10, 1998.

Jupe A., Jones R., Wilson S. and Cowles J., *"The role of microearthquake monitoring in hydrocarbon reservoir management"* SPE 63131, SPE Annual Technical Conference and Exhibition, Dallas, TX, October 1-4, 2000.

King G.E., *"Thirty Years of Gas Shale Fracturing: What Have We Learned?"* SPE 133456, SPE Annual Technical Conference and Exhibition, Florence, Italy, September 19-22, 2010.

Le Calvez J.H., Bennett L., Tanner K.V., Grant W.D., Nutt L., Jochen V., Underhill W. and Drew J., *"Monitoring microseismic fracture development to optimize stimulation and production in aging fields"*, The Leading Edge, Vol. 24, pp. 72-75, January 2005.

Liu X., Zhou Z.Q., Li X.W., Li Z.X., Xu Y.G. and Chen B.C., *"Understanding Hydraulic Fracture Growth in Tight Oil Reservoirs by Integrating Microseismic Mapping and Fracture Modeling"* SPE 102372, SPE International Oil & Gas Conference and Exhibition, Beijing, China, December 5-7, 2006.

Lolon E.P., Cipolla C.L., Weijers L., Hesketh R.E. and Grigg M.W., *"Evaluating Horizontal Well Placement and Hydraulic Fracture Spacing/Conductivity in the Bakken Formation, North Dakota"* SPE 124905, SPE Annual Technical Conference and Exhibition, New Orleans, LA, October 4-7, 2009.

Matthews H.L., Schein G. and Malone M., *"Stimulation of Gas Shales: They're All the Same – Right?"* SPE 106070, SPE Hydraulic Fracturing Technology Conference, College Station, TX, January 29-31, 2007.

Maxwell S.C., Shemata J., Campbell E. and Quirk D., *"Microseismic Deformation Rate Monitoring"* SPE 116596, SPE Annual Technical Conference and Exhibition, Denver, CO, September 21-24, 2008.

Maxwell S.C. and Urbancic T.I., *"The Potential Role of Passive Seismic Monitoring for Real-Time 4D Reservoir Characterization"*, SPE Reservoir Evaluation & Engineering, Vol. 8, pp. 70-76, February 2005.

Maxwell S.C. and Urbancic T.I., *"The role of passive microseismic monitoring in the instrumented oil field"*, The Leading Edge, Vol. 20, pp. 636-639, June 2001.

Maxwell S.C., Urbancic T.I., Demerling C. and Prince M., *"Real-Time 4D Passive Seismic Imaging of Hydraulic Fracturing"*, SPE/ISRM 78191, SPE/ISRM Rock Mechanics Conference, Irving, TX, October 20-23, 2002.

Maxwell S.C., Waltman C.K., Warpinski N.R., Mayerhofer M.J. and Boroumand N., *"The Imaging Seismic Deformation Induced by Hydraulic Fracture Complexity"*, SPE Reservoir Evaluation & Engineering, Vol. 12, pp. 48-52, February 2009.

Mohammad N.A., *"A Comparison of Hydraulic Fracture Modeling with Downhole and Surface Microseismic Data in a Stacked Fluvial Pay System"*, 2009, MS Project, Colorado School of Mines, Golden, CO, 64 p., 197 p., 215 p.

Moreland P., Bill Barrett Corporation, personal communication, 2010.

Quirein, J.A., Grable J., Cornish B.E., Stamm R., Zannoni S., Gordy D., Dennis S. and Brewer R., *"Microseismic Fracture Monitoring"*, SPWLA 47th Annual Logging Symposium, Veracruz, Mexico, June 4-7, 2006.

Singh I. and Miskimins J.L., *"A Numerical Study of the Effects of Packer-Induced Stresses and Stress Shadowing on Fracture Initiation and Stimulation of Horizontal Wells"* CSUG/SPE 136856, Canadian Unconventional Resources & International Petroleum Conference, Calgary, Alberta, Canada, October 19-21, 2010.

Sleefe G.E., Warpinski N.R. and Engler B.P., *"The Use of Broadband Microseisms for Hydraulic-Fracture Mapping"*, SPE Formation Evaluation, Vol. 10, pp. 233-239, December 1995.

Stimlab, GOHFER™ LAS User Manual, Version 2007 SP4.

Stimlab, WinGOHFER™ User Manual, Version 2007 SP4.

Vermylen J.P. and Zoback M.D., *"Hydraulic Fracturing, Microseismic Magnitudes, and Stress Evolution in the Barnett Shale, Texas, USA"* SPE 140507, SPE Hydraulic Fracturing Technology Conference and Exhibition, The Woodlands, Texas, January 24-26, 2011.

Vulgamore T., Clawson T., Pope C., Wolhart S., Mayerhofer M., Machovoe S. and Waltman C., *"Applying Hydraulic Fracture Diagnostics To Optimize Stimulations in the Woodford Shale"* SPE 110029, SPE Annual Technical Conference and Exhibition, Anaheim, CA, November 11-14, 2007.

Warpinski N., *"Microseismic Monitoring: Inside and Out"*, JPT, Vol. 61, pp. 80-85, November 2009a.

Warpinski N., Wolhart S.L. and Wright C.A., *"Analysis and Prediction of Microseismicity Induced by Hydraulic Fracturing"*, SPE Journal, Vol. 9, pp. 24-33, March 2004.

Warpinski N.R., *"Integrating Microseismic Monitoring With Well Completions, Reservoir Behavior, and Rock Mechanics"* SPE 125239, SPE Tight Gas Completions Conference, San Antonio, TX, June 15-17, 2009b.

Warpinski N.R., Griffin L.G., Davis E.J. and Grant T., *"Improving Hydraulic Frac Diagnostics by Joint Inversion of Downhole Microseismic and Tiltmeter Data"* SPE 102690, SPE Annual Technical Conference and Exhibition, San Antonio, TX, September 24 -27, 2006.

Warpinski N.R., Wright T.B., Uhl J.E., Engler B.P., Drozda P.M., Peterson R.E. and Branagan P.T., *"Microseismic Monitoring of the B-Sand Hydraulic Fracture Experiment at the DOE/GRI Multisite Project"* , SPE Journal, Vol. 4, pp. 242-250, September 1999.

Waters G., Dean B., Downie R., Kerrihard K., Austbo L.and McPherson B., *"Simultaneous Hydraulic Fracturing of Adjacent Horizontal Wells in the Woodford Shale"* SPE 119635, SPE Hydraulic Fracturing Technology Conference, The Woodlands, TX, January 19-21, 2009.

Weijers L., Wright C., Mayerhofer M. and Cipolla C., *"Developing Calibrated Fracture Growth Models for Various Formations and Regions Across the United States"* SPE 96080, SPE Annual Technical Conference and Exhibition, Dallas, TX, October 9-12, 2005.

Weijers, L., personal communication, 2010 and 2011.

Wills P.B., DeMartini D.C., Vinegar H.J., Shylapobersky J., Deeg W.F., Woerpel J.C., Fix J.E., Sorrells G.G. and Adair R.G., *"Active and passive imaging of hydraulic fractures"*, The Leading Edge, Vol. 11, pp. 15-22, July 1992.

Zhu X., Gibson J., Ravindran N., Zinno R. and Sixta D., *"Seismic Imaging of hydraulic fractures in Carthage tight sands: A pilot study"*, The Leading Edge, Vol. 15, p. 218, March 1996.

Zimmer U., Maxwell S., Waltman C. and Warpinski N., *"Microseismic Monitoring Quality-Control (QC) Reports as an Interpretative Tool for Nonspecialists"*, SPE Journal, Vol. 14, pp. 737-745, December 2009.

APPENDIX A

Table A.1: Model Parameter Overview of Parameters Decreased by 25% for the Sensitivity Analysis of the Longitudinal Combined Microseismic Models

	Stage I	*Stage II*	*Stage III*	*Stage IV*	*Stage V*
PDMSF [1/psi]	0.003375	0.00375	0.0015	0.001875	0.002625
PDL [1/psi]	0.0001875	0.000225	0.001125	0.00135	0.000675
TSC [-]	0.0001875	0.0002175	0.001125	0.00135	0.000675
Tort. Pre-Factor [psi/bpm^2]	0.1125	0.1125	0.075	0.075	0.1125
Tectonic Strain [microstrains]	52.5	48.75	33.75	41.25	97.5
Perf. Coeff. [-]	0.2775	0.225	0.18	0.1875	0.3975
Frict. Coeff. [-]	0.0225	0.0375	0.045	0.0525	0.0675
Perf. Factor [-]	0.2625 *(07:15:47-07:37:56)* 0.3375 *(07:37:57-07:40:06)* 0.4275 *(07:40:07-07:49:09)* 0.465 *(07:49:10-08:12:56)* 0.285 *(08:12:57-08:16:31)* 0.2475 *(08:16:32-10:29:00)*	0.3375 *(14:26:30-14:50:00)* 0.45 *(14:50:01-15:18:27)* 0.2625 *(15:18:28-15:24:34)* 0.225 *(15:24:35-15:27:00)* 0.1875 *(15:27:01-17:34:00)*	0.4125 *(07:02:50-07:20:14)* 0.6225 *(07:20:15-07:51:23)* 0.24 *(07:51:24-07:57:09)* 0.15 *(07:57:10-10:08:00)*	0.5175 *(13:18:00-13:39:22)* 0.5775 *(13:39:23-14:08:18)* 0.2625 *(14:08:19-14:12:00)* 0.1875 *(14:12:01-15:22:20)* 0.15 *(15:22:21-15:30:26)* 0.135 *(15:30:27-15:42:42)* 0.12 *(15:42:43-15:53:04)* 0.0975 *(15:53:05-16:26:00)*	0.4125 *(07:09:00-07:36:47)* 0.435 *(07:36:48-07:41:17)* 0.45 *(07:41:18-07:58:46)* 0.75 *(07:58:47-10:18:00)*

Table A.2: Model Parameter Overview of Parameters Increased by 25% for the Sensitivity Analysis of the Longitudinal Combined Microseismic Models

	Stage I	*Stage II*	*Stage III*	*Stage IV*	*Stage V*
PDMSF [1/psi]	0.005625	0.00625	0.0025	0.003125	0.004375
PDL [1/psi]	0.0003125	0.000375	0.001875	0.00225	0.001125
TSC [-]	0.0003125	0.0003625	0.001875	0.00225	0.001125
Tort. Pre-Factor [psi/bpm^2]	0.1875	0.1875	0.125	0.125	0.1875
Tectonic Strain [microstrains]	87.5	81.25	56.25	68.75	162.5
Perf. Coeff. [-]	0.4625	0.375	0.3	0.3125	0.6625
Frict. Coeff. [-]	0.0375	0.0625	0.075	0.875	0.1125
Perf. Factor [-]	0.4375 *(07:15:47-07:37:56)* 0.5625 *(07:37:57-07:40:06)* 0.7125 *(07:40:07-07:49:09)* 0.775 *(07:49:10-08:12:56)* 0.475 *(08:12:57-08:16:31)* 0.4125 *(08:16:32-10:29:00)*	0.5625 *(14:26:30-14:50:00)* 0.75 *(14:50:01-15:18:27)* 0.4375 *(15:18:28-15:24:34)* 0.375 *(15:24:35-15:27:00)* 0.3125 *(15:27:01-17:34:00)*	0.6875 *(07:02:50-07:20:14)* 1.0375 *(07:20:15-07:51:23)* 0.4 *(07:51:24-07:57:09)* 0.25 *(07:57:10-10:08:00)*	0.8625 *(13:18:00-13:39:22)* 0.9625 *(13:39:23-14:08:18)* 0.4375 *(14:08:19-14:12:00)* 0.3125 *(14:12:01-15:22:20)* 0.25 *(15:22:21-15:30:26)* 0.225 *(15:30:27-15:42:42)* 0.20 *(15:42:43-15:53:04)* 0.1625 *(15:53:05-16:26:00)*	0.6875 *(07:09:00-07:36:47)* 0.725 *(07:36:48-07:41:17)* 0.75 *(07:41:18-07:58:46)* 1.25 *(07:58:47-10:18:00)*

Table A.3: Model Parameter Overview of Parameters Decreased by 25% for the Sensitivity Analysis of the Transverse Combined Microseismic Models

	Stage I	*Stage II*	*Stage III*	*Stage IV*	*Stage V*
PDMSF [1/psi]	0.0015	0.00375	0.00075	0.0015	0.0015
PDL [1/psi]	0.000375	0.0003	0.00075	0.000375	0.00075
TSC [-]	0.000375	0.0002475	0.00075	0.000375	0.00075
Tort. Pre-Factor [psi/bpm^2]	0.075	0.1125	0.075	0.075	0.1125
Tectonic Strain [microstrains]	37.5	48.75	37.5	37.5	105
Perf. Coeff. [-]	0.315	0.24	0.18	0.1875	0.3975
Frict. Coeff. [-]	0.0225	0.0375	0.045	0.0525	0.0675
Perf. Factor [-]	0.225 *(07:15:47-07:37:56)* 0.3375 *(07:37:57-07:40:06)* 0.3825 *(07:40:07-07:49:09)* 0.4125 *(07:49:10-08:12:56)* 0.21 *(08:12:57-08:16:31)* 0.18 *(08:16:32-09:07:47)* 0.165 *(09:07:48-09:12:28)* 0.15 *(09:12:29-09:27:52)* 0.135 *(09:27:53-09:32:33)* 0.1125 *(09:32:34-09:42:41)* 0.09 *(09:42:42-09:57:53)* 0.075 *(09:57:54-10:29:00)*	0.3375 *(14:26:30-14:50:00)* 0.45 *(14:50:01-15:18:27)* 0.1875 *(15:18:28-15:24:34)* 0.15 *(15:24:35-15:27:00)* 0.1425 *(15:27:01-16:09:55)* 0.1275 *(16:09:56-16:19:46)* 0.12 *(16:19:47-16:20:39)* 0.1125 *(16:20:40-16:31:13)* 0.105 *(16:31:14-16:39:34)* 0.09 *(16:39:35-16:49:25)* 0.0825 *(16:49:26-17:12:08)* 0.0675 *(17:12:09-17:34:00)*	0.4125 *(07:02:50-07:20:14)* 0.6075 *(07:20:15-07:51:23)* 0.1725 *(07:51:24-07:57:09)* 0.1275 *(07:57:10-10:08:00)*	0.4875 *(13:18:00-13:39:22)* 0.54 *(13:39:23-14:08:18)* 0.2025 *(14:08:19-14:12:00)* 0.165 *(14:12:01-15:11:41)* 0.1425 *(15:11:42-15:22:00)* 0.0975 *(15:22:01-15:30:26)* 0.09 *(15:30:27-15:42:42)* 0.075 *(15:42:43-15:53:04)* 0.0525 *(15:53:05-16:26:00)*	0.3375 *(07:09:00-07:36:47)* 0.3675 *(07:36:48-07:41:17)* 0.405 *(07:41:18-07:58:46)* 0.255 *(07:58:47-08:10:28)* 0.2325 *(08:10:29-08:57:00)* 0.2025 *(08:57:01-10:18:00)*

Table A.4: Model Parameter Overview of Parameters Increased by 25% for the Sensitivity Analysis of the Transverse Combined Microseismic Models

	Stage I	*Stage II*	*Stage III*	*Stage IV*	*Stage V*
PDMSF [1/psi]	0.0025	0.00625	0.00125	0.0025	0.0025
PDL [1/psi]	0.000625	0.0005	0.00125	0.000625	0.00125
TSC [-]	0.000625	0.0004125	0.00125	0.000625	0.00125
Tort. Pre-Factor [psi/bpm^2]	0.125	0.1875	0.125	0.125	0.1875
Tectonic Strain [microstrains]	62.5	81.25	62.5	62.5	175
Perf. Coeff. [-]	0.525	0.40	0.30	0.3125	0.6625
Frict. Coeff. [-]	0.0375	0.0625	0.075	0.0875	0.1125
Perf. Factor [-]	0.375 *(07:15:47-07:37:56)* 0.5625 *(07:37:57-07:40:06)* 0.6375 *(07:40:07-07:49:09)* 0.6875 *(07:49:10-08:12:56)* 0.35 *(08:12:57-08:16:31)* 0.30 *(08:16:32-09:07:47)* 0.275 *(09:07:48-09:12:28)* 0.25 *(09:12:29-09:27:52)* 0.225 *(09:27:53-09:32:33)* 0.1875 *(09:32:34-09:42:41)* 0.15 *(09:42:42-09:57:53)* 0.125 *(09:57:54-10:29:00)*	0.5625 *(14:26:30-14:50:00)* 0.75 *(14:50:01-15:18:27)* 0.3125 *(15:18:28-15:24:34)* 0.25 *(15:24:35-15:27:00)* 0.2375 *(15:27:01-16:09:55)* 0.2125 *(16:09:56-16:19:46)* 0.20 *(16:19:47-16:20:39)* 0.1875 *(16:20:40-16:31:13)* 0.175 *(16:31:14-16:39:34)* 0.15 *(16:39:35-16:49:25)* 0.1375 *(16:49:26-17:12:08)* 0.1125 *(17:12:09-17:34:00)*	0.6875 *(07:02:50-07:20:14)* 1.0125 *(07:20:15-07:51:23)* 0.2875 *(07:51:24-07:57:09)* 0.2125 *(07:57:10-10:08:00)*	0.8125 *(13:18:00-13:39:22)* 0.90 *(13:39:23-14:08:18)* 0.3375 *(14:08:19-14:12:00)* 0.275 *(14:12:01-15:11:41)* 0.2375 *(15:11:42-15:22:00)* 0.1625 *(15:22:01-15:30:26)* 0.15 *(15:30:27-15:42:42)* 0.125 *(15:42:43-15:53:04)* 0.0875 *(15:53:05-16:26:00)*	0.5625 *(07:09:00-07:36:47)* 0.6125 *(07:36:48-07:41:17)* 0.675 *(07:41:18-07:58:46)* 0.425 *(07:58:47-08:10:28)* 0.3875 *(08:10:29-08:57:00)* 0.3375 *(08:57:01-10:18:00)*

CONTENTS OF THE CD-ROM

APPENDIX B:

- GOHFER™ Models
  - Combined Models
    - Stage I
    - Stage II
    - Stage III
    - Stage IV
    - Stage V
  - Downhole Models
    - Stage II
    - Stage III
    - Stage IV
    - Stage V
  - Surface Models
    - Stage I
    - Stage II
    - Stage III
    - Stage IV
    - Stage V
- Log Files
  - Treatment Well – Part 1
  - Treatment Well – Part 2
- Microseismic Data
  - Downhole
  - Surface
- Pump Curves
  - Stage I
  - Stage II
  - Stage III
  - Stage IV
  - Stage V
- Transform™ Model